Numerieke studie van magnetische processen:
uitbreiding van de Landau-Lifshitz-Gilbert-aanpak
van de nano- tot de microschaal

Numerical Study of Magnetic Processes:
Extending the Landau-Lifshitz-Gilbert Approach
from Nanoscale to Microscale

Ben Van de Wiele

Promotoren: prof. dr. ir. L. Dupré, prof. dr. ir. D. De Zutter
Proefschrift ingediend tot het behalen van de graad van
Doctor in de Ingenieurswetenschappen: Toegepaste Natuurkunde

Vakgroep Elektrische Energie, Systemen en Automatisering
Voorzitter: prof. dr. ir. J. Melkebeek
Faculteit Ingenieurswetenschappen
Academiejaar 2009 - 2010

UNIVERSITEIT
GENT

ISBN 978-90-8578-333-6
NUR 928, 959
Wettelijk depot: D/2010/10.500/9

Numerical Study of Magnetic Processes: Extending the Landau-Lifshitz-Gilbert Approach from Nanoscale to Microscale

Ben Van de Wiele

Dissertation submitted to obtain the academic degree of
Doctor in Physical Engineering

Publicly defended at Ghent University on March 2, 2010

Supervisors:

Prof. dr. ir. L. Dupré
Electrical Energy Laboratory
Department of Electrical Energy, Systems and Automation
Faculty of Engineering, Ghent University
St.-Pietersnieuwstraat 41, B-9000 Ghent, Belgium

Prof. dr. ir. D. De Zutter
Department of Information Technology
Faculty of Engineering, Ghent University
St.-Pietersnieuwstraat 41, B-9000 Ghent, Belgium

Members of the examining board:

Prof. dr. ir. R. Van de Walle (chairman)	Ghent University, Belgium
Dr. ir. I. Bogaert (secretary)	Ghent University, Belgium
Prof. dr. ir. L. Dupré (supervisor)	Ghent University, Belgium
Prof. dr. ir. D. De Zutter (supervisor)	Ghent University, Belgium
Dr. ir. O. Bottauscio	Istituto Nazionale di Ricerca Metrologica, Italy
Prof. dr. ir. J. Melkebeek	Ghent University, Belgium
Prof. dr. B. Van Waeyenberge	Ghent University, Belgium
Prof. dr. R. Van Keer	Ghent University, Belgium

Dankwoord

Vier en een half jaar zijn gepasseerd. Velen hebben me tijdens deze periode gevraagd: 'Wat doe je nu eigenlijk?' Het antwoord bleek niet altijd even eenvoudig. Neen, wij hebben geen drie maanden zomerverlof en, ja, als je doctoreert ben je een soort student, maar word je tóch betaald. Ik probeerde uit te leggen dat natuurkunde ondanks de benaming slechts heel weinig te maken heeft met de dieren- en plantenwereld. Neen, ik onderzocht wat er zich afspeelde binnenin magnetische materialen, magneten, je weet wel... Wie er écht meer van willen weten kan grasduinen in dit boek.

Doctoreren bleek een heel uitdagende job te zijn die, op het eerste zicht, nogal contraproductief leek: voor elke onderzoeksvraag die je oploste kwamen er verschillende nieuwe vragen bij. Op die manier kwamen er steeds meer bomen bij in het spreekwoordelijke bos waarin het alsmaar makkelijker werd verloren te lopen. Het is slechts dankzij de vele discussies met jullie, promotoren, dat ik tussen de bomen door het bos kon blijven zien! Femke, je bent te vroeg van ons heengegaan. Zonder jouw klare kijk op de wiskundige formules en je inzicht in de numerieke algoritmes zou dit werk onmogelijk geweest zijn. Daniël, bedankt voor de interesse in mijn onderzoek en de snelle opvolging ervan. Luc, ik apprecieer je kritische en soms pertinente, terugkerende vragen ten zeerste. Samen met de daaropvolgende intense discussies gaven ze me inzicht in de verschillende problemen, eigen aan mijn onderzoek. Ik geef toe, ondanks de duidelijke probleemstelling zijn niet alle vragen opgelost... Bedankt ook dat ik steeds mijn mening kan zeggen zonder een blad voor de mond te hoeven nemen, ik beschouw dit niet als vanzelfsprekend!

Goed onderzoek kan enkel verricht worden in een aangename werkomgeving en, bureaugenoten, aangenaam werken is het zeker geweest. In onze bureau heerst een voor mij ideale mix van werkijver en ontspanning, vaak ondersteund door een vrolijk deuntje. Tom, bedankt om de 'vergaderingen' op vrijdagmiddag voor te zitten. Lode, ik zal de ochtendlijke gesprekken over de kindjes steeds onthouden. Ik wens je het beste toe in je nieuwe job. Guillaume Hartenbreker, nooit verlegen om een guitige kwinkslag, bij jou kan ik steeds terecht. Ik hoop ten zeerste dat we nog vele jaren kunnen samenwerken. Nele, je bent er pas enkele maanden, maar onderzoekstalent herken je meteen, jij hebt het! Het is een plezier om je in de bureau te hebben. Bedankt ook aan alle andere collega's voor de ontspannende babbels. Jan Fostier

bedank ik graag voor de tijd die hij steeds wou vrijmaken wanneer ik (nog maar eens) een implementatiefout had waar ik zelf niet aan uit raakte.

De werking van een onderzoeksgroep is als een (elektrische?) machine waarin elk radertje onmisbaar is. Ik bedank hier vooreerst de vakgroepvoorzitters Prof. Melkebeek (EESA), Prof. Lagasse en later Prof. De Zutter (Intec) voor de onderzoeksmogelijkheden die ze me gegeven hebben. Ook de verschillende leden van de ATP staf verdienen mijn dank voor hun bereidwillige hulp. In het bijzonder wil ik Ingrid Dubois, ooit aan mij voorgesteld als de moeder-kloek van de onderzoeksgroep EELAB, in de schijnwerpers plaatsen. Nic Vermeulen en Bert De Vuyst bedank ik voor het draaiende houden van het uitgebreide computerpark.

Een gezonde geest in een gezond lichaam. Pol en Siesse, de 20 km door Brussel is de ideale (wekelijkse?) drogreden om de stoere mannenpraat nog eens boven te halen en meer nog, om samen met de vrouwen, Annelies en Tine, eens gezellig bij te klappen. Bert, Mieke, Steven, Pim en Veerle, een Lokers cafébezoek is steeds een verademing. Vanaf deze zomer hoop ik er vaker bij te zijn. Vrienden, we zien elkaar minder dan vroeger, maar daarom zijn de contacten niet minder deugddoend.

Mijn ouders, papa en mama, het is goed om weten dat we steeds kunnen terugvallen op jullie. Jullie hebben me alle kansen gegeven in het leven die je als ouder kan geven. Dit werk is ook jullie verdienste! Ook mijn zussen, hun wederhelften en schoonfamilie bedank ik voor hun interesse, steun en hulp in de voorbije jaren en vooral in de laatste maanden. Het geluk schuilt in de kleine dingen zegt men. Voor jou, Arne, gaat dit zeker op, alhoewel je snel groot wordt. Wat er tijdens de werkdag ook gebeurt, je speelplezier en vrolijk gebabbel doen direct alles vergeten. Je zal een fiere grote broer zijn! Sara, bedankt dat je geduldig mijn scherpe kantjes wil bijschaven. Het is niet vanzelfsprekend om tegelijkertijd je doctoraat af te werken, een zoon groot te brengen en onze jongste spruit te dragen. Ik bewonder je hiervoor! Je bent mijn toeverlaat, mijn liefde zonder wie ik dit werk nooit tot een goed einde zou brengen.

Een man wiens grijze haren niet enkel een immense ervaring in het magnetische onderzoeksdomein verbergen, maar ook een enorme levenswijsheid, vatte ons onlangs als volgt samen wat *geluk in het leven* uitmaakt: op de eerste plaats '*a good health*', op de tweede plaats '*to love and to be loved*' en op de derde plaats '*to be passionate in your profession*'. Sara, Arne, kleine spruit in mama's buik, familie, vrienden, bureaugenoten en promotoren, jullie dragen bij tot het geluk in mijn leven! Bedankt hiervoor!

Ben Van de Wiele
13/02/2010

Contents

Samenvatting

Het gebruik van ferromagnetische materialen is alomtegenwoordig in onze moderne samenleving. Men vindt ze terug in verschillende toepassingen. In de informatietechnologie worden ze gebruikt als opslagmedium voor zowel analoge opslagmedia (bijvoorbeeld cassettebanden) als voor digitale opslagmedia (vb. MRAM). In de laatste jaren wordt als ICT-toepassing ook onderzoek gedaan om ferromagnetische materialen te gebruiken voor datatransmissie. Ferromagnetische materialen zijn tevens van essentieel belang in elektrische vermogenstoestellen zoals transformatoren en elektrische machines en in kleinere elektrische actuatoren. In deze toepassingen wordt het magnetisch materiaal gebruikt als circuit voor de magnetische fluxlijnen. Ook de mechanische eigenschappen van ferromagnetische materialen worden veelvuldig uitgebuit. De sterkte van ijzergebaseerde materialen wordt gebruikt in de civiele techniek, in het transport,... In alle voornoemde magnetische én mechanische toepassingen bepaalt de microstructuur van het materiaal de (macroscopische) magnetische en mechanische eigenschappen.

In het ICT toepassingsgebied hebben numerieke modellen gebaseerd op de micromagnetische theorie een zeer belangrijke rol gespeeld in de ontwikkeling en verbetering van nieuwe magnetische componenten. De hier gebruikte term 'micromagnetische theorie' is enigszins misleidend aangezien de theorie de magnetisatieprocessen beschrijft op de nanoschaal. Aangezien de term echter in de wetenschappelijke literatuur sterk ingeburgerd is zullen we deze verder in dit doctoraatsproefschrift gebruiken. De kleine, submicrometerafmetingen vergemakkelijken de numerieke beschrijving van de magnetisatieprocessen in het ICT-toepassingsgebied. In dit doctoraatswerk echter breiden we het toepassingsgebied van numerieke micromagnetische berekeningen uit van de klassieke nanometerschaal tot de nieuwe micrometerschaal. Op die manier kunnen micromagnetische simulaties een beter inzicht verschaffen in de magnetische processen die de efficiëntie bepalen van elektrisch staal, gebruikt in vermogenstoepassingen en actuatoren. Verder kan een micromagnetische studie van de relaties tussen de microstructuur van het materiaal enerzijds en de macroscopische magnetische eigenschap-

pen anderzijds belangrijk zijn in de ontwikkeling van magnetische niet-destructieve evaluatietechnieken voor bijvoorbeeld constructiestaal. Inderdaad, gedurende het gebruik kan een veranderende microstructuur resulteren in een eventueel gevaarlijke verandering in de mechanische eigenschappen (breuk). Omdat nu ook het magnetische gedrag afhangt van de microstructuur zullen veranderingen in de microstructuur ook veranderingen in de magnetische eigenschappen veroorzaken. Het opvolgen van de magnetische eigenschappen kan dus een vroege detectie van dreigend gevaar mogelijk maken.

Het eerste deel van deze thesis geeft een overzicht van de micromagnetische theorie. Het magnetostatisch veld krijgt hier speciale aandacht omdat dit interactieveld een zeer grote invloed heeft op de magnetisatieprocessen in ferromagnetische materialen. In macroscopische applicaties is ook het hysteresisgedrag van het ferromagnetische materiaal van groot belang. Daarom introduceren we magnetische hysteresis als een natuurlijk gevolg van de energiebeschouwingen in de micromagnetische theorie.

In de micromagnetische theorie beschrijft de Landau-Lifshitz-Gilbert (LLG) vergelijking de dynamica van de lokale magnetisatie op de nanometerruimteschaal en de picosecondetijdsschaal. Om deze theorie toe te passen op de micrometerruimteschaal moeten dan ook geavanceerde numerieke algoritmes toegepast worden. Deze technieken worden in Deel II van dit werk voorgesteld. Vooreerst is een nieuw stap-in-de-tijdalgoritme gebruikt voor het oplossen van de LLG vergelijking. Het stap-in-de-tijdschema is gebaseerd op de analytische oplossing van de LLG vergelijking onder een constant interactieveld. Bijgevolg behoudt deze oplossingsmethode de intrinsieke eigenschappen van de LLG vergelijking en maakt ze gebruik van grote stappen in de tijd mogelijk. Dit minimaliseert het aantal benodigde evaluaties van het interactieveld en optimaliseert het geheugengebruik. Het ontwikkelde stap-in-de-tijd schema is uitgebreid gevalideerd door het vergelijken van resultaten voor gesimuleerde omkeringsprocessen met resultaten bekomen met andere micromagnetische schema's ontwikkeld aan andere instituten.

Om de rekentijd nog verder terug te dringen werd de evaluatie van één enkel interactieveld geoptimaliseerd. Een eindige-differentie-discretisatie is toegepast om het interactieveld —bestaande uit het Zeeman, het magnetostatisch, het uitwisselings-, het anisotropie- en het magneto-elastisch veld— te bepalen doorheen het beschouwde materiaalmonster. Omdat bijna alle rekentijd besteed wordt aan het evalueren van het magnetostatische veld zijn twee verschillende algoritmes onderzocht om deze berekeningen te versnellen. Vooreerst zijn schema's gebaseerd op snelle Fourier transformaties geïmplementeerd ter bepaling van het magnetostatische veld. Deze schema's buiten de convolutiestructuur uit, aanwezig in de uitdrukking voor het magnetostatische veld. Ze hebben een zeer grote tijdsefficiëntie, maar behoeven een aanzienlijke hoeveelheid computergeheugen. Vervolgens is een numeriek

schema gebaseerd op het snelle multipoolalgoritme bestudeerd. In dit schema is de magnetostatische kern herschreven in termen van sferische harmonieken zodat de analytische uitdrukking gesplitst is in een deel afkomstig van de bron en een deel afkomstig van het observatiepunt. Ondanks de geoptimaliseerde implementatie is dit schema ongeveer een factor vijf trager vergeleken met het snelle Fourier transformatie gebaseerde algoritme. Het geheugengebruik is echter een factor acht voordeliger.

De benodigde rekentijd hangt sterk af van de nauwkeurigheid waarmee het interactieveld wordt berekend. In het bijzonder versnelt het gebruik van een grovere ruimtediscretisatie de berekeningen enorm. In de klassieke submicrometer micromagnetische toepassingen is de grootte van de ruimtediscretisatie beperkt door de materiaalafhankelijke uitwisselingslengte. In dit doctoraatswerk bepalen we het effect van het gebruik van een tot viermaal grovere ruimtediscretisatie wanneer macroscopische magnetische eigenschappen worden bestudeerd in het nieuwe toepassingsgebied met werkstukdimensies groter dan $1\,\mu$m. In dezelfde context is ook de invloed van de snellere, maar minder nauwkeurige evaluatie van het magnetostatische veld bestudeerd. We concluderen dat zowel het gebruik van een grovere discretisatie als het gebruik van een minder nauwkeurig evaluatieschema voor het magnetostatische veld mogelijk zijn als men niet beoogt de kleine ruimtelijke details van de magnetisatieprocessen te ontleden.

In het derde deel wordt het ontwikkelde numerieke model gebruikt in drie verschillende toepassingsgebieden. Eerst is een klassiek toepassingsgebied beschouwd. De invloed van de geometrie en de temperatuur op omklapprocessen en op de stabiliteit van micromagnetische evenwichtstoestanden in magnetische nanostrips is onderzocht. Omklapprocessen worden hier gedefinieerd als de mechanismen die plaatsvinden bij het evolueren van één bepaalde magnetische verzadigingstoestand naar een verzadigingstoestand met tegengestelde magnetisatie. De simulaties tonen hoe de geometrie van de uiterste randen de relaxatietijd sterk beïnvloedt: een scherpe tip alsook toegevoegde nucleatieplaatsen versnellen het omklapproces. Ook een stijgende temperatuur geeft aanleiding tot kortere omklaptijden wegens de groter wordende thermische fluctuaties in het materiaal. In hetzelfde klassieke toepassingsgebied zijn de omklapmodes onderzocht in oneindig lange ferromagnetische draden. We besloten dat, afhankelijk van de dimensies van de dwarsdoorsnede, het omklapmechanisme evolueert van een precessionele rotatiebeweging gecombineerd met een knikbeweging (<100 nm), over een mechanisme gedomineerd door verschillende magnetische wervels (tot 500 nm) naar een omklappingsmechanisme bepaald door domeinvorming.

Een tweede toepassingsgebied waarin we het ontwikkelde micromagnetische schema gebruiken is de studie van magnetische domeinen in films met loodrechte uniaxiale anisotropie. Verschillende modellen in de

domeintheorie beschrijven hier de verwachtte domeinconfiguraties, afhankelijk van de anisotropiesterkte. Deze modellen veronderstellen dat er uniform gemagnetiseerde regio's aanwezig zijn in het ferromagnetische object dat groter is dan $1\,\mu$m. Het micromagnetische model is aangewend om de domeinconfiguraties te simuleren. De vergelijking tussen de simulatieresultaten en de domeinconfiguraties voorspeld door de verschillende domeintheoriemodellen toont dat zelfs het meest verfijnde domeintheoriemodel de effectieve domeinstructuur slechts gedeeltelijk beschrijft. Deze vergelijking valideert het micromagnetische model op de ruimteschaal groter dan $1\,\mu$m en bewijst zijn toegevoegde waarde in dit onderzoeksdomein.

Als laatste onderzoeksdomein, is het micromagnetische schema gebruikt bij de studie van hysteresiseigenschappen van ferromagnetische materialen. In dit deel is het ontwikkelde micromagnetische hysteresismodel vergeleken met het klassieke, macroscopische Preisach model. Eerst zijn de geheugeneigenschappen onderzocht. Dit zijn macroscopische eigenschappen die bij constructie zijn vervat in het Preisach model en experimenteel waargenomen worden. Omdat het micromagnetische model gebaseerd is op de fysische interacties aanwezig in het materiaal moeten deze eigenschappen ook inherent aanwezig zijn in het model. Dit werd aangetoond in verschillende simulaties en valideert dus ook het micromagnetische hysteresismodel. Ten tweede zijn de energiestromen in het ferromagnetische systeem geanalyseerd. De energie die is toegevoegd in, gedissipeerd door en opgeslagen in het ferromagnetische materiaal is uitgesplitst in zowel het micromagnetische hysteresismodel als in het macroscopische Preisach model. Een opmerkelijke overeenkomst tussen beide modellen is bekomen. Meer nog, in het micromagnetische hysteresismodel is verder een onderscheid gemaakt tussen de verschillende mechanismen aangewend om de energie op te slaan in het ferromagnetische materiaal. Dit maakte het mogelijk om de herschikking van de interne energie te bestuderen bij het doorlopen van de hysteresislus. Deze studie is opnieuw een validatie van het micromagnetische hysteresismodel en toont zijn vermogen om ons inzicht in ferromagnetische hysteresisprocessen verder te vergroten.

Summary

In our modern society, ferromagnetic materials are used in many applications. In information technology, they are used as the storage medium in analogue storage devices as magnetic tapes and in digital storage devices such as magnetic random access memory's (MRAMs). Furthermore, research is now ongoing to use ferromagnetic materials for data transmission. Ferromagnetic materials are also indispensable in electrical power devices such as transformers and electrical machines and in smaller electrical actuators. Here, the ferromagnetic material guides the magnetic flux lines. Also the mechanical properties of ferromagnetic materials are exploited ubiquitously. The strength of iron based materials is used in construction, transportation, etc. In all these magnetic and mechanic applications, the microstructure of the material determines the (macroscopic) magnetic and mechanical properties.

In the information technology application area, numerical models based on the micromagnetic theory have enabled the development of the magnetic devices. Here, the small sub-micrometer dimensions of the magnetic samples facilitated the numerical description. The term 'micromagnetic theory' can be somewhat misleading since it describes magnetization processes on the *nanometer* scale. We will stick however to this term since it is widely adopted in literature. In this PhD, we extend the numerical micromagnetic application area from the (classical) nanometer scale to the micrometer scale. In this way, micromagnetic simulations can provide a better insight in the magnetic processes which determine the efficiency of electrical steels used in power devices and actuators. Furthermore, the micromagnetic study of the relations between the materials' microstructure and the corresponding macroscopic magnetic properties is important in the development of magnetic non destructive evaluation techniques for e.g. construction steel. Indeed, during life time, a changing microstructure can result in a possibly dangerous change in the mechanical properties (failure). Since also the magnetic behavior depends on the microstructure, changes in the microstructure will also imply changing magnetic properties. Hence, the monitoring of macroscopic magnetic properties can enable the early detection of threatening failure.

In the first part of this thesis, an overview is given of the micromagnetic theory. Special attention is devoted to the magnetostatic field since this interaction field has a very large influence on the magnetization processes in soft ferromagnetic materials. In the macroscopic applications, also the hysteresis behavior of the ferromagnetic material is very important. Therefore, we introduce magnetic hysteresis as a natural consequence of the energy considerations made in the micromagnetic theory.

In the micromagnetic theory, the Landau-Lifshitz-Gilbert (LLG) equation describes the local magnetization dynamics on the nanometer length scale and the picosecond time scale. To employ the theory on the micrometer length scale, highly efficient numerical techniques have to be adopted. These techniques are presented in Part II of this thesis. A new time stepping algorithm is used to time step the LLG equation. The time stepping scheme is based on the analytical solution of the LLG equation under constant interaction fields. Consequently, this solution method preserves the intrinsic properties of the LLG equation and enables the use of large time steps. This minimizes the number of field evaluations and optimizes the memory requirements. The developed time stepping scheme is extensively validated by comparing simulation results of reversal processes with other micromagnetic schemes, developed at other institutions.

To further minimize the execution time, the evaluation of one single field is optimized. A finite difference discretization is applied to determine the effective field composed of the Zeeman, magnetostatic, exchange, anisotropy and magnetoelastic field throughout the considered sample. Since almost all CPU time goes to the evaluation of the magnetostatic field, two different algorithms are investigated to accelerate the computations. First, fast Fourier transform based schemes are used to evaluate the magnetostatic field. These schemes exploit the convolution structure of the expression for the magnetostatic field. They have a very high time efficiency but require considerable memory. Second, a scheme based on the fast multipole method is studied. In this scheme, the magnetostatic interaction kernel is rewritten in terms of spherical harmonics to split the analytical expression in a source and receiver part. Despite the optimized implementation, this scheme is about a factor 5 less time efficient, but requires also a factor 8 less memory resources compared to the fast Fourier transform based schemes.

The CPU time strongly depends on the accuracy used to evaluate the interaction field. In particular, the use of a larger discretization size vastly accelerates the computations. In the classical sub-micrometer micromagnetic applications, the spatial discretization is restricted to the material dependent exchange length. In this PhD, we determine the effect of employing a four times coarser discretization size when macroscopic magnetic properties are studied in the new application area with sample dimensions larger than $1\,\mu$m. In the

same context, also the influence of the faster, low accuracy evaluation of the magnetostatic field is studied. It is concluded that both the use of a coarser discretization size and the use of a low accuracy evaluation scheme for the magnetostatic field are possible if one is not interested to resolve the fine scale details of the magnetization processes.

In the third part, the developed numerical model is applied to three different application areas. First, a classical application area is considered. On the one hand, the influence of geometry and temperature on the magnetic reversal mechanism and stability of the micromagnetic equilibrium state is studied in nanostrips. The simulations show how the geometry of the outer edges of the strip has a large influence on the relaxation time: sharp tips and nucleation pads accelerate the reversal. Also an increasing temperature speeds up the reversal process due to the growing thermal fluctuations present in the material. On the other hand, reversal modes are investigated in infinite ferromagnetic wires. It is found that, depending on the cross sectional dimensions, the reversal mechanism evolves from a precessional switching movement combined with a buckling effect for small dimensions (<100 nm) over a reversal mode dominated by various vortices (up to 500 nm) to a reversal mechanism determined by domain formation.

A second research area to which we apply the developed micromagnetic scheme is the study of magnetic domains in platelets with perpendicular uniaxial anisotropy. Different domain theory models describe the expected domain configurations, depending on the anisotropy strength. These models are based on the assumption that only uniformly magnetized regions exist in ferromagnetic samples larger than $1\,\mu$m. The micromagnetic numerical scheme is used to simulate the domain configurations. The comparison of the simulation results to the domain configurations predicted by the different domain theory models reveals that even the most refined domain theory model is only to a limited extent capable of describing the actual domain configurations. The comparison validates the micromagnetic model on the length scale larger than $1\,\mu$m and demonstrates its added value in this research domain.

As a last research area, the micromagnetic scheme is used to study hysteresis properties of ferromagnetic materials. Here, the developed micromagnetic hysteresis model is compared to the classical, macroscopic Preisach model. First, the memory properties are considered. These are macroscopic hysteresis properties that are experimentally observed in all magnetic materials and described by the Preisach model by construction. Since the micromagnetic hysteresis model is physics based, it should incorporate the memory properties inherently. This is proven in different simulations which validates the micromagnetic hysteresis model. Second, the energy flows in the ferromagnetic system are studied. The energy added to, dissipated by and stored in the ferromagnetic material is separated in the micromagnetic hysteresis scheme

as well as in the macroscopic Preisach model. A remarkable correspondence is found between the two models. Moreover, in the micromagnetic hysteresis model, a distinction is made between the different mechanisms to store the internal energy and it is shown how the internal energy is rearranged when running through the hysteresis loop. This study again validates the developed micromagnetic hysteresis model and shows its ability to further increase our knowledge about the ferromagnetic hysteresis processes.

List of abbreviations, notations and symbols

Abbreviations

2D	two dimensional
2.5D	two and a half dimensional
3D	three dimensional
BEM	boundary element method
CPU	central processing unit
FORC	first order reversal curve
FFT	fast Fourier transform
FFTW	fastest Fourier transform of the West
FEM	finite element method
FD	finite difference
FMM	fast multipole method
LLG	Landau-Lifshitz-Gilbert
MP	multipole
NDE	non-destructive evaluation
PDF	Preisach distribution function

Material constants

a	cubic lattice constant
A	stiffness constant
$\mathbf{C}$	fourth rank elastic constant tensor
c_{11}, c_{12}, c_{44}	elastic constants in Voigt's notation
G	modulus of rigidity
K_1	first order cubical anisotropy constant
K_2	second order cubical anisotropy constant
K_u	uniaxial anisotropy constant
l_{exch}	exchange length

M_s	saturation magnetization
α	damping constant
γ_G	gyromagnetic constant
λ_{100}	magnetostriction constant corresponding to the $< 100 >$ direction
λ_{111}	magnetostriction constant corresponding to the $< 111 >$ direction
ν	Poisson's ratio
σ	conductivity

Mathematical symbols

$\cdot$	dot product
$\times$	cross product
$*$	convolution product
∇	gradient
$\nabla\cdot$	divergence
$\nabla\times$	curl
$\imath$	imaginary number: $\imath = \sqrt{-1}$
$\tilde{f}$	Fourier transform of f
$\delta(\mathbf{r})$	spatial Dirac distribution
$\delta_{a,b}$	Kronecker delta: $\delta_{a,b} = 1$ if $a = b$, otherwise $\delta_{a,b} = 0$
$\mathbf{r}$	3D space vector
$\mathbf{r}_i$	3D space vector defining the center of discretization cell i
t	time
δt	microscopic time step
ΔT	macroscopic time step
Δ	space discretization size
α_i, $i = 1,2,3$	direction cosines of $\mathbf{m}$ with respect to the cubical anisotropy axes
$< . >$	macroscopic, average quantity
$\mathbf{e}_i$, $i = 1,2,3$ or x,y,z	Cartesian coordinate system
$\mathbf{e}_u, \mathbf{e}_v, \mathbf{e}_w$	coordinate system corresponding to the cubic lattice axes
N	total number of discretization cells
N_i, $i = x,y,z$	number of discretization cells in the x, y and z direction
$\mathcal{O}(.)$	scaling order

Symbols in micromagnetism and electromagnetism

ϕ_G	Gibbs free energy density
ϕ_a	Zeeman (applied field) energy density
ϕ_{ani}	anisotropy energy density
ϕ_{exch}	exchange energy density
ϕ_{ms}	magnetostatic energy density

ϕ_{me}	magnetoelastic energy density
ϕ_{th}	thermal fluctuations energy density
E_{tot}	total energy
$\mathbf{H}_a$	applied field
$\mathbf{H}_{ani}$	anisotropy field
$\mathbf{H}_{exch}$	exchange field
$\mathbf{H}_{ms}$	magnetostatic field
$\mathbf{H}_{me}$	magnetoelastic field
$\mathbf{H}_{th}$	thermal field
$\mathbf{H}_{eddy}$	eddy current field
$\mathbf{H}_{eff}$	effective field
$\mathbf{j}_{eddy}$	eddy current
ψ_{ms}	magnetostatic potential
ρ_{ms}	magnetostatic charge density
τ_{ms}	magnetostatic surface charge density
$\boldsymbol{\sigma}$	stress tensor
$\boldsymbol{\epsilon}$	strain tensor
$\mathbf{B}_{ms}$	magnetostatic induction
$\mathbf{A}_{ms}$	magnetostatic vector potential
E_{ms}	magnetostatic energy
$\mathbf{M}$	magnetization field
$\mathbf{m}$	normalized magnetization field
μ_0	vacuum permeability
$\mathbf{N}$	demagnetizing tensor
T	temperature
f	frequency

List of Publications

Articles in international SCI journals

1. B. Van de Wiele, L. Dupré, and F. Olyslager, “Memory properties in a Landau-Lifshitz hysteresis model for thin ferromagnetic sheets," *Journal of Applied Physics*, vol. 99, no 8, Art. No. 08G101, 2006.

2. B. Van de Wiele, F. Olyslager, and L. Dupré, “Fast semianalytical time integration schemes for the Landau-Lifshitz equation," *IEEE Transactions on Magnetics*, vol. 43, no 6, pp. 2017-2019, 2007.

3. B. Van de Wiele, F. Olyslager, and L. Dupré, “Fast numerical three-dimensional scheme for the simulation of hysteresis in ferromagnetic grains," *Journal of Applied Physics*, vol. 101, Art. No. 073909, 2007.

4. B. Van de Wiele, L. Dupré, and F. Olyslager, “Memory properties in a 3D micromagnetic model for ferromagnetic samples," *Physica B*, vol. 403, pp. 342-345, 2008.

5. B. Van de Wiele, L. Dupré, and F. Olyslager, “Influence of space discretization size in 3D micromagnetic modeling," *Physica B*, vol. 403, pp. 372-375, 2008.

6. B. Van de Wiele, L. Dupré, and F. Olyslager, “Accelerated 3D numerical scheme for the evaluation of hysteresis in ferromagnetic grains," *IEEE Transactions on Magnetics*, vol. 44, no 6, pp. 850-853, 2008.

7. B. Van de Wiele, A. Manzin, O. Bottauscio, M. Chiampi, L. Dupré, and F. Olyslager, “Finite difference and edge finite element approaches for dynamic micromagnetic modelling," *IEEE Transactions on Magnetics*, vol. 44, no 11, pp. 3137-3140, 2008.

8. B. Van de Wiele, F. Olyslager, and L. Dupré, “Application of the fast multipole method for the evaluation of magnetostatic fields in micromagnetic computations," *Journal of Computational Physics*, vol. 227, pp. 9913-9932, 2008.

9. B. Van de Wiele, A. Manzin, L. Dupré, F. Olyslager, O. Bottauscio, and M. Chiampi, “Comparison of finite-difference and finite-element schemes for magnetization processes in 3-D particles," *IEEE Transactions on Magnetics*, vol. 44, no 11, pp. 3137-3140, 2009.

10. A. Van den Berg, L. Dupré, B. Van de Wiele, and G. Crevecoeur, “Meso hysteresis model for ferromagnetic materials by minimization of the micromagnetic free energy," *Journal of Applied Physics*, vol. 105, no 7, Art. No. 07D503, 2009.

11. B. Van de Wiele, L. Dupré, F. Olyslager, and D. De Zutter, “Thermally initiated reversal modes in infinite periodic ferromagnetic wires," *IEEE Transactions on Magnetics*, vol. 45 no 11, pp. 5212-5215, 2009.

12. B. Van de Wiele, L. Dupré, F. Olyslager, and D. De Zutter, “On the accuracy of FFT based magnetostatic field evaluation schemes in micromagnetic hysteresis modelling," *Journal of Magnetism and Magnetic Materials*, vol. 322, pp. 469-476, 2010.

13. A. Van den Berg, L. Dupré, B. Van de Wiele, and G. Crevecoeur, “A mesoscopic hysteresis model based on the unconstrained minimization of the Gibbs free energy," *IEEE Transactions on Magnetics*, vol. 46, no 2, pp. 220-223, 2010.

14. A. Manzin, B. Van de Wiele, O. Bottauscio, L. Dupré, F. Olyslager, and D. De Zutter, “Numerical analysis of the influence of geometry and temperature on switching processes in magnetic nanostrips," *IEEE Transactions on Magnetics*, vol. 46, no 2, pp. 243-246, 2010.

15. B. Van de Wiele, L. Dupré, and D. De Zutter, “Micromagnetic study of magnetic domains in platelets with perpendicular uniaxial anisotropy," *Journal of Applied Physics*, in press for May 2010.

Articles in conference proceedings

1. B. Van de Wiele, L. Dupré, and F. Olyslager, “Memory properties in a 3D micromagnetic model for ferromagnetic samples," *Proceedings of the 6th International Symposium on Hysteresis and Micromagnetics (HMM)*, Naples, Italy, CD-rom, Jun 4-6, 2007.

2. B. Van de Wiele, L. Dupré, and F. Olyslager, “Influence of space discretization size in 3D micromagnetic modeling," *Proceedings of the 6th International Symposium on Hysteresis and Micromagnetics (HMM)*, Naples, Italy, CD-rom, Jun 4-6, 2007.

3. B. Van de Wiele, L. Dupré, and F. Olyslager, “Accelerated 3D numerical scheme for the evaluation of hysteresis in ferromagnetic grains," *Proceedings of the 16th International Conference on the Computation of Electromagnetic Fields (COMPUMAG)*, Aachen, Germany, pp. 101-102, Jun 24-28, 2007.

4. B. Van de Wiele, F. Olyslager, and L. Dupré, “Fast multipole algorithm for the evaluation of magnetostatic fields in 3D ferromagnetic samples," *Proceedings of the 24th International Review of Progress in Applied Computational Electromagnetics (ACES)*, Niagara Falls, Canada, CD-rom, Mar 30 - Apr 4, 2008.

5. B. Van de Wiele, A. Manzin, O. Bottauscio, M. Chiampi, L. Dupré, and F. Olyslager, “Finite difference and edge finite element approaches for dynamic micromagnetic modelling," *Proceedings of the IEEE International Magnetics Conference (INTERMAG)*, Madrid, Spain, pp. 426, May 4-8, 2008.

6. B. Van de Wiele, A. Manzin, L. Dupré, F. Olyslager, O. Bottauscio, and M. Chiampi, “Comparison of finite-difference and finite-element schemes for magnetization processes in 3-D particles," *Proceedings of the 13th Biennial IEEE Conference on Electromagnetic Field Computation (CEFC)*, Athens, Greece, pp. 57, May 11-15, 2008.

7. B. Van de Wiele, L. Dupré, and F. Olyslager, “Thermally activated reversal modes in infinite periodic ferromagnetic wires," *Proceedings of the 7th International Symposium on Hysteresis and Micromagnetics (HMM)*, Gaithersburg, MD, USA, May 11-14, 2009.

8. A. Van den Berg, L. Dupré, B. Van de Wiele, and G. Crevecoeur, “A mesoscopic hysteresis model based on the unconstrained minimization of the Gibbs free energy," *Proceedings of the 19th Soft Magnetic Materials*

Conference (SMM), Turin, Italy, Sep 6-9, 2009.

9. A. Manzin, B. Van de Wiele, O. Bottauscio, L. Dupré, F. Olyslager, and D. De Zutter, "Numerical analysis of the influence of geometry and temperature on switching processes in magnetic nanostrips," *Proceedings of the 19th Soft Magnetic Materials Conference (SMM)*, Turin, Italy, Sep 6-9, 2009.

Conference abstracts

1. B. Van de Wiele, L. Dupré, and F. Olyslager, "Memory properties in a Landau-Lifshitz hysteresis model for thin ferromagnetic sheets," *Book of abstracts of the 50th annual conference on Magnetism and Magnetic Materials (MMM)*, San Jose, CA, USA, pp. 136, Oct 30 - Nov 3, 2005.

2. B. Van de Wiele, F. Olyslager, and L. Dupré, "Fast semianalytical time integration schemes for the Landau-Lifshitz equation," *Book of abstracts of the 10th Joint MMM/Intermag conference*, Baltimore, MD, USA, pp. 181, Jan 7-11, 2007.

3. A. Van den Berg, L. Dupré, B. Van de Wiele, and G. Crevecoeur, "Meso hysteresis model for ferromagnetic materials by minimization of the micromagnetic free energy," *Book of abstracts of the 53th annual conference on Magnetism and Magnetic Materials (MMM)*, Austin, TX, USA, CD-rom, Nov 10-14, 2008.

4. B. Van de Wiele, L. Dupré, and D. De Zutter, "Micromagnetic study of magnetic domains in platelets with perpendicular uniaxial anisotropy," *Proceedings of the 11th Joint MMM-Intermag Conference*, Washington DC, USA, CD-rom, Jan 18-22, 2010.

Numerical Study of Magnetic Processes: Extending the Landau-Lifshitz-Gilbert Approach from Nanoscale to Microscale

CHAPTER 1

General introduction

1.1. Ferromagnetic materials and their applications

In our modern society, ferromagnetic materials are used in many applications. The magnetic properties of the material are exploited from the microscopic up to the macroscopic scale.

In the macroscopic range, ferromagnetic materials are the basis entities of electrical machines and transformers. Here ferromagnetic materials are used as conductors for the magnetic field flux in magnetic circuits in the same way as e.g. copper is used as a conductor for electrical currents in electrical circuits. Consequently, the magnetic properties of the ferromagnetic material have a large impact on the efficiency of electrical machines and transformers. A large amount of research aims to gain a deeper understanding of the ferromagnetic materials in order to develop optimized, high performing materials which minimize the magnetic losses in the electrical machines and transformers. Here, the question arises which microscopic structure of the material ensures the optimal macroscopic magnetic properties for a given application and what manufacturing techniques should be employed to obtain such a structure.

In the microscopic range, magnetic materials have since long been used to store data. In magnetic tapes as videotapes or music tapes, the analogue output signal (video frame, music, data, etc.) directly relates to the local magnetization on the tape. On a smaller scale, magnetic materials are used as the building stones of magnetic storage devices as MRAMs (Magnetic Random Access Memory) in computers. Here, a bit of information (0 or 1) corresponds to a positive or negative magnetization. In the research domain of these magnetic storage devices, the main challenge is to make smaller devices and to develop strategies that ensure shorter reading and writing times. Recently, a lot of effort is devoted to the development of the so called Racetrack Memory,

which will store the digits in magnetic nanowires. In all these applications, there is a need for a better understanding of the magnetization dynamics on an ever decreasing space and time scale.

Another domain where the magnetic properties of magnetic materials are exploited are magnetic sensors which pick up variations in the magnetic field near a test object by a change in their magnetic material properties. Also in this research domain, there is an ongoing pursuit towards miniaturization.

The magnetic properties of (ferromagnetic) materials are also exploited in an indirect way. In construction, transportation, utilities, etc. iron based materials are broadly used. Here, the microstructure of the material is controlled during the fabrication of the work pieces to obtain materials with specific mechanical properties. Since also the magnetic properties of the material depend on the microstructure, the constant on-line monitoring of the magnetic material properties can indicate if the intended microscopic structure is obtained and thus if the mechanical requirements are met. The relations between the microscopic structure and the magnetic material properties on the one hand and between the microscopic structure and the mechanical properties on the other hand can also be exploited during the life time of the iron based structure. Indeed, due to cyclic loading, irradiation, etc. the microstructure of the material can change leading to deteriorating mechanical properties which can lead to failure. These changes in microstructure result also in changing magnetic material properties. Hence since magnetic experiments are rather cheap, a good knowledge of the distinct relations between microstructure and magnetic material properties will not only be valuable in the continuous monitoring of production processes, but will also open the way to large scale magnetic Non-Destructive Evaluation (NDE).

1.2. Illustrations of the relation microstructure – magnetic properties

1.2.1 Influence of the manufacturing technique

The ferromagnetic cores in electrical machines and transformers typically consist of stacked thin laminations fabricated out of larger electrical steel sheets to minimize the eddy current losses (see further). The microstructure of the electrical steel sheets is adjusted to meet the magnetic material requirements defined during the design process of the electrical machine or transformer. The fabrication of the laminations out of the sheet however can introduce local changes in the materials' microstructure. This is shown in Fig. 1.1 presenting the grain configuration near to the edges of work pieces before and after punching and laser cutting it out of the steel sheet. It is clear that the punching technique elongates the grains in a direction perpendicular to the cutting

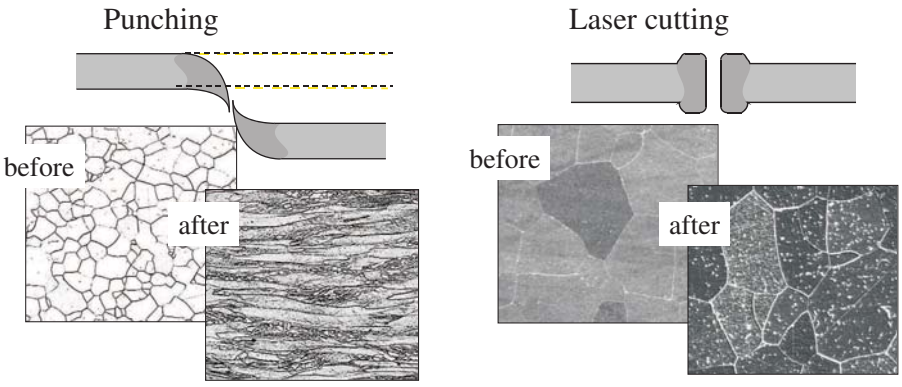

Figure 1.1: Influence of different manufacturing techniques on the grain structure.

edge, while the laser cutting technique introduces stresses due to the nonuniform heating of the sample.

The variations in the microstructure introduce changes in the magnetic properties. To demonstrate this, Fig. 1.2 shows the hysteresis loops for ring cores with an identical shape, fabricated out of the same steel sheet using different techniques. Here, spark erosion is a chemical technique which introduces only limited changes to the original microstructure. It is clear that the magnetic properties of the work pieces are substantially affected by the fabrication technique and thus by the microstructure of the magnetic material. This effect should be taken into account during the design of electrical machines and transformers [2].

1.2.2 Fatigue damage in iron based materials

The cyclic mechanical loading of iron based materials leads to irreversible changes in the microstructure of the material. Even when the stress amplitudes remain under the yield strength, cyclic loading can deform the material on a small length scale around inherent lattice imperfections. As the number of loading cycles increases, the forward and backward movement of dislocations (line imperfections in the iron lattice) results in a change in the dislocation density, the dislocation structure and the accumulation of stresses. In the end, micro-cracks appear in the zones with accumulated stresses leading to fatigue fracture of the specimen. This continuous change in the microstructure of the material also results in a continuous change in the macroscopic magnetic (hysteresis) properties. To demonstrate this, Fig. 1.3. shows hysteresis loops measured at different time points during a fatigue test. The slope of the hysteresis loop decreases when approaching the failure. This is again an

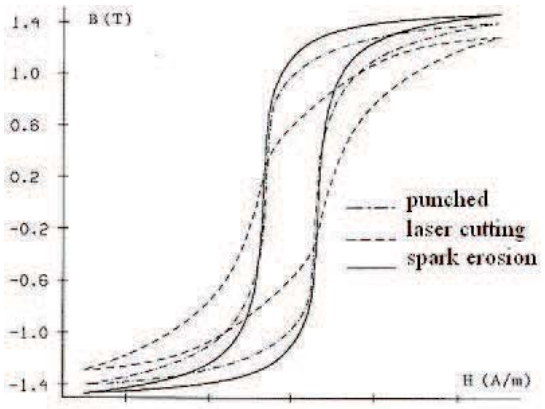

Figure 1.2: Experimental magnetic hysteresis loops measured on identical ring cores fabricated out of the same electrical steel sheet using different techniques.

example where a change in the microstructure of the material results at the one hand in a change in the mechanical properties and on the other hand in a change of the macroscopic magnetic properties.

The above relation can be exploited to monitor the mechanical properties of the iron based material during its life time cycle. An NDE technique based on this effect can reveal fatigue damage at an early stage, before micro-cracks can be observed. By evaluating the different levels of fatigue damage, using simple magnetic measurements, it can become possible to predict the expected life time of the specimen. In this application a thorough understanding of the relation between the materials' microstructure and the macroscopic magnetic properties is required.

1.3. Numerical computation of magnetic processes

In order to obtain a clear understanding of the different relations between the microstructure of the material and the macroscopic magnetic properties, one has to rely on sophisticated numerical computations. Indeed, distinguishing the different relations relying only on experiments is hardly feasible since it is practically very difficult to prepare samples where only one microscopic parameter is adjusted to investigate its influence on the magnetic properties. Therefore we have developed during this PhD work a numerical algorithm able to compute the magnetic processes based on the micromagnetic theory.

The micromagnetic theory describes the physical interactions in the magnetic material on a nanometer length scale and a picosecond time scale. The theory has been successfully used in the development of the above mentioned

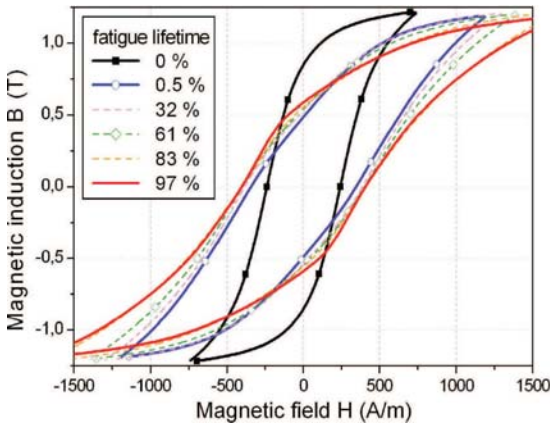

Figure 1.3: Changes in magnetic hysteresis properties during cyclic loading (from [3])

storage entities and more generally in the research for ultra fast digital magnetic components. This is the classical research domain where micromagnetic computations are used. Various topics are studied: the stability of magnetization states, reversal mechanisms between states representing a digital 1 and a digital 0 in diverse geometries, oscillating magnetic processes, domain wall displacements in nanowires, etc. Since the dimensions of the investigated entities are relatively small and the time frame which is simulated in most cases corresponds to the one of the fast magnetization processes, the numerical problems remain limited. Furthermore, most of these simulations deal with samples which have an ideal microstructure (no lattice imperfections, boundary effects, etc.) and have well defined material parameters.

The micromagnetic theory is a general physics based theory able to describe the magnetization processes in any magnetic material. Consequently, it is also applicable to ferromagnetic materials as electrical steels. Indeed, the same interactions are present as in the magnetic digital components, only their strength can vary depending on the microscopic material parameters. However, the numerical schemes which were successful in the classical micromagnetic research domain can generally not be adopted to this new research domain of micromagnetic numerical simulations in larger ferromagnetic samples. The main reason for this is twofold. First there is the wide range in physical length scales: the micromagnetic description itself is situated at the nanometer length scale, which is also the length scale of material imperfections as dislocations. The dimensions of the grains present in the material on the other hand can vary from nanometers to micrometers, while the thickness of an electrical steel sheet ranges up to 1 mm. Second, there is a wide range in the considered time scales. The micromagnetic processes take place on a ps

time scale while the variations in the externally applied fields take place at the ms time scale. To overcome these wide ranges in the time and length scales as much as possible, sophisticated numerical techniques are required. These techniques are developed during this PhD work.

The numerical scheme is applicable in micromagnetic research domains starting from the classical sub-micrometer sized objects up to a scale of the order of $10\,\mu$m, which is the length scale on which magnetic domains determine the magnetization processes. The efficiency of the numerical scheme is demonstrated and its applicability is shown in (i) the classical micromagnetic research domain, (ii) the study of magnetic domains and (iii) the study of hysteresis properties of ferromagnetic materials.

1.4. Outline of the thesis

This PhD thesis is divided into three parts. The first part comprises Chapters 2 to 5 and gives an outline of the micromagnetic theory and magnetic hysteresis. At the end of this first part, the research challenges are summarized and the goals of the PhD are put forward. The second part comprises Chapters 6 to 9 and focuses on the developed numerical algorithms used in the micromagnetic scheme. In third part comprising Chapters 10 to 12, the micromagnetic scheme is applied on different topics.

In Chapter 2, we give an overview of the micromagnetic theory. From the minimization of the Gibbs free energy, the micromagnetic equilibrium conditions are deduced. The Landau-Lifshitz-Gilbert equation is introduced to describe dynamics in the micromagnetic theory. Further, eddy currents and thermal fluctuations are added to the model. For this chapter, the textbook [4] written by H. Krönmuller and M. Fähnle served as a guideline. A more detailed description of the micromagnetic theory can be found in this reference work.

In Chapter 3, the magnetostatic energy term is treated in more detail. Expressions for the magnetostatic field are deduced from Maxwell's equation and from the microscopic view point. It is shown how the magnetostatic energy is minimized when magnetic domains are introduced. Further, demagnetizing factors and the influence of the magnetostatic interactions in closed magnetic circuits are discussed.

In Chapter 4, magnetic hysteresis is outlined. Here we start with the explanation of hysteresis properties in a simple bistable system as also discussed by G. Bertotti in [5]. The hysteresis properties encountered in this simple system are then translated to the full micromagnetic problem. In this way, it is shown that magnetic hysteresis is inherently incorporated in the micromagnetic description.

In Chapter 5, we summarize the challenges encountered in the micromagnetic description of magnetization processes in micromagnetically large samples. A short overview of the international micromagnetic and hysteresis research is given together with an overview of the research context at the department of Electrical Energy, Systems and Automation and at the department of Information Technology. This clarifies the framework where this PhD work fits in and from this the research goal is defined.

In Chapter 6, we present the developed numerical (hysteresis) micromagnetic scheme. The space and time discretization of the micromagnetic expressions is performed. The effectiveness of the micromagnetic scheme is extensively evaluated by comparing simulation results obtained with other micromagnetic schemes.

In Chapter 7, we comment on two magnetostatic field evaluation schemes based on fast Fourier transforms. Their efficiency is compared and the possibility of treating infinite periodic structures is discussed.

In Chapter 8, we introduce the Fast Multipole Method to evaluate the magnetostatic field. A thorough description of the applied techniques to speed up the computations is given. The efficiency of the scheme is compared with the efficiency of the fast Fourier transform based algorithms of Chapter 7. Also here the possibility of treating infinite periodic structures is discussed.

In Chapter 9, we comment on the accuracy required for the micromagnetic computations in the context of (hysteresis) simulations applied on micromagnetically large samples. In particular, the optimal spatial discretization and the influence of the low accuracy evaluation of the magnetostatic field is investigated.

In Chapter 10, the developed micromagnetic scheme is applied on some classical submicrometer sized problems. First, the magnetic stability of nanostrips is investigated with respect to the geometry and thermal effects. Second, the different reversal modes in infinite periodic wires are determined, depending on the cross sectional dimensions of the wire.

In Chapter 11, the micromagnetic scheme is used to study the magnetic domains in platelets with perpendicular uniaxial anisotropy. The micromagnetic simulations are compared to the predictions made within the domain theory.

In Chapter 12, hysteresis properties are examined. First, it is shown that the memory properties are inherently present in the micromagnetic scheme. Second, the instantaneously added, stored and dissipated energy is determined when running through the hysteresis loop and comparison is made with the energy description in the (macroscopic) Preisach description of the magnetic hysteresis.

Finally, in Chapter 13, we present the general conclusions and propose suggestions for further research.

Part I

Micromagnetic Theory and Hysteresis

CHAPTER 2

Micromagnetic theory

2.1. Magnetic moments and historical context

In this section we outline the origin of the magnetic properties of iron based materials. The structure of ferromagnetic materials is discussed and the quantum mechanical origin of the atomistic magnetic moments is briefly described. Furthermore, the different historical steps in the foundation of the micromagnetic theory are described, starting from the experiments that observed domain structures in ferromagnetic materials.

2.1.1 Origin of the magnetic moment in iron

Ferromagnetic materials are mainly composed of iron atoms. For temperatures below $770^{\circ}C$ these atoms are arranged in a body centered cubic (bcc) lattice. As shown in Fig. 2.1 a bcc unit cell contains in total 2 whole atoms: 1 central atom and 8 atoms at the corners belonging for $1/8^{th}$ to the unit cell. The size of a unit cell, expressed by the lattice constant a, is $0.286\,nm$. The (macroscopic) magnetic properties of a ferromagnetic material originates from the magnetic moments of each distinct atom in the lattice.

In order to explain the presence of the magnetic moment of the iron atom we have to rely on quantum physics. An atom contains a nucleus and different electrons moving around the nucleus. Here, the nucleus as well as the electrons have an intrinsic magnetic spin moment, denoted by $\mathbf{m}_n$ and $\mathbf{m}_e$ respectively. Furthermore, the movement of each electron contributes to a total orbital spin magnetic moment $\mathbf{m}_L$. From the quantum theory, one can deduce that the nucleus magnetic moment $\mathbf{m}_n$ as well as the orbital magnetic moment $\mathbf{m}_L$ are much smaller than the electron magnetic moments $\mathbf{m}_e$ and that the electrons have a large probability to move in different regions around the nucleus. These regions, called orbitals, can contain a prescribed number of elec-

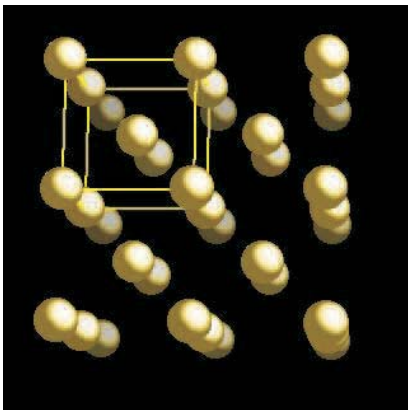

Figure 2.1: Iron atoms placed in bcc lattice

trons and with each orbital a distinct energy state is associated: an electron moving in the orbital has a certain amount of energy. From statistical physics it is clear that the orbitals associated with the lowest energy states are filled. The relativistic quantum mechanical Dirac equation explains that the electron magnetic spins can only have two possible values: spin up and spin down. In completely filled orbitals, the electrons appear in couples with spin up and down, hence completely filled orbitals do not contribute to the total magnetic moment. In iron the orbital corresponding to the highest energy state that still contains electrons is the $3d$ orbital. The orbital can contain 14 electrons, but has only 8. From the quantum mechanical analysis, on obtains that the lowest energy state corresponds to a state where the $3d$ orbital contains 5 electrons with spin up and 3 electrons with spin down. Hence, from all electrons in the iron atom, only two contribute to the total magnetic moment of the atom. A quantum mechanical measure for one single spin magnetic momentum is the Bohr magneton $\mu_{Bohr} = 9.2741 10^{-24} Am^2$, hence following the (simplified) reasoning above, the amplitude of the total magnetic moment of one iron atom is $|\boldsymbol{\mu}_{Fe}| = 2\mu_{Bohr} = 8.61 10^{-23} Am^2$. The amplitude of the atomic magnetic moment can also be expressed as $|\boldsymbol{\mu}_{Fe}| = M_s V_{atom}$ with $M_s = 1.7451 10^6 Am^{-1}$ the spontaneous magnetization and V_{atom} the volume one atom occupies in the bcc lattice, i.e. $a^3/2 = 1.1701 10^{-29} m^3$ [4]. Starting from this reasoning, the amplitude of the atomic magnetic moment is $|\boldsymbol{\mu}_{Fe}| = 2.2\mu_{Bohr}$, which is in fairly good agreement with the above theory.

In a different, classical, view point the magnetic moment of an (iron) atom originates from a circular movement of the electrons around the atoms' nucleus. In that way, an atom is associated with an elementary dipole in which a negative charge $-q$ circles around a positive charge $+q$. The moving neg-

ative charge can now be seen as a current which generates a magnetic field corresponding to the magnetic field generated by the magnetic moment of the atom.

2.1.2 Foundation of the micromagnetic theory

Since long it is known that in general a ferromagnetic material is not homogeneously magnetized but various magnetization patterns can be present. The first visualization of magnetic domains was performed by Bitter in 1903, using the interaction between magnetic iron oxide particles and the magnetic stray fields exerted by the domains and domain walls [6]. Some years later, Weiss developed the molecular field theory and introduced the first ideas to explain the existence of magnetic domains, also called Weiss domains [7]. This hypothesis was confirmed by Barkhausen in 1919 who showed experimentally that the magnetization processes in ferromagnets take place discontinuously by so called Barkhausen jumps. In 1931, Sixtus and Tonks showed that these Barkhausen jumps are due to the discontinuous movement of domain boundaries [8].

In this period, the (relativistic) quantum theory was in full development and insight was gained in the quantum mechanical origin of the magnetic moments and their interactions. However, it was already understood very rapidly that this new theory would not be able to explain the magnetization patterns predicted by Weiss and seen by Bitter. The reason for this is that the difference between the quantum mechanical length scale and the length scale of magnetic domains is too large, still nowadays. On the other hand, the macroscopic theory of electromagnetism developed by Maxwell in the nineteenth century [9] was also unsatisfactory to explain the domain structures in ferromagnetic materials. Indeed, in Maxwell's equations, the material properties are described by constitutive laws using macroscopic, volume averaged quantities as permeability and susceptibility, which disables the description of the magnetization processes on the microscopic scale.

A new theory was needed to bridge the gap between the quantum mechanical description of *discrete, microscopic* spins on the one hand and the *continuous, macroscopic* Maxwell description on the other hand. The aim was to develop a theory describing the magnetization processes in terms of *continuous, microscopic* quantities on an intermediate scale. The theory needed to be in accordance with the underlying quantum mechanics, but should also be able to explain the experimental foundings as magnetic domain formation. In 1932, Bitter describes this quest in [10] as follows

> *"... This indicates that we have to deal, not with an aggregate of dipoles, but with a vector field. We may expect to derive the laws governing the behavior of this vector field from general quantum-mechanical principles, but since the*

attempts so far made have not been entirely successful, it may be worth trying to formulate them independently, with reference to experimental results only."

Eventually, Landau and Lifshitz founded the basis of the micromagnetic theory in 1935 [11]. They introduced a continuum expression for the quantum mechanical exchange energy and gave a first interpretation of domain patterns as the magnetization configuration which minimizes the magnetostatic energy (see further).

2.2. Micromagnetic energy terms

In the micromagnetic theory, the magnetic moments $\boldsymbol{\mu}_i$ of the atoms are homogenized to a continuum vector field $\mathbf{M}(\mathbf{r})$:

$$\mathbf{M}(\mathbf{r}) = \sum_{i=1}^{N} \frac{\boldsymbol{\mu}_i}{\mathrm{d}V}. \tag{2.1}$$

Here $\mathrm{d}V$ is a volume, large enough to contain a huge number of elementary magnetic moments $\boldsymbol{\mu}_i$, but small enough to ensure that the vector field varies smoothly. A good length scale will be derived in Section 2.3.2. Since $\mathbf{M}(\mathbf{r})$ varies only smoothly, the magnetization in the volume $\mathrm{d}V$ is considered constant, with an amplitude corresponding to the amplitude of the enclosed magnetic moments. This leads to the proposition that the continuum field has a fixed, material dependent amplitude M_s, but a time and space varying orientation

$$\mathbf{M}(\mathbf{r},t) = M_s \mathbf{m}(\mathbf{r},t). \tag{2.2}$$

This is in accordance with the underlying quantum mechanic theory where each atomistic magnetic moment also has a constant amplitude but a varying orientation. The vector field $\mathbf{M}(\mathbf{r},t)$ is subject to different interactions present in the ferromagnetic material. With each type of interaction an energy contribution is associated. The micromagnetic theory is based on the minimization of the magnetic Gibbs free energy present in the magnetic system. Since the micromagnetic theory is a continuum theory positioned between the quantum mechanical and the macroscopic, Maxwell description of magnetic materials, the continuum theoretical expressions for the internal energy terms may be derived either from the quantum mechanical expressions of magnetic interactions or from symmetry considerations based on experimental knowledge. In what follows, we will present the different contributing energy terms.

2.2.1 Exchange energy

This energy contribution has its origin in the mutual interaction between the spins **S** belonging to adjacent ions, known as the exchange coupling described by Heisenberg [12]. A continuum expression will be derived by homogenization of the quantum mechanic expression as well as from symmetry considerations.

Homogenization of the quantum mechanical expression

The continuum expression for the energy term can be derived from the homogenization of the Heisenberg exchange Hamiltonian [12]

$$\hat{\mathcal{H}}_{exch} = -2\sum_{i\neq j} J_{ij}(\mathbf{r}_{ij})\hat{\mathbf{S}}_i(\mathbf{r}_i)\cdot\hat{\mathbf{S}}_j(\mathbf{r}_j), \tag{2.3}$$

with $J_{ij}(\mathbf{r}_{ij})$ the exchange integral between the ions with spins S_i and S_j at positions $\mathbf{r}_i$ and $\mathbf{r}_j$. In principal, the hamiltonian (2.3) consists of the interactions between all ions, but when the variations in spin orientation between neighboring ions are small, it is sufficient to consider only the interactions J_0 between the 6 nearest neighbors of the atom. A translation of the quantum mechanical operators in (2.3) to classical quantities implies replacing the spins **S** by the magnetization

$$\mathbf{M} = M_s\mathbf{m} = \frac{g\mu_{Bohr}}{V_{atom}}\mathbf{S}, \tag{2.4}$$

with g the Landé factor (for iron $g \approx 2$ as derived above). This results in the following expression for the exchange energy density around one atom

$$\phi_{exch}(\mathbf{r}_i) = -\frac{2}{V_{atom}}\frac{V_{atom}^2 M_s^2}{g^2\mu_{Bohr}^2}J_0\sum_{j\neq i}^{nn}\mathbf{m}_i\cdot\mathbf{m}_j. \tag{2.5}$$

The summation runs only over the z nearest neighbors (nn) of the atom (the self interaction $i=j$ is excluded). If now only small angles ϕ_{ij} between neighboring magnetic moments are considered, as depicted in Fig. 2.2, each component $q = x,y,z$ of $\mathbf{m}_j(\mathbf{r}_j)$ can be expanded in a Taylor series around the corresponding component of $\mathbf{m}_i(\mathbf{r}_i)$

$$m_{q,j}(\mathbf{r}_j) = m_{q,i}(\mathbf{r}_i) + \mathbf{r}_{ij}\cdot\nabla m_{q,j}(\mathbf{r}_j) + \frac{1}{2}(\mathbf{r}_{ij}\cdot\nabla)^2 m_{q,j}(\mathbf{r}_j). \tag{2.6}$$

When the summations over the ν nearest neighbors are elaborated, terms as $\mathbf{r}_{ij}\cdot\nabla m_{q,j}(\mathbf{r}_j)$ and cross terms of $\frac{1}{2}(\mathbf{r}_{ij}\cdot\nabla)^2 m_{q,j}(\mathbf{r}_j)$ as $\sum x_{ij}y_{ij}\frac{\partial^2 m_{n,i}}{\partial x_{ij}\partial y_{ij}}$ cancel

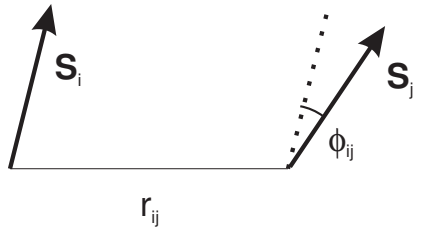

Figure 2.2: Two adjacent spins and their coordinates

out due to symmetry. This reduces the summation in (2.5) to

$$\sum_{j\neq i}^{nn}\mathbf{m}_i\cdot\mathbf{m}_j=\nu+\frac{1}{2}\sum_{q=1}^{3}m_{q,i}\left[\frac{\partial^2 m_{q,i}}{\partial x_{ij}^2}\sum_{j\neq i}^{nn}x_{ij}^2+\frac{\partial^2 m_{q,i}}{\partial y_{ij}^2}\sum_{j\neq i}^{nn}y_{ij}^2+\frac{\partial^2 m_{q,i}}{\partial z_{ij}^2}\sum_{j\neq i}^{nn}z_{ij}^2\right]. \quad (2.7)$$

Since in a cubic lattice

$$\sum_{j\neq i}^{nn}x_{ij}^2=\sum_{j\neq i}^{nn}y_{ij}^2=\sum_{j\neq i}^{nn}z_{ij}^2=\frac{1}{3}\sum_{j\neq i}^{nn}r_{ij}^2 \quad (2.8)$$

expression (2.7) reduces to

$$\sum_{j\neq i}^{nn}\mathbf{m}_i\cdot\mathbf{m}_j=\nu+\frac{1}{6}\sum_{j\neq i}^{nn}r_{ij}^2\mathbf{m}_i\cdot\nabla^2\mathbf{m}_i. \quad (2.9)$$

Using the vector identity

$$\nabla^2(\mathbf{u}\cdot\mathbf{u})=2\left[(\nabla u_1)^2+(\nabla u_2)^2+(\nabla u_3)^2\right]+2(\mathbf{u}\cdot\nabla^2\mathbf{u})=0, \quad (2.10)$$

ϕ_{exch} can be written as

$$\phi_{exch}(\mathbf{r}_i)=-2\frac{V_{atom}M_s^2}{g^2\mu_{Bohr}^2}J_0\left[\nu-\frac{1}{6}\sum_{j\neq i}^{nn}r_{ij}^2\sum_{q=1}^{3}(\nabla m_{i,q})^2\right]. \quad (2.11)$$

The first term describes the exchange energy of a homogeneously magnetized material. This constant term can be omitted since the (potential) energy of a system is always determined apart from a constant. Further, in a cubic lattice it holds that

$$\sum_{j\neq i}^{nn}r_{ij}^2=6a^2, \quad (2.12)$$

leading to

$$\phi_{exch}(\mathbf{r}_i) = 2\frac{V_{atom}M_s^2}{g^2\mu_{Bohr}^2}J_0a^2\sum_{q=1}^{3}(\nabla m_{i,q})^2. \tag{2.13}$$

When the exchange stiffness A is introduced to incorporate all the material constants, a continuum expression for the quantum mechanical exchange Hamiltonian (2.3) is derived as

$$\phi_{exch}(\mathbf{r}) = A\sum_{q=1}^{3}(\nabla m_q(\mathbf{r}))^2. \tag{2.14}$$

For iron, J_0 and thus A is a positive constant, implying that the exchange energy in a ferromagnetic material is minimal when the magnetization is parallel.

Derivation from symmetrical considerations

The macroscopic construction of the exchange energy term starts from the observation that on a small length scale parallel magnetization configurations are favored. Hence, ϕ_{exch} should be proportional with the variation of the magnetization. Expressions as $\nabla \cdot \mathbf{m}$ and $\nabla \times \mathbf{m}$ are insufficient since they would lead to a vanishing exchange energy in the case of zero divergence or zero curl respectively. An expression $\nabla\mathbf{m}$ results in a second order tensor while we aim for a scalar quantity. Hence, it is natural to come to an expression such as (2.14). Indeed, this is an isotropic scalar expression which, for positive A, increases for larger variations in the magnetization. In this reasoning, the actual value of A should be derived from measurements.

Minimization of the exchange energy

A virtual ferromagnetic material, only subject to exchange interactions will be uniformly magnetized. Indeed, for a uniform magnetization ∇m_q is zero for all $q = 1\ldots3$ and the exchange energy (2.14) is zero.

2.2.2 Anisotropy energy

The anisotropy energy results from the interactions between the magnetic moments and the materials' lattice axes. The quantum mechanical origin of the magnetocrystalline anisotropy is based on the coupling between spin moments and the electronic orbital moments (L–S-coupling) at the one hand and the coupling between the spin moment and the anisotropic crystal field acting on an atom on the other hand [13]. Here we will limit ourselves to a phenomenological derivation based on symmetry considerations.

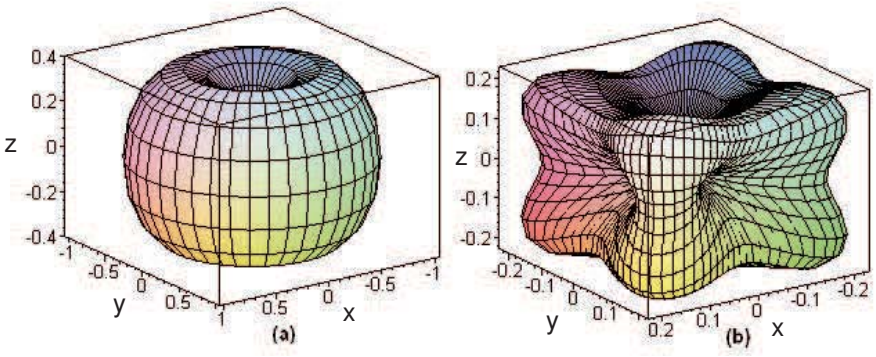

Figure 2.3: a. Energy surface in the case of uniaxial anisotropy with easy magnetization axis along the z-axis. b. Energy surface in the case of cubic anisotropy with easy magnetization axes along the x, y and z direction.

Uniaxial anisotropy

In a first class of materials as e.g. copper, it is found that in a monocrystal, the magnetization tends to align along a certain direction of the material lattice. When the magnetization is oriented along this strong magnetocrystalline anisotropy axis –in positive or negative sense– the anisotropy energy in the material is minimized. From these observations, the uniaxial anisotropy energy density can be expressed by

$$\phi_{ani} = K_{u,0} + K_{u,1}\sin^2(\theta) + K_{u,2}\sin^4(\theta) + \ldots \tag{2.15}$$

with θ the angle between the magnetization and the anisotropy axis $\mathbf{u}$. The first term is a constant and can thus be omitted. In general the third term is negligible compared with the second term. Expressed in terms of the continuum magnetization field $\mathbf{m}$, ϕ_{ani} can then be written as ($K_u = K_{u,1}$)

$$\phi_{ani}(\mathbf{r}) = K_u\{1 - [\mathbf{m}(\mathbf{r}) \cdot \mathbf{u}]^2\}. \tag{2.16}$$

The energy surface of this energy term is shown in Fig. 2.3.

Cubical anisotropy

In a second class of materials as e.g. iron and nickel, cubical anisotropy effects are observed. In the case of iron, it is found that in a monocrystal the material saturates preferably along $< 100 >$ lattice directions. Larger fields are required to saturate the sample along $< 110 >$ directions and $< 111 >$ directions, see Fig. 2.4.a. The easy magnetization directions $< 100 >$ correspond to orientations along the edges of the lattice basis cell, while the medium and

hard magnetization directions ($< 110 >$ and $< 111 >$) correspond to orientations along the plane and space diagonals of the lattice basis cell respectively, as shown in Fig. 2.4.b.

The easy $< 100 >$ directions are orthogonal and can thus be associated with a coordinate system $(\mathbf{u}_1\mathbf{u}_2\mathbf{u}_3)$. Whenever the angle between the magnetization and one of these three axes is zero, the anisotropy energy density ϕ_{ani} should be minimal. Hence it is obvious to describe ϕ_{ani} in terms of the direction cosines

$$\alpha_i(\mathbf{r}) = \mathbf{m}(\mathbf{r}) \cdot \mathbf{u}_i \qquad i = 1 \ldots 3. \tag{2.17}$$

The cubical anisotropy energy should be equal for an angle which is enclosed with the positive or negative direction of the axis $\mathbf{u}_i$, thus $\phi_{ani} \propto \alpha_i^2$. Further the wanted expression should stay unchanged due to an interchange of the indices i. Based on these symmetry consideration, a possible expression is thus

$$\phi_{ani}(\mathbf{r}) = K_0(\alpha_1^2(\mathbf{r}) + \alpha_2^2(\mathbf{r}) + \alpha_3^2(\mathbf{r})). \tag{2.18}$$

Since $\alpha_1^2 + \alpha_2^2 + \alpha_3^2 = 1$ this results in a constant energy contribution. Higher order terms give rise to angle dependencies.

$$\begin{aligned} \phi_{ani}(\mathbf{r}) = K_1 &\left[\alpha_1^2(\mathbf{r})\alpha_2^2(\mathbf{r}) + \alpha_2^2(\mathbf{r})\alpha_3^2(\mathbf{r}) + \alpha_1^2(\mathbf{r})\alpha_3^2(\mathbf{r})\right] \\ &+ K_2\left[\alpha_1^2(\mathbf{r})\alpha_2^2(\mathbf{r})\alpha_3^2(\mathbf{r})\right]. \end{aligned} \tag{2.19}$$

The energy surface corresponding to the second order term is shown in Fig. 2.3.b.

Polycrystalline materials

Polycrystalline ferromagnetic materials contain many grains. In each grain, a local $(\mathbf{u}_1\mathbf{u}_2\mathbf{u}_3)$ coordinate system which coincides with the easy magnetization directions can be defined. In these materials, the anisotropy energy is minimized when in each grain the magnetization is aligned with one of the $< 100 >$ directions. Hence, when only the anisotropy energy is taken into account, the material is only uniformly magnetized in the grains and changes in the magnetization appear on the grain boundaries. Similar conclusions can be drawn for polycrystalline uniaxial materials.

2.2.3 Magnetoelastic energy

Magnetoelastic effects find their origin in the displacement of atoms in the material lattice and the resulting deformations of the electron clouds surrounding the atoms. Macroscopically, it is observed that the dimensions of a ferromagnetic sample change when a time varying external magnetic field is applied.

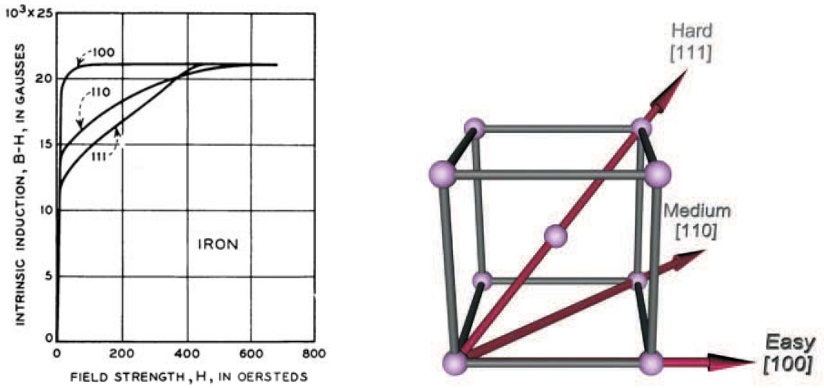

Figure 2.4: a. Magnetization curves for a single iron crystal for different crystallographic axes orientations (From [14], original data from [15]). b. Easy, medium and hard magnetization axes in iron.

Conversely, it is also observed that the magnetization configurations change when a time varying external mechanic stress is applied. Hence it is clear that the magnetic processes in the material are coupled with the elastic processes, giving rise to a magnetoelastic energy contribution ϕ_{me}.

Continuum mechanics of solids [16]

In accordance with the homogenization of the distinct magnetic moments to the continuum vector field $\mathbf{m}(\mathbf{r},t)$, the distinct displacements of lattice atoms are homogenized to a continuum displacement field $\mathbf{s}(\mathbf{r},t)$ from which the strain tensor field $\boldsymbol{\epsilon}(\mathbf{r},t)$ is derived as

$$\boldsymbol{\epsilon}(\mathbf{r},t) = \frac{1}{2}\left[\nabla\mathbf{s}(\mathbf{r},t) + \mathbf{s}(\mathbf{r},t)\nabla\right]. \tag{2.20}$$

Here, the divergence operator in the second term acts on the right hand side of $\mathbf{s}(\mathbf{r},t)$ resulting in a symmetrical tensor $\boldsymbol{\epsilon}(\mathbf{r},t)$ that describes displacements, without rotations. This first assumption is applicable for ferromagnetic materials. The continuum stress tensor field $\boldsymbol{\sigma}(\mathbf{r},t)$ is derived from $\boldsymbol{\epsilon}(\mathbf{r},t)$ by Hooke's law

$$\boldsymbol{\sigma}(\mathbf{r},t) = \mathbf{C}\cdot\cdot\boldsymbol{\epsilon}(\mathbf{r},t). \tag{2.21}$$

Here, $\mathbf{C}$ is a fourth rank tensor composed of the elastic constants of the given material and '$\cdot\cdot$' is the double inner product. In general $\mathbf{C}$ contains 81 tensor elements. However, the symmetry of the material lattice is reflected in the

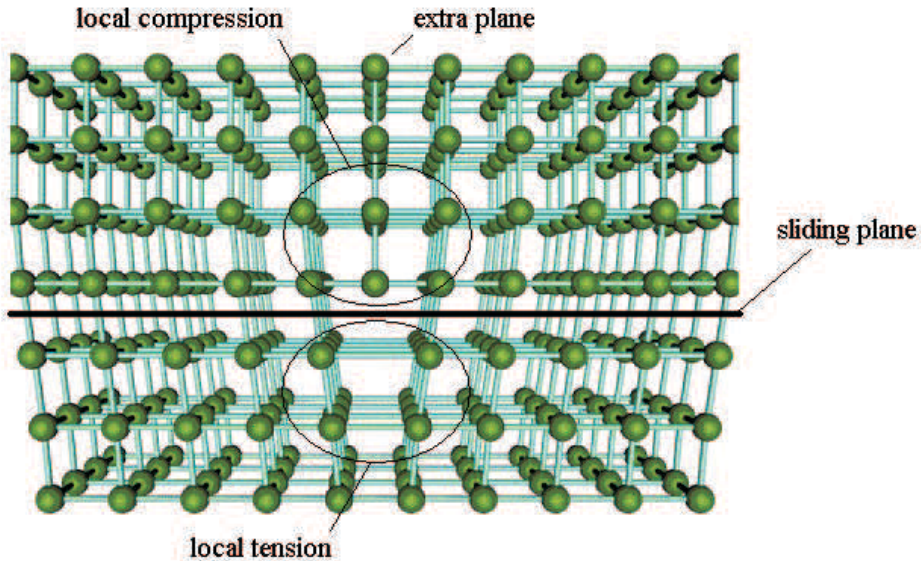

Figure 2.5: Structure of an edge dislocation and it characteristic stress distribution introduced in the lattice.

symmetry properties of the tensor elements, reducing the number of different non-zero elements considerably.

Strains in ferromagnetic materials

The elastic description of the ferromagnetic material starts with the proper definition of the total strain tensor $\boldsymbol{\epsilon}_{tot}(\mathbf{r},t)$. In what follows we will omit the place and time dependencies $(\mathbf{r},t)$ for clarity. Different contributions can be distinguished.

$$\boldsymbol{\epsilon}_{tot} = \boldsymbol{\epsilon}_{ext} + \boldsymbol{\epsilon}_{def} + \boldsymbol{\epsilon}_{sp} + \boldsymbol{\epsilon}_{el} \tag{2.22}$$

The first term $\boldsymbol{\epsilon}_{ext}$ corresponds to the strain due to externally applied forces, while the second term $\boldsymbol{\epsilon}_{def}$ corresponds to the internal strain due to imperfections in the material lattice. Indeed, imperfections in the lattice are accompanied by small displacements of the atoms and, according to expression (2.20), with strains and thus stresses. Since each imperfection has a different local atom structure, each imperfection introduces a characteristic strain and stress distribution in the material. As an example, Fig. 2.5 shows an edge dislocation and the regions with compression and tension surrounding the imperfection. Both strain $\boldsymbol{\epsilon}_{ext}$ and $\boldsymbol{\epsilon}_{def}$ terms can be determined using purely

mechanical computations [17].

$$\begin{aligned} \nabla \cdot \boldsymbol{\sigma}_{ext} + \mathbf{f}_{ext} &= 0 \\ \nabla \cdot \boldsymbol{\sigma}_{def} + \mathbf{f}_{def} &= 0 \\ \mathbf{n} \cdot \boldsymbol{\sigma}_{ext}|_{surface} &= \mathbf{F}_{ext}. \end{aligned} \tag{2.23}$$

Here, $\mathbf{f}_{ext}$ denotes the external volume forces, while $\mathbf{f}_{def}$ stands for the internal volume forces due to the lattice imperfections and $\mathbf{F}_{ext}$ corresponds to the external surface forces.

The magnetostrictive terms $\boldsymbol{\epsilon}_{sp}$ and $\boldsymbol{\epsilon}_{el}$ depend on the elastic material properties as well on the local magnetization. The term $\boldsymbol{\epsilon}_{sp}$ is related with the spontaneous magnetostriction due to spin ordering. In the case of a cubic lattice, $\boldsymbol{\epsilon}_{sp}$ is given by

$$\boldsymbol{\epsilon}_{sp} = \begin{bmatrix} \frac{3}{2}\lambda_{100}(\alpha_1^2 - \frac{1}{3}) & \lambda_{111}\alpha_1\alpha_2 & \lambda_{111}\alpha_1\alpha_3 \\ \lambda_{111}\alpha_1\alpha_2 & \frac{3}{2}\lambda_{100}(\alpha_2^2 - \frac{1}{3}) & \lambda_{111}\alpha_2\alpha_3 \\ \lambda_{111}\alpha_1\alpha_3 & \lambda_{111}\alpha_2\alpha_3 & \frac{3}{2}\lambda_{100}(\alpha_3^2 - \frac{1}{3}) \end{bmatrix}. \tag{2.24}$$

Here, λ_{100} and λ_{111} are the magnetostriction constants corresponding to the $< 100 >$ and the $< 111 >$ directions respectively. The spontaneous magnetostriction (2.24) is directly depending on the local magnetization in terms of the direction cosines α_i (2.17).

The elastic strain tensor $\boldsymbol{\epsilon}_{el}$ is closely related with $\boldsymbol{\epsilon}_{sp}$. Indeed, the total strain tensor due to magnetostriction $\boldsymbol{\epsilon}_{sp} + \boldsymbol{\epsilon}_{el}$ has to meet the compatibility requirement

$$\nabla \times \left[\nabla \times (\boldsymbol{\epsilon}_{sp} + \boldsymbol{\epsilon}_{el})\right]^T = 0. \tag{2.25}$$

This condition describes the fact that the deformations in the material should be compatible with each other, meaning that no holes may arise in the material due to non-continuous displacements in adjacent regions. Hence, the magnetization field $\mathbf{m}$ determines the elastic strain $\boldsymbol{\epsilon}_{el}$ indirectly since $\boldsymbol{\epsilon}_{sp} + \boldsymbol{\epsilon}_{el}$ has to meet the compatibility condition (2.25).

One should keep in mind that in all expressions, the properties are space and time dependent. Hence, if one wants to introduce the magnetoelastic interactions in the micromagnetic simulations, changing external stresses and/or a changing microscopic structure of the material results in a reevaluation of the mechanical problem (2.23), while a changing magnetization results in a reevaluation of the compatibility condition (2.25).

Magnetoelastic energy density

The magnetoelastic energy density is given by

$$\phi_{me} = -\frac{1}{2}\boldsymbol{\epsilon}_{tot} \cdot\cdot \mathbf{C} \cdot\cdot \boldsymbol{\epsilon}_{tot}. \tag{2.26}$$

Introducing the expression (2.22) yields

$$\begin{aligned}\phi_{me} = &-\frac{1}{2}\boldsymbol{\epsilon}_{ext} \cdot\cdot \mathbf{C} \cdot\cdot \boldsymbol{\epsilon}_{ext} - \frac{1}{2}\boldsymbol{\epsilon}_{def} \cdot\cdot \mathbf{C} \cdot\cdot \boldsymbol{\epsilon}_{def} \\ &-\frac{1}{2}\boldsymbol{\epsilon}_{sp} \cdot\cdot \mathbf{C} \cdot\cdot \boldsymbol{\epsilon}_{sp} - \frac{1}{2}\boldsymbol{\epsilon}_{el} \cdot\cdot \mathbf{C} \cdot\cdot \boldsymbol{\epsilon}_{el} \\ &-\boldsymbol{\epsilon}_{ext} \cdot\cdot \mathbf{C} \cdot\cdot \boldsymbol{\epsilon}_{def} - \boldsymbol{\epsilon}_{ext} \cdot\cdot \mathbf{C} \cdot\cdot \boldsymbol{\epsilon}_{sp} - \boldsymbol{\epsilon}_{ext} \cdot\cdot \mathbf{C} \cdot\cdot \boldsymbol{\epsilon}_{el} \\ &-\boldsymbol{\epsilon}_{def} \cdot\cdot \mathbf{C} \cdot\cdot \boldsymbol{\epsilon}_{sp} - \boldsymbol{\epsilon}_{def} \cdot\cdot \mathbf{C} \cdot\cdot \boldsymbol{\epsilon}_{el} - \boldsymbol{\epsilon}_{sp} \cdot\cdot \mathbf{C} \cdot\cdot \boldsymbol{\epsilon}_{el}\end{aligned} \tag{2.27}$$

In our perspective, only the energy terms interacting with the magnetization field $\mathbf{m}$ are of interest. The other describe only purely mechanical energy contributions in the system. Moreover, based on the compatibility condition (2.25), it is shown in [4] that the following is valid:

$$\boldsymbol{\epsilon}_{sp} \cdot\cdot \boldsymbol{\epsilon}_{el} = -\boldsymbol{\epsilon}_{el} \cdot\cdot \boldsymbol{\epsilon}_{el}. \tag{2.28}$$

Hence, the expression for the magnetoelastic energy density (2.27) reduces to

$$\begin{aligned}\phi_{me} = &-\frac{1}{2}\boldsymbol{\epsilon}_{sp} \cdot\cdot \mathbf{C} \cdot\cdot \boldsymbol{\epsilon}_{sp} \\ &+\frac{1}{2}\boldsymbol{\epsilon}_{el} \cdot\cdot \mathbf{C} \cdot\cdot \boldsymbol{\epsilon}_{el} \\ &-(\boldsymbol{\sigma}_{ext} + \boldsymbol{\sigma}_{def}) \cdot\cdot (\boldsymbol{\epsilon}_{sp} + \boldsymbol{\epsilon}_{el}).\end{aligned} \tag{2.29}$$

The three different terms can be interpreted as follows:

- The first term only depends on the spontaneous magnetostrictive strains. In the case of ferromagnetic materials this term can be elaborated as

$$\phi_{me,1} = \left[\frac{9}{4}(c_{11} - c_{12})\lambda_{100}^2 - \frac{9}{2}c_{44}\lambda_{111}^2\right](\alpha_1^2\alpha_2^2 + \alpha_2^2\alpha_3^2 + \alpha_1^2\alpha_3^2), \tag{2.30}$$

  with c_{11}, c_{12} and c_{44} elastic constants in Voigt's notation [1]. Since this energy contribution has the same form as (2.19), this term is a magnetostrictive contribution to the cubic anisotropy energy density. However, in iron this contribution is negligible since the coefficient between squared brackets in (2.30) is about thousand times smaller than K_1.
- The second term is the self energy density of the elastic magnetostrictive strains.

- The third term is the magnetoelastic coupling which takes into account the influence of the external applied stresses and the stresses due to defects present in the material.

2.2.4 Zeeman energy

The Zeeman energy density ϕ_a results from the interaction between the magnetic material and the external applied field $\mathbf{H}_a$. From a quantum mechanical as well as from a macroscopic (experimental) point of view it is known that magnetic moments align parallel to an external field. In the continuum approach, this results in

$$\phi_a(\mathbf{r}) = -\mu_0 M_s \mathbf{m}(\mathbf{r}) \cdot \mathbf{H}_a. \tag{2.31}$$

From this energy term it is clear that a hypothetical ferromagnetic material, only subject to the Zeeman interaction, aligns uniformly with the applied field $\mathbf{H}_a$.

2.2.5 Magnetostatic energy

The origin of the magnetostatic energy density ϕ_{ms} is found in the magnetostatic field $\mathbf{H}_{ms}$ generated by the ferromagnetic body itself. From the quantum mechanic theory it is known that each magnetic moment generates a magnetic field. Summing the fields, generated by all the magnetic moments in the ferromagnetic sample, results in the magnetostatic field. A macroscopic description of $\mathbf{H}_{ms}$ and the resulting energy density ϕ_{ms} starts with the static Maxwell equations. The magnetostatic energy density is given by

$$\phi_{ms}(\mathbf{r}) = -\frac{1}{2}\mu_0 M_s \mathbf{m}(\mathbf{r}) \cdot \mathbf{H}_{ms}(\mathbf{r}). \tag{2.32}$$

This expression is analogous with (2.31) except for the factor $1/2$. This can be understood as follows. Consider two magnetic dipoles $\mathbf{m}_i$ and $\mathbf{m}_j$, generating magnetostatic fields $\mathbf{H}^i_{ms}(\mathbf{r})$ and $\mathbf{H}^j_{ms}(\mathbf{r})$ respectively. The energy related with the magnetic dipole $\mathbf{m}_i$ placed in the magnetostatic field generated by the magnetic dipole $\mathbf{m}_j$ is

$$\phi^i_{ms} = -\mu_0 M_s \mathbf{m}_i \cdot \mathbf{H}^j_{ms}(\mathbf{r}_i). \tag{2.33}$$

Vice versa, the energy related with the magnetic dipole $\mathbf{m}_j$ placed in the magnetostatic field generated by the magnetic dipole $\mathbf{m}_i$ is

$$\phi^j_{ms} = -\mu_0 M_s \mathbf{m}_j \cdot \mathbf{H}^i_{ms}(\mathbf{r}_j). \tag{2.34}$$

Both expressions describe the same interaction and thus have an identical value. Hence, the factor $1/2$ makes sure the energy between two dipoles is only counted once.

The magnetostatic interactions have a very large influence on the magnetization processes in ferromagnetic materials. Therefore, a separate comprehensive outline on this interaction term is given in Chapter 3.

2.3. Minimization of the Gibbs free energy

In the previous section, the different micromagnetic energy terms that contribute to the total Gibbs free energy density ϕ_G are derived

$$\phi_G = \phi_{exch} + \phi_{ani} + \phi_{me} + \phi_a + \phi_{ms}. \tag{2.35}$$

In this section a micromagnetic equilibrium condition will be derived corresponding to a minimal total Gibbs free energy.

2.3.1 Variational description

Since the amplitude of the considered vector field $\mathbf{m}(\mathbf{r},t)$ is constant, only the orientation in each space point can vary in order to minimize ϕ_G at a given time point t. Hence, in the minimization process, the constraint

$$\sum_{i=1}^{3} m_i^2(\mathbf{r},t) = 1 \qquad \forall \mathbf{r},t \tag{2.36}$$

has to be met. In what follows the space and time dependency will be omitted for clarity. This leads to the variational problem

$$\begin{aligned}
\delta\phi_G &= \delta \int_V \left[\phi_{exch} + \phi_{ani} + \phi_{me} + \phi_a + \phi_{ms} + \lambda \left(\sum_{i=1}^{3} m_i^2 - 1 \right) \right] \mathrm{d}\mathbf{r} \\
&= \int_V \left(\delta\phi_{exch} + \delta\phi_{ani} + \delta\phi_{me} + \delta\phi_a + \delta\phi_{ms} + 2\lambda \sum_{i=1}^{3} m_i \delta m_i \right) \mathrm{d}\mathbf{r} \\
&= 0.
\end{aligned} \tag{2.37}$$

Here, λ is the Langrange parameter and V is the volume of the magnetic material. Expression (2.37) leads to a set of coupled differential equations. Now, the different variations in (2.37) will be considered separately.

- The variation of ϕ_{exch} yields

$$\begin{aligned}\int_V \delta\phi_{exch}\,\mathrm{d}\mathbf{r} &= \int_V \delta\left(A\sum_{i=1}^{3}(\nabla m_i)^2\right)\mathrm{d}\mathbf{r}\\ &= \int_V 2A\sum_{i=1}^{3}(\nabla m_i)\delta(\nabla m_i)\,\mathrm{d}\mathbf{r},\end{aligned} \tag{2.38}$$

with V the volume of the ferromagnetic sample. Now, it holds that

$$\begin{aligned}(\nabla m_i)\delta(\nabla m_i) &= (\nabla m_i)\nabla\delta m_i\\ &= \nabla\cdot(\nabla m_i\delta m_i) - \nabla^2 m_i\delta m_i.\end{aligned} \tag{2.39}$$

Applying Gauss' theorem, the first term can be transformed to a surface integral over the surface of the considered volume V when introduced in (2.38)

$$\int_V \delta\phi_{exch}\,\mathrm{d}\mathbf{r} = 2A\sum_{i=1}^{3}\int_{\partial V}\nabla m_i\delta m_i\cdot\mathbf{n}\,\mathrm{d}S - 2A\sum_{i=1}^{3}\int_V \nabla^2 m_i\delta m_i\,\mathrm{d}\mathbf{r}. \tag{2.40}$$

- For the variation of ϕ_{ani} and ϕ_{me} we restrict ourselves to

$$\int_V \delta\phi_{ani}\,\mathrm{d}\mathbf{r} = \sum_{i=1}^{3}\int_V \frac{\partial\phi_{ani}}{\partial m_i}\delta m_i\,\mathrm{d}\mathbf{r} \tag{2.41}$$

and

$$\int_V \delta\phi_{me}\,\mathrm{d}\mathbf{r} = \sum_{i=1}^{3}\int_V \frac{\partial\phi_{me}}{\partial m_i}\delta m_i\,\mathrm{d}\mathbf{r}. \tag{2.42}$$

- The variation of ϕ_a yields

$$\begin{aligned}\int_V \delta\phi_a\,\mathrm{d}\mathbf{r} &= -\mu_0 M_s\int_V \mathbf{H}_a\cdot\delta\mathbf{m}\,\mathrm{d}\mathbf{r}\\ &= -\mu_0 M_s\sum_{i=1}^{3}\int_V H_{a,i}\delta m_i\,\mathrm{d}\mathbf{r}.\end{aligned} \tag{2.43}$$

- The variation of ϕ_{ms} results in

$$\begin{aligned}\int_V \delta\phi_{ms}\,\mathrm{d}\mathbf{r} &= -\frac{1}{2}\mu_0 M_s\int_V \delta(\mathbf{H}_{ms}\cdot\mathbf{m})\,\mathrm{d}\mathbf{r}\\ &= -\frac{1}{2}\mu_0 M_s\int_V (\delta\mathbf{H}_{ms}\cdot\mathbf{m} + \mathbf{H}_{ms}\cdot\delta\mathbf{m})\,\mathrm{d}\mathbf{r}.\end{aligned} \tag{2.44}$$

Indeed, here also $\mathbf{H}_{ms}$ depends on $\mathbf{m}$. Due to the reciprocity theorem [5] it holds that

$$\int_V \delta\mathbf{H}_{ms} \cdot \mathbf{m}\,\mathrm{d}\mathbf{r} = \int_V \mathbf{H}_{ms} \cdot \delta\mathbf{m}\,\mathrm{d}\mathbf{r}. \tag{2.45}$$

Hence, this variation reduces to

$$\int_V \delta\phi_{ms}\,\mathrm{d}\mathbf{r} = -\mu_0 M_s \sum_{i=1}^{3} \int_V H_{ms,i}\delta m_i\,\mathrm{d}\mathbf{r}. \tag{2.46}$$

Inserting the above results in (2.37) yields

$$\begin{aligned}\delta\phi_G = \int_V \sum_{i=1}^{3} \Big(&-2A\nabla^2 m_i + \frac{\partial\phi_{ani}}{\partial m_i} + \frac{\partial\phi_{me}}{\partial m_i} - \mu_0 M_s H_{a,i} \\ &- \mu_0 M_s H_{ms,i} + 2\lambda m_i \Big)\delta m_i\,\mathrm{d}\mathbf{r} \\ &+ 2A \int_{\partial V} \sum_{i=1}^{3} \nabla m_i \delta m_i \cdot \mathbf{n}\,\mathrm{d}S.\end{aligned} \tag{2.47}$$

This variation is zero if the integrand of the volume and surface integrals for all δm_i are separately zero. Hence, in every volume point of the considered ferromagnetic body the following three conditions should be fulfilled

$$\begin{gathered}-2A\nabla^2 m_i + \frac{\partial\phi_{ani}}{\partial m_i} + \frac{\partial\phi_{me}}{\partial m_i} - \mu_0 M_s H_{a,i} - \mu_0 M_s H_{ms,i} + 2\lambda m_i = 0 \\ (i = 1,2,3)\end{gathered} \tag{2.48}$$

and for each surface point the following three equilibrium conditions have to be met

$$\mathbf{n} \cdot \nabla m_i = 0 \qquad (i = 1,2,3). \tag{2.49}$$

Expression (2.49) represents a Neumann boundary condition for every component of the magnetization field. It states that the derivative of the magnetization in the direction of the surface normal $\mathbf{n}$ at the boundary vanishes so it has only a tangential component.

The volume equilibrium condition (2.48) still contains the unknown Lagrange parameter λ. This parameter can be eliminated by first multiplying expression (2.48) for m_i with m_j and vice versa and then subtracting the results. This yields

$$H_{eff,i} M_s m_j - H_{eff,j} M_s m_i = 0 \tag{2.50}$$

with

$$H_{eff,i} = \frac{2A}{\mu_0 M_s}\nabla^2 m_i - \frac{1}{\mu_0 M_s}\frac{\partial\phi_{ani}}{\partial m_i} - \frac{1}{\mu_0 M_s}\frac{\partial\phi_{me}}{\partial m_i} + H_{a,i} + H_{ms,i}. \tag{2.51}$$

The three volume conditions corresponding to expression (2.50) can be summarized in

$$\mathbf{M} \times \mathbf{H}_{eff} = 0. \tag{2.52}$$

These minimum energy conditions are known as Brown's equations. It turns out that the minimal Gibbs free energy states are magnetic configurations where in each point of the material the micromagnetic condition of a vanishing magnetic torque $\mathbf{N} = \mu_0 \mathbf{M} \times \mathbf{H}_{eff}$ is met. Here, the effective field $\mathbf{H}_{eff}(\mathbf{r}, t)$ is defined as a continuum vector field that varies on the same time and length scale as $\mathbf{m}(\mathbf{r}, t)$ and accounts for all micromagnetic interactions in the material. From this it is clear that the magnetic equilibrium configurations can be determined by solving (2.52) and (2.49) together, for every volume point and for each surface point of the material respectively. This corresponds to solving a system of coupled equations represented by a rather complicated nonlinear integrodifferential equation, since $\mathbf{H}_{ms}$ and $\boldsymbol{\epsilon}_{sp}$, depend both on $\mathbf{m}$ by means of integral expressions. Due to the complexity of the micromagnetic system, a large number of local minima that meet conditions (2.52) and (2.49) can exist.

2.3.2 Effective field terms

In the previous Section, the effective field $\mathbf{H}_{eff}(\mathbf{r}, t)$ has arisen from the micromagnetic theory as the continuum vector field which accounts for all interactions that determine the behavior of the magnetization field $\mathbf{m}(\mathbf{r}, t)$. The different micromagnetic interactions have an associated term contributing to $\mathbf{H}_{eff}(\mathbf{r}, t)$

$$\mathbf{H}_{eff}(\mathbf{r}, t) = \mathbf{H}_{exch}(\mathbf{r}, t) + \mathbf{H}_{ani}(\mathbf{r}, t) + \mathbf{H}_{me}(\mathbf{r}, t) + \mathbf{H}_{a}(t) + \mathbf{H}_{ms}(\mathbf{r}, t). \tag{2.53}$$

The external applied field $\mathbf{H}_a$ is considered to be uniform in space and is the only term which is not depending on $\mathbf{m}(\mathbf{r}, t)$. The magnetostatic field contribution $\mathbf{H}_{ms}$ is described in detail in Chapter 3. In what follows we will again omit the $(\mathbf{r}, t)$ dependency.

The exchange field can thus be defined as

$$\mathbf{H}_{exch} = \frac{2A}{\mu_0 M_s} \nabla^2 m_i \mathbf{e}_i. \tag{2.54}$$

Here, and in what follows, the Einstein summation convention is used: when indices appear twice, summation is made. The anisotropy field is defined as

$$\mathbf{H}_{ani} = -\frac{1}{\mu_0 M_s} \frac{\partial \phi_{ani}}{\partial m_i} \mathbf{e}_i. \tag{2.55}$$

The magnetoelastic field is defined as

$$\mathbf{H}_{me} = -\frac{1}{\mu_0 M_s}\frac{\partial \phi_{me}}{\partial m_i}\mathbf{e}_i. \tag{2.56}$$

Micromagnetic length scale

In the introduction of Section 2.2, the magnetic continuum field $\mathbf{m}(\mathbf{r},t)$ was said to be defined on a length scale that is large enough to contain a huge number of atoms, but small enough to ensure that the vector field varies smoothly. A characteristic length scale can be derived based on the exchange field (2.54). Indeed, the exchange interaction strongly disfavors variations on very small length scales. Hence, variations of the magnetization can only start to occur on a certain, material dependent length scale denoted by the *exchange length*, given by

$$l_{exch} = \sqrt{\frac{2A}{\mu_0 M_s^2}}. \tag{2.57}$$

In the case of pure iron $l_{exch} = 2.8\,nm$ [5].

Soft and hard magnetic materials

Another interesting characteristic value is the dimensionless parameter (here for cubic anisotropy)

$$\kappa = \frac{H_{ani}}{M_s} = \frac{2K_1}{\mu_0 M_s^2}. \tag{2.58}$$

This ratio gives a natural measure of the relative strength of anisotropy and magnetostatic effects. Magnetostatic effects dominate in *soft magnetic materials*, for which $\kappa << 1$. Anisotropy effects dominate in *hard magnetic materials*, where $\kappa \geq 1$. For pure iron $\kappa = 0.026$ [5].

2.4. Dynamics in micromagnetism

Given a constant external applied field $\mathbf{H}_a$, the geometry and the material parameters of a given sample, Brown's equations (2.49) and (2.52) provide us the complete set of local energy minima. When in equilibrium, the ferromagnetic system is in a state corresponding to one of these minima. If we now switch $\mathbf{H}_a$ to another value, the energy landscape changes: some energy minima disappear, while other are created. It is clear that the new equilibrium state of the magnetic system will depend on the magnetization history, i.e. the former equilibrium state. The Landau-Lifshitz equation not only tells us to which new

minimum energy point the system evolves, but also which trajectory the system follows between the two equilibrium states.

2.4.1 Landau-Lifshitz-Gilbert equation

The description of the temporal behavior of $\mathbf{m}(\mathbf{r},t)$ starts in the quantum theory. Let us consider an elementary magnetic moment $\boldsymbol{\mu}_i$ that also caries a corresponding angular momentum $\mathbf{J}_i$. From quantum mechanics it is known that the two are directly proportional to each other $\boldsymbol{\mu}_i = \gamma \mathbf{J}_i$. Since in iron $\mathbf{J}_i$ comes from electron spins, γ equals q_e/m_e, i.e. the charge of the electron divided by its mass. In a classical description, the rate of change of the angular moment is given by the torque $\mathbf{N}$ exerted on the magnetic moment

$$\frac{\partial \mathbf{J}_i}{\partial t} = \mu_0 \mathbf{m}_i \times \mathbf{H} \tag{2.59}$$

which yields

$$\frac{\partial \mathbf{m}_i}{\partial t} = \gamma_G \mathbf{m}_i \times \mathbf{H} \tag{2.60}$$

with $\gamma_G = \mu_0 \gamma$. Translated to the continuum micromagnetic description (and omitting the $(\mathbf{r},t)$ dependency) this results in

$$\frac{\partial \mathbf{m}}{\partial t} = \gamma_G \mathbf{m} \times \mathbf{H}_{eff}. \tag{2.61}$$

This expression is in accordance with the equations of Brown: when the system is in equilibrium, the magnetization does not vary in time. However, when the system is not in equilibrium, expression (2.61) describes in every space point a precessional movement of the magnetization field $\mathbf{m}$ around the local effective field $\mathbf{H}_{eff}$ and thereby never reaching equilibrium. A second term has to be added to (2.61) in order to make an evolution of $\mathbf{m}$ towards $\mathbf{H}_{eff}$ possible. Gilbert [18] proposed the following expression

$$\frac{\partial \mathbf{m}}{\partial t} = \gamma_G \mathbf{m} \times \mathbf{H}_{eff} - \alpha_G \mathbf{m} \times \frac{\partial \mathbf{m}}{\partial t}, \tag{2.62}$$

with α_G the Gilbert damping constant. From Fig. 2.6 it is clear that the extra term results in a damped precession movement of the magnetization field $\mathbf{m}$ around $\mathbf{H}_{eff}$.

Landau and Lifshitz proposed another expression which describes the same phenomenon [11]

$$\frac{\partial \mathbf{m}}{\partial t} = \gamma_L \mathbf{m} \times \left(\mathbf{H}_{eff} - \alpha_L \mathbf{m} \times \mathbf{H}_{eff} \right), \tag{2.63}$$

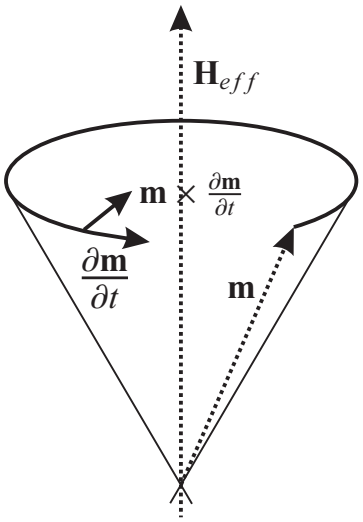

Figure 2.6: Damped precessional movement of the magnetization field $\mathbf{m}(\mathbf{r},t)$ around $\mathbf{H}_{eff}(\mathbf{r},t)$.

known as the Landau-Lifshitz equation. This expression is equivalent with the Gilbert equation. This is proven by making the vector product of $\mathbf{m}$ with the left and right hand side of (2.63) and using $\mathbf{m} \times (\mathbf{m} \times (\mathbf{m} \times \mathbf{H}_{eff})) = -\mathbf{m} \times \mathbf{H}_{eff}$

$$\begin{aligned} \mathbf{m} \times \frac{\partial \mathbf{m}}{\partial t} &= \gamma_L \mathbf{m} \times (\mathbf{m} \times \mathbf{H}_{eff}) + \gamma_L \alpha_L \mathbf{m} \times \mathbf{H}_{eff} \\ &= \frac{1}{\alpha_L} \left(\gamma_L \mathbf{m} \times \mathbf{H}_{eff} - \frac{\partial \mathbf{m}}{\partial t} \right) + \gamma_L \alpha_L \mathbf{m} \times \mathbf{H}_{eff} \end{aligned} \tag{2.64}$$

A rearrangement of the different terms results in

$$\frac{\partial \mathbf{m}}{\partial t} = \gamma_L (1 + \alpha_L^2) \mathbf{m} \times \mathbf{H}_{eff} - \alpha_L \mathbf{m} \times \frac{\partial \mathbf{m}}{\partial t} \tag{2.65}$$

This is equivalent with the Gilbert equation (2.62) with

$$\gamma_L = \frac{\gamma_G}{1 + \gamma_G^2 \alpha_G^2} = \frac{\gamma_G}{1 + \alpha^2} \tag{2.66}$$

$$\gamma_L \alpha_L = \gamma_G \frac{\gamma_G \alpha_G}{1 + \gamma_G^2 \alpha_G^2} = \gamma_G \frac{\alpha}{1 + \alpha^2}. \tag{2.67}$$

The gyromagnetic constant γ_G is equal to $-2.21\,10^5\,mA^{-1}s^{-1}$. The value of α is comprised between 0 and 1. For $\alpha = 0$ there is no damping, thus only a precessional movement without energy dissipation. For $\alpha = 1$ the damping is large. In what follows we will use α as the parameter to describe the damping, rather than α_G or α_L, resulting in the Landau-Lifshitz-Gilbert (LLG) equation

$$\frac{\partial \mathbf{m}}{\partial t} = \frac{\gamma_G}{1+\alpha^2}\mathbf{m} \times \mathbf{H}_{eff} + \frac{\alpha\gamma_G}{1+\alpha^2}\mathbf{m} \times \Big(\mathbf{m} \times \mathbf{H}_{eff}\Big). \tag{2.68}$$

2.4.2 Micromagnetic time scale

From the LLG equation we can estimate on which time scale the continuum magnetization field $\mathbf{m}(\mathbf{r},t)$ varies. If we consider the amplitude of the effective field $\mathbf{H}_{eff}$ of the order of M_s (for iron $1.72\,10^6\,Am^{-1}$) the right hand side is $\mathcal{O}(10^{12}s^{-1})$. Combined with the fact that $|\mathbf{m}(\mathbf{r},t)| = 1$, we can conclude that the orientation of the continuum magnetization field varies on a sub-picosecond time scale. Hence, the time scale as well as the length scale on which the micromagnetic theory describes the magnetization processes is between the time and length scales encountered in quantum mechanics on the one hand and encountered in macroscopic magnetization processes on the other hand.

2.4.3 Properties of the LLG equation

The LLG equation incorporates several properties required in the micromagnetic description

- The LLG equation preserves the amplitude of the magnetization field $\mathbf{m}(\mathbf{r},t)$.
  This property is easily proven by scalar multiplying the left and right hand side with $\mathbf{m}$. This leads to

$$\begin{aligned}\mathbf{m}\cdot\frac{\partial \mathbf{m}}{\partial t} &= \frac{1}{2}\frac{\partial}{\partial t}|\mathbf{m}|^2 \\ &= \mathbf{m}\cdot\left[\frac{\gamma_G}{1+\alpha^2}\mathbf{m} \times \mathbf{H}_{eff} + \frac{\alpha\gamma_G}{1+\alpha^2}\mathbf{m} \times \Big(\mathbf{m} \times \mathbf{H}_{eff}\Big)\right] \\ &= 0.\end{aligned} \tag{2.69}$$

- The LLG equation guarantees the continuous decrease in energy for constant applied fields $\mathbf{H}_a$.
  This property is proven by considering the fact that

$$\mathbf{H}_{eff} = -\frac{1}{\mu_0 M_s}\frac{\partial \phi_G}{\partial \mathbf{m}}. \tag{2.70}$$

Hence it holds that

$$\frac{\partial \phi_G}{\partial t} = -\mu_0 M_s \mathbf{H}_{eff} \cdot \frac{\partial \mathbf{m}}{\partial t}. \tag{2.71}$$

Thus, introducing the LLG equation in (2.71), the temporal variation of the total energy $E_{tot} = \int_V \phi_G \mathrm{d}\mathbf{r}$ can be written as

$$\begin{aligned} \frac{\partial E_{tot}}{\partial t} &= -\mu_0 M_s \frac{\alpha \gamma_G}{1+\alpha^2} \int_V \mathbf{H}_{eff} \cdot (\mathbf{m} \times (\mathbf{m} \times \mathbf{H}_{eff}))\, \mathrm{d}\mathbf{r} \\ &= -\mu_0 M_s \frac{\alpha \gamma_G}{1+\alpha^2} \int_V ((\mathbf{m} \cdot \mathbf{H}_{eff})^2 - H_{eff}^2)\, \mathrm{d}\mathbf{r}. \end{aligned} \tag{2.72}$$

Due to the Cauchy-Schwartz inequality the right hand side of (2.72) is negative (γ_G has a negative value and $|\mathbf{m}| = 1$).
From equation (2.72) it is also clear that equilibrium is indeed reached when $\mathbf{m}$ aligns with $\mathbf{H}_{eff}$. Indeed, in that case, the term between brackets becomes zero.

- The LLG equation conserves the Gibbs free energy in the case of zero damping.
  This property was already discussed before and results directly from equation (2.72).

2.5. Eddy currents

Another time dependent process, present in ferromagnetic materials originates in Maxwell's equations. Following Faraday's law, changes in the magnetic field $\mathbf{B}$ result in electric fields

$$\nabla \times \mathbf{E} = -\frac{\partial \mathbf{B}}{\partial t} \tag{2.73}$$

and thus in electrical currents

$$\mathbf{j}_{eddy} = \sigma \mathbf{E} \tag{2.74}$$

with σ the conductivity of the material. These eddy currents introduce additional magnetic fields in the ferromagnetic material

$$\nabla \cdot \mathbf{H}_{eddy} = 0 \tag{2.75}$$

$$\nabla \times \mathbf{H}_{eddy} = \mathbf{j}_{eddy}. \tag{2.76}$$

After taking the curl of expression (2.76) and considering (2.75) and (2.74) one gets

$$\begin{aligned} \nabla^2 \mathbf{H}_{eddy} &= -\sigma \nabla \times \mathbf{E} \\ &= \sigma \frac{\partial \mathbf{B}}{\partial t}. \end{aligned} \tag{2.77}$$

With $\mathbf{B} = \mu_0(\mathbf{M} + \mathbf{H})$ this yields

$$\nabla^2 \mathbf{H}_{eddy} = \sigma \mu_0 \left(\frac{\partial \mathbf{M}}{\partial t} + \frac{\partial \mathbf{H}}{\partial t} \right). \tag{2.78}$$

In a full dynamical description of the magnetization processes in ferromagnetic materials, the field $\mathbf{H}_{eddy}$ has to be added to the effective field (2.53).

The above derivation started from Maxwell's equations and thus from macroscopic field quantities. It is interesting to see how to fit this macroscopic description in the micromagnetic framework. Some observations can be made:

- In the micromagnetic model, the magnetization and field variations occur on very different time scales. Ranging from the sub-picosecond time scale on which the LLG dynamics takes place to the slow time scale on which the applied field varies. This gives rise to eddy currents, running on very different length scales: the fast microscopic magnetization dynamics in e.g. domain walls gives rise to local eddy currents around the domain wall (as e.g. described in the Pry and Bean Model [19]), while the slow macroscopic magnetization evolution due to changes in the applied field gives rise to eddy currents running through the whole material.
- The above Maxwell description yields the time derivative of the magnetic field $\mathbf{H}$. Now, the question arises which magnetic field has to be taken into account. In a macroscopic view point, the applied field and magnetostatic field suffice. In the micromagnetic viewpoint however, all field terms contributing to the effective field (2.53) need to be included.

2.6. Thermal fluctuations

Up to now the influence of the temperature is neglected (T=0 K). In reality thermal fluctuations affect the magnetization processes in the ferromagnetic material. At zero temperature, the position and orientation of the atoms in the material lattice are frozen at a certain state. For higher temperatures however, the atoms start to vibrate around their equilibrium position and orientation. Consequently, the magnetic moment of the atoms vibrate around their equilibrium state. From an energetic point of view, the thermal fluctuations add a small amount of energy to the atoms so they have some extra kinetic energy to move around the equilibrium position defined by the minimum of their po-

tential well. The higher the temperature, the more (kinetic) energy is added to the system.

Following Brown [20] the thermal effects can be introduced in the micromagnetic theory by adding a fluctuating field $\mathbf{H}_{th}(\mathbf{r},t)$ to the effective field (2.53). The thermal field $\mathbf{H}_{th}(\mathbf{r},t)$ is assumed to be a Gaussian random process with zero mean value in each direction $q = x,y,z$ and to be uncorrelated in both space and time

$$\langle H_{th,q}(\mathbf{r},t)\rangle = 0, \tag{2.79}$$

$$\langle H_{th,p}(\mathbf{r},t)H_{th,q}(\mathbf{r}',t')\rangle = 2D\delta_{pq}\delta(\mathbf{r}-\mathbf{r}',t-t'). \tag{2.80}$$

The amplitude of the thermal fluctuations is derived from the fluctuation-dissipation theorem

$$D = \frac{\alpha k_B T}{|\gamma_G|\mu_0 M_s V} \tag{2.81}$$

with k_B the Boltzmann constant and V the volume of the particle or the discretization volume in the considered numerical algorithm. Hence, the thermal field can be expressed as

$$\mathbf{H}_{th} = \boldsymbol{\eta}(\mathbf{r},t)\sqrt{\frac{2\alpha k_B T}{|\gamma_G|\mu_0 M_s \Delta^3 \delta t}} \tag{2.82}$$

with δt the time span or the time step used in the numerical algorithm and $\boldsymbol{\eta}(\mathbf{r},t)$ a stochastic vector whose components are Gaussian random numbers, uncorrelated in space and time, with zero mean value and dispersion 1.

The influence of $\mathbf{H}_{th}$ on the micromagnetic energy landscape is now explained with the help of Fig. 2.7, which shows an energy function only depending on one parameter X with two minima A and B. From previous sections it was clear that for $T = 0\,K$ a micromagnetic equilibrium state corresponds to a minimum in the total Gibbs free energy, as e.g. equilibrium point A in Fig. 2.7. Thermal fluctuations add a stochastic energy density

$$\phi_{th}(\mathbf{r},t,T) = -\mu_0 M_s \mathbf{m}(\mathbf{r},t)\cdot\mathbf{H}_{th}(\mathbf{r},t,T) \tag{2.83}$$

to the Gibbs free energy ϕ_G. For $T > 0\,K$, the statistical distributed extra kinetic energy makes the micromagnetic system fluctuate around the minimum (potential) Gibbs free energy point. In Fig. 2.7, an additional thermal energy $E_{th,1}$ makes the micromagnetic system fluctuate around the minimum Gibbs free energy state A. From this, it is obvious that some extra amount of energy can enable the micromagnetic system to jump across an energy barrier and initiate the transition to another equilibrium point. In Fig. 2.7, adding thermal fluctuations with $E_{th} > E_{th,2}$ will enable the system to cross the energy barrier between the states A and B.

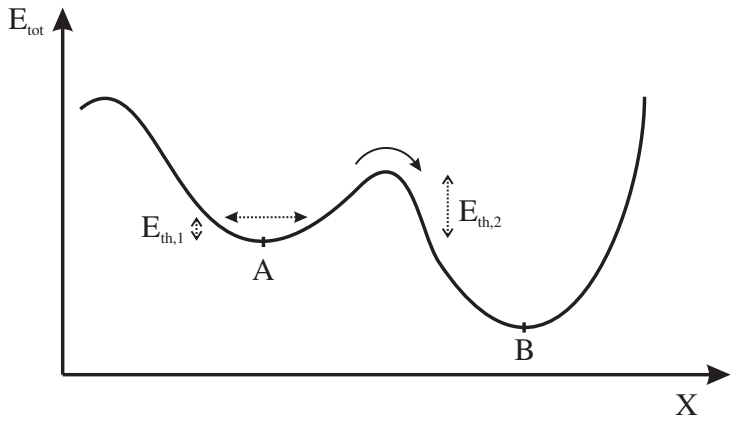

Figure 2.7: Influence of thermal fluctuations on the micromagnetic equilibrium states.

The amplitude of the thermal fluctuations are Gaussian distributed, thus there is always a probability that the thermal fluctuations are large enough to jump across energy barriers. Since $\mathbf{H}_{th} \propto \sqrt{T}$, this probability increases for larger temperatures. Moreover, even at low or moderate temperatures, the micromagnetic system will jump across energy barriers if one waits long enough. Indeed, due to the Gaussian nature of the thermal agitation, at some point in time the amplitude of $\mathbf{H}_{th}$ will be large enough to cross barriers between different equilibrium points. After very long waiting times the micromagnetic systems can eventually end up in the global Gibbs free energy minimum. This process is for instance the reason for the demagnetization of magnetic tapes.

To conclude, it should be stressed that the fluctuations take place self-consistently, not changing the total energy of the system. The thermal fluctuations only initiate the transition between successive equilibrium states. The eventual path between the equilibrium states is determined by the LLG equation. Here, the changes of energy are exclusively due to the dissipation described by the LLG equation.

CHAPTER 3

Magnetostatic energy

In Chapter 2 the magnetostatic energy density is introduced shortly as

$$\begin{aligned}\phi_{ms}(\mathbf{r}) &= -\frac{1}{2}\mu_0 M_s \mathbf{m}(\mathbf{r}) \cdot \mathbf{H}_{ms}(\mathbf{r}) \\ &= -\frac{1}{2}\mu_0 \mathbf{M}(\mathbf{r}) \cdot \mathbf{H}_{ms}(\mathbf{r}).\end{aligned} \tag{3.1}$$

Here, this energy term is outlined in more detail.

3.1. Maxwell description of the magnetostatic field

Magnetostatic fields have a very large influence on the magnetization dynamics in ferromagnetic bodies. The fields originate in Maxwell's equations in the absence of currents

$$\begin{aligned}\nabla \cdot \mathbf{B}_{ms}(\mathbf{r}) &= 0 \\ \nabla \times \mathbf{H}_{ms}(\mathbf{r}) &= 0.\end{aligned} \tag{3.2}$$

These equations can be written in two equivalent forms. One is based on the magnetostatic induction $\mathbf{B}_{ms}(\mathbf{r}) = \mu_0(\mathbf{H}_{ms}(\mathbf{r}) + \mathbf{M}(\mathbf{r}))$

$$\begin{aligned}\nabla \cdot \mathbf{B}_{ms}(\mathbf{r}) &= 0 \\ \frac{1}{\mu_0}\nabla \times \mathbf{B}_{ms}(\mathbf{r}) &= \mathbf{j}_{ms}(\mathbf{r}),\end{aligned} \tag{3.3}$$

where the magnetization current $\mathbf{j}_{ms}(\mathbf{r}) = \nabla \times \mathbf{M}(\mathbf{r})$ is introduced (analogue to a static current $\mathbf{j}(\mathbf{r})$). It is natural to chose the vectorial potential $\mathbf{A}_{ms}(\mathbf{r})$, with $\mathbf{B}_{ms}(\mathbf{r}) = \nabla \times \mathbf{A}_{ms}(\mathbf{r})$ to characterize the problem (3.3). When the Coulomb gauge $\nabla \cdot \mathbf{A}_{ms}(\mathbf{r}) = 0$ is adopted, the vector potential is the solution

of the vectorial Poisson problem

$$\nabla^2 \mathbf{A}_{ms}(\mathbf{r}) = -\mu_0 \mathbf{j}_{ms}(\mathbf{r}), \tag{3.4}$$

which yields

$$\begin{aligned}\mathbf{A}_{ms}(\mathbf{r}) &= \frac{\mu_0}{4\pi}\int_\Omega \frac{\nabla' \times \mathbf{M}(\mathbf{r}')}{|\mathbf{r}-\mathbf{r}'|}\,\mathrm{d}\mathbf{r}' \\ &= \frac{\mu_0}{4\pi}\int_\Omega \nabla' \times \frac{\mathbf{M}(\mathbf{r}')}{|\mathbf{r}-\mathbf{r}'|}\,\mathrm{d}\mathbf{r}' - \frac{\mu_0}{4\pi}\int_\Omega \nabla'\left(\frac{1}{|\mathbf{r}-\mathbf{r}'|}\right) \times \mathbf{M}(\mathbf{r}')\,\mathrm{d}\mathbf{r}'.\end{aligned} \tag{3.5}$$

where ∇' only acts on $\mathbf{r}'$ and Ω denotes total space. Gauss' theorem enables us to rewrite the first term in this expression to a surface integral, while for the second term it holds that $\nabla' \frac{1}{\mathbf{r}-\mathbf{r}'} = -\nabla \frac{1}{\mathbf{r}-\mathbf{r}'}$, which leads to

$$\mathbf{A}_{ms}(\mathbf{r}) = \frac{\mu_0}{4\pi}\oint_{\partial\Omega} \mathbf{n} \times \frac{\mathbf{M}(\mathbf{r}')}{|\mathbf{r}-\mathbf{r}'|}\,\mathrm{d}S + \frac{\mu_0}{4\pi}\int_\Omega \nabla \frac{1}{|\mathbf{r}-\mathbf{r}'|} \times \mathbf{M}(\mathbf{r}')\,\mathrm{d}\mathbf{r}'. \tag{3.6}$$

Since the integrals run over total space and at infinity the magnetization is zero, the first term is zero. The volume integral in the second term can be restricted to the volume V of the magnetic material.

$$\mathbf{A}_{ms}(\mathbf{r}) = \frac{\mu_0}{4\pi}\int_V \nabla \frac{1}{|\mathbf{r}-\mathbf{r}'|} \times \mathbf{M}(\mathbf{r}')\,\mathrm{d}\mathbf{r}'. \tag{3.7}$$

Another approach to solve (3.2) is based on the scalar magnetic field $\mathbf{H}_{ms}$

$$\begin{aligned}\nabla \cdot \mathbf{H}_{ms}(\mathbf{r}) &= \rho_{ms}(\mathbf{r}) \\ \nabla \times \mathbf{H}_{ms}(\mathbf{r}) &= 0,\end{aligned} \tag{3.8}$$

where the magnetic charge density $\rho_{ms}(\mathbf{r}) = -\nabla \cdot \mathbf{M}(\mathbf{r})$ is introduced (analogue to the electrical charge density in the electrostatic counterpart of (3.2)). In this case, it is natural to chose the scalar potential $\psi_{ms}(\mathbf{r})$, with $\mathbf{H}_{ms}(\mathbf{r}) = -\nabla\psi_{ms}(\mathbf{r})$ to characterize the problem (3.8). The scalar potential is now the solution of the scalar Poisson problem

$$\nabla^2 \psi_{ms}(\mathbf{r}) = -\rho_{ms}(\mathbf{r}), \tag{3.9}$$

which yields

$$\begin{aligned}\psi_{ms}(\mathbf{r}) &= \frac{1}{4\pi}\int_\Omega \frac{\nabla' \cdot \mathbf{M}(\mathbf{r}')}{|\mathbf{r}-\mathbf{r}'|}\,\mathrm{d}\mathbf{r}' \\ &= \frac{1}{4\pi}\int_\Omega \nabla' \cdot \frac{\mathbf{M}(\mathbf{r}')}{|\mathbf{r}-\mathbf{r}'|}\,\mathrm{d}\mathbf{r}' - \frac{1}{4\pi}\int_\Omega \nabla'\left(\frac{1}{|\mathbf{r}-\mathbf{r}'|}\right) \cdot \mathbf{M}(\mathbf{r}')\,\mathrm{d}\mathbf{r}',\end{aligned} \tag{3.10}$$

Again, Gauss' theorem enables us to rewrite the first term in this expression to a surface integral and $\nabla' \frac{1}{\mathbf{r}-\mathbf{r}'} = -\nabla \frac{1}{\mathbf{r}-\mathbf{r}'}$, which leads to

$$\psi_{ms}(\mathbf{r}) = \frac{1}{4\pi} \oint_{\partial\Omega} \frac{\mathbf{M}(\mathbf{r}')}{|\mathbf{r}-\mathbf{r}'|} \cdot \mathbf{n}\, \mathrm{d}S + \frac{1}{4\pi} \int_{\Omega} \nabla \frac{1}{|\mathbf{r}-\mathbf{r}'|} \cdot \mathbf{M}(\mathbf{r}')\, \mathrm{d}\mathbf{r}'. \tag{3.11}$$

Since the integrals run over total space and at infinity the magnetization is zero, the first term is zero. Also here, the second integral can be restricted to the volume V of the magnetic material.

$$\psi_{ms}(\mathbf{r}) = \frac{1}{4\pi} \int_{V} \nabla \frac{1}{|\mathbf{r}-\mathbf{r}'|} \cdot \mathbf{M}(\mathbf{r}')\, \mathrm{d}\mathbf{r}' \tag{3.12}$$

The general expression for the magnetostatic field $\mathbf{H}_{ms}$ originating from a ferromagnetic volume V is now derived by taking the curl of (3.7) and dividing the result by μ_0 or by taking the negative divergence of (3.12), which yields

$$\begin{aligned} \mathbf{H}_{ms}(\mathbf{r}) &= -\frac{1}{4\pi} \int_{V} \nabla\nabla \frac{1}{|\mathbf{r}-\mathbf{r}'|} \cdot \mathbf{M}(\mathbf{r}')\, \mathrm{d}\mathbf{r}' \\ &= -\frac{1}{4\pi} \int_{V} \left\{ \frac{\mathbf{M}(\mathbf{r}')}{|\mathbf{r}-\mathbf{r}'|^3} - 3\frac{[\mathbf{M}(\mathbf{r}') \cdot (\mathbf{r}-\mathbf{r}')](\mathbf{r}-\mathbf{r}')}{|(\mathbf{r}-\mathbf{r}')|^5} \right\} \mathrm{d}\mathbf{r}'. \end{aligned} \tag{3.13}$$

3.2. Microscopic approach

A ferromagnetic material consists of a huge number of atoms with a fixed magnetic moment. In quantum mechanics, the relativistic Dirac equation describes the origin of this magnetic moment: the microscopic currents responsible for the field derive from the electronic motion inside atoms and from the electron spin angular momentum. In a corresponding classic view the magnetic moment of an atom can be associated with the movement of a negative charge $-q$ circling around a positive charge $+q$ with angular frequency ω. This classical elementary dipole is shown in Fig. 3.1. In what follows we will derive the magnetic field generated by the magnetic moments of the atoms inside a magnetic body V.

The magnetic vector potential $\mathbf{a}(\mathbf{r})$ generated by k charges q_k moving at a speed $\mathbf{v}_k$ is given by

$$\mathbf{a}(\mathbf{r}) = \frac{\mu_0}{4\pi} \sum_{k} \frac{q_k \mathbf{v}_k}{|\mathbf{r}-\mathbf{r}_k|}. \tag{3.14}$$

Applying this formula to the elementary magnetic dipole of Fig. 3.1 and averaging the result yields the magnetic vector potential of the elementary mag-

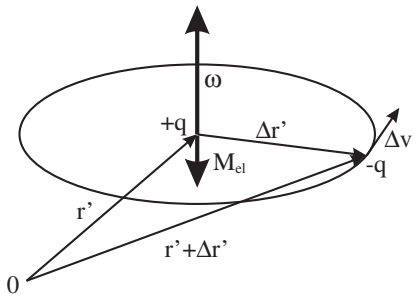

Figure 3.1: Elementary magnetic dipole

netic dipole

$$\mathbf{a}_{el}(\mathbf{r}) = -\frac{\mu_0}{4\pi}\left\langle \frac{q\Delta\mathbf{v}}{|\mathbf{r}-\mathbf{r}'-\Delta\mathbf{r}'|}\right\rangle, \tag{3.15}$$

where the brackets refer to the averaging process and $q > 0$. Since $\Delta\mathbf{r}' \ll \mathbf{r}-\mathbf{r}'$, the denominator can be expanded around $\mathbf{r}-\mathbf{r}'$

$$\mathbf{a}_{el}(\mathbf{r}) = -\frac{\mu_0}{4\pi}\left\langle \frac{q\Delta\mathbf{v}}{|\mathbf{r}-\mathbf{r}'|} - q\Delta\mathbf{v}(\Delta\mathbf{r}'\cdot\nabla)\frac{1}{|\mathbf{r}-\mathbf{r}'|}\right\rangle. \tag{3.16}$$

Here, the first term is zero since $\langle\Delta\mathbf{v}\rangle = 0$. Taking into account that $\Delta\mathbf{v} = \boldsymbol{\omega}\times\Delta\mathbf{r}'$ yields

$$\begin{aligned}\mathbf{a}_{el}(\mathbf{r}) &= \frac{\mu_0}{4\pi}q\langle\boldsymbol{\omega}\times\Delta\mathbf{r}'\Delta\mathbf{r}'\cdot\nabla\rangle\frac{1}{|\mathbf{r}-\mathbf{r}'|}\\ &= \frac{\mu_0}{4\pi}q\boldsymbol{\omega}\times\langle\Delta\mathbf{r}'\Delta\mathbf{r}'\rangle\cdot\nabla\frac{1}{|\mathbf{r}-\mathbf{r}'|}.\end{aligned} \tag{3.17}$$

Now is

$$\langle\Delta\mathbf{r}'\Delta\mathbf{r}'\rangle = \frac{R^2}{2}\begin{bmatrix}1&0&0\\0&1&0\\0&0&1\end{bmatrix} \tag{3.18}$$

with R the radius of the circular trajectory of the negative charge in the elementary dipole of Fig. 3.1. This results in

$$\mathbf{a}_{el}(\mathbf{r}) = \frac{\mu_0}{4\pi}q\frac{R^2}{2}\boldsymbol{\omega}\times\nabla\frac{1}{|\mathbf{r}-\mathbf{r}'|}. \tag{3.19}$$

The magnetic moment of a current $\mathbf{j}$ can also be written as

$$\mathbf{M} = \frac{1}{2}\int_\Omega \mathbf{r}'\times\mathbf{j}(\mathbf{r}')\,\mathrm{d}\mathbf{r}' \tag{3.20}$$

where $\mathbf{j}$ is confined to Ω. For the case of the elementary dipole, Ω is restricted to the circle on which the negative charge $-q$ moves and $\mathbf{j} = -q\boldsymbol{\omega}/2\pi$, this results in

$$\mathbf{M}_{el} = -\frac{1}{2}R.q\frac{\boldsymbol{\omega}}{2\pi}.2\pi R = -q\frac{R^2}{2}\boldsymbol{\omega}. \tag{3.21}$$

Introducing this expression in (3.19) gives

$$\mathbf{a}_{el}(\mathbf{r}) = -\frac{\mu_0}{4\pi}\mathbf{M}_{el} \times \nabla\frac{1}{|\mathbf{r}-\mathbf{r}'|}. \tag{3.22}$$

From this, the magnetic field $\mathbf{h}_{el}(\mathbf{r})$ generated by an elementary magnetic dipole can be written as

$$\begin{aligned}\mathbf{h}_{el}(\mathbf{r}) &= \frac{1}{\mu_0}\nabla \times \mathbf{a}_{el}(\mathbf{r}) \\ &= -\frac{1}{4\pi}\nabla \times \left(\mathbf{M}_{el} \times \nabla\frac{1}{|\mathbf{r}-\mathbf{r}'|}\right) \\ &= -\frac{1}{4\pi}\nabla\nabla\frac{1}{|\mathbf{r}-\mathbf{r}'|} \cdot \mathbf{M}_{el}.\end{aligned} \tag{3.23}$$

This is the field generated by one distinct atom in the ferromagnetic material, which can be seen as a point in the considered ferromagnetic material. Hence, the magnetic field generated by all atoms in the ferromagnetic body is obtained by adding up all magnetic fields from each distinct atom, i.e. from each point in the magnetic body, which is performed by an integration over the volume of the magnetic body

$$\begin{aligned}\mathbf{H}(\mathbf{r}) &= -\frac{1}{4\pi}\int_V \nabla\nabla\frac{1}{|\mathbf{r}-\mathbf{r}'|} \cdot \mathbf{M}(\mathbf{r}')\,\mathrm{d}\mathbf{r}' \\ &= -\frac{1}{4\pi}\int_V \left\{\frac{\mathbf{M}(\mathbf{r}')}{|\mathbf{r}-\mathbf{r}'|^3} - 3\frac{[\mathbf{M}(\mathbf{r}')\cdot(\mathbf{r}-\mathbf{r}')](\mathbf{r}-\mathbf{r}')}{|(\mathbf{r}-\mathbf{r}')|^5}\right\}\mathrm{d}\mathbf{r}'.\end{aligned} \tag{3.24}$$

This is exactly the same result as the magnetostatic field $\mathbf{H}_{ms}$ obtained from the macroscopic Maxwell equations. Hence, we can interpret the magnetostatic field as the field generated by all magnetic dipoles in the considered magnetic material.

3.3. Uniformly magnetized media

Let us now consider the magnetostatic field generated by a uniformly magnetized finite body V. In this case, the volume integrals in the expression for the magnetic vector potential $\mathbf{A}_{ms}$ (3.5) and in the expression for the magnetic scalar potential ψ_{ms} (3.10) reduce to surface integrals. Indeed, in the material

$\nabla \times \mathbf{M}(\mathbf{r}') = 0$ and $\nabla \cdot \mathbf{M}(\mathbf{r}') = 0$. At the body surfaces at the contrary, the magnetization undergoes a sudden variation because $\mathbf{M} = 0$ outside the material leading to

$$\mathbf{A}_{ms}(\mathbf{r}) = -\frac{\mu_0}{4\pi} \int_{\partial V} \frac{\mathbf{n} \times \mathbf{M}(\mathbf{r}')}{|\mathbf{r} - \mathbf{r}'|} \, \mathrm{d}S \tag{3.25}$$

and

$$\psi_{ms}(\mathbf{r}) = \frac{1}{4\pi} \int_{\partial V} \frac{\mathbf{n} \cdot \mathbf{M}(\mathbf{r}')}{|\mathbf{r} - \mathbf{r}'|} \, \mathrm{d}S \tag{3.26}$$

The quantity $-\mathbf{n} \times \mathbf{M}$ can now be interpreted as a magnetic surface current

$$\mathbf{k}_{ms}(\mathbf{r}) = -\mathbf{n} \times \mathbf{M}(\mathbf{r}), \tag{3.27}$$

while the quantity $\mathbf{n} \cdot \mathbf{M}$ can be interpreted as a magnetic surface charge density π_{ms}

$$\pi_{ms}(\mathbf{r}) = \mathbf{n} \cdot \mathbf{M}(\mathbf{r}). \tag{3.28}$$

Hence $\mathbf{A}_{ms}$ and ψ_{mls} are written as

$$\mathbf{A}_{ms}(\mathbf{r}) = \frac{\mu_0}{4\pi} \int_{\partial V} \frac{\mathbf{k}_{ms}(\mathbf{r}')}{|\mathbf{r} - \mathbf{r}'|} \, \mathrm{d}\mathbf{r}' \tag{3.29}$$

$$\psi_{ms}(\mathbf{r}) = \frac{1}{4\pi} \int_{\partial V} \frac{\pi_{ms}(\mathbf{r}')}{|\mathbf{r} - \mathbf{r}'|} \, \mathrm{d}\mathbf{r}'. \tag{3.30}$$

Now we take a finite cylinder, uniformly magnetized along its axis as in Fig. (3.2.a). Here, the magnetic surface current (3.27) is zero on the two bases and constant over the shell of the cylinder. The magnetic charges on the other hand are zero on the shell and constant (with opposite sign) on the two bases of the cylinder. Hence (3.29) and (3.30) reduce to

$$\mathbf{A}_{ms}(\mathbf{r}) = \frac{\mu_0}{4\pi} \int_{\text{shell}} \frac{\mathbf{k}_{ms}}{|\mathbf{r} - \mathbf{r}'|} \, \mathrm{d}\mathbf{r}' \tag{3.31}$$

$$\psi_{ms}(\mathbf{r}) = \frac{1}{4\pi} \int_{\text{top}} \frac{\pi_{ms}}{|\mathbf{r} - \mathbf{r}'|} \, \mathrm{d}\mathbf{r}' - \frac{1}{4\pi} \int_{\text{bottom}} \frac{\pi_{ms}}{|\mathbf{r} - \mathbf{r}'|} \, \mathrm{d}\mathbf{r}'. \tag{3.32}$$

From these equations it is clear that in the first approach, the uniformly magnetized cylinder is replaced by an equivalent surface magnetization density $\mathbf{k}_{ms}$ over the shell of the cylinder, while in the second approach, the uniformly magnetized cylinder is replaced by equivalent surface charge densities π_{ms} on the bases of the cylinder. This is shown in Fig. 3.2.

The magnetostatic fields can thus also be computed based on the equivalent magnetic currents or the magnetostatic charges. In what follows, we will always use equivalent magnetic charges to replace uniformly magnetized regions. Figure 3.3 shows the magnetostatic fields induced by the uniformly

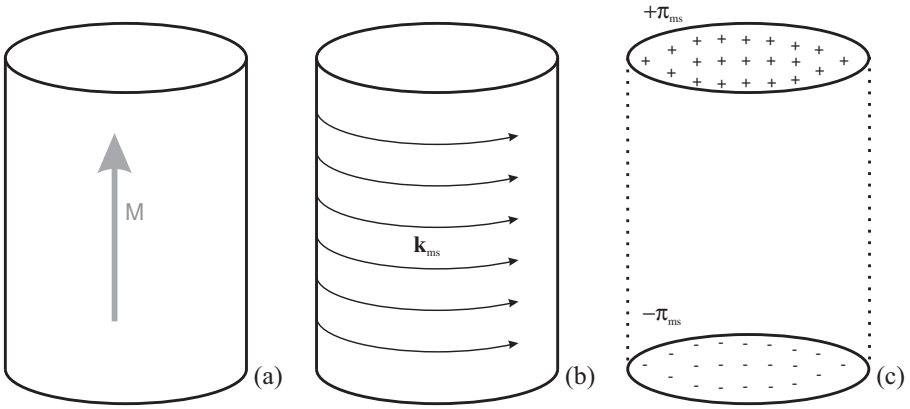

Figure 3.2: Uniformly magnetized cylinder (a), represented by an equivalent surface magnetic current density $\mathbf{k}_{ms} = -\mathbf{n} \times \mathbf{M}$ (b) and by equivalent surface magnetic charge densities $\pi_{ms} = \mathbf{n} \cdot \mathbf{M}$ (c).

magnetized iron cylinder of Fig. 3.2 in an axial plane. The field pattern is understood by considering the charge distributions in Fig. 3.2.c and interpret them in their electrostatic counterpart: the magnetostatic field lines start at the positive charges at the top face of the cylinder and arrive at negative charges at the bottom face of the cylinder. The far field pattern of $\mathbf{H}_{ms}$ created by the cylinder is that of a dipole, while the fields in the cylinder are mainly oriented in the opposite directions compared to the magnetization $\mathbf{M}$.

In a more general case, a piecewise homogeneously magnetized sample can be equivalently represented by different magnetic currents and magnetic charge densities on the surfaces of the discontinuous jumps in the magnetization. The charge density representing the discontinuity surface between a region with magnetization $\mathbf{M}_1$ and $\mathbf{M}_2$ is equal to

$$\pi_{ms} = \mathbf{n}_1 \cdot \mathbf{M}_1 + \mathbf{n}_2 \cdot \mathbf{M}_2 \tag{3.33}$$

with $\mathbf{n}_1$ and $\mathbf{n}_2$ the unit vectors normal to the discontinuity surface pointing into the region with magnetization $\mathbf{M}_1$ and $\mathbf{M}_2$ respectively.

3.4. Magnetostatic energy

The magnetostatic energy in total space is given by

$$\begin{aligned} E_{ms} &= \int_{\Omega} \phi_{ms}(\mathbf{r})\, \mathrm{d}\mathbf{r} \\ &= -\frac{\mu_0}{2} \int_{\Omega} \mathbf{H}_{ms}(\mathbf{r}) \cdot \mathbf{M}(\mathbf{r})\, \mathrm{d}\mathbf{r} \end{aligned} \tag{3.34}$$

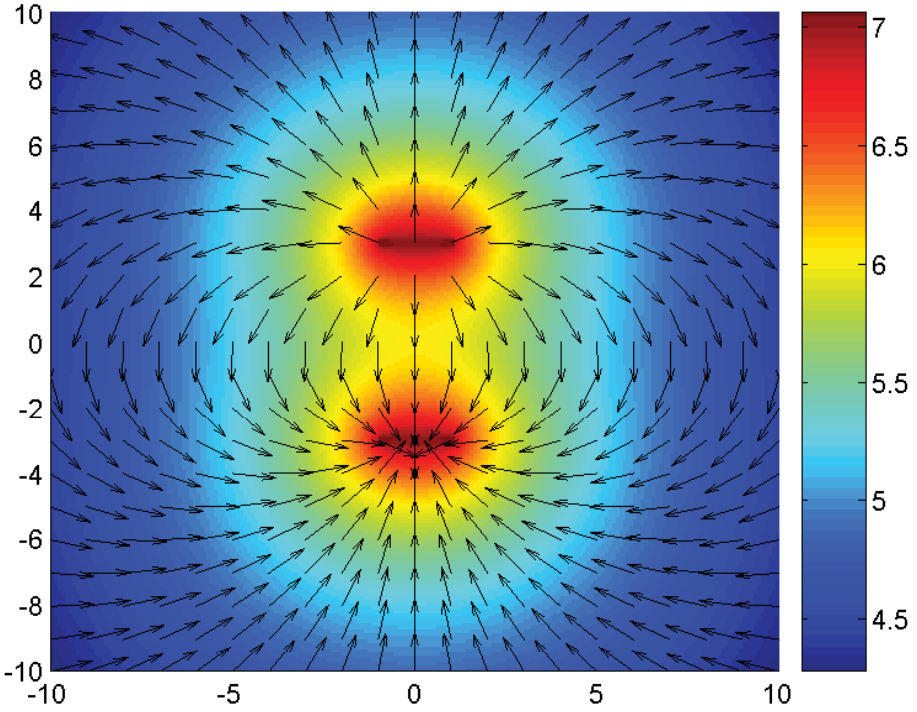

Figure 3.3: Magnetostatic field induced by the uniformly magnetized iron cylinder of Fig. 3.2 in an axial plane. The field strength is given on a logarithmic scale $[Am^{-1}]$, while the direction of the field is given by the arrows.

The integral, calculated over total space Ω, can be restricted to the volume integral over the magnetic body V since only in this volume $\mathbf{M}(\mathbf{r}) \neq 0$

$$E_{ms} = -\frac{\mu_0}{2} \int_V \mathbf{H}_{ms}(\mathbf{r}) \cdot \mathbf{M}(\mathbf{r}) \, \mathrm{d}\mathbf{r}. \tag{3.35}$$

We can also derive an equivalent identity for the magnetostatic energy by inserting $\mathbf{M} = (1/\mu_0)\mathbf{B}_{ms} - \mathbf{H}_{ms}$ in (3.34)

$$E_{ms} = -\frac{1}{2} \int_\Omega \mathbf{H}_{ms}(\mathbf{r}) \cdot \mathbf{B}_{ms}(\mathbf{r}) \, \mathrm{d}\mathbf{r} + \frac{\mu_0}{2} \int_\Omega H_{ms}^2(\mathbf{r}) \, \mathrm{d}\mathbf{r}. \tag{3.36}$$

Rewriting the first integral by introducing the scalar magnetostatic potential $\mathbf{H}_{ms} = -\nabla\psi_{ms}$, yields

$$\begin{aligned} -\frac{1}{2}\int_\Omega \mathbf{H}_{ms}(\mathbf{r})\cdot\mathbf{B}_{ms}(\mathbf{r})\,\mathrm{d}\mathbf{r} &= \frac{1}{2}\int_\Omega \nabla\psi_{ms}(\mathbf{r})\cdot\mathbf{B}_{ms}(\mathbf{r})\,\mathrm{d}\mathbf{r} \\ &= \frac{1}{2}\int_\Omega \nabla\cdot[\psi_{ms}(\mathbf{r})\mathbf{B}_{ms}(\mathbf{r})]\,\mathrm{d}\mathbf{r} \\ &\quad -\frac{1}{2}\int_\Omega \psi_{ms}(\mathbf{r})(\nabla\cdot\mathbf{B}_{ms}(\mathbf{r}))\,\mathrm{d}\mathbf{r}. \end{aligned} \tag{3.37}$$

All integrals are calculated over total space Ω. The second integral equals zero since $\nabla\cdot\mathbf{B}_{ms} = 0$ while the first integral can be rewritten as a surface integral over a closed surface that is going to infinity. Because the fields ψ_{ms} and $\mathbf{B}_{ms}$ are zero at infinity, the resulting surface integral is also zero. In that way, the expression (3.36) for the total magnetostatic energy reduces to

$$E_{ms} = \frac{\mu_0}{2}\int_\Omega H_{ms}^2(\mathbf{r})\,\mathrm{d}\mathbf{r}. \tag{3.38}$$

This expression shows that the minimum possible magnetostatic energy state of a magnetic configuration is a state where E_{ms} is zero which corresponds to a zero magnetostatic field in each point of the material. Considering the equivalent expression (3.35) this means that in the magnetic material $\mathbf{H}_{ms}$ has a large component opposite to $\mathbf{M}$. Indeed, the integral $\int \mathbf{H}_{ms}(\mathbf{r})\cdot\mathbf{M}(\mathbf{r})\,\mathrm{d}\mathbf{r}$ over the magnetic body is negative.

3.5. Minimization of the magnetostatic energy

Equation (3.38) shows that the magnetostatic energy of a magnetic system is minimal (i.e. zero) when the system does not generate magnetostatic fields $\mathbf{H}_{ms} = 0$. This corresponds to a system that does not contain any magnetic charges. Following Section 3.3 this is the case when at the surface between two uniformly magnetized regions (magnetizations $\mathbf{M}_1$ and $\mathbf{M}_2$)

$$\pi_{ms} = \mathbf{n}_1\cdot\mathbf{M}_1 + \mathbf{n}_1\cdot\mathbf{M}_2 = 0 \tag{3.39}$$

holds with $\mathbf{n}_i$ the normal unit vector on the surface pointing in the region i ($i = 1,2$). The condition $\pi_{ms} = 0$ can be met in two ways. First, both terms can be zero individually, which occurs when $\mathbf{M}_i$ is perpendicular to $\mathbf{n}_i$ leading to 180 degree domain walls as depicted in Fig. 3.4.a. Second, both terms can have equal amplitude, but an opposite sign

$$\pi_{ms} = -\frac{\sqrt{2}}{2}M + \frac{\sqrt{2}}{2}M = 0 \tag{3.40}$$

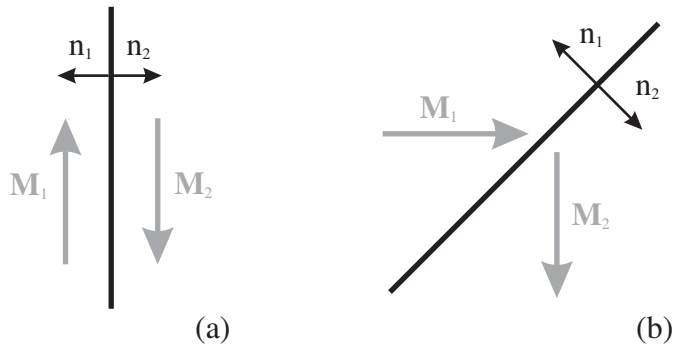

Figure 3.4: (a) 180 degree domain wall (b) 90 degree domain wall.

which occurs for 90 degree domain walls as depicted in Fig. 3.4.b.

A uniformly magnetized medium as the cylinder in Fig. 3.2 generates large magnetostatic fields (see Fig. 3.3). The sample contains a single magnetic domain as shown in Fig. 3.5.a. When the same sample comprises two domains, magnetized in the opposite direction and separated by a 180 degree domain wall the magnetostatic energy is already reduced to a great extent. In Fig. 3.5.b the magnetic charges at the top and bottom faces induce smaller fields in the air surrounding the sample. The magnetostatic energy can further be reduced to zero by introducing closure domains separated from the other domains by 90 degree domain walls as depicted in Fig. 3.5.c and d. Indeed, in these configurations no magnetic charges appear.

Two considerations should be made when looking at Fig. 3.5. First, discontinuous magnetization jumps are assumed, corresponding to a zero domain wall thickness. When also other energy terms are also considered, it turns out that the magnetization changes continuously between magnetic domains, leading to domain walls of finite width. Since in these domain walls $\nabla \cdot \mathbf{M} \neq 0$ magnetic charges are present in the domain wall. These will contribute to the magnetostatic energy. However, the total magnetostatic energy will remain small and thus also magnetic domain configurations containing (closure) domains separated by 180 degree and 90 degree domain walls with *finite* thickness still are preferred.

Second, the generated magnetostatic fields only depend on the geometry of the magnetic body, but not on its actual dimensions. Figure 3.5 does not show a length scale. A magnetic sample, double in size, will generate identical configurations of magnetostatic fields. This results also from scale invariance of the equation for $\mathbf{H}_{ms}$ (3.13). The expressions within the integrandum scale with $1/r^3$, while the integration itself introduces a factor proportional to r^3.

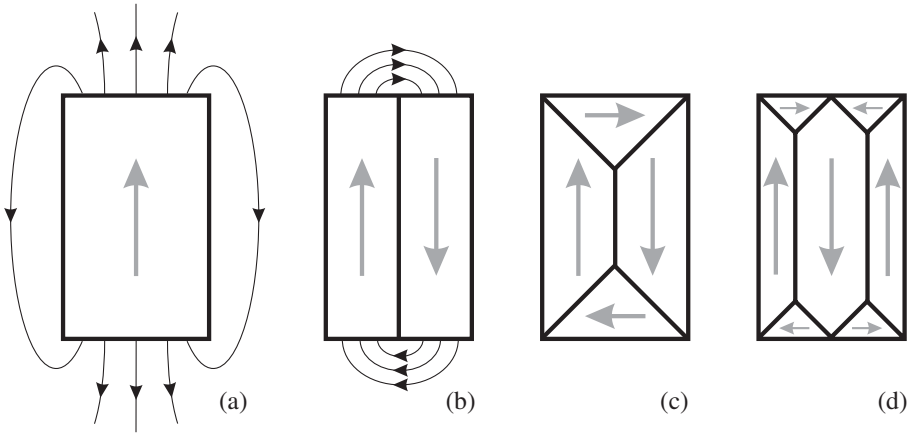

Figure 3.5: Magnetostatic field induced in the air surrounding (a) a uniformly magnetized sample, (b) a sample containing two magnetic domains separated by 180 degree domain walls, (c) and (d) a sample containing (closure) domains separated by 90 and 180 degree domain walls.

The magnetic domains in Fig. 3.5.c and d give rise to an average magnetization which is zero. Let us now consider also the Zeeman energy. When an external magnetic field $\mathbf{H}_a$ is applied, the magnetic configuration in the sample will change. This is shown in Fig. 3.6 for a central part of a magnetic sheet. First, the sheet is demagnetized: the net magnetization in the sheet is zero at a zero applied field. Now an increasing external field $\mathbf{H}_a$ is applied. Hence, the average magnetization will travel along the virgin curve to saturation. Several intermediate magnetization configurations are shown. Due to the minimization of the Zeeman energy, the closure domains oriented in the same direction of the external magnetic field grow as the external field increases, while the closure domains oriented in the opposite directions diminish. This results in a growing net magnetization in the direction of the external field $\mathbf{H}_a$. At each time point, the magnetostatic energy is kept low by ensuring the continuity of the flux lines through the sample as shown in Fig. 3.6. However, it is obvious that at the extreme ends of the sheet a growing number of magnetic charges will appear, leading to growing magnetic fields through the sample and a growing magnetostatic energy. Hence, to reach saturation large applied fields are needed to overcome the created magnetostatic fields.

3.6. Demagnetizing factors

From the above sections, it is clear that the magnetostatic fields in a certain sample strongly depend on the sample shape, but not on its actual dimensions.

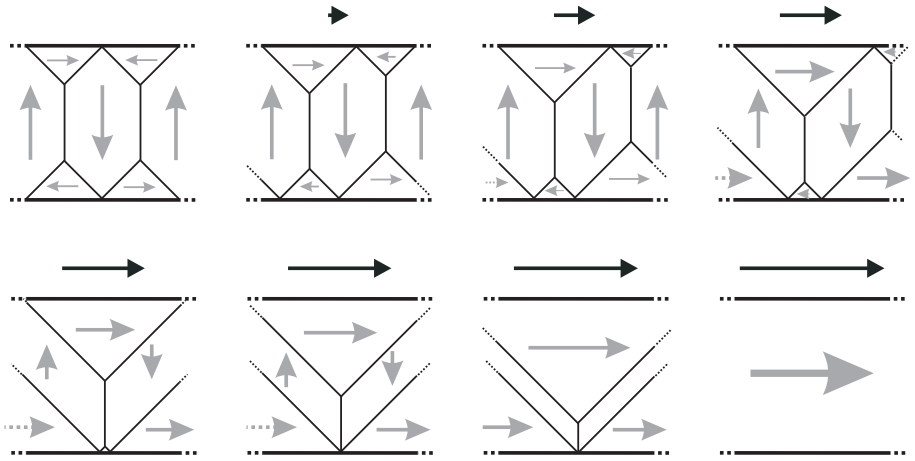

Figure 3.6: From top-left to bottom-right: domain configurations in a central part of a magnetic sheet subjected to an increasing external magnetic field, depicted by the black arrow.

Hence, for a uniformly magnetized sample, one can try to describe the relation between the magnetization and the generated magnetostatic field by some macroscopic constitutive law, only depending on dimensionless parameters expressing the ratio between characteristic geometry lengths. From expression (3.13) it is clear that in general, the magnetostatic field inside a magnetic body is not constant, even when uniformly magnetized. One can prove that this is only the case in a uniformly magnetized ellipsoidal body. In that case the magnetostatic field can be written as

$$\mathbf{H}_{ms} = -\mathbf{N} \cdot \mathbf{M}, \tag{3.41}$$

with $\mathbf{N}$ the demagnetization tensor. When the xyz axes are chosen along the principal axes of the ellipsoid, $\mathbf{N}$ reduces to a diagonal tensor

$$\begin{bmatrix} H_{ms,x} \\ H_{ms,y} \\ H_{ms,z} \end{bmatrix} = - \begin{bmatrix} N_x & 0 & 0 \\ 0 & N_y & 0 \\ 0 & 0 & N_z \end{bmatrix} \begin{bmatrix} M_x \\ M_y \\ M_z \end{bmatrix}. \tag{3.42}$$

The actual values of the so called demagnetizing factors N_x, N_y and N_z depend on the mutual ratios of the length of the principle axes. The demagnetizing factors are positive ($\mathbf{H}_{ms}$ is always opposite to $\mathbf{M}$) and obey the constraint

$$N_x + N_y + N_z = 1, \tag{3.43}$$

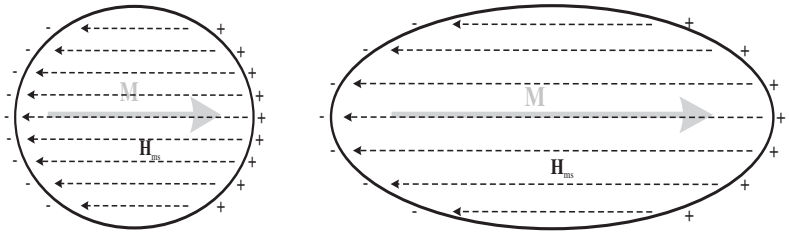

Figure 3.7: Magnetostatic fields in two prolate ellipsoids.

which immediately defines the demagnetizing factors of a sphere to be $1/3$ because of symmetry.

For ellipsoids of revolution, two principal axes are of equal length resulting in identical corresponding demagnetizing factors. When the z-axis is the rotational symmetry axis it holds that $N_x = N_y$. Analytical expressions in terms of r, the ratio of the lengths of the symmetry and traverse axes, can now be determined for N_z and thus also for N_x and N_y using (3.43). For an oblate spheroid (a disk) one gets

$$N_z = \frac{1}{1-r^2}\left[1 - \frac{r}{\sqrt{1-r^2}}\arcsin\left(\sqrt{1-r^2}\right)\right] \qquad r < 1, \tag{3.44}$$

while for a prolate spheroid (a cigar) one gets

$$N_z = \frac{1}{r^2-1}\left[\frac{r}{\sqrt{r^2-1}}\ln\left(r + \sqrt{r^2-1}\right) - 1\right] \qquad r > 1. \tag{3.45}$$

These expressions only depend on the ratio r which again demonstrates the scale invariance of the magnetostatic field. As an example, the magnetostatic field inside two prolate spheroids, magnetized along the rotational symmetry axis is shown in Fig. 3.7. Since the samples are uniformly magnetized, magnetic charges are only initiated at the body surface. Due to the ellipsoidal shape, the magnetic charges appear in such a configuration that the magnetostatic fields generated in the material are parallel to the magnetization direction and have a constant amplitude, depending on the ratio r.

For other uniformly magnetized sample geometries, the magnetostatic field in the sample can not be given by expression (3.41) since the $\mathbf{H}_{ms}$ differs in the sample from point to point. However, a *magnetometric* demagnetization tensor $\mathbf{N}$, only depending on the sample shape can be defined starting from

the magnetostatic energy per unit volume

$$\begin{aligned}\phi_{ms} &= \frac{1}{V}\int_V \frac{1}{2}\mathbf{H}_{ms}(\mathbf{r})\cdot\mathbf{M}(\mathbf{r})\,\mathrm{d}\mathbf{r} \\ &= \frac{1}{2}\mathbf{M}\cdot\mathbf{N}\cdot\mathbf{M}.\end{aligned} \tag{3.46}$$

In that way the magnetometric demagnetization tensor $\mathbf{N}$ expresses some sort of average magnetostatic field. For a rectangular prism, the elements of $\mathbf{N}$ can be computed analytically [21]. When the xyz axes are chosen along the principal axes of the rectangular prism, $\mathbf{N}$ reduces also in this case to a diagonal tensor. Let us consider now, analogously to the ellipsoidal geometry, a rectangular prism with equal axes along the x- and y-direction, i.e. a square ground plane. The magnetometric demagnetizing factor along the z axis can then be expressed in terms of the ratio r between the edge length along the z-axis and the edge length along the x- and y-axis (for $r > 0$)

$$\begin{aligned}\pi N_z = &\left(r - \frac{1}{r}\right)\ln\frac{\sqrt{r^2+2}+1}{\sqrt{r^2+2}-1} + \frac{2}{r}\ln(\sqrt{2}+1) + r\ln\frac{\sqrt{r^2+1}+1}{\sqrt{r^2+1}-1} \\ &+ 2\arctan\left(\frac{1}{r\sqrt{r^2+2}}\right) + \frac{2(1-r^2)}{3r}\sqrt{r^2+2} + \frac{2(1-r^3)}{3r} \\ &- \frac{2^{3/2}}{3r} + \frac{2}{3}\sqrt{r^2+1}\left(2r - \frac{1}{r}\right).\end{aligned} \tag{3.47}$$

It is clear that for a cube all magnetometric demagnetizing factors are $1/3$. Figure 3.8 shows the demagnetizing factors corresponding to the longest dimension versus the ratio r for ellipsoids of revolution and the magnetometric demagnetizing factors for rectangular prisms with square cross sections. For identical r, the magnetizing factors N_z for the rectangular prisms are always larger then for the ellipsoids. Even for very elongated prisms, the demagnetizing factor is not negligible. Hence, also for very elongated prisms, the influence of the magnetostatic fields on the magnetic system is still present.

The fact that the magnetostatic field has a large component opposite to the magnetization has lead to the term demagnetizing factors and in extension, *demagnetizing field*, which is also used to depict the magnetostatic field. Indeed, when an external field $\mathbf{H}_a$ is applied to a magnetic sample in order to saturate it, the magnetic material itself generates a demagnetizing field with a large opposite component, diminishing the local influence of the applied field. The (magnetometric) demagnetizing factors quantify the strength of the demagnetizing effect. Figure 3.8 shows that the demagnetizing effect along a certain direction diminishes when the sample gets more elongated in that direction. This effect is also visible when the hysteresis loops (see Chapter 4) for different sample geometries are considered. When the demagnetizing effects along

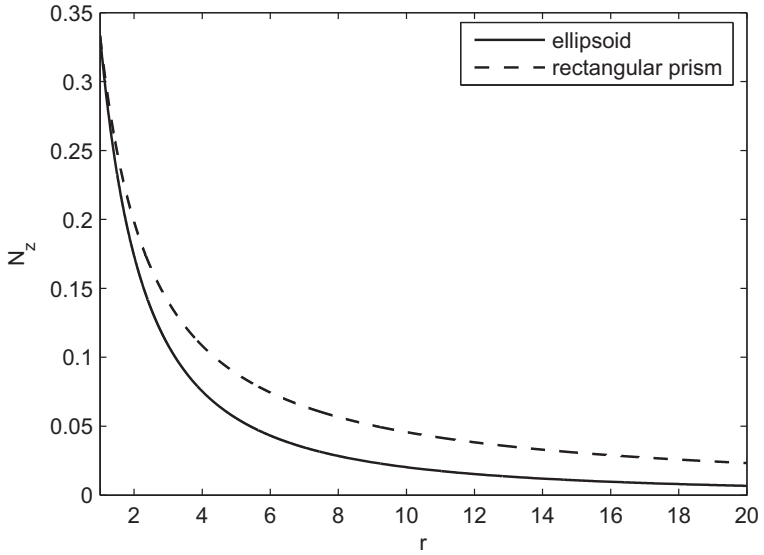

Figure 3.8: Demagnetizing factors for ellipsoids of revolution and rectangular prisms with square cross section versus r, the ratio between the largest and the smallest dimension.

the direction of the external applied field are small (i.e. when the sample is elongated in the direction of the applied field), a small external field suffices to saturate the sample. Figure 3.9 shows simulated hysteresis loops of rectangular prisms where the external field is applied parallel to the longest edge of the prism. For increasing prism heights, smaller fields have to be applied to saturate the sample.

3.7. Closed magnetic circuits

We have seen that the magnetostatic fields are closely related with the sample geometry and have a substantial effect on the magnetic behavior. When magnetic (hysteretic) properties are considered to characterize or study the magnetic properties of a material, one needs to minimize the magnetostatic influence. Indeed, when magnetic charges appear, the magnetostatic energy contribution largely exceeds the energy contributions originating from the interactions between the studied material parameters and the magnetic hysteresis behavior. To alleviate this problem, experiments are generally performed on closed magnetic circuits as ring cores or rectangular frames, see Fig. 3.10. In these configurations the flux lines are closed in the material resulting in a charge free magnetic system, giving rise to a minimum magnetostatic energy. The small length scale on which the micromagnetic theory is applied does not

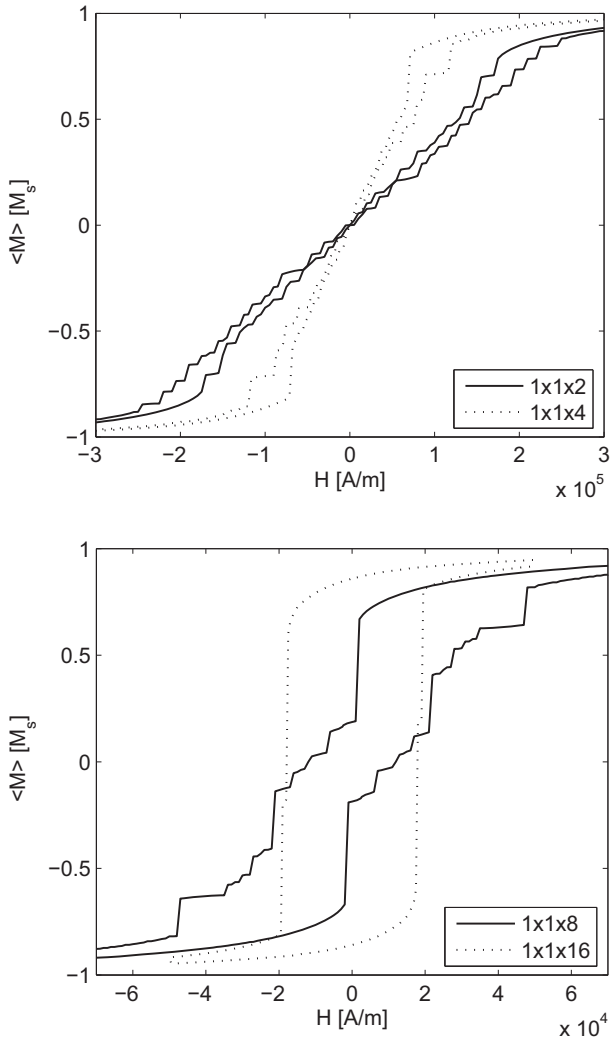

Figure 3.9: Hysteresis loops for cuboid samples with identical material parameters, but different heights expressed by their aspect ratios.

allow us to use macroscopic closed circuits of this type in numerical micromagnetic simulations.

A special case of a closed circuit is an infinitely long ferromagnetic wire, Fig. 3.10.c. In this case the magnetic flux lines close in the material at infinity avoiding the generation of magnetic charges and thus the presence of long demagnetizing effects along the longitudinal direction. This is also expressed by the demagnetization factors described in Section 3.6. From Fig. 3.8 it is clear

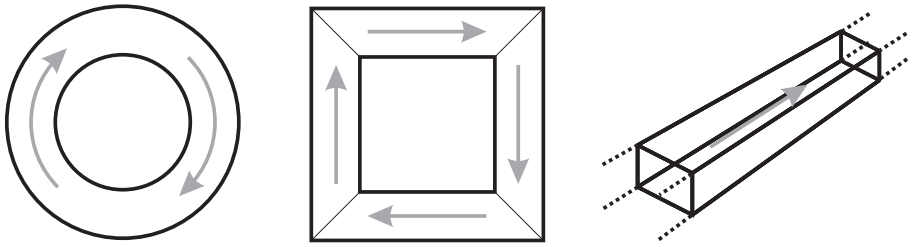

Figure 3.10: Magnetic charge free configurations: (a) ring core, (b) rectangular frame, (c) infinitely long ferromagnetic wire.

that the (magnetometric) demagnetizing factor corresponding to the longitudinal direction decreases to zero for (infinitely) long geometries. The demagnetizing effects in the cross section however do not disappear. Indeed, since the constraint (3.43) holds, the demagnetizing factors D_x and D_y corresponding to the cross section directions are non zero. Consequently, in an infinite wire with square cross section, the magnetometric demagnetizing factors D_x and D_y are $1/2$.

When the aim is to describe the magnetization processes in the bulk of ferromagnetic materials, one could argue if it is possible to consider a magnetic body, infinite in all directions. In that way, the influence of the boundaries could disappear in all directions together with the demagnetizing effects. Unfortunately, this is not possible. As stated by Bertotti [5]:

> "*The effect of the magnetic charges does not vanish with increasing body size, and the final result obtained in the limit of infinite size will still depend on the body shape, that is, on the way the charges are sent to infinity*."

This quote should be interpreted as follows. We have seen that the demagnetizing factors only depend on the sample shape, but not on its actual dimensions. In that way the demagnetizing factors of a sphere are $1/3$. When the radius of the sphere is increased, the demagnetizing factors and thus the demagnetizing effects stay unaltered, even when the radius is infinite. Consider now a prolate ellipsoid. For this geometry, the demagnetizing factors are different from these from the sphere mentioned before. When now the length of the main axes is increased, the demagnetizing factors stay unaltered, also for infinite axes lengths. Hence, the demagnetizing effects in the same infinite ferromagnetic medium are different depending on the fact if it is obtained from (in this example) a growing sphere or a growing ellipsoid.

CHAPTER 4

Magnetic hysteresis

4.1. Introduction

In Chapter 2 we have seen that the evolution of the local magnetization field $\mathbf{m}(\mathbf{r},t)$ is determined by the total Gibbs free energy resulting in a complex energy landscape with many local minima and saddle points. Due to the interaction with the applied field, the energy landscape changes in time: some local energy minima vanish while others are created. Here, the LLG equation describes the evolution of the micromagnetic system in the time varying energy landscape. This traveling of the micromagnetic system between successive local energy states gives rise to hysteresis effects. In this chapter hysteresis is introduced and some general hysteretic properties are discussed. This is first done for a simple bistable system with a maximum number of two local minima and then extended to the micromagnetic problem.

4.2. Hysteresis in a bistable system

This section is to a large extent based on chapter 2 of the handbook *Hysteresis in Magnetism*, written by G. Bertotti [5]. It describes a very simple bistable hysteretic system and gives an intuitive insight in some basic hysteretic properties. In a next section, we will extend the discussion to the micromagnetic system and come to an understanding of the micromagnetic origin of macroscopic magnetic hysteresis.

4.2.1 Equilibrium states in a bistable system

Let us consider a system whose free energy is given by the expression

$$f(x) = x^4 - 2x^2, \tag{4.1}$$

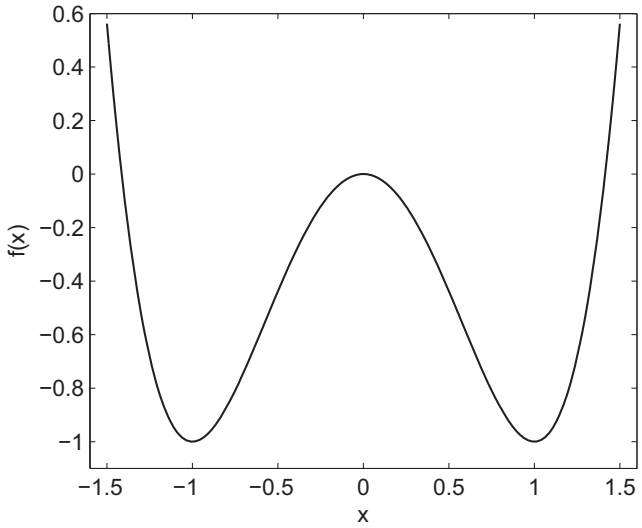

Figure 4.1: Free energy of a bistable system under zero input.

where x is some dimensionless state variable. This free energy function is shown in Fig. 4.1. It has two local minima at $x = \pm 1$ and a maximum at $x = 0$. Furthermore, an external force field h acts upon the system. Hence the free energy of the system under nonzero input h will be

$$g(x,h) = x^4 - 2x^2 - hx. \tag{4.2}$$

Let us now look at the states occupied by the system for varying input h. In general the systems' equilibrium states are defined by the local minima: $\partial g/\partial x = 0$ together with $\partial^2 g/\partial x^2 > 0$. In Fig. 4.2, the shape of the free energy $g(x,h)$ is shown for successive values of h. First, for h increasing from $-\infty$, the system occupies the only present minimum (Fig. 4.2.A). At a certain value $h = -h_c$ a second minimum is created. At $h = 0$ (Fig. 4.2.B) the two minima have the same energy and for $h > 0$ the newly created minimum becomes also the global minimum. Due to its history however, the system stays in the original (local) energy minimum. At $h = h_c$ (Fig. 4.2.C) the initially occupied minimum vanishes and becomes an inflection point. At this point the system evolves towards the lower minimum energy state. The energy difference between the two states is dissipated as heat. For larger inputs $h > h_c$ there is only one minimum (Fig. 4.2.D). If the external field is now decreased, a similar discussion applies: a second minimum is introduced at $h = h_c$, at $h = 0$ (Fig. 4.2.E) both minima have the same energy and at $h = -h_c$ (Fig. 4.2.F) the system returns to the only local minimum present in the system.

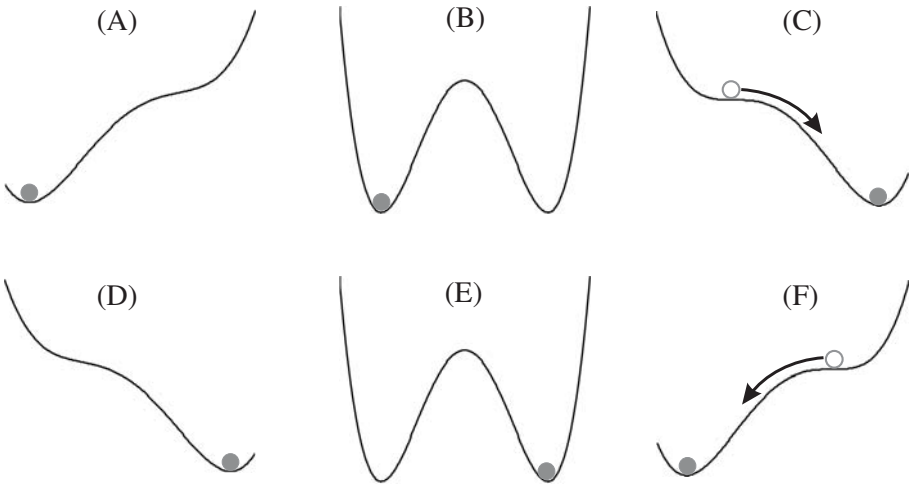

Figure 4.2: Minimum energy states occupied by the bistable system for varying input h, (following [5]).

In Fig. 4.3 the equilibrium values of the state variable x for which the system is in equilibrium are plotted versus the input parameter h. Due to the presence of the two minima, the curve is not single valued, but gives rise to an hysteresis loop. Hysteresis is encountered in a wide range of research areas where processes are described with some output x that is not a single valued function of the input h. Hysteresis properties are for instance also seen in economics [22], soil science [23], hydrology [24], granular processes [25], psychology [26], etc. Although the presented bistable system is very simple, it can show already a lot of properties present in hysteretic processes. In what follows we will highlight some which will be important in the micromagnetic hysteresis description of ferromagnetic materials.

4.2.2 Energy dissipation

First we take a detailed look at the surface of the hysteresis loop 4.3. Therefore, the curve $h(x)$ for which

$$\frac{\partial g}{\partial x}(x,h) = \frac{\partial f(x)}{\partial x} - h(x) = 0 \tag{4.3}$$

or

$$h(x) = \frac{\partial f(x)}{\partial x}. \tag{4.4}$$

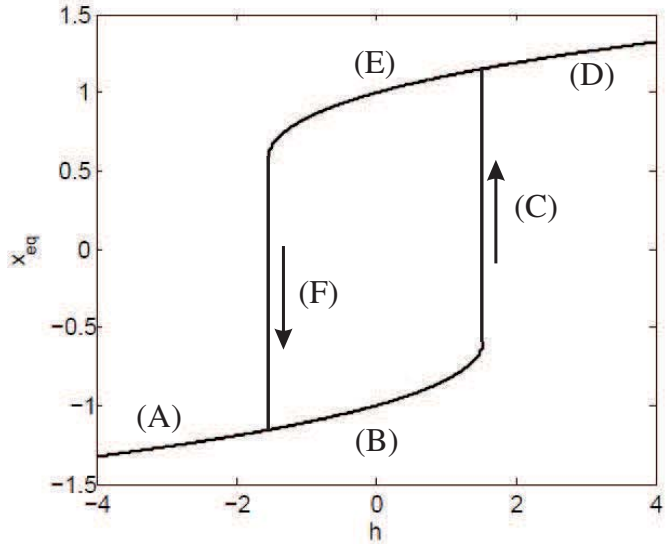

Figure 4.3: Hysteresis loop of the bistable system. The numbers refer to the equilibrium points of Fig. 4.2, following [5].

is plotted in Fig. 4.4. The branches for which $\partial^2 g/\partial x^2 = \partial^2 f/\partial x^2 > 0$ correspond to the stable equilibrium points of the considered system. Indeed, three branches exist with $\partial g/\partial x = 0$: two stable branches (full lines) corresponding to the energy minima and one metastable branch (dashed line) corresponding to the energy maximum. The dotted lines represent the jump of the system from the inflection point to the stable energy minimum. The resulting figure corresponds to the hysteresis loop from Fig. 4.3 with inverse axes.

The surface of the hysteresis loop can now be computed as two times the shaded area S of Fig. 4.4

$$\begin{aligned} S &= -\int_{-x_c}^{x_f} [h(x) - h_c]\,\mathrm{d}x \\ &= -\int_{-x_c}^{x_f} \left[\frac{\partial f}{\partial x} - h_c\right]\mathrm{d}x \\ &= -\int_{-x_c}^{x_f} \left[\frac{\partial g}{\partial x}\right]_{h=h_c}\mathrm{d}x \\ &= g(-x_c,h_c) - g(-x_f,h_c) \end{aligned} \tag{4.5}$$

This corresponds to the energy difference between the metastable energy state at the deflection point and the stable energy minimum. Hence, the total sur-

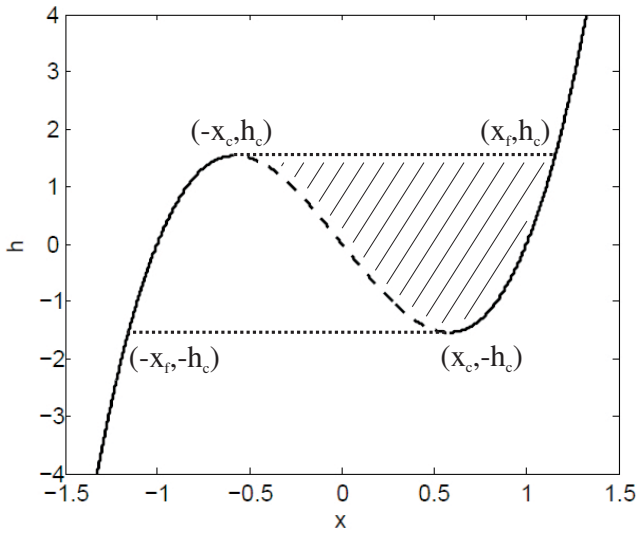

Figure 4.4: Extremum points in the bistable system, given by expression (4.4), following [5].

face of the hysteresis loop is equal to the energy dissipated by the system during one cycle of the external applied force.

Energetically, two different processes can be distinguished when running through the hysteresis loop. In the stable hysteresis branches there is a reversible exchange of energy from the input field towards the system. A Δh increase of the input field makes the minimum state gain a certain amount of energy Δg. Since the system stays in the same minimum, an identical decrease in energy is encountered when the input field is diminished by a same amount Δh, hence the same branch is covered. On the contrary, when the system is at the deflection point of the energy curve, a small increase δh of the input field results in an *irreversible* dissipation of energy between the system and the thermal bath. Since the system has moved to an other minimum, an identical decrease δh of the input field will not result in the exchange of the same amount of energy. Hence, different branches are described.

4.2.3 Rate (in)dependence

In the above description no time scale is given on which the input field is changed: the system is considered to adapt instantaneously to the input field and occupy an energy minimum at each point in time. In this case, the time scale on which the input field changes does not play a role. However, in the bistable system, the time scale, to a certain extent, does play a role.

On the one hand, the energy difference Δg between the deflection point and the global energy minimum is dissipated as heat. Hence, some kind of relaxation process with a characteristic time scale takes place in the system. This characteristic time scale depends on the considered system. Hence, the assumption of the instantaneous adaption to new input fields only holds when the time scale of the relaxation process is much smaller than the time scale on which the input field changes.

On the other hand, the changes in the input field should be not too slow. In most physical processes, there are some stochastic fluctuating energy contributions related with the systems temperature, e.g. due to the brownian movement of particles, etc. These fluctuating energy contributions enable to jump across energy barriers towards the global energy minimum. These stochastic fluctuations are only very small compared to the effect of the other processes defining the system. Only when the system stays in the energy states for a very long time, the probability of jumping across energy barriers towards the global energy minimum becomes non negligible. Hence for very slow varying input fields, no hysteresis is expected since the system always relaxes to the global energy minimum.

To conclude it is clear that over a very large time scale, the hysteretic system is rate independent. The shape of the hysteresis loop does not change as long as the input field varies fast enough to ensure that thermal energy fluctuations cannot influence the system and slow enough to ensure that the system can always relax to the local minimum.

4.3. Hysteresis in the micromagnetic system

From the energetic description of the simple bistable model it is clear that hysteresis effects will also be encountered in the micromagnetic system. Indeed, the micromagnetic system evolves also from one energy minimum to the other in the total Gibbs free energy landscape. In the micromagnetic model the input field is the external applied magnetic field $\mathbf{H}_a$ and the state variable magnetization field $\mathbf{m}(\mathbf{r},t)$. In what follows we will consider only unidirectional applied fields and the resulting average magnetization along the same axis $\mathbf{e}_a$. This leads to scalar hysteresis loops representing the relation $< M >=< \mathbf{M} > \cdot \mathbf{e}_a$ and $H_a = \mathbf{H}_a \cdot \mathbf{e}_a$.

4.3.1 (Ir)reversibility and branching

Analogous to the bistable model, the average magnetization $< M >$ depends on the local minima in the Gibbs free energy occupied by the system. However, due to the complexity of the micromagnetic energy landscape various local minima exist. The minima in the total Gibbs free energy change due to

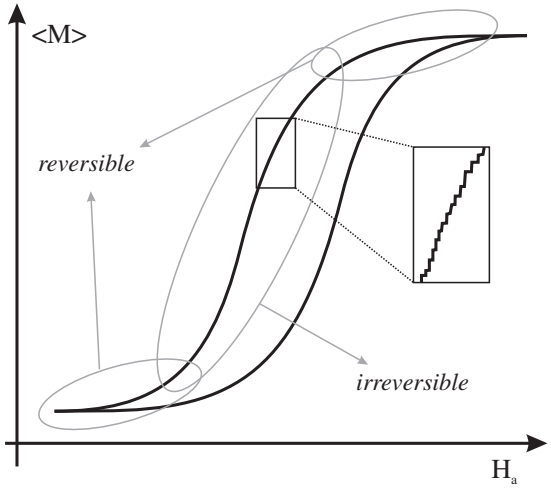

Figure 4.5: Magnetic hysteresis loop, enlarged are the Barkhausen jumps corresponding to irreversible magnetization processes.

variations of the applied field. When the applied field is varied from large, positive values to large negative values and vice versa, this results in a hysteresis loop, shown in Fig. 4.5.

In the ferromagnetic material, changes in the average magnetization now result from two different mechanisms. First, there are *reversible* changes in the magnetization. Here, the micromagnetic system stays in the same local energy minimum, but due to the variation of the applied field, the position of the minimum changes. This gives rise to continuous changes in magnetization. In general, close to saturation, the changes in magnetization are mainly reversible in nature, see Fig. 4.5. When saturated, the material is in the global energy minimum. When the applied field diminishes, the minimum rises continuously and vice versa. This gives rise to identical magnetization paths for increasing and decreasing applied field values as can be seen in Fig. 4.6: the magnetization curves $a - b$ and $b - c$ almost coincide.

Second, there are *irreversible* changes in the magnetization. Away from saturation, the changes in magnetization are dominated by irreversible processes. Here, local energy minima occupied by the micromagnetic system vanish successively and the system evolves again and again to new local energy minima, dissipating the energy differences as heat. This gives rise to discontinuous changes in the magnetization as shown in the enlarged view in Fig. 4.5. The jumps in magnetization are known as Barkhausen jumps [27]. In general, it is difficult to make a strict division between the reversible and irreversible magnetization processes. Indeed, between the irreversible Barkhausen jumps,

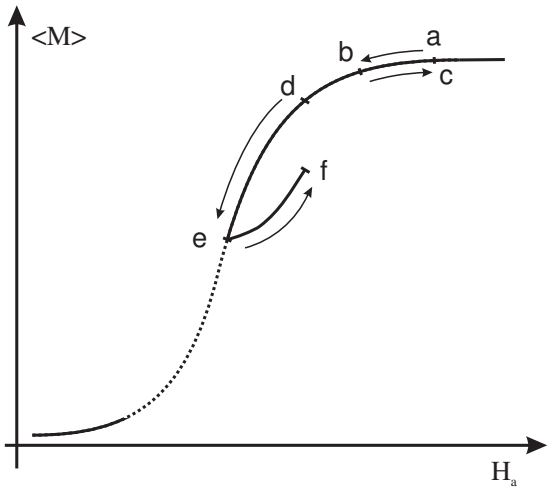

Figure 4.6: Transition curves illustrating the mainly reversible and mainly irreversible parts of the magnetic hysteresis loop.

reversible magnetization changes take place, see Fig. 4.5. Since the micromagnetic system jumps towards different energy minima, the magnetization path is different for increasing and decreasing applied field values. In Fig. 4.6 the magnetization curve $d - e$ is different from the curve $e - f$.

Figure 4.6 shows some key features present in magnetic hysteresis. Due to the successive irreversible evolution from energy minimum to energy minimum, there is a history dependence in the magnetic system. In general, a new branch is always created when the external field switches sign: a *reversal point* is generated and a new branch emanates, this effect is known as *branching*. Hence, the magnetic system contains some *memory*. Indeed, the branch $e - f$ is completely determined by the reversal point e, i.e. the magnetization history, and the present applied field. The memory properties of ferromagnetic materials are described by Madelung's rules.

4.3.2 Madelung's rules

It is clear that a lot of microscopic material parameters influence the Gibbs free energy and thus the magnetic properties of the material. In spite of the variety of characteristics among different magnetic materials some general features are observed in the macroscopic hysteresis behavior. These features have been described already in 1905 by Madelung [28] and are known as Madelung's rules. They describe the memory properties of magnetic materials. Consider-

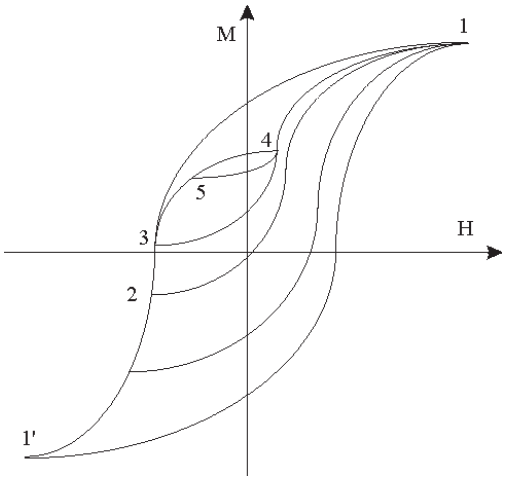

Figure 4.7: Transition curves illustrating Madelung's rules

ing the hysteresis curves in Fig. 4.7, these experimentally established rules can be stated as follows:

- *Branching:* the path of any transition (reversal) curve is uniquely determined by the coordinates of the reversal point, from which the curve emanates.
- *return-point-memory:* if any point 4 of the curve 3-4-1 becomes a new reversal point, then the curve 4-5-3 originating at point 4 returns to the initial point 3.
- *wiping-out property:* if the point 5 of the curve 4-5-3 becomes the newest reversal point and if the transition curve 5-4 extends beyond the point 4, it will pass along the part 4-1 of curve 3-4-1, as if the previous closed loop 4-5-4 never existed.

Since Madelung's rules are the only general hysteretic properties observed in all magnetic materials, any magnetic hysteresis model should be able to describe them.

4.3.3 Energy dissipation

Based on the same considerations as for the bistable system, the surface of the magnetic hysteresis loop corresponds to the losses in the ferromagnetic material. Figure 4.8 shows experimentally obtained hysteresis loops measured on the same sample. The frequency of the applied field is varied. It is clear that the hysteresis loops broaden when the frequency of the applied field increases. Consequently, the losses in the material grow for higher frequencies.

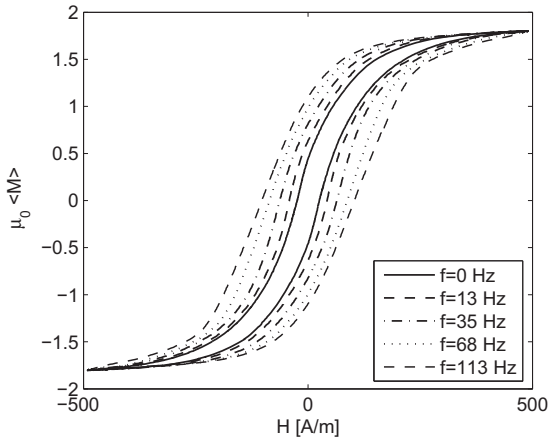

Figure 4.8: Hysteresis loops measured for different rates of changes of the applied field. In the experiments, the applied field is controlled in such a way that the resulting magnetization is varying sinusoidally with the presented frequencies. Material: M2H, grain oriented FeSi, measured in the rolling directions.

This growing loss dissipation, is due to the joule losses, which for one cycle can be calculated as

$$\frac{P}{f} = \int_V \frac{\mathrm{d}\mathbf{r}}{V} \int_0^{1/f} \frac{|\mathbf{j}_{eddy}(\mathbf{r},t)|^2}{\sigma}\,\mathrm{d}t. \tag{4.6}$$

Here, $\mathbf{j}(\mathbf{r},t)$ is the continuum eddy current field derived from (2.76), f is the considered frequency and V is the material volume. From Section 2.5 it is clear that larger frequencies lead to larger eddy currents and thus to increasing eddy current losses.

Micromagnetic description

From the micromagnetic point of view, the loss dissipation in the ferromagnetic material is due to the damping term in the LLG equation (2.68). At each barkhausen jump, the energy difference is dissipated as heat in the damped precession movement. Hence, in the micromagnetic approach, the dissipated energy corresponds to the energy difference confined in the effective fields before and after the barkhausen jump. Here, the effective field includes $\mathbf{H}_{eddy}$ originating from the eddy currents. It is clear that, when a material is considered with no conductivity ($\sigma = 0$), the energy dissipation is only due to the 'static' effective field terms described in (2.53).

Macroscopic description

Following the *loss separation theory* of Bertotti [5], all losses are due to currents running on different space and time scales in the ferromagnetic material. According to the theory, three different mechanisms contribute to the total losses.

$$\frac{P}{f} = C_0 + C_1 f + C_2 \sqrt{f}. \tag{4.7}$$

The contributing losses in one cycle are shown for different frequencies in Fig. 4.9 for the same material as in Fig. 4.8. The three loss contributions are

- *Hysteresis losses* $\propto C_0$*:* these losses are due to hysteresis currents resulting from the discontinuous variation of the local magnetization during barkausen jumps. Hence, the spatial scale corresponds to the nanometer scale describing domain walls and the temporal scale is defined by the LLG equation, i.e. order picoseconds.
- *Classical losses* $\propto C_1 f$*:* these losses correspond to the eddy currents in a macroscopic description where the magnetization processes are considered to be fully homogeneous in space. The currents and thus the length scale are determined by the geometry of the sample. The time scale corresponds to the variations of the external applied field.
- *Excess losses* $\propto C_2 \sqrt{f}$*:* these losses are caused by excess currents originating in the magnetic domain structure, the dynamics of the domain walls and their mutual interaction. The spatial and temporal scale are intermediary, corresponding to the size of the magnetic domains and their evolution. In macroscopic models, the excess losses are determined on mathematical grounds.

Discussion

Both theories are in accordance with each other due to the duality between currents and magnetic fields

$$\mathbf{j} = \nabla \times \mathbf{H}. \tag{4.8}$$

However, the micromagnetic description is more fundamental since it still describes losses when the conductivity is zero. The different time and length scales described in the loss separation theory can be attributed to the different space and time scales of the various micromagnetic interactions. In the micromagnetic approach, little or no research is yet performed on the frequency dependence of the different effective field terms and the associated losses.

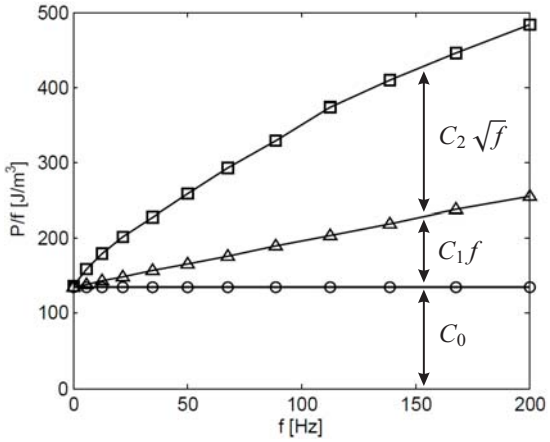

Figure 4.9: Loss separation following the *loss separation theory* for hysteresis loops measured on the same material as Fig. 4.8.

4.3.4 Rate (in)dependence

Following the example of the bistable system, we have seen that hysteresis processes are time independent over a wide time range. This is also the case for the micromagnetic hysteresis system. To guarantee rate independence, the external field should vary on a much larger time scale than the relaxation processes in the magnetic material. In the micromagnetic context, one relaxation time scale corresponds to the one on which Barkhausen jumps occur and thus with the time scale described by the LLG equation. Another relaxation time scale corresponds to the eddy currents. The system is only in equilibrium when no currents are present in the material.

From Fig. 4.9 it is clear that the shape of the hysteresis loop is affected by the frequency of the applied field. For an iron based sample with thickness smaller than 1 mm, a the rate of change of the applied field smaller than $1\,Hz$, gives rise to identical hysteresis loops. In this time frame, all eddy currents are damped out and rate independent hysteresis loops are described. The resulting hysteresis loop is also known as the quasi static hysteresis loop.

In the micromagnetic hysteresis system the external field should not vary too slowly. Indeed, in the micromagnetic description, thermal fluctuations can make the system jump across energy barriers towards to the global energy minimum, see Section 2.6. When the applied fields vary on this very slow time scale, the hysteresis loop narrows and in the limit all hysteresis effects disappear when the system has the time to relax successively to the global energy minimum. The described time scale depends on temperature. For moderate temperatures, this can correspond to years.

Hence we can conclude that a micromagnetic hysteresis system is rate independent over a very wide time span. To obtain rate independent hysteresis loops at moderate temperatures, the variation in the external applied field should be faster than the order of months and slower than the order of seconds.

CHAPTER 5

Context and aim of the conducted research

5.1. Challenges in micromagnetic hysteresis simulation

In the previous chapters a general overview is given of the micromagnetic theory and of magnetic hysteresis. From this outline it is clear that the micromagnetic description of magnetization processes is a truly multi-physics problem:

- *Solid state physics*: The microstructure of the ferromagnetic material needs to be characterized. Most material parameters are known from literature, but the actual microstructure and composition of the material depends on the manufacturing technique. The magnetic properties of the material are influenced by grain orientation, grain size distribution, dislocation density, distribution of dislocations, precipitates, microscopic cracks, sample roughness, etc. These are parameters defining the sample that need to be determined in the context of solid state physics. Furthermore, most of these parameters evolve in time, particulary when the material is subjected to forces. Here, the understanding of the mechanical relaxation processes is important. The magnetic properties of the material will change under altering mechanical properties of the material.
- *Elasticity theory*: The structure of the ferromagnetic material is described by solid state physics. The elasticity theory translates the material structure in mathematical formula determining the strains and stresses in the ferromagnetic material. The diverse length scales of the physical description ranges also here from the atomistic scale (dislocations, interstitials) over the intermediate grain scale to the macroscopic scale of the sample. This makes the computation of the total stress and strain distribution through-

out the whole sample a challenging problem, in particular when the microstructure of the material changes in time. The micromagnetic system is influenced by the local stress and strain due to the magnetoelastic interaction.

- *Magnetoelastic theory*: In Section 2.2.3 it is explained that the interplay between the local magnetization and the local stress results in a rather complex evaluation of the stress and strains. The magnetoelastic coupling complicates the above mentioned elastic description of the considered ferromagnetic material.
- *Electromagnetic theory*: The computation of the magnetostatic field $\mathbf{H}_{ms}$ and the eddy current field $\mathbf{H}_{eddy}$ in the sample is based on Maxwell's equations. Due to the large interaction radius of both phenomena, both evaluations result into very burdensome computations which, for large sample sizes, can not be elaborated using the classical techniques. Hence, one has to develop efficient numerical techniques. Moreover, from Chapter 3, it is clear that the magnetostatic fields have a large influence on the hysteresis phenomena. It should be investigated which boundary conditions can be used in order to minimize the magnetostatic interactions. The computation of $\mathbf{H}_{eddy}$ is complicated by the large differences in time scales.
- *Statistical physics*: The thermal fluctuations are statistically distributed. Hence, their influence on the magnetization processes, in particular on magnetization switching processes, leads to a stochastical description. Numerically, this results in Monte Carlo simulations.

For most of the above aspects, the large differences in space and time scale complicate the numerical solution.

5.2. International research context

5.2.1 Micromagnetic modelling

Numerical micromagnetic schemes have been adopted for the design of various magnetic applications, leading to a miniaturization of magnetic elements [29]. A lot of research effort has for instance devoted to the simulation of magnetic tapes, see e.g. [30, 31]. Here, one of the aims is to optimize the writing heads and to minimize the affected zone on the magnetic tape in order to increase the data density. In this context, the stability of the magnetic information is important: how do neighboring magnetized regions affect each other, what is the thermal stability?
A second topic is magnetic patterned media used in random access memories (MRAM) and future sensor applications, see e.g. [32, 33]. Also here, miniaturization of the application device is the aim. Some of the research questions are how external fields affect the magnetization of the different magnetic elements

and how they interact mutually.
Other topics are magnetization processes in (arrays of) magnetic nanoparticles [34] and nanowires [35], spin torque oscillators [36], spin-valves [37], etc.

A common aspect of all these research topics is the limited size of the considered material samples, i.e. from the nanometer to micrometer length scale. Since the micromagnetic length scale is of the same order (see Section 2.3.2), the difficulties in the numerical algorithms are rather limited. Furthermore, in most cases the considered material is a monocrystal without any defects. Hence, inhomogeneities in the material structure do not influence the magnetization processes and magnetoelastic interactions are neglected.

Up to now, only very little research is performed incorporating all material interactions described in Chapter 2 in numerical simulations, probably due to the interplay of the different described research areas and to the huge computational burden. However, the currently available large computer resources combined with sophisticated numerical techniques open the opportunity to start research in this field. There is definitely a need for this research as indicated by Aharoni [38] at the opening of the third International Symposium on Hysteresis Modeling and Micromagnetics (2001):

> *At some stage, computations must also address the possible effect of crystalline imperfections, by having some subdivisions with, for example, different anisotropy than the others. Surface roughness alone is most probably sufficient to account for the nucleation, as in the De Blois experiment. It is, however, quite likely that crystalline defects, such as dislocations, and impurity atoms, affect the rest of the magnetization curve, after nucleation. They seem very likely to have a large effect on the domain wall motion, but at this stage their role is an open question, that should be investigated.*

5.2.2 Hysteresis modelling

Various hysteresis models are developed to describe the macroscopic hysteresis properties of ferromagnetic materials. A widely used hysteresis model is the Preisach model [39]. It is designed to describe the uniaxial hysteresis properties of magnetic materials, but is also extended to a vectorial description of hysteresis processes. The Jiles-Atherton model [40] is a physics based model considering the principles of losses in the material, the movement of the domain walls, etc. Both macroscopic hysteresis models are mathematical in nature and are constructed to incorporate the memory properties described in Section 4.3.2. The material characteristics are included by fitting model parameters to experimental data. In the energetic model [41], the total Gibbs free energy is determined on statistical grounds. The model describes hysteresis properties as branching, closure of minor loops, etc. Some model parameters need to be fitted.

In the last few years another type of hysteresis models has emerged. Mesoscopic hysteresis models describe hysteresis processes on the domain length scale. These models are based on a simplified interpretation of the different micromagnetic energy terms, assuming the magnetization processes are dominated by domains and domain wall movement. Van den Berg et al. [42] include the magnetostatic interactions rigorously, resulting in a hysteresis model that describes Madelung's rules. Daniel et al. [43] include the magneto-mechanical behavior in their description, but result into single valued B-H characteristics.

5.3. Research context at EESA and Intec

At the Department of Electrical Energy, Systems and Automation (EESA) and more in particular at the Electrical Energy Lab (EELAB) there is a long history in hysteresis modelling. The properties of the Preisach model have been extensively studied and used to characterize the magnetic material parameters of electrical steels [44]. The model is predominantly used in the department to introduce the hysteresis properties in magnetic flux computations in electrical steels used in transformers and electrical machines incorporating hysteresis effects [45, 46]. Furthermore, research is performed related to the determination of magnetic material parameters of ferromagnetic samples and their dependence on the manufacturing techniques by using inverse numerical techniques [46]. Also work is performed on magnetostriction modelling in electrical machines and transformers [47].

EELAB also has a large expertise in the experimental magnetic hysteresis characterization of ferromagnetic materials. These material parameters determine the mechanical and the magnetic properties of the material. Hence a change in the magnetic properties can be related to a change in the mechanical material properties. This research can lead to magnetic non destructive evaluation techniques in ferromagnetic materials [1]. From the experiments it is clear that the investigated relations between mechanical and magnetic material properties is most pronounced at very low frequencies where only hysteresis losses (see Section 4.3.3) are observed.

In the last two years, also a mesoscopic hysteresis model is developed at EELAB. This model is based on the reinterpretation of the micromagnetic energy terms on the length scale of magnetic domains.

At the Department of Information Technology (Intec) and more in particular the Electromagnetics Group, a large experience is available in the numerical solution of Maxwell's equations. Here, highly efficient evaluation techniques such as Fast Fourier Transforms (FFTs) and Multilevel Fast Multipole Algorithms (MLFMA) are used to compute very large electromagnetic scattering problems using boundary integral equations and volume integral equa-

tions. With respect to boundary integral techniques, the emphasis is on the development of efficient preconditioners [48], a broadband MLFMA [49] and the parallellization of the MLFMA, while volume integral techniques are applied in imaging techniques based on the solution of inverse scattering problems [50,51].

5.4. Research goal

The presented doctoral thesis fits in the framework of *the identification and evaluation of the relations between microstructural material aspects and macroscopic magnetic material behavior of ferromagnetic materials, based on a numerical micromagnetic hysteresis model*. Up to now, this identification has mainly been performed based on experimental work. In the experiments however it is very difficult to alter only one microscopic parameter without influencing others. Hence it is very hard to distinguish relations between specific microstructural and macroscopic magnetic parameters. Numerical experiments alleviate this problem and allow for a systematic and time efficient study to determine the investigated relations.

5.4.1 Assumptions

As demonstrated above, the *development of a numerical micromagnetic hysteresis scheme* is a multiphysics problem which cannot be tackled all at once. Therefore some assumptions are made:

1. The microscopic structure of the considered material and the resulting stress and strain fields are considered to be known and is input of the micromagnetic model.
2. The magnetoelastic interaction is considered in the *relaxed approach*. In this approach, the small magnetoelastic energy term (2.30) depending only on the spontaneous magnetostrictive strains and the second magnetoelastic energy term in (2.29) corresponding to the self energy density of the elastic magnetostrictive strains are neglected. Furthermore, the elastic strain tensor $\boldsymbol{\epsilon}_{el}$ is disregarded. The magnetoelastic energy term density is then described as
$$\phi_{me} = -(\boldsymbol{\sigma}_{ext} + \boldsymbol{\sigma}_{def}) \cdot\cdot \boldsymbol{\epsilon}_{sp}(\mathbf{m}). \tag{5.1}$$
Hence, in the relaxed approach only the stresses $\boldsymbol{\sigma}_{ext}$ and $\boldsymbol{\sigma}_{def}$ as present in the non magnetic material are taken into account. Following the above assumption, these are input of the micromagnetic model. The stresses influence the magnetization due to the interaction with the spontaneous magnetostrain $\boldsymbol{\epsilon}_{sp}(\mathbf{m})$. The relaxed approach is acceptable for low magnetostrictive materials [52] as ferromagnetic materials. From (5.1) it is clear that the

input stress influences the magnetization. This enables the description of magnetization processes as the pinning of magnetic domain walls. However, the influence of the magnetization on the stress and strain in the material (and thus on the microstructure) is disregarded. This disables the description of magnetostrictive effects. Further, it is known that the magnetoelastic interaction can result in a changing microstructure [1]. In the relaxed approach, this effect can also not be described.

3. In the experimental work investigating the relations between the microstructure and the macroscopic magnetic properties, it is seen that the relations are most pronounced at very low frequencies, i.e. in time independent hysteresis loops. Therefore, the external applied field $\mathbf{H}_a$ is assumed to vary quasistatically. In this frequency range the classical and excess losses, both originating in joule dissipation of eddy currents are negligible.
4. Eddy currents $\mathbf{j}_{eddy}$ and the related eddy current fields $\mathbf{H}_{eddy}$ are neglected. The conductivity is assumed to be zero. Since the applied fields are considered to vary on a low frequency time scale, this corresponds to neglecting the local eddy currents due to the fast evolution of the local magnetization during Barkhausen jumps. This results in an underestimation of the hysteresis losses in the loss separation theory (Section 4.3.3).
5. A temperature range up to only moderate temperatures is considered. Hence, thermal fluctuations have only a second order influence on the magnetization processes. Thermal fluctuations will only be considered as the trigger mechanism to initiate magnetization processes. Further, when hysteresis processes are considered, the time scales are considered to be short, so no dominant thermal relaxation processes take place. Combined with assumption 4 this results in time independent hysteresis loops.

5.4.2 Conducted research

In this doctoral thesis we present an *efficient numerical micromagnetic scheme able to describe magnetization processes up to the domain length scale* under the assumptions of Section 5.4.1. The numerical scheme is optimized to describe hysteresis processes in micrometer sized magnetic structures, but is also useful for the description of magnetization processes in more classical micromagnetic structures as nanoparticles, nanowires, tapes, etc. The evaluation of the long range interacting magnetostatic field limits the considered sample dimensions and determines the computational burden. In this work, *the number of magnetostatic field evaluations is minimized by introducing a highly stable micromagnetic time stepping scheme. Further, sophisticated numerical techniques are presented, required to evaluate the magnetostatic field in a highly time and memory efficient way*. Optimal model parameters are put forward that guarantee the best computa-

tional efficiency. The micromagnetic scheme is validated considering various magnetization processes in ferromagnetic materials: (i) reversal processes are described in the the classical micromagnetic, sub-micrometer sized objects, (ii) domain configurations are studied in micromagnetically large platelets, and (iii) hysteresis properties are studied.

This work exploits and contributes to the numerical experience, existing at Intec, and the experience concerning hysteresis modeling and magnetization processes in ferromagnetic materials, existing at EESA. The presented work contributes to the development of a full micromagnetic hysteresis scheme able to distinguish the different relations between the microstructure and the macroscopic magnetic material properties.

Part II

Numerical Algorithms

CHAPTER 6

Numerical micromagnetic scheme

In this chapter we will present the micromagnetic numerical scheme developed during the PhD to simulate the magnetic behavior in micromagnetically large ferromagnetic samples. It is based on the time stepping of the Landau-Lifshitz-Gilbert equation (2.68). Here, an appropriate space and time discretization scheme is indispensable in order to minimize the CPU and memory requirements and hence guarantee the efficiency of the numerical scheme. To minimize the computational burden, the time stepping scheme itself has to be very stable to enable the use of large time steps. Further the computation of one time step should be as fast as possible and with a minimum use of memory. In what follows, the space discretization is outlined, an appropriate discretization of the effective field terms is given and efficient time stepping schemes for the LLG are presented. The resulting micromagnetic scheme is validated by comparing simulation results with results obtained from other micromagnetic codes. Further, a micromagnetic hysteresis scheme is presented, able to simulate time independent hysteresis loops.

6.1. Geometry discretization

The computational domain $\mathcal{D}$ is a rectangular prism composed of regularly placed cubic FD cells of identical size $\Delta \times \Delta \times \Delta$. This computational domain $\mathcal{D}$ encloses the 3D ferromagnetic sample. The different material parameters are defined in each FD cell that coincides with the material: the exchange stiffness A, anisotropy constants K_1 and K_2 (cubic anisotropy) or just K_u (uniaxial anisotropy), anisotropy axes and the local stress $\boldsymbol{\sigma}$. FD cells that not coincide with the ferromagnetic sample have the properties of free space. In this way,

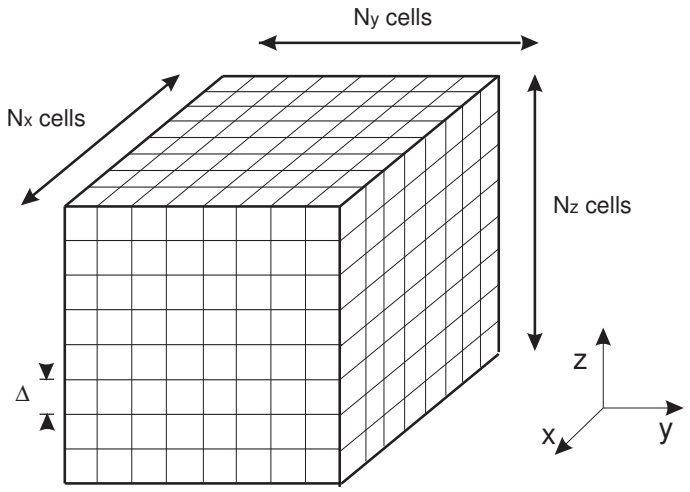

Figure 6.1: Discretization of the computational domain $\mathcal{D}$. The FD cells have edges of width Δ.

Table 6.1: Microscopic material constants for pure iron.

quantity	value	unit
$\mu_0 M_s$	2.16	[T]
A	$1.5\,10^{-11}$	[Jm^{-3}]
K_1	$0.48\,10^5$	[Jm^{-3}]
K_2	$-0.50\,10^5$	[Jm^{-3}]
λ_{100}	$22\,10^{-6}$	[]
λ_{111}	$-21\,10^{-6}$	[]
c_{11}	241	[GPa]
c_{12}	146	[GPa]
c_{44}	112	[GPa]

curved boundaries of the ferromagnetic body are discretized using staircase-like surfaces. The FD discretization is shown in Fig. 6.1. In total, there are $N = N_x \times N_y \times N_z$ discretization cells.

FD cells coinciding with the magnetic material are considered to be uniformly magnetized, corresponding to the local magnetization in the center of the FD cell, i.e. the micromagnetic magnetization field $\mathbf{m}(\mathbf{r},t)$ is considered to be constant throughout the entire cell with a value corresponding to the field at the center of the FD cell. The material constants for pure iron are given in Table 6.1. Following the micromagnetic theory, only the orientation of $\mathbf{m}(\mathbf{r},t)$ can vary and the amplitude stays fixed $|\mathbf{m}(\mathbf{r},t)| = 1$. In FD cells outside the ferromagnetic sample $\mathbf{m}(\mathbf{r},t) = 0$ holds.

As presented in Part I, the dynamics of the magnetization field $\mathbf{m}(\mathbf{r},t)$ are determined by the effective field $\mathbf{H}_{eff}$ through the LLG equation. Therefore, the CPU time consumption and the memory requirements for the presented time stepping scheme depends on: (i) the efficient computation of the considered effective field terms and (ii) the efficiency of the used time stepping scheme for the LLG equation.

6.2. Evaluation of the effective field terms

In this section we will present discretized expressions for $\mathbf{H}_{exch}$, $\mathbf{H}_{ani}$, $\mathbf{H}_{me}$ and $\mathbf{H}_{ms}$. The applied field $\mathbf{H}_a$ and thermal fluctuating field $\mathbf{H}_{th}$ are straightforward to implement since, at a given time instant, $\mathbf{H}_a$ is constant over the structure and $\mathbf{H}_{th}$ (2.82) is computed using a Gaussian number generator. All these field terms determine the effective field needed to time step the LLG equation. We will comment on the time and memory requirements needed to evaluate the terms. To start, $6N$ numbers are required to save the three components of $\mathbf{m}$ and $\mathbf{H}_{eff}$ in each FD cell. In principle, $2N$ in stead of $3N$ numbers suffice to store the local magnetization field since $|\mathbf{m}=1|$, but in this case the memory savings are minimal compared with the computational overhead.

6.2.1 Discretization of the exchange field

The exchange field

$$\mathbf{H}_{exch} = \frac{2A}{\mu_0 M_s}\nabla^2 m_i \mathbf{e}_i \tag{6.1}$$

is discretized using standard finite difference formula to approximate the Lapliacian [53]. Hence $\mathbf{H}_{exch}$ in a general cell (p,q,r) is computed as

$$\begin{aligned}\mathbf{H}_{exch}^{p,q,r} = \frac{2A}{\mu_0 M_s}\frac{1}{\Delta^2}\Big(&m_i^{p-1,q,r}+m_i^{p+1,q,r}+m_i^{p,q-1,r}+m_i^{p,q+1,r}\\ &+m_i^{p,q,r-1}+m_i^{p,q,r+1}-6m_i^{p,q,r}\Big)\mathbf{e}_i.\end{aligned} \tag{6.2}$$

Special attention should go to the FD cells near the boundaries of the computational domain. At the edges of the sample, the boundary condition (2.49) has to be met. Therefore, expression (6.2) has to be adjusted. For instance, for a FD cell at with $p=0$ the exchange field is given by

$$\begin{aligned}\mathbf{H}_{exch}^{p,q,r} = \frac{2A}{\mu_0 M_s}\frac{1}{\Delta^2}\Big(&\frac{2}{3}m_i^{1,q,r}+m_i^{0,q-1,r}+m_i^{0,q+1,r}\\ &+m_i^{0,q,r-1}+m_i^{0,q,r+1}-\frac{14}{3}m_i^{0,q,r}\Big)\mathbf{e}_i.\end{aligned} \tag{6.3}$$

and analogous for cell at other edges [54]. The use of higher order approximation schemes is investigated in [55].

From equation (6.2) it is clear that the evaluation of $\mathbf{H}_{exch}$ scales $\mathcal{O}(N)$. Indeed, for each cell q ($q = 1 \ldots N$) expression (6.2) has to be evaluated. There is no extra memory required for the evaluation of H_{exch}. Since the FD description of the exchange field is completely local, the FD discretization is advantageous compared to a finite element method (FEM) description. When a FEM is adopted, the exchange interaction gives rise to a large system of coupled equations described by a large stiffness matrices, which needs to be solved. This problem, characteristic to the FEM description, is partially alleviated by substituting the large algebraic system derived from the exchange term by a set of reduced algebraic systems [56].

6.2.2 Discretization of the anisotropy field

In Chapter 2 the anisotropy field was defined as

$$\mathbf{H}_{ani} = -\frac{1}{\mu_0 M_s} \frac{\partial \phi_{ani}}{\partial m_i} \mathbf{e}_i. \tag{6.4}$$

In the case of *uniaxial anisotropy*, the anisotropy energy density ϕ_{ani} is determined by (2.16) and expression (6.4) results in (with $\mathbf{u}$ the uniaxial anisotropy axis)

$$\mathbf{H}_{ani} = \frac{2K_1}{\mu_0 M_s} (\mathbf{m} \cdot \mathbf{u}) \mathbf{u}, \tag{6.5}$$

which is straightforward to implement.

In the case of *cubical anisotropy*, the anisotropy energy density was given by

$$\phi_{ani} = K_1 \left(\alpha_1^2 \alpha_2^2 + \alpha_2^2 \alpha_3^2 + \alpha_1^2 \alpha_3^2 \right) + K_2 \alpha_1^2 \alpha_2^2 \alpha_3^2 \tag{6.6}$$

with $\alpha_i = \mathbf{m} \cdot \mathbf{u}_i$. The cubical anisotropy axes $\mathbf{u}_1$, $\mathbf{u}_2$ and $\mathbf{u}_3$ are defined with respect to the general coordinate system $\mathbf{e}_1 \mathbf{e}_2 \mathbf{e}_3$ as

$$\mathbf{u}_1 = F_{11} \mathbf{e}_1 + F_{12} \mathbf{e}_2 + F_{13} \mathbf{e}_3 \tag{6.7}$$

$$\mathbf{u}_2 = F_{21} \mathbf{e}_1 + F_{22} \mathbf{e}_2 + F_{23} \mathbf{e}_3 \tag{6.8}$$

$$\mathbf{u}_3 = F_{31} \mathbf{e}_1 + F_{32} \mathbf{e}_2 + F_{33} \mathbf{e}_3. \tag{6.9}$$

The matrix $\mathbf{F}$ defining the relation between the lattice axes and the general coordinate system $\mathbf{e}_1 \mathbf{e}_2 \mathbf{e}_3$ can be defined using Euler angles. Applying the chain rule to (6.4) yields

$$\mathbf{H}_{ani} = -\frac{1}{\mu_0 M_s} \frac{\partial \phi_{ani}}{\partial \alpha_j} \frac{\partial \alpha_j}{\partial m_i} \mathbf{e}_i. \tag{6.10}$$

Here, $\frac{\partial \phi_{ani}}{\partial \alpha_j}$ is directly determined by (6.6). To determine $\frac{\partial \alpha_j}{\partial m_i}$, $\mathbf{m}$ is expressed in the two different bases

$$\mathbf{m} = \alpha_1 \mathbf{u}_1 + \alpha_2 \mathbf{u}_2 + \alpha_3 \mathbf{u}_3 = m_1 \mathbf{e}_1 + m_2 \mathbf{e}_2 + m_3 \mathbf{e}_3. \tag{6.11}$$

By combining (6.9) and (6.11) $\mathbf{m}$ can be written in terms of α_j

$$m_1 = F_{11}\alpha_1 + F_{21}\alpha_2 + F_{31}\alpha_3 \tag{6.12}$$
$$m_2 = F_{12}\alpha_1 + F_{22}\alpha_2 + F_{32}\alpha_3 \tag{6.13}$$
$$m_3 = F_{13}\alpha_1 + F_{23}\alpha_2 + F_{33}\alpha_3 \tag{6.14}$$

or in matrix notation $\mathbf{m} = \mathbf{F}^T \boldsymbol{\alpha}$. This results in

$$\frac{\partial \alpha_j}{\partial m_i} = \left[\left(F^T \right)^{-1} \right]_{ji}. \tag{6.15}$$

By combining the above expressions, the cubic anisotropy field can be determined as

$$\begin{bmatrix} H_{ani,x} & H_{ani,y} & H_{ani,z} \end{bmatrix} = -\frac{1}{\mu_0 M_s} \begin{bmatrix} \frac{\partial \phi_{ani}}{\partial \alpha_1} & \frac{\partial \phi_{ani}}{\partial \alpha_2} & \frac{\partial \phi_{ani}}{\partial \alpha_3} \end{bmatrix} \begin{bmatrix} & F^T & \end{bmatrix}^{-1}. \tag{6.16}$$

The implementation of this expression is straightforward.

In the numerical scheme, grains are defined as an ensemble of a large number of FD cells with identical anisotropy axes. Both the evaluation of the uniaxial and the cubical anisotropy field (6.5) and (6.16) are purely local computations, meaning that no input from other FD cells is needed to compute $\mathbf{H}_{ani}$ in a given cell. Hence, to compute $\mathbf{H}_{ani}$ in N cells, $\mathcal{O}(N)$ computations suffice. Further, no extra memory space is required.

6.2.3 Discretization of the magnetoelastic field

The magnetoelastic field

$$\mathbf{H}_{me} = -\frac{1}{\mu_0 M_s} \frac{\partial \phi_{me}}{\partial m_i} \mathbf{e}_i \tag{6.17}$$

is evaluated within the relaxed approach. In this approach, the magnetoelastic energy density ϕ_{me} reduces to

$$\phi_{me} = -\frac{3}{2}\lambda_{100} \sum_{i=1}^{3} \sigma_{ii} \alpha_i^2 - \frac{3}{2}\lambda_{111} \sum_{i \neq j} \sigma_{ij} \alpha_i \alpha_j \tag{6.18}$$

with $\boldsymbol{\sigma}$ the stress introduced in the material by defects and externally applied forces. Expression (6.18) is achieved after inserting (2.24) in (5.1). The derivation of $\mathbf{H}_{me}$ in terms of $\mathbf{m}$ is analogous to the derivation made for $\mathbf{H}_{ani}$. This results in

$$\begin{bmatrix} H_{me,x} & H_{me,y} & H_{me,z} \end{bmatrix} = -\frac{1}{\mu_0 M_s} \begin{bmatrix} \frac{\partial \phi_{me}}{\partial \alpha_1} & \frac{\partial \phi_{me}}{\partial \alpha_2} & \frac{\partial \phi_{me}}{\partial \alpha_3} \end{bmatrix} \begin{bmatrix} \\ F^T \\ \\ \end{bmatrix}^{-1}. \tag{6.19}$$

The stress field $\boldsymbol{\sigma}$ in (6.18) is determined in each cell at the start of the algorithm and stays fixed during the simulation. As mentioned, each defect has its characteristic stress distribution, which can be determined based on micromechanical considerations [17]. The total stress is determined by adding all characteristic stresses introduced by the different defects, assuming that the defects are in an equilibrium state and the defect density is not too large, so no interaction takes place between the defects. In what follows we will provide the different expressions for the stress distributions of some defects as valid in the bcc lattice of iron.

The non-zero components of the stress tensor $\boldsymbol{\sigma}^{edge}$ characteristic for an *edge dislocation* running through the origin, with dislocation line parallel to the z-axis and Burgers vector $\mathbf{b}$ parallel to the x-axis are given by [57]

$$\sigma_{11}^{edge} = -\tau_0 \frac{by(3x^2 + y^2)}{(x^2 + y^2)^2} \tag{6.20}$$

$$\sigma_{22}^{edge} = \tau_0 \frac{by(x^2 - y^2)}{(x^2 + y^2)^2} \tag{6.21}$$

$$\sigma_{33}^{edge} = 2\tau_0 \frac{\nu y}{x^2 + y^2} \tag{6.22}$$

$$\sigma_{12}^{edge} = \sigma_{21}^{edge} = \tau_0 \frac{bx(x^2 - y^2)}{(x^2 + y^2)^2} \tag{6.23}$$

with

$$\tau_0 = \frac{G}{2\pi(1 - \nu)} \tag{6.24}$$

Here is b the length of the Burgers vector of the edge dislocation and G and ν are the modulus of rigidity and Poisson's ratio respectively. In the monocrystal the Burgers vector is parallel to a $< 111 >$ direction, while the dislocation line is parallel to a $< 110 >$ direction [58]. So the stress tensor $\boldsymbol{\sigma}^{edge}$ has to be rotated to the proper lattice axes orientations. An edge dislocation in a simple cubic lattice is shown in Fig. 6.2.

The non-zero components of the stress tensor $\boldsymbol{\sigma}^{scr}$ characteristic for a *screw dislocation* running through the origin and with dislocation line parallel to the

z-axis are given by [57]

$$\sigma_{13}^{scr} = \sigma_{31}^{scr} = -\frac{Gb}{2\pi}\frac{y}{x^2+y^2} \tag{6.25}$$

$$\sigma_{23}^{scr} = \sigma_{32}^{scr} = -\frac{Gb}{2\pi}\frac{x}{x^2+y^2} \tag{6.26}$$

For a screw dislocation the Burgers vector $\mathbf{b}$ is parallel to the dislocation line and parallel to a $<111>$-direction. So the stress tensor $\boldsymbol{\sigma}^{scr}$ should also be rotated to correspond to the description of the lattice axes orientations. A screw dislocation in a simple cubic lattice is shown in Fig. 6.2.

The components of the strain tensor $\boldsymbol{\epsilon}^{pd}$ of a *point defect* are given by [59]

$$\epsilon_{ij}^{pd} = -\frac{3}{2}\frac{a^3\left((1+\beta)^{1/3}-1\right)}{r^3}\frac{r_i r_j}{r^2} \tag{6.27}$$

with $r_{i=1,2,3} = (x,y,z)$ respectively, $r = \sqrt{x^2+y^2+z^2}$ and with a the lattice constant of iron. The mismatch parameter β is defined as the relative difference in volume between the distorted volume (V) and undistorted volume (V_0)

$$V = V_0(1+\beta). \tag{6.28}$$

For instance, a foreign atom bigger than a lattice atom is described by a characteristic volume expansion, $\beta > 1$ and a vacancy or foreign atom smaller than a lattice atom is described by a characteristic volume reduction, $\beta < 1$. The stress components σ_{ij}^{pd} are calculated from (6.27) using Hooke's law (2.21). The resulting stress $\boldsymbol{\sigma}^{pd}$ is isotropic, thus independent of lattice directions and should not be rotated to fit the lattice axes orientation.

From a mechanical point of view, grain boundaries correspond to a mismatch of neighboring lattice axes. This mismatch is fitted by the introduction of dislocations. Hence a grain boundary can be interpreted as a plane of dislocations. Due to the interplay between the dislocations, the orientation of the stresses is hard to describe, but the amplitude of the stress will drop as $1/r$, with r the distance to the grain boundary. Hence, the stress generated by a grain boundary is simulated as a stress tensor with random main stress orientation and an amplitude decreasing as $1/r$ with respect to the distance to the grain boundary.

As the computation of the anisotropy field, also the evaluation of $\mathbf{H}_{me}$ is purely local and thus scales $\mathcal{O}(N)$ if N cells are considered. The components of the stress tensor however need to be stored. This results in an extra $6N$ numbers stored in the computer memory since the stress matrix is symmetrical.

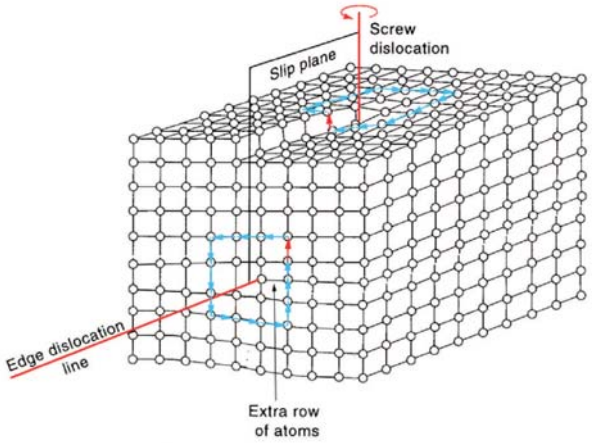

Figure 6.2: Schematic view of an edge dislocation and a screw dislocation in a simple cubic lattice, from [60].

6.2.4 Discretization of the magnetostatic field

In Chapter 3, the magnetostatic field was defined as

$$\mathbf{H}_{ms}(\mathbf{r}) = -\frac{M_s}{4\pi}\int_V \nabla\nabla\frac{1}{|\mathbf{r}-\mathbf{r}'|}\cdot\mathbf{m}(\mathbf{r}')\,\mathrm{d}\mathbf{r}'. \tag{6.29}$$

The magnetostatic field values have to be obtained in the center $\mathbf{r}_i$ of each FD cell $i = 1\ldots N$. Since the magnetization field in each FD cell is considered to be constant in each FD cell j, the volume integral in (6.29) can be subdivided in N integrals over the volumes $\mathcal{V}$ of the FD cells (with center $\mathbf{r}_j$, $j = 1\ldots N$). Because all cells have the same volume $\mathcal{V}$, the magnetostatic field can be discretized as

$$\mathbf{H}_{ms}(\mathbf{r}_i) = -\frac{M_s}{4\pi}\sum_{\substack{j=1\\ j\neq i}}^{N}\int_{\mathcal{V}} \nabla_{\boldsymbol{\rho}}\nabla_{\boldsymbol{\rho}}\frac{1}{|\mathbf{r}_i-\mathbf{r}_j+\boldsymbol{\rho}|}\,\mathrm{d}\boldsymbol{\rho}\cdot\mathbf{m}_j. \tag{6.30}$$

Here, $\mathbf{m}_j$ is the (constant) magnetization field in FD cell j and $\nabla_{\boldsymbol{\rho}}$ acts only on $\boldsymbol{\rho}$. The self contribution to the magnetostatic field (j=i) is left out, according to [61]. The self contribution leads to a constant magnetostatic field, antiparallel with the magnetization field of the considered FD cell. As such, the energy contribution to the total energy corresponding to the magnetostatic self interaction is constant in time and independent of the orientation of the magnetization field. Hence, this contribution has no role in the minimization

of the total Gibb's free energy. This is also clear from the LLG equation. Indeed, the magnetization dynamics only depend on the torque $\propto \mathbf{m} \times \mathbf{H}_{eff}$, thus a component of the effective field (anti-)parallel with the local magnetization has no influence on the magnetization dynamics.

From expression (6.30), it is clear that $\mathcal{O}(N)$ computations are required to evaluate $\mathbf{H}_{ms}$ in one single FD cell. Hence, the classical computation of $\mathbf{H}_{ms}$ in all N FD cells scales $\mathcal{O}(N^2)$. Moreover, in a classical $\mathbf{H}_{ms}$ evaluation scheme $\mathcal{O}(N^2)$ numbers have to be used to store the mutual interactions between the FD cells.

The comparison of the computational burden and the memory requirements needed to evaluate the different effective field terms shows that almost all computational effort goes to the evaluation of the magnetostatic field. In Chapter 7, $\mathcal{O}(N \log N)$ evaluation schemes that exploit the convolution structure of (6.30) by using Fast Fourier Transforms are presented to evaluate $\mathbf{H}_{ms}$. Chapter 8 presents an $\mathcal{O}(N)$ scheme based on the reformulation of the kernel $1/|\mathbf{r} - \mathbf{r}'|$ by adopting the Fast Multipole Method.

6.3. Semi-analytical time stepping schemes for the LLG equation

The availability of an highly efficient time stepping algorithm is indispensable in the development of a numerical micromagnetic scheme intended to simulate magnetization processes in (micromagnetically) large objects. The best time efficiency is achieved when the time stepping scheme enables the use of large time steps with a minimum of effective field term evaluations.

6.3.1 Introduction

In Chapter 2 it is found that the Landau-Lifshitz-Gilbert equation

$$\frac{\partial \mathbf{m}}{\partial t} = \frac{\gamma_G}{1+\alpha^2}\mathbf{m} \times \mathbf{H}_{eff} + \frac{\alpha\gamma_G}{1+\alpha^2}\mathbf{m} \times \Big(\mathbf{m} \times \mathbf{H}_{eff}\Big). \tag{6.31}$$

describes the temporal evolution of the magnetization field $\mathbf{m}(\mathbf{r}, t)$. In Section 2.4.3 it is outlined that this equation has three main properties: (i) preservation of the magnetization field amplitude, (ii) the decrease in total Gibbs free energy under a constant applied field and (iii) conservation of the Gibbs free energy in the case of zero damping. An optimal time stepping scheme used to discretize (6.31) meets these properties, combined with a good stability of the method, i.e. a good convergence. Different types of time stepping schemes for the LLG equation are developed [62].

First there are implicit methods as e.g. implicit Euler. Generally, these methods have a good stability, but do not preserve the magnetization amplitude or the energy when $\alpha = 0$. Furthermore, the use of implicit time stepping

schemes require the solution of a large system of coupled non-linear equations at each time step, leading to very high simulation times. To alleviate this problem, semi-implicit schemes are constructed as in [63] that circumvent the solution of the system of coupled equations.

A lot of attention [64,65,66,67] has been paid to *geometrical integrators* that naturally preserve the properties of the LLG equation by exploiting symmetries, invariant quantities, hamiltonian structures etc. These are for instance based on Lie-group methods and Cayley transforms. Here, the local magnetization field vector can only vary on the unit sphere. The methods preserve the magnetization amplitude, but not all of them meet the two other properties.

In [62], a geometrical integration method based on the mid point rule is presented that incorporates all three properties of the LLG equation and is unconditionally stable. Being an implicit method, the system of non-linear equations is solved using a quasi-Newton iterative technique. This limits the applicability of the method for the large systems we aim at.

Second, there are explicit methods. When applying explicit 'off-the-shelf' methods as the Euler method, Heun method or Runge Kutta methods, there is no need to solve the large system of coupled equations, but the properties of the LLG equation are not incorporated. Applying these methods requires for instance a renormalization of the $\mathbf{m}(\mathbf{r},t)$ every time step.

During the PhD work two explicit time stepping schemes are developed that meet the three properties of the LLG equation and have a good stability. Since no coupled system of non-linear equations has to be solved, the two methods are very time and memory efficient. The time stepping schemes itself scale $\mathcal{O}(N)$ so their computational cost is limited compared to the evaluation of the magnetostatic field. Moreover, due to their stability, large time steps can be taken which limits the number of effective field evaluations. The outstanding properties of the presented time stepping schemes are at the origin of the excellent efficiency of the developed micromagnetic numerical scheme.

6.3.2 Semi-analytical time stepping schemes

Forward semi-analytical time stepping scheme

In the forward semi-analytical time stepping scheme, the magnetization dynamics is evaluated analytically at $t_i + \delta t$ by introducing in each FD cell a local (u,v,w) coordinate system with the u-axis parallel to $\mathbf{H}_{eff}(t_i)$. The LLG-equation (6.31) can be solved analytically in this coordinate system when $\mathbf{H}_{eff}(t)$ is kept constant during the time step

$$\mathbf{H}_{eff}(t) = H_{eff}(t_i)\mathbf{e}_u \quad t_i \leq t \leq t_i + \delta t. \tag{6.32}$$

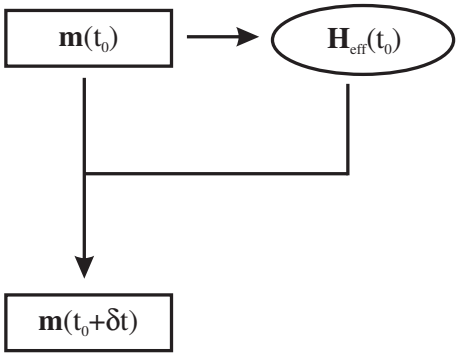

Figure 6.3: Flow chart of the forward semi-analytical time stepping scheme. Each time step, one effective field evaluation is needed.

During the time step $\mathbf{m}$ evolves from $\mathbf{m}(t_i) = u_i\mathbf{e}_u + v_i\mathbf{e}_v + w_i\mathbf{e}_w$ to $\mathbf{m}(t_i + \delta t) = u_{i+1}\mathbf{e}_u + v_{i+1}\mathbf{e}_v + w_{i+1}\mathbf{e}_w$ with

$$\begin{aligned} u_{i+1} &= \frac{e^{q\alpha\delta t}(1+u_i) - e^{-q\alpha\delta t}(1-u_i)}{e^{q\alpha\delta t}(1+u_i) + e^{-q\alpha\delta t}(1-u_i)} \\ v_{i+1} &= 2\frac{v_i\cos(q\delta t) - w_i\sin(q\delta t)}{e^{q\alpha\delta t}(1+u_i) + e^{-q\alpha\delta t}(1-u_i)} \\ w_{i+1} &= 2\frac{v_i\sin(q\delta t) + w_i\cos(q\delta t)}{e^{q\alpha\delta t}(1+u_i) + e^{-q\alpha\delta t}(1-u_i)} \end{aligned} \tag{6.33}$$

and with $q = \gamma_G H_{eff}(t_i)/(1+\alpha^2)$. In this forward semi-analytical time stepping scheme, the effective field (2.53) has to be evaluated once every time step. An overview of the scheme is shown in Fig. 6.3. The computations (6.33) itself scale as $\mathcal{O}(N)$ and do not require extra memory space.

predictor-corrector semi-analytical time stepping scheme

The second developed time stepping scheme is a predictor-corrector (p/c) extension of the first scheme. The predictor part obtains a preliminary estimate $\hat{\mathbf{m}}(t_i + \delta t)$ of the magnetization field, calculated with the forward semi-analytical method. Based on this estimated value $\hat{\mathbf{m}}(t_i + \delta t)$ the estimated effective field $\hat{\mathbf{H}}_{eff}(t_i + \delta t)$ is computed. In the corrector part, the actual value $\mathbf{m}(t_i + \delta t)$ is obtained by again applying the expressions (6.33), but using an intermediate effective field $\mathbf{H}_{eff}(t_i + \delta t/2)$ instead of $\mathbf{H}_{eff}(t_i)$ with

$$\mathbf{H}_{eff}(t_i + \delta t/2) = \frac{1}{2}\left[\mathbf{H}_{eff}(t_i) + \hat{\mathbf{H}}_{eff}(t_i + \delta t)\right]. \tag{6.34}$$

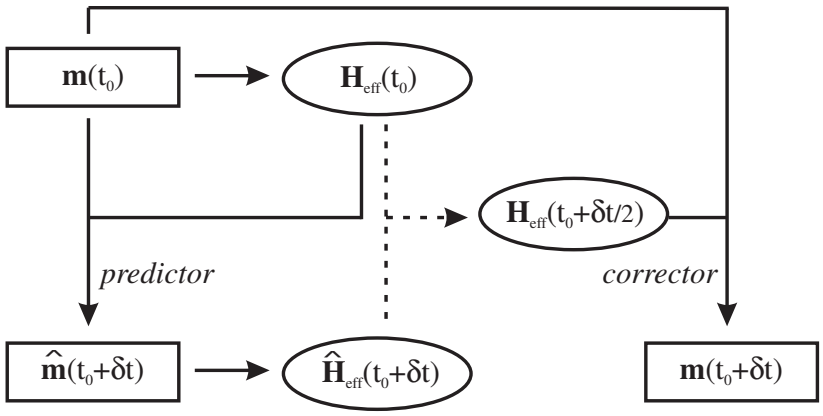

Figure 6.4: Flow chart of the predictor-corrector time stepping scheme. Each time step, two effective field evaluations are needed.

Hence, in this p/c semi-analytical time stepping scheme, the effective field (2.53) has to be evaluated twice every time step. Figure 6.4 shows an overview of this time stepping scheme. This scheme needs an extra $6N$ numbers memory space to store the predictor values of the magnetization field $\hat{\mathbf{m}}(t_i + \delta t)$ and the effective field $\hat{\mathbf{H}}_{eff}(t_i + \delta t)$.

6.3.3 Performance study

When studying the performance of the developed time stepping schemes, special attention is devoted to the time efficiency and the accuracy of the time stepping schemes. Therefore, the influence of the different model parameters is studied. Furthermore, the preservation of the properties of the LLG equation is demonstrated. This study is based on the simulation of the magnetization process between two representative micromagnetic equilibrium states. The tests are performed on a cubic iron monocrystal divided in $64 \times 64 \times 64$ FD cells. Cells of different sizes are tested. The orientation of the crystallographic easy axes is defined by the Euler angles $\phi = 1.0$, $\theta = 0.5$ and $\psi = 0.25$. The initial configuration is a saturated state in the y-direction. In the test, the applied field is altered to

$$\mathbf{H}_a = -2.010^5\, Am^{-1}\mathbf{e}_x + 1.010^5\, Am^{-1}\mathbf{e}_z \tag{6.35}$$

In this study, we are only interested in the equilibrium state and not in the details of the dynamics to approach this state. Hence, the equilibrium states reached in the experiments are compared and not the dynamics itself. The

correctness of the description of the dynamic magnetization process towards equilibrium is evaluated in Section 6.4.

In order to evaluate the two proposed semi-analytical time stepping procedures, comparison is made with three other explicit integration schemes: the forward Euler scheme, the predictor-corrector Heun scheme and a fourth order Runge-Kutta integration scheme [68]. These schemes are, just like the proposed semi-analytical methods, single-step methods: they only use the information at the beginning of the time step to compute the magnetization field values at a successive time point. Depending on the integration scheme, the slope on the magnetization curve $\mathrm{d}\mathbf{m}/\mathrm{d}t$ has to be evaluated several times. This slope is given by the LLG-equation (6.31), thus for each computation of the slope $\mathrm{d}\mathbf{m}/\mathrm{d}t$ the effective field has to be evaluated once. In the Euler scheme the slope and thus $\mathbf{H}_{eff}$ has to be evaluated once per time step, while in Heuns scheme twice. Hence the computational burden in both schemes is similar with the forward semi-analytical time stepping scheme and the predictor-corrector semi-analytical time stepping scheme respectively. Further, comparison is made with a fourth order Runge-Kutta integration scheme. This scheme needs four effective field evaluations during each time step and is seen as a robust reference scheme.

Variation of the time step length δt

In a first series of numerical experiments the convergence properties of the different schemes are investigated. Therefore, the length of the time steps δt is varied, while keeping the damping constant and the discretization size fixed: $\alpha = 1.0$ and $\Delta = 8\,\mathrm{nm}$. All simulations are compared with the Runge-Kutta scheme with $\delta t = 510^{-15}\,\mathrm{s}$ as a reference. The upper part of Fig. 6.5 shows that for all time stepping schemes the number of time steps to obtain equilibrium is inversely proportional to the used time step δt and is similar for all schemes. The calculation time however, varies with the number of effective field evaluations, see second part of Fig. 6.5. Hence, for a given time step δt, the forward semi-analytical and the forward Euler at the one hand and the p/c semi-analytical and the Heun scheme on the other hand give rise to similar calculation times. The convergence properties of the schemes differ however. The first part of Fig. 6.5 shows that the forward Euler and Heun scheme only converge for time steps $\delta t < 3\,\mathrm{ps}$, while the forward semi-analytical scheme and the p/c semi-analytical scheme start to diverge from $\delta t = 4\,\mathrm{ps}$ and $\delta t = 7\,\mathrm{ps}$ respectively.

The last part of Fig. 6.5 shows the precision of the time stepping schemes, defined as the mean deviation of the magnetization field $\mathbf{m}^i$ in FD cells i ($i = 1 \ldots N$) from their corresponding value $\mathbf{m}^i_{ref}$ in the reference simulation,

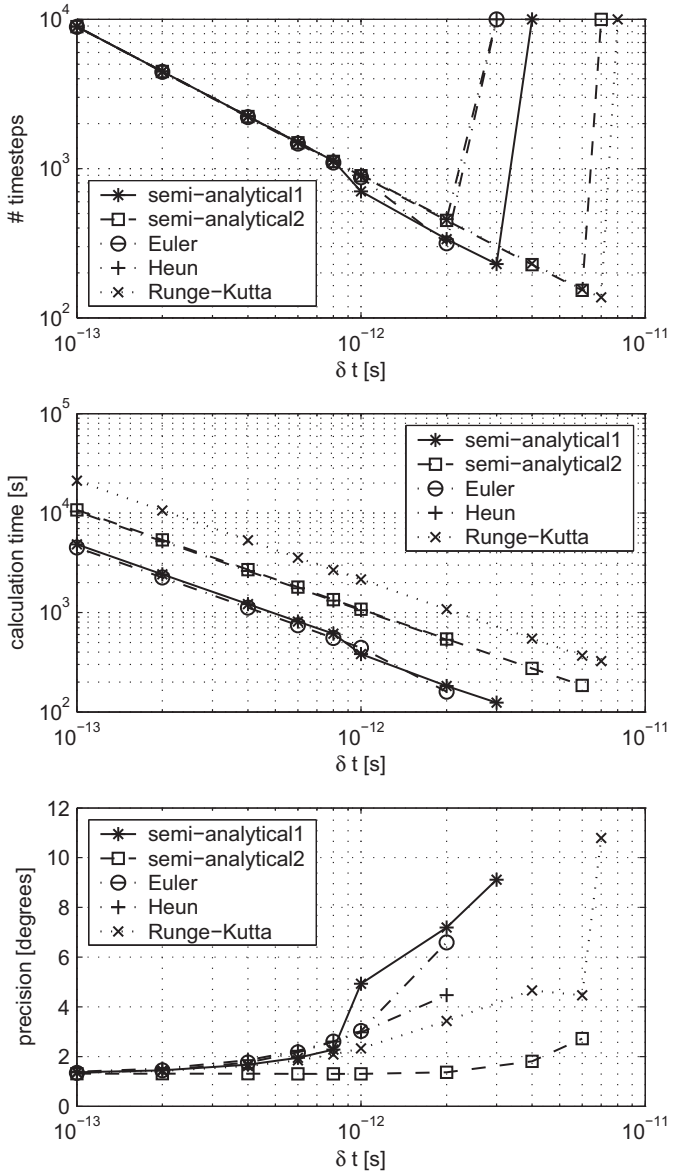

Figure 6.5: Number of time steps needed to reach equilibrium (top), calculation time needed to reach equilibrium (middle) and precision (bottom) versus used time step δt, with discretization size $\Delta = 8\,\text{nm}$ and damping constant $\alpha = 1.0$. "semi-analytical1" is the forward semi-analytical scheme and "semi-analytical2" is the p/c semi-analytical scheme. The out-of-place points indicate divergence.

expressed as the angle between the dipoles

$$\text{precision} = 2\arcsin\left(\frac{1}{N}\sum_{i=1}^{N}\frac{|\mathbf{m}^i - \mathbf{m}^i_{ref}|}{2}\right). \tag{6.36}$$

For larger δt all time stepping schemes have a deteriorating precision. For large δt, the forward semi-analytical time stepping scheme has the worst precision, the p/c semi-analytical scheme on the other hand has a precision better then the fourth order Runge-Kutta scheme.

In particular, the stability of the p/c scheme is remarkable since it has excellent convergence properties combined with a very high precision. It has stability properties similar to the fourth order Runge-Kutta scheme but needs only half as much effective field evaluations and is thus twice as fast. The stability of the semi-analytical time stepping schemes results from the higher order extrapolation of the local magnetization trajectory. Indeed, the use of the analytical expressions (6.33) guarantee an extrapolation which is better than a first order (cf. forward Euler scheme) or a second order (cf. Heun scheme) approximation.

Variation of the discretization size Δ

Based on the expressions (6.33) one can see that smaller time steps will be required for decreasing discretization size Δ. Indeed, when discretized, $\mathbf{H}_{exch}$ and thus $\mathbf{H}_{eff}$ is proportional to A/Δ^2, see (6.2). From (6.33) it is clear that, in order to have a good description of the precession movement, the quantity $q\delta t$ should be smaller than a period 2π. Since

$$q\delta t \propto H_{eff}\delta t \propto \frac{A\delta t}{\Delta^2}, \tag{6.37}$$

a small discretization size Δ requires the use of a small time step δt.

The discussion in the above section can be repeated for other discretization sizes Δ. In each scheme, an optimal time efficiency is obtained when the time step δt is as large as possible combined with an acceptable precision. As mentioned before, this optimal length of the time step δt varies with the used spatial discretization which is shown in the first part of Fig. 6.6: when Δ is reduced, a smaller time step δt has to be used.

The calculation time, needed to reach equilibrium when using these optimal time steps δt, is shown in the second part of Fig. 6.6. For smaller discretization sizes, the time step δt has to be decreased which results in larger simulation times. Both semi-analytical time stepping schemes have a very good time efficiency, particularly when a larger spatial discretization is used. The accuracy of the developed time stepping scheme will be investigated in more detail in the next sections.

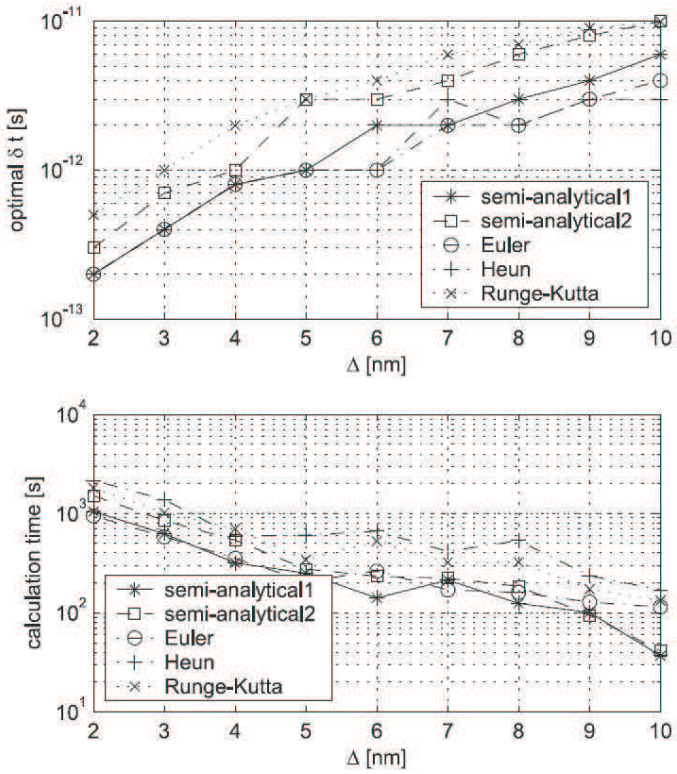

Figure 6.6: Optimal time step δt (top), calculation time (middle) and precision when an optimal time step is used (bottom) versus discretization size Δ. "semi-analytical1" is the forward semi-analytical scheme and "semi-analytical2" is the p/c semi-analytical scheme.

One can ask if a discretization size up to $\Delta = 10\,\text{nm}$ is physical since this discretization is larger then the exchange length l_{exch} (here 2.8 nm) which is known to be the lower limit on which magnetization non-uniformities are possible in soft magnetic materials, see Section 2.3.2. Yet another characteristic length in magnetic materials is given by the domain wall thickness which is, in the case of pure iron, about 70 nm. Hence, when a discretization size up to 10 nm is used, the thickness of the domain wall corresponds to several FD cells. In Section 9.2 we will go more into detail on this subject.

Variation of the damping constant α

Large damping constants make the magnetization field relax fast to the local effective field and have a stabilizing effect on the micromagnetic system. This makes the use of larger time steps possible. The value of α influences the path

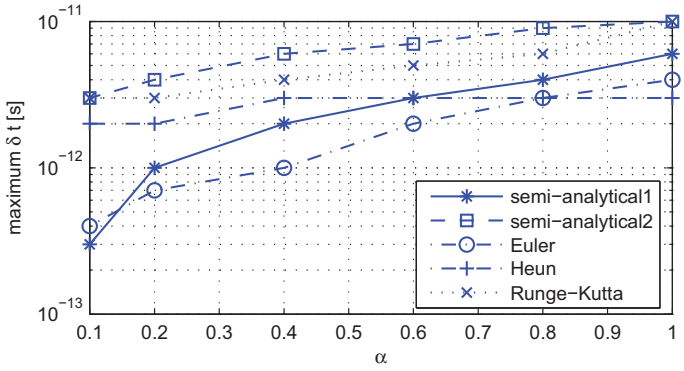

Figure 6.7: Maximum δt for which converge is reached for varying damping constant α. "semi-analytical1" is the forward semi-analytical scheme and "semi-analytical2" is the p/c semi-analytical scheme.

the system traverses towards equilibrium, but not the equilibrium state itself. Indeed, the damping constant has no influence on the energy landscape, but due to the faster damping the trajectory to the equilibrium point contains less oscillations. Hence, in simulations where one is only interested in the equilibrium states and not in the transition between the equilibrium states, α can be chosen to have an optimal time efficiency. Here, a large damping constant is considered as a numerical damping superimposed on the physical damping. Figure 6.7 shows the optimal time step δt for the considered time stepping schemes. It shows that for smaller damping constants α, smaller time steps δt have to be taken which results in larger simulation times. For $\alpha < 1$, the p/c semi-analytical time stepping scheme shows even better convergence than the fourth order Runge-Kutta scheme. A damping factor $\alpha = 1.0$ is the most time efficient.

Porter et al. started from the semi-analytical time stepping scheme to present a 'precession axis modified' semi-analytical time stepping scheme [69] which enables the use of yet larger time steps for a given damping constant α. In their analysis, they add a scalar multiple of $\mathbf{m}$ to the effective field: $\mathbf{H}'_{eff} = \mathbf{H}_{eff} + \lambda\mathbf{m}$. Since the dynamics of the magnetization field only depends on the torque $\propto \mathbf{m} \times \mathbf{H}_{eff}$ (see LLG equation) this does not effect the evolution of the magnetization. With a good choice of λ however, larger time steps can be taken. This can be understood by inspecting the expressions (6.33). The addition of $\lambda\mathbf{m}$ increases the amplitude of the effective field and consequently the quantity $\alpha q \delta t$, which determines the damping in expression (6.33). Hence, the addition of $\lambda\mathbf{m}$ to the effective field increases the damping in the micromagnetic system and is thus equivalent with a choice of a larger damping constant α.

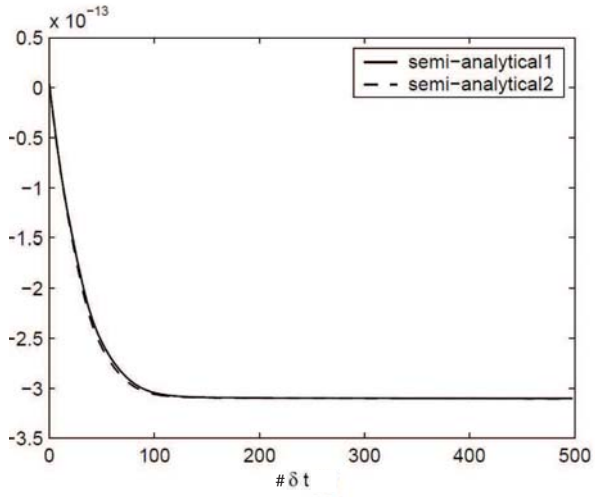

Figure 6.8: The total energy ϕ_{tot} during the evolution towards equilibrium. "semi-analytical1" denotes the forward semi-analytical time stepping scheme, while "semi-analytical2" denotes the predictor-corrector semi-analytical scheme.

Preservation of the properties of the LLG equation

- The semi-analytical time stepping schemes preserve the magnetization amplitude. Indeed, the expressions (6.33) do not influence the magnetization amplitude, with notations of (6.33):

$$u_{i+1}^2 + v_{i+1}^2 + w_{i+1}^2 = 1. \tag{6.38}$$

- In Fig. 6.8, the total energy ϕ_{tot} is shown during the evolution towards equilibrium using the two presented time stepping schemes. For the two schemes, a continuous decrease in the total free energy is shown.
- The Gibbs free energy is conserved in the case of zero damping. Indeed, with $\alpha = 0$, the expressions (6.33) reduce to

$$\begin{aligned} u_{i+1} &= u_i \\ v_{i+1} &= v_i \cos(q\delta t) - w_i \sin(q\delta t) \\ w_{i+1} &= v_i \sin(q\delta t) + w_i \cos(q\delta t). \end{aligned} \tag{6.39}$$

  It is clear that these expressions describe a precessional movement of the magnetization around the local effective field without damping. Indeed, the projection of the magnetization field on the local effective field does not change in time: $u_{i+1} = u_i$, hence no energy is dissipated.

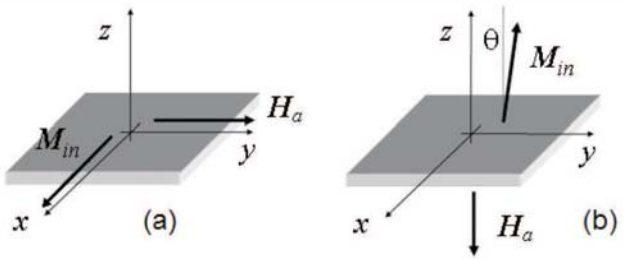

Figure 6.9: Geometry of the studied configurations: (a) Precessional switching and (b) damping switching

6.4. Comparison with other micromagnetic schemes

In a collaboration with the 'Istituto Nazionale di Ricerca Metrologica' (INRIM, Turin, Italy) the presented time stepping scheme for the LLG equation is validated extensively [70,71] by comparing simulation results obtained with our FD code, with the Finite Element code designed at INRIM [72,70,71] and with the NIST/OOMF (National Institute of Standards and Technology / Object Oriented Micromagnetic Framework) code [73] developed at NIST, US.

In the approach adopted at INRIM, the spatial discretization of the LLG equation is handled by a finite element method (FEM), employing tetrahedral elements and edge vector shape functions for the description of the magnetization field. The time evolution is treated with a FD scheme based on the midpoint rule [62]. The magnetostatic field is obtained by solving the Poisson equation with a hybrid finite element/boundary element method (FEM/BEM) to handle the open boundary problem.

The NIST/OOMF scheme is a 2.5 dimensional FD code. The considered geometries are thin films, enabling a FD discretization in only two dimensions. The magnetization field however keeps its full 3D character. The magnetostatic field is computed using fast Fourier transforms.

In the considered simulations, switching processes in various geometries are studied. Here, the magnetization states in the non-equilibrium points is of interest so the damping constant α cannot be chosen as a function of time efficiency ($\alpha \ll 1$). In this 'classical' micromagnetic research domain, the discretization size should also be similar to or smaller than the exchange length (see Section 9.2).

6.4.1 Comparison of switching processes in thin films

The time stepping procedures are compared by analyzing precessional and damping switching in square thin films ($200\,\text{nm} \times 200\,\text{nm} \times 5\,\text{nm}$) with uniaxial

Table 6.2: Time step and discretization size to reach convergence

Analyzed case	δt (ps)		Δ (nm)	
	M1	M2	M1	M2
P1 ($K_u = 0$, $l_{exch} \sim 5\,\text{nm}$)	0.09	0.075	2.5	5
P2 ($K_u = 0$, $l_{exch} \sim 7.5\,\text{nm}$)	0.03	0.025	2.5	5.5
P3 ($K_u = 0$, $l_{exch} \sim 10\,\text{nm}$)	0.02	0.02	2.5	7.5
P4 ($K_u = 10\,\text{kJ/m}^3$, $l_{exch} \sim 7.5\,\text{nm}$)	0.03	0.025	2.5	5.5
P5 ($K_u = 40\,\text{kJ/m}^3$, $l_{exch} \sim 7.5\,\text{nm}$)	0.03	0.025	2.5	5.5
D1 ($K_u = 0$, $l_{exch} \sim 7.5\,\text{nm}$)	0.03	0.025	2.5	5.5

anisotropy. The schemes of the studied configurations are depicted in Fig. 6.9. The magnetization is initially uniform with an amplitude $M_s = 800\,\text{kA/m}$. The damping coefficient α is equal to 0.02, while the (uniaxial) anisotropy constant K_u and the exchange length l_{exch} are reported in Table 6.2, together with the time step δt and the discretization size Δ required to reach convergence. In our FD scheme, the choice of Δ is influenced by the film thickness, since a cubic cell discretization has to be introduced ($\Delta = 2.5\,\text{nm}$ for all the analyzed cases). On the contrary, in the FEM method developed at INRIM, the 3-D mesh can be unstructured and its refinement can be varied, depending on the material exchange length l_{exch} and on the demagnetizing effects. To limit the number of unknowns only a spatial subdivision is imposed along the film thickness, thus, for the FEM scheme, the values of Δ reported in Table 6.2 refer to the discretization in the (x, y)-plane. In the figures and tables, the FD scheme developed in this PhD work is denoted by M1, while the FEM scheme developed at INRIM is denoted by M2.

The accuracy of the two methods is verified by comparison with the NIST/OOMMF code, which provides the reference simulation results. In the precessional switching cases (P1 to P5), the film is subjected to a $40\,\text{kA/m}$ external field applied along the y-direction, and an initial magnetization along the x-axis.

Table 6.2 shows that when stronger exchange phenomena are considered (i.e. for increasing exchange length), smaller time steps have to be used. A sufficiently small time step has to be adopted in both our FD scheme and in the FEM scheme in order to converge with the results of the NIST/OOMF code as well evidenced in Fig. 6.10, which reports the time evolutions of the average magnetization components when an exchange length $\sim 5\,\text{nm}$ (case P1) and $\sim 7.5\,\text{nm}$ (case P2) is considered. With an appropriate choice of the time step and the discretization size Δ, the methods are in excellent agreement with each other and with the simulation results provided by the NIST/OOMF code, also in the prediction of the local magnetization during the switching process, see Fig. 6.11.

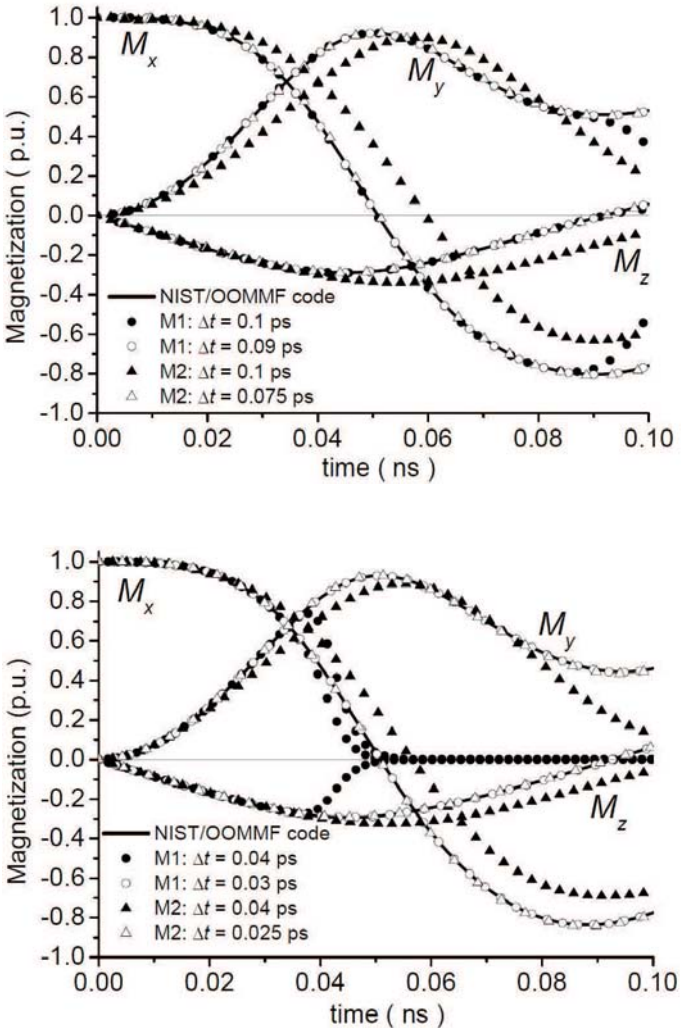

Figure 6.10: Time evolution of the average magnetization components, evidencing the role of the time step choice for case P1 (top) and case P2 (bottom). The used discretization size is reported in Table 6.2.

Figure 6.12 reports the time evolution of the average magnetization components when an anisotropy constant K_u of $10\,\mathrm{kJ/m^3}$ and of $40\,\mathrm{kJ/m^3}$ is considered. The anisotropy axis is parallel to the x-axis. The presence of anisotropy effects slows down the switching processes until a limit value of K_u, over which the magnetization reversal does not take place. In the FEM scheme, the results are computed with a discretization size in the (x,y)-plane

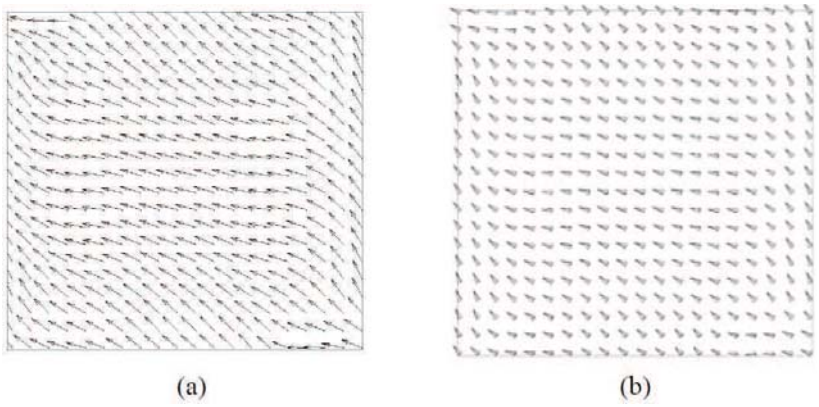

Figure 6.11: Spatial distribution of the magnetization field, computed for case P1 at time instant $t = 0.09\,\text{ns}$ with our FD scheme (a) and the FEM scheme (b).

comparable to the exchange length. This leads to a small discrepancy in comparison with the solution obtained with our FD scheme, which is in perfect agreement with the results of the NIST/OOMMF code. As shown in Table 6.2, the addition of the anisotropy contribute does not influence the choice of δt and Δ to reach convergence.

In the damping switching case D1, the magnetization reversal is obtained by applying a $1000\,\text{kA/m}$ external field almost antiparallel to the initial magnetization state. To start reversal processes, the initial magnetization is assumed to make an angle of 10 degrees with the z-axis. As an example, Fig. 6.13 reports the time evolution of the magnetization components along the z-direction and in the (x, y)-plane, with an exchange length of $\sim 7.5\,\text{nm}$. The damping switching processes, which are sensibly slower than the precessional ones, are affected by the oscillating behavior of the magnetization components along the x and y-axes. Also in this critical case the appropriate choice of δt and Δ leads to a very satisfactory agreement between the two procedures and the NIST/OOMF code.

6.4.2 Comparison of magnetization processes in 3D geometries

The NIST/OOMF code is only applicable for 2D geometries, thus comparison can only be made with the FEM code developed at INRIM. Since the simulation results where in accordance for the considered 2D geometries, also an agreement in the simulation results for 3D sample geometries is expected. This is investigated for different geometries and material parameters. Further, the influence of the material properties and the spatial discretization on the time step ensuring convergence is studied.

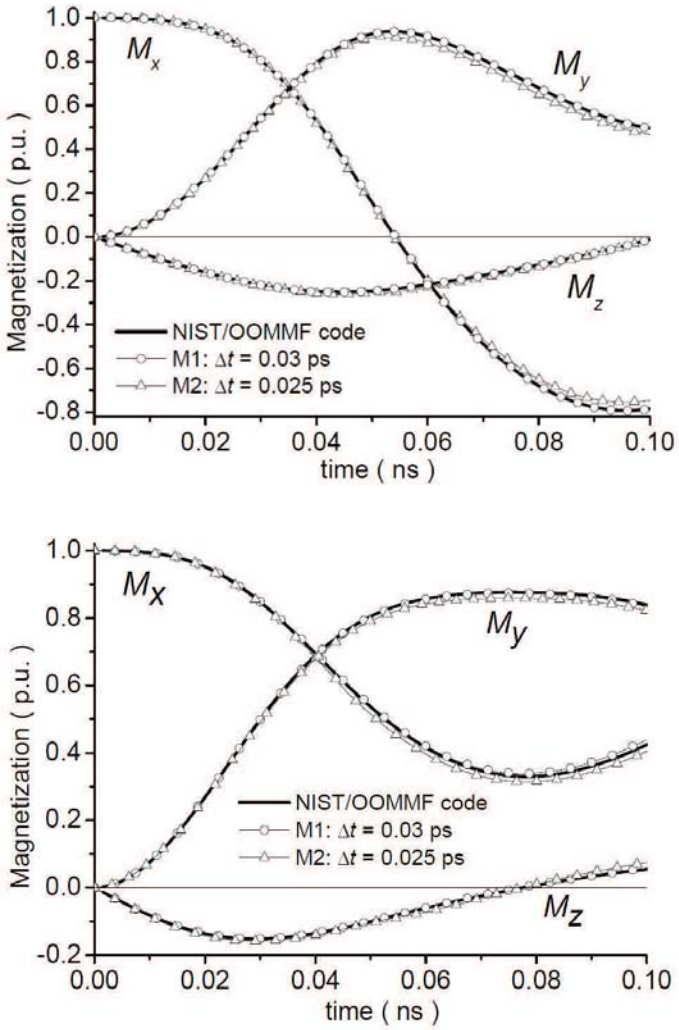

Figure 6.12: Time evolution of the average magnetization components for case P4 (top) and case P5 (bottom). The used discretization size is reported in Table 6.2.

In the reference case, the relaxation process for a cube with edges of 20 nm, initially saturated along the z-axis ($M_s = 1400\,\mathrm{kA/m}$) is considered with $A = 35\,\mathrm{pJ/m}$ and $\alpha = 0.02$. The uniaxial anisotropy is parallel to the z-axis with $K_u = 500\,\mathrm{kJ/m^3}$. An external field with amplitude of $1.1\,M_s$, oriented along the direction $(\mathbf{e}_x - \mathbf{e}_z)$, is applied. Therefore, a reference simulation is considered describing the relaxation process for a cube with edges of 20 nm,

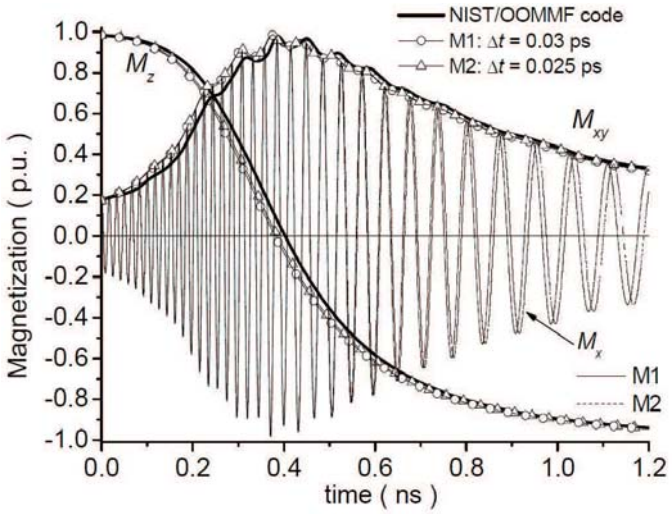

Figure 6.13: Time evolution of the average magnetization components for case D1. To evidence the oscillating behavior of the magnetization components in the (x,y)-plane, also the transient evolution of M_x, computed with our FD scheme and the FEM scheme is shown. The used discretization size is reported in Table 6.2.

initially saturated along the z-axis ($M_s = 14000\,\mathrm{kA/m}$) with exchange stiffness $A = 35\,\mathrm{pJ/m}$ and $\alpha = 0.02$.

The reference simulation is performed using FD cells with edges of 2.5 nm and FEM tetrahedrons with sides of $\sim 2.5\,\mathrm{nm}$. In this case the spatial discretization is not constrained by the exchange length (about 5.3 nm), but by the sample dimensions. Indeed, a sufficient number of FD cells or tetrahedrons should be employed to accurately compute the magnetostatic field. As evidenced in Fig. 6.14, which reports the time evolution of the average magnetization components, the agreement between the presented methods is very good.

To establish the influence of the discretization size Δ on the maximum time step, simulations with smaller values of Δ are performed. As shown in Table 6.3, in both schemes the decrease of Δ leads to the obligatory use of smaller time steps δt to avoid numerical instabilities in the time evolution.

The same reversal process for a sample identical to the reference case except for the exchange constant ($A = 15\,\mathrm{pJ/m}$) is computed. The dynamics of the average magnetization components is shown in Fig. 6.15, evidencing a good agreement between the two methods. Although the magnetization phenomena are very similar in this case compared with the reference (see Fig. 6.14), a larger time step can be used due to the smaller value of the exchange constant (see Table 6.3).

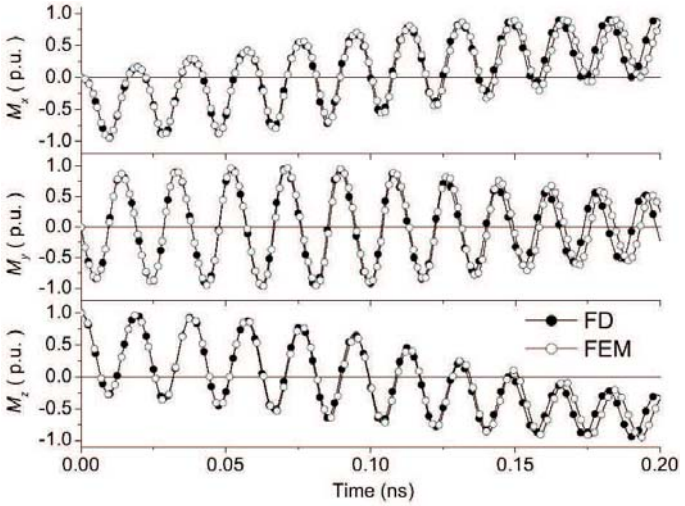

Figure 6.14: Time evolution of the average magnetization components for the reference case.

Table 6.3: Influence of various parameters on the maximum time step. Larger time steps lead to instabilities.

Studied parameter	value	δt [fs] FD	FEM2
Reference	—	40	17
Δ	2 nm	20	14
Δ	1.25 nm	9.0	5.0
A	15 pJ/m	100	50
α	0.1	60	20

To analyze the influence of the damping constant on the maximum time step, α is increased up to 0.1. The time evolution of the average magnetization components is shown in Fig. 6.16. Due to the strong damping, the system evolves to an equilibrium state in about 0.12 ns, while in both previous cases with $\alpha = 0.02$, the equilibrium state is reached only after about 0.8 ns. The stabilizing effect of the large damping constant makes the use of larger time steps possible, see Table 6.3, and guarantees a perfect agreement between the two methods.

The sample dimension has a strong influence on the magnetization phenomena. To show this, simulations are performed for a sample with the material properties of the reference case, but with dimensions of 60 nm. In the 20 nm sized samples described above, the magnetization stays quasi uniform during the entire reversal process. This is not the case for the 60 nm sample. Since

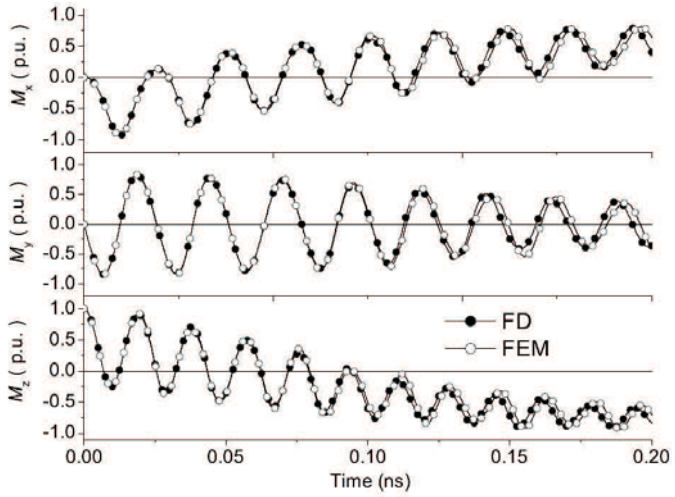

Figure 6.15: Time evolution of the average magnetization components. Compared with the reference case, the exchange constant is smaller: $A = 15\,\mathrm{pJ/m}$.

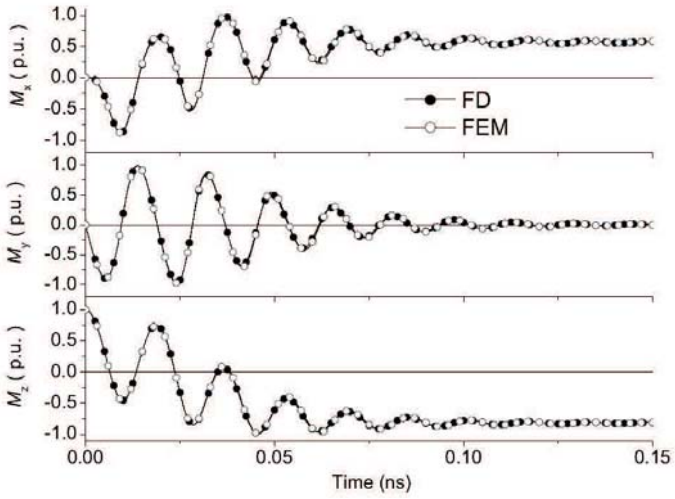

Figure 6.16: Time evolution of the average magnetization components. Compared to the reference case, the damping constant is larger: $\alpha = 0.1$.

non-uniform magnetization states are formed, a sufficiently small discretization mesh has to be used. Simulations are performed with our FD scheme using different discretization sizes Δ. The results converge when diminishing Δ up to 1.5 nm. This small discretization size is needed to properly reconstruct

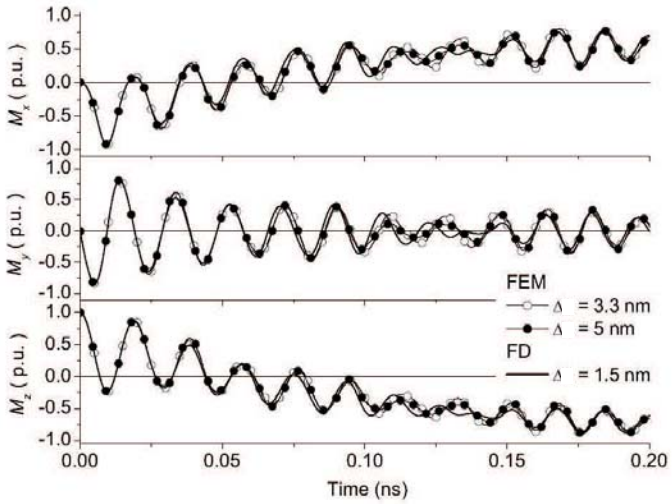

Figure 6.17: Time evolution of the average magnetization components for a 60 nm cube with material parameters identical to the reference case. Curves are simulated using the FEM scheme with different discretization sizes. The curves simulated with the FD scheme with $\Delta = 1.5\,\text{nm}$ are added as a reference.

the local variations of the magnetization. The relaxation process is also simulated with the FEM scheme diminishing the discretization size. However, since the use of the FEM/BEM formulation for the magnetostatic field leads to fully-populated matrices, CPU time and memory requirements restrict the minimum applicable Δ to 3.3 nm. The curves computed with the FEM scheme tend to converge to the curves simulated with the FD scheme ($\Delta = 1.5\,\text{nm}$), suggesting the correctness of the approaches. The relaxation of the average magnetization components is shown in Fig. 6.17. The magnetization states in the plane $y = 0$ on time point $t = 65\,\text{ps}$ for the reference case and the 60 nm particle are shown in Fig. 6.18.

Finally, a precessional switching process ($\alpha = 0$) is described in a spherical sample with a radius of 50 nm. Initially, the particle is saturated ($M_s = 1400\,\text{kA/m}$) along the x-axis, which coincides with the uniaxial anisotropy axis ($K_u = 500\,\text{kJ/m}^3$). A field with amplitude 400 kA/m is applied along the positive y-axis. The exchange constant is 35 pJ/m. Since the magnetization stays uniform during the reversal process, the dynamical behavior can also be calculated analytically [5]. The time evolution of the average magnetic components is shown in Fig. 6.19. In the FEM simulation tetrahedrons with edges of $\sim 5\,\text{nm}$ and a time step of 75 fs are used. The resulting curves align perfectly with the analytical solution. This is not the case for our FD simulation with the same discretization size. The cubical discretization of the curved boundaries

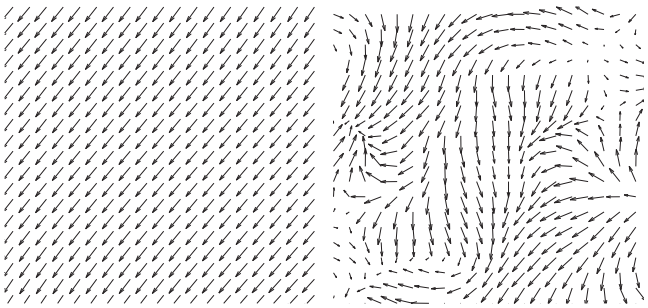

Figure 6.18: Magnetization states in the plane $y = 0$ at time instant $t = 65\,\text{ps}$ for the reference case with 20 nm edges (left) and for the case with 60 nm edges (right).

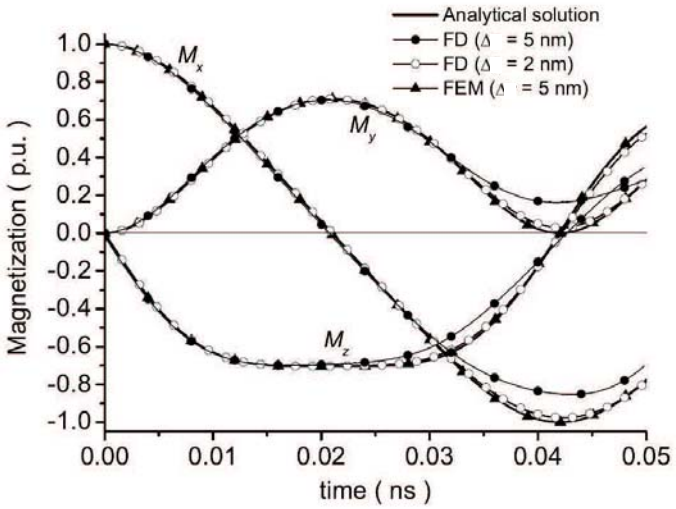

Figure 6.19: Time evolution of the average magnetization components during the precessional switching in a sphere.

introduce some discrepancies. The results gradually improve when smaller FD cells are used. When a discretization of 2 nm is used, the agreement with the analytical solution is very good (Fig. 6.19). However, the obligatory use of small FD cells results in a larger problem size and smaller time steps: $\delta t = 10\,\text{fs}$ compared with $\delta t = 200\,\text{fs}$ when $\Delta = 5\,\text{nm}$. In [74] methods are presented to correct the errors introduced by the cubical discretization of curved boundaries.

6.4.3 Conclusion

When comparing the simulation results for the different magnetization phenomena, one concludes that the correctness of the developed micromagnetic scheme is guaranteed. In comparison with the FEM scheme, the excellent stability, the time and memory efficiency of the predictor-corrector semi-analytical time stepping scheme and of the magnetostatic field evaluation techniques (described in Chapter 7) are striking. Due to the cubical discretization of curved boundaries, the developed FD scheme has however difficulties handling complex geometrical structures. In this case, the use of smaller discretization cells is required.

Since the FEM scheme uses a semi-implicit time stepping algorithm, it does not preserve the magnetization amplitude which limits the time step length. Further, the FEM/BEM approach leads to a worse time and memory efficiency due to the LU factorization of the fully populated magnetostatic problem matrix. This makes the FEM scheme only suited for the simulation of small micromagnetic problems. The method is however able to describe curved boundaries.

6.5. Micromagnetic hysteresis scheme

In the former sections we presented an accurate micromagnetic scheme that enables the simulation of magnetization processes in large structures during the transition from one equilibrium state to another. When this scheme is used successively to determine equilibrium states for varying applied fields, one can come to the simulation of hysteresis loops. To simulate quasi-static hysteresis loops, a second time discretization level is introduced on which the applied field varies. This macroscopic time scale is much larger than the time scale of the LLG equation guaranteeing the intended rate independent hysteresis description (see Section 4.3.4).

6.5.1 Discretization of the applied field

The quasi-static applied magnetic field $\mathbf{H}_a$ is discretized on a macroscopic timescale ΔT of the order of ms and approximated with a piecewise constant time function. It is assumed that at the moment the applied field $\mathbf{H}_a$ jumps from a constant value to the next one, the material is in static micromagnetic equilibrium. This assumption is motivated by the different time scales involved. Indeed, the magnetization dynamics described by the LLG-equation (6.31) is discretized on a microscopic timescale δt of the order of ps. In each FD cell the evolution of the magnetization field $\mathbf{m}(\mathbf{r}, t)$ is computed through time stepping until a new static micromagnetic equilibrium is obtained corre-

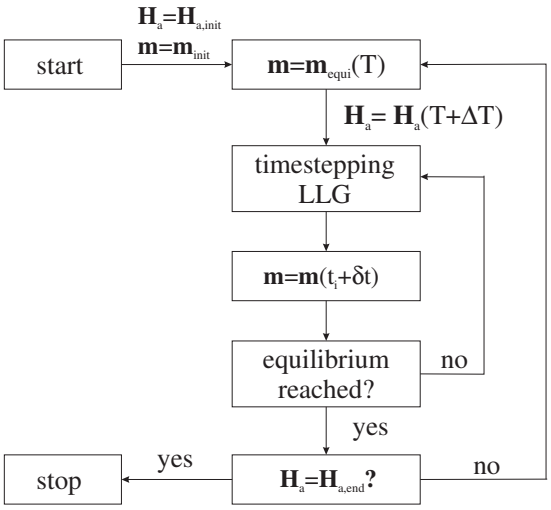

Figure 6.20: Flowchart of the micromagnetic hysteresis scheme.

sponding to the new constant value for the applied field $\mathbf{H}_a$. The numerical scheme is shown in Fig. 6.20. Starting from an initial magnetization state $\mathbf{m}_{init}$ and applied field $\mathbf{H}_{a,init} = \mathbf{H}_a(T)$, the applied field jumps to the next constant value $\mathbf{H}_a = \mathbf{H}_a(T + \Delta T)$. The corresponding new equilibrium magnetization is computed by successively integrating the LLG-equation through time stepping with steps $\delta t \ll \Delta T$: during each time step $[t_i, t_i + \delta t]$ the orientation of the magnetization field $\mathbf{m}(\mathbf{r}, t)$ in every FD cell is computed until an equilibrium condition is fulfilled. Starting from this new equilibrium state the applied field takes a next jump $\mathbf{H}_a(T + 2\Delta T) - \mathbf{H}_a(T + \Delta T)$ and a next magnetic equilibrium state is computed. This scheme is continued until the applied field $\mathbf{H}_a$ has reached its end value $\mathbf{H}_{a,end}$.

To check wether equilibrium is reached, the following stopping criterium is verified for a number of test cells.

$$\frac{|\mathbf{m}(t_i) - \mathbf{m}(t_i + \delta t)|}{\delta t} < \epsilon\, ps^{-1} \tag{6.40}$$

where δt is expressed in ps. A typical value for ϵ is 0.01. When the criterium (6.40) is fulfilled for all test cells, equilibrium is reached and the applied field $\mathbf{H}_a$ takes a next jump.

6.5.2 Optimization of the number of applied field jumps

The number of macroscopic time steps in the quasi-static applied field has an influence on the precision and the time efficiency of the micromagnetic hys-

Table 6.4: Discretization of the applied field

$\#\,\Delta T$	ϵ_{rms}	$\#\,\delta t$
100	0.0128	6723
200	0.0078	7346
400	0.0049	9174
600	0.0033	8617
800	0.0017	8780
1000	—	9739

teresis scheme. To determine the optimal number of macroscopic time steps $\#\Delta T$ (i.e. the optimal number of applied field jumps), the hysteresis loop for an ellipsoidal grain with semi-axes of $0.288\,\mu m$, $0.288\,\mu$m and $0.576\,\mu$m is simulated. In the simulations, the number of applied field jumps in the interval $[-5\,10^5\,\mathrm{A/m},\ 5\,10^5\,\mathrm{A/m}]$ is varied. The sample has a cubic anisotropy with easy axes parallel to the semi-axes and the applied field parallel to the main axis. In the simulation of the loop shown in Fig. 6.21, $\mathbf{H}_a$ is described with 1000 field jumps. The particular form of the loop –narrow in the center and bulky at the bottom and at the top – is due to a sudden creation of domains in the grain (top and bottom), these domains deform smoothly according to the applied field $\mathbf{H}_a$ (center). The internal magnetization configurations are e.g. described in [75]. The root mean square deviation

$$\epsilon_{rms} = \frac{1}{\#\Delta T}\sqrt{\sum_{i=1}^{\#\Delta T}\Big(< M(T_i) > - < M_{ref}(T_i) >\Big)^2} \tag{6.41}$$

of the other loops (simulated with less time steps ΔT) with respect to this reference loop is shown in Table 6.4, where also the total number of microscopic time steps δt is given. One can conclude that a deviation of less than 1 percent is already achieved when 200 macroscopic time steps are used and the number of microscopic time steps increases only slowly with the number of macroscopic time steps.

6.6. Conclusion

In this chapter, we have presented the micromagnetic (hysteresis) scheme. We have found that the time and memory efficiency of the micromagnetic simulations is determined by the efficiency of the time stepping scheme for the LLG equation on the one hand and by the efficient evaluation of the effective field terms on the other hand.

Two time and memory efficient semi-analytical time stepping schemes developed during this PhD have been presented. The semi-analytical time step-

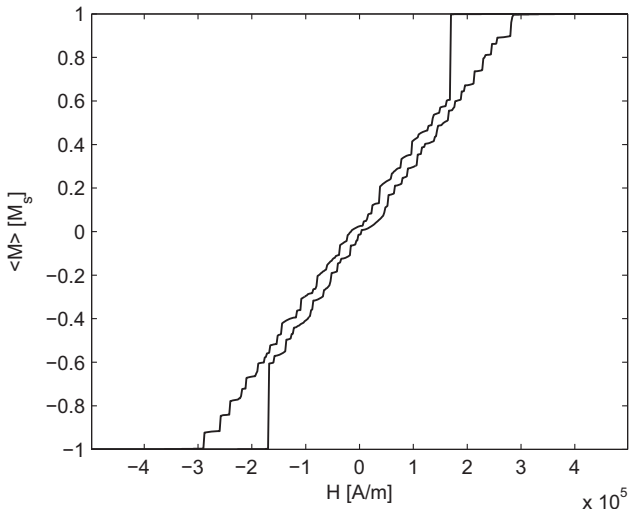

Figure 6.21: Reference hysteresis loop of an ellipsoidal iron sample with semi-axes of $0.288\,\mu$m, $0.288\,\mu$m and $0.576\,\mu$m. The applied field is parallel to the main axis and is described as a staircase function with 1000 field jumps.

ping schemes preserve the properties of the LLG equation inherently. Further, the use of analytical expressions guarantees a higher order extrapolation of the local magnetization trajectories enabling the use of very large time steps, while limiting the number of effective field evaluations. These properties of the semi-analytical time stepping schemes make them perfectly suited for the simulation of magnetization processes in micromagnetically large samples.

In a collaboration with INRIM, a comparison is made between simulation results obtained with the presented micromagnetic schemes and simulation results obtained with FEM based code and with the NIST/OOMF code. This comparison has proven the accuracy of the developed micromagnetic schemes. Further it is shown how the time stepping of the LLG equation can result into a micromagnetic hysteresis scheme able to describe time independent hysteresis loops.

Concerning the evaluation of the effective field terms it has become clear that an accelerated computation of the magnetostatic field is indispensable since the classical evaluation scales $\mathcal{O}(N^2)$, while the other effective field evaluations scale $\mathcal{O}(N)$. The algorithms that assure such an accelerated evaluation of $\mathbf{H}_{ms}$ will be presented in the next chapters.

CHAPTER 7

Fast Fourier Transform based evaluation of the magnetostatic field

7.1. Introduction

From Chapter 6 it is clear that the effective field has to be evaluated several thousands of times during one simulation. In Section 6.2.4 we concluded that for the classical evaluation of the magnetostatic field the computational time and memory requirements both scale $\mathcal{O}(N^2)$ while the computation of the other effective field terms only scales $\mathcal{O}(N)$ and requires no extra memory. In this chapter we will exploit the convolution structure of the discretized expression for the magnetostatic field in a FD cell with center $\mathbf{r} = \mathbf{r}_j$ (cfr. Section 6.2.4)

$$\mathbf{H}_{ms}(\mathbf{r}_i) = -\frac{M_s}{4\pi} \sum_{\substack{j=1 \\ j\neq i}}^{N} \int_{\mathcal{V}} \nabla_i \nabla_i \frac{1}{|\mathbf{r}_i - \mathbf{r}_j + \boldsymbol{\rho}|} \, \mathrm{d}\boldsymbol{\rho} \cdot \mathbf{m}_j \tag{7.1}$$

by using Fast Fourier Transforms (FFTs). This reduces the computational burden to $\mathcal{O}(N \log N)$ and the memory requirements to $\mathcal{O}(N)$. We recall that $\mathcal{V}$ is the volume of a FD cell, $\mathbf{m}_j$ is the uniform magnetization of the FD cell at $\mathbf{r} = \mathbf{r}_j$ and that $\boldsymbol{\rho}$ is an integration variable.

In micromagnetic computations, FFTs are widely used for the evaluation of the magnetostatic field, see e.g. [76, 77, 78]. In [79], two FFT based methods to compute the magnetostatic field in 2D structures are compared. The *constant magnetization method* starts from a discretization where a uniform magnetization field is assumed in each discretization cell. The *constant charge*

method [80, 81] starts from a discretization where a uniform magnetic charge density is assumed in each cell. In [79], the constant magnetization method which is used in this PhD work (see Section 6.1) is concluded to have superior convergence properties. Within this method, two approaches are adopted to compute the magnetostatic field.

In a first approach, a FFT based scheme evaluates the magnetostatic fields using the direct relation between $\mathbf{H}_{ms}$ and the uniform magnetization field in each discretization cell. This FFT scheme provides results with a high accuracy. A second alternative FFT scheme evaluates, the magnetostatic field by taking the gradient of the scalar magnetic potential ψ_{ms} which is in turn computed using the relation between ψ_{ms} and the uniform magnetization in each discretization cell. This FFT scheme has a lower accuracy, but is faster and requires less memory. In this chapter, the convolution theory is first outlined and remarks are given about periodic structures, then the two FFT schemes are presented and their performance is determined. Finally, the evaluation of $\mathbf{H}_{ms}$ in periodic structures is described.

7.2. Convolution theorem and periodicity

In general electromagnetic problems, convolution structures like (7.1) arise frequently, where the fields $f(\mathbf{r})$ are expressed as a convolution of a Green's function $g(\mathbf{r})$ with the sources $s(\mathbf{r})$. The Green's function and its dimensionality depends on the physical problem and its description. Now consider a problem where the sources and the field entity are scalar, e.g. the electrostatic problem where the electric potential is evaluated in terms of N distributed electrical charges.

$$f(\mathbf{r}_i) = \sum_{j=1}^{N} g(\mathbf{r}_i - \mathbf{r}_j) s(\mathbf{r}_j) \tag{7.2}$$

When the sources are placed on a regular grid, this class of problems can be computed rapidly by adopting the convolution theorem [82]. The one dimensional convolution theorem states that:

If a signal s_j is periodic with period N, so that it is completely determined by the N values $s_0 \ldots s_{N-1}$, then its discrete convolution with a response function of finite duration N is related to the discrete Fourier transform pair

$$f^j = \sum_{k=-N/2+1}^{N/2} g^{j-k} s^k \Leftrightarrow \tilde{f}^n = \tilde{g}^n \tilde{s}^n \tag{7.3}$$

Here $\tilde{g}^n$, $(n = 0, \ldots, N-1)$ is the discrete Fourier transform of the values g^j, $(j = 0, \ldots, N-1)$, while $\tilde{s}^n$, $(n = 0, \ldots, N-1)$ is the discrete Fourier transform of the

values s^k, $(k = 0, \ldots, N-1)$.

By definition, the discrete Fourier transform of a function f is given by

$$\tilde{f}^k = \sum_{n=0}^{N-1} f^n \mathrm{e}^{-\imath 2\pi kn/N}, \tag{7.4}$$

while the inverse discrete Fourier transform is given by

$$f^n = \frac{1}{N} \sum_{k=0}^{N-1} \tilde{f}^k \mathrm{e}^{\imath 2\pi kn/N}. \tag{7.5}$$

Here, and in what follows, Fourier transformed quantities are denoted with a tilde. The definition of the (inverse) Fourier transform and the convolution theorem are easily extended to three dimensions.

The convolution theorem is based on the periodicity of the signals. In numerical applications, the data is only periodic in one or more directions if periodic boundary conditions are (partially) adopted. When the sources are not periodic, the input data has to be zero padded: the same number of zeros has to be added in the considered direction. By doing so, the input data for a 3D computational domain Ω, non periodic in any direction and consisting of $N_x \times N_y \times N_z$ FD cells has dimensions $2N_x \times 2N_y \times 2N_z$. In that way unwanted side effects originating from the cyclic nature of Fourier transforms are excluded. Hence, the source data is stored in 3D matrices. It has following entries in the plane $z = k$, $(0 \leq k < N_z)$

$$\begin{bmatrix} s^{0,0,k} & \cdots & s^{0,N_y-1,k} & 0 \cdots 0 \\ \vdots & \ddots & \vdots & \vdots \ddots \vdots \\ s^{N_x-1,0,k} & \cdots & s^{N_x-1,N_y-1,k} & 0 \cdots 0 \\ 0 & \cdots & 0 & 0 \cdots 0 \\ \vdots & \ddots & \vdots & \vdots \ddots \vdots \\ 0 & \cdots & 0 & 0 \cdots 0 \end{bmatrix}. \tag{7.6}$$

The Green's function elements also have to be adapted to fit the cyclic nature of the convolution theorem. Therefore, the 3D matrix has following en-

tries in the plane $z = k$, $(0 \leq k < N_z)$

$$\begin{bmatrix} g^{0,0,k} & \cdots & g^{0,N_y-1,k} & 0 & g^{0,-(N_y-1),k} & \cdots & g^{0,-1,k} \\ \vdots & \ddots & \vdots & \vdots & \vdots & \ddots & \vdots \\ g^{N_x-1,0,k} & \cdots & g^{N_x-1,N_y-1,k} & 0 & g^{N_x-1,-(N_y-1),k} & \cdots & g^{N_x-1,-1,k} \\ 0 & \cdots & 0 & 0 & \cdots & 0 & \\ g^{-(N_x-1),0,k} & \cdots & g^{-(N_x-1),N_y-1,k} & 0 & g^{-(N_x-1),-(N_y-1),k} & \cdots & g^{-(N_x-1),-1,k} \\ \vdots & \ddots & \vdots & \vdots & \vdots & \ddots & \vdots \\ g^{-1,0,k} & \cdots & g^{-1,N_y-1,k} & 0 & g^{-1,-(N_y-1),k} & \cdots & g^{-1,-1,k} \end{bmatrix}. \tag{7.7}$$

When considering periodic boundary conditions in the x, y and z-direction, the matrices containing the source data are not zero padded and the matrix representing the Green's function is restricted to half its range. For the Green's function matrix, this results in the following entries in the plane $z = k$, $(0 \leq k < N_z)$

$$\begin{bmatrix} g^{0,0,k} & \cdots & g^{0,N_y/2-1,k} & 0 & g^{0,-(N_y/2-1),k} & \cdots & g^{0,-1,k} \\ \vdots & \ddots & \vdots & \vdots & \vdots & \ddots & \vdots \\ g^{N_x/2-1,0,k} & \cdots & g^{N_x/2-1,N_y/2-1,k} & 0 & g^{N_x/2-1,-(N_y/2-1),k} & \cdots & g^{N_x/2-1,-1,k} \\ 0 & \cdots & 0 & 0 & \cdots & 0 & \\ g^{-(N_x/2-1),0,k} & \cdots & g^{-(N_x/2-1),N_y/2-1,k} & 0 & g^{-(N_x/2-1),-(N_y/2-1),k} & \cdots & g^{-(N_x/2-1),-1,k} \\ \vdots & \ddots & \vdots & \vdots & \vdots & \ddots & \vdots \\ g^{-1,0,k} & \cdots & g^{-1,N_y/2-1,k} & 0 & g^{-1,-(N_y/2-1),k} & \cdots & g^{-1,-1,k} \end{bmatrix}. \tag{7.8}$$

When periodic boundary condition are only applied in one or two directions, a combination of the formulas (7.6) to (7.8) has to be made.

However, special attention should go to the interpretation of these formulas. These formulas describe a periodic structure in the sense that FD cells interact with the closest FD cells (or their images) within the same period. This is shown in Fig. 7.1 for the case of a structure that is only periodic in the x-direction. Each FD cell interacts with the FD cells in the $N_x/2 - 1$ planes left and right from the considered cell. This can be easily derived from the entries of the matrix (7.8). This description implies that no interaction takes place with the infinite number of images of the FD cells in all other periods in the x-direction. Hence, when exploiting the cyclic nature of the FFTs as depicted here, field entities are computed in each FD cell originating from one period of the structure (with the considered FD cell central in this period). This means that an infinite periodic repetition is not described. If one aims to describe also these periodic images, periodic Green's functions should be used.

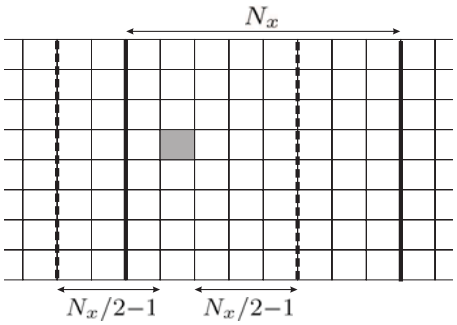

Figure 7.1: Interaction cells for a structure periodic in the x-direction with period N_x cells. The gray colored FD cell interacts with the FD cells in $N_x/2-1$ planes left and right from the cell.

7.3. FFT based evaluation schemes for the magnetostatic field

7.3.1 Direct magnetostatic field evaluation (scheme 1)

In this approach, further referred to as *scheme 1*, the action of the second $\nabla_{\boldsymbol{\rho}}$ operator in (7.1) is first accounted for, yielding

$$\mathbf{H}_{ms}(\mathbf{r}_i) = -\frac{M_s}{4\pi}\sum_{\substack{j=1\\ j\neq i}}^{N}\int_{\mathcal{V}} \nabla_{\boldsymbol{\rho}}\frac{\mathbf{r}_i-\mathbf{r}_j+\boldsymbol{\rho}}{|\mathbf{r}_i-\mathbf{r}_j+\boldsymbol{\rho}|^3}\,\mathrm{d}\boldsymbol{\rho}\cdot\mathbf{m}_j. \tag{7.9}$$

Applying Gauss' theorem on this gives

$$\mathbf{H}_{ms}(\mathbf{r}_i) = -\frac{M_s}{4\pi}\sum_{\substack{j=1\\ j\neq i}}^{N}\int_{\partial\mathcal{V}} \frac{(\mathbf{r}_i-\mathbf{r}_j+\boldsymbol{\rho})}{|\mathbf{r}_i-\mathbf{r}_j+\boldsymbol{\rho}|^3}\,\mathbf{u}_S\,\mathrm{d}\boldsymbol{\rho}\cdot\mathbf{m}_j, \tag{7.10}$$

with $\mathbf{u}_S$ the normal unit vector pointing outward of the surface $\partial\mathcal{V}$ of the FD cell. Rewriting (7.10) explicitly as a convolution product yields

$$\mathbf{H}_{ms}(\mathbf{r}_i) = \sum_{\substack{j=1\\ j\neq i}}^{N}\mathbf{g}(\mathbf{r}_i-\mathbf{r}_j)\cdot\mathbf{m}_j, \tag{7.11}$$

with $\mathbf{g}(\mathbf{r})$ the symmetrical Green's function tensor

$$\mathbf{g}(\mathbf{r}) = \begin{bmatrix} g_{xx}(\mathbf{r}) & g_{xy}(\mathbf{r}) & g_{xz}(\mathbf{r}) \\ g_{xy}(\mathbf{r}) & g_{yy}(\mathbf{r}) & g_{yz}(\mathbf{r}) \\ g_{xz}(\mathbf{r}) & g_{yz}(\mathbf{r}) & g_{zz}(\mathbf{r}) \end{bmatrix} \tag{7.12}$$

Now, the discrete convolution theorem [82] is applied to the product (7.11):

$$\begin{aligned}
\tilde{H}^{i,j,k}_{ms,x} &= \tilde{g}^{i,j,k}_{xx}\tilde{m}^{i,j,k}_{x} + \tilde{g}^{i,j,k}_{xy}\tilde{m}^{i,j,k}_{y} + \tilde{g}^{i,j,k}_{xz}\tilde{m}^{i,j,k}_{z},\\
\tilde{H}^{i,j,k}_{ms,y} &= \tilde{g}^{i,j,k}_{xy}\tilde{m}^{i,j,k}_{x} + \tilde{g}^{i,j,k}_{yy}\tilde{m}^{i,j,k}_{y} + \tilde{g}^{i,j,k}_{yz}\tilde{m}^{i,j,k}_{z},\\
\tilde{H}^{i,j,k}_{ms,z} &= \tilde{g}^{i,j,k}_{xz}\tilde{m}^{i,j,k}_{x} + \tilde{g}^{i,j,k}_{yz}\tilde{m}^{i,j,k}_{y} + \tilde{g}^{i,j,k}_{zz}\tilde{m}^{i,j,k}_{z}.
\end{aligned} \tag{7.13}$$

Following the convolution theorem, one computes the magnetostatic field by:

1. Fourier transforming the magnetization data m_x, m_y and m_z after zero padding in the non-periodic dimensions.
2. performing the point wise products (7.13) of the Fourier transformed magnetization data with the Fourier transformed Green's tensor elements (7.12).
3. inverse Fourier transforming the result of the previous step.

The elements in the Green's function matrices can be determined by evaluating the integrals in (7.10) using a Gaussian quadrature formula. The explicit expressions for the Green's tensor elements are given in Appendix A. When an adequate high order Gaussian quadrature formula is used to compute the tensor elements, the magnetostatic fields generated by the uniformly magnetized FD cells can be computed up to any wanted accuracy. In this work, a 6 digits accuracy is used since all other computations are single precision. The accuracy of the scheme is checked by comparison with analytical expressions provided in [21].

In this context, it should be noted that at sufficiently large distances (e.g. 20 FD cells), the magnetostatic field generated by a FD cell

$$\mathbf{H}^{FD}_{ms}(\mathbf{r}) = -\frac{M_s}{4\pi}\int_{\mathcal{V}} \nabla\nabla\frac{1}{|\mathbf{r}+\boldsymbol{\rho}|}\,\mathrm{d}\boldsymbol{\rho}\cdot\mathbf{m}_j \tag{7.14}$$

and the magnetostatic field generated by a magnetic dipole

$$\mathbf{H}^{dip}_{ms}(\mathbf{r}) = -\frac{M_s}{4\pi}\nabla\nabla\frac{1}{|\mathbf{r}|}\cdot\mathbf{m}_j \tag{7.15}$$

are identical within the intended accuracy. The use of the expression (7.15) to describe the magnetostatic interaction between sufficiently distant FD cells vastly accelerates the evaluation of the Green's matrix elements.

7.3.2 Potential based magnetostatic field evaluation (scheme 2)

In this approach, further referred to as *scheme 2*, first the scalar magnetic potential $\psi_{ms}(\mathbf{r})$ is computed in each FD cell. Afterwards, the magnetostatic field

is evaluated by taking the negative gradient of the magnetic potential

$$\mathbf{H}_{ms}(\mathbf{r}) = -\nabla\psi_{ms}(\mathbf{r}). \tag{7.16}$$

Analogous to expression (7.9), the magnetic potential in a point $\mathbf{r}_i$ is given by

$$\psi_{ms}(\mathbf{r}_i) = \frac{M_s}{4\pi}\sum_{j=1}^{N}\int_{\mathcal{V}} \nabla_{\boldsymbol{\rho}}\frac{1}{|\mathbf{r}_i - \mathbf{r}_j + \boldsymbol{\rho}|}\,\mathrm{d}\boldsymbol{\rho}\cdot\mathbf{m}_j. \tag{7.17}$$

Note that for the evaluation of the magnetic potential, the self contribution has to taken into account to come to accurate results. The correction for the self contribution is made when the magnetostatic field is derived from ψ. Applying Gauss theorem on (7.17) gives

$$\psi_{ms}(\mathbf{r}_i) = \frac{M_s}{4\pi}\sum_{j=1}^{N}\int_{\partial\mathcal{V}} \frac{1}{|\mathbf{r}_i - \mathbf{r}_j + \boldsymbol{\rho}|}\mathbf{u}_{\mathbf{S}}\,\mathrm{d}\boldsymbol{\rho}\cdot\mathbf{m}_j, \tag{7.18}$$

with $\mathbf{u}_S$ the normal unit vector pointing outward of the surface $\partial\mathcal{V}$ of the FD cell. Rewriting (7.18) explicitly as a convolution product yields

$$\psi_{ms}(\mathbf{r}_i) = \sum_{j=1}^{N}\mathbf{f}(\mathbf{r}_i - \mathbf{r}_j)\cdot\mathbf{m}_j, \tag{7.19}$$

with $\mathbf{f}(\mathbf{r})$ the Green's function vector

$$\mathbf{f}(\mathbf{r}) = \left[\, f_x(\mathbf{r})\;\; f_y(\mathbf{r})\;\; f_z(\mathbf{r}) \,\right]. \tag{7.20}$$

Adopting the convolution theorem gives

$$\tilde{\psi}_{ms}^{i,j,k} = \tilde{f}_x^{i,j,k}\tilde{m}_x^{i,j,k} + \tilde{f}_y^{i,j,k}\tilde{m}_y^{i,j,k} + \tilde{f}_z^{i,j,k}\tilde{m}_z^{i,j,k}. \tag{7.21}$$

Hence, one computes the magnetic potential by:

1. Fourier transforming the magnetization data m_x, m_y and m_z after zero padding in non periodic directions.
2. performing the point wise products (7.21) of the Fourier transformed magnetization data with the Fourier transformed Green's vector elements (7.20)
3. inverse Fourier transforming the result of the previous step.

Again, the elements in the Green's function vector can be determined by evaluating the integrals in (7.18) using a Gaussian quadrature formula or can be evaluated analytically in closed form [61]. The explicit expressions for the Green's vector elements are given in Appendix A. Also in this case, the magnetic potential generated by a dipole can be used to describe the magnetostatic

interaction between sufficiently distant FD cells to accelerate the evaluation of the Green's function elements.

To derive the magnetostatic field $\mathbf{H}_{ms}(\mathbf{r})$ in each FD cell (i,j,k) one has to take minus the gradient of the local magnetic potential $\psi_{ms}(\mathbf{r})$. This is approximated numerically using the following formula

$$\begin{bmatrix} H_{ms,x}^{i,j,k} \\ H_{ms,y}^{i,j,k} \\ H_{ms,z}^{i,j,k} \end{bmatrix} = \frac{1}{2\Delta} \begin{bmatrix} \psi_{ms}^{i-1,j,k} - \psi_{ms}^{i+1,j,k} \\ \psi_{ms}^{i,j-1,k} - \psi_{ms}^{i,j+1,k} \\ \psi_{ms}^{i,j,k-1} - \psi_{ms}^{i,j,k+1} \end{bmatrix}. \tag{7.22}$$

The self contribution of each FD cell to the magnetic field in its center has to be subtracted in the last step of these computations. The numerical evaluation of the gradient (7.22) introduces discretization errors in the computed values of the magnetostatic fields. Hence this scheme results in a low accuracy evaluation of $\mathbf{H}_{ms}$, compared to the accuracy of scheme 1.

7.3.3 Performance study

The timing and memory consumption of the different magnetostatic field evaluation schemes is described here for a non-periodic structure, but can easily be repeated for (partially) periodic structures. Hence all FFT data have dimensions $2N_x \times 2N_y \times 2N_z$, $(N = N_x N_y N_z)$. It is the intention to develop an algorithm that allows to compute the magnetostatic fields multiple times for different magnetic configurations in a fast way. Hence, generic computations are performed as much as possible during the set up phase of the algorithm in order to avoid duplication of computations. In that respect, the Green's functions matrices are constructed and Fourier transformed only once during set up. Due to the symmetry properties of the Green's function elements, the Fourier transformed Green's function matrices are real or purely imaginary.

The number of computations for the evaluation of $\mathbf{H}_{ms}$ in one time step is shown in Table 7.1. In both schemes all three zero padded magnetization matrices are Fourier transformed. Each (inverse) Fourier transform requires $\mathcal{O}(N \log N)$ computations. Since FFTs are used in many research areas, very fast and sophisticated codes have been developed. In our implementation, routines are used included in the FFTW library [83]. These routines are further optimized in the zero padded case. In Appendix B, it is outlined how 1D FFTs on rows containing only zeros are excluded, leading to much faster (but still $\mathcal{O}(N \log N)$) computation of the FFTs.

In Fourier space, $9 \times 4N$ *real* $\times$ *complex* multiplications are performed to evaluate the point wise products (7.13) in the direct computation scheme, while scheme 2 only needs $3 \times 4N$ *real* $\times$ *complex* multiplications to evaluate (7.21). The first scheme needs 3 inverse Fourier transforms while the sec-

Table 7.1: Number of computations for the evaluation of $\mathbf{H}_{ms}$ for N FD cells (no periodicity).

	scheme 1	scheme 2
forward FFTs	3	3
point wise products	$9 \times 4N$	$3 \times 4N$
inverse FFTs	3	1
gradients	0	N

ond scheme only needs one. Additionally, in the low accuracy $\mathbf{H}_{ms}$ evaluation scheme based on the magnetic potential, the gradient of the magnetic potential ψ has to be evaluated in every FD cell, which is done in $\mathcal{O}(N)$ computations.

The memory requirements for both FFT based evaluation schemes are shown in Table 7.2. The different contributions are expressed in terms of *real* numbers. In both schemes $3N$ real numbers are used to save the magnetization data and the resulting magnetostatic field data. One can reduce the memory requirements to save the magnetization data to $2N$ instead of $3N$ by only storing the azimuth and zenith angles exploiting the fact that the magnetization amplitude is constant. However, the small memory gains do not justify the extra CPU time due the numerous evaluations of goniometric functions. In scheme 1 and scheme 2, the Fourier transformed Green's function elements are stored in respectively 6 and 3 matrices containing 4N *real* numbers. In scheme 1, $3 \times 8N$ *real* numbers are required to store the $3 \times 4N$ *complex* values of the Fourier transformed magnetization components. For each Fourier transformed magnetostatic field component $\tilde{H}_{ms,q}$ $(q = x,y,z)$ in (7.13), the point wise products are elaborated first and directly inverse Fourier transformed to the actual field components $H_{ms,q}$ $(q = x,y,z)$. Hence $8N$ real numbers are needed to sequentially store a Fourier transformed magnetostatic field component. In scheme 2, the magnetization components M_q $(q = x,y,z)$ are Fourier transformed, multiplied point wise with the corresponding Green's function matrix f_q and added to the Fourier transformed magnetic potential $\tilde{\psi}$, one after the other. In that way only one Fourier transformed magnetic component has to be known at the time, limiting the required memory for the Fourier transformed magnetization components to $4N$ *complex* values. In total the magnetostatic field evaluation scheme based on the magnetic potential requires about half of the memory compared to the direct evaluation scheme.

Due to the numerical evaluation of the gradient operator (7.22), scheme 2 is expected to have a lower accuracy compared to scheme 1. The accuracy of the magnetic potential based FFT scheme is determined by comparing the magnetostatic field values obtained by both schemes for iron monocrystals of different dimensions in a micromagnetic equilibrium state encountered in the

Table 7.2: Memory requirements for the evaluation of $\mathbf{H}_{ms}$ expressed in real numbers for N FD cells (no periodicity).

	scheme 1	scheme 2
$\mathbf{m}$	$3 \times N$	$3 \times N$
$\mathbf{H}_{ms}$	$3 \times N$	$3 \times N$
$\tilde{\mathbf{g}}/\tilde{\mathbf{f}}$	$6 \times 4N$	$3 \times 4N$
$\tilde{\mathbf{m}}$	$3 \times 8N$	$1 \times 8N$
$\tilde{\mathbf{H}}_{ms}/\tilde{\psi}$	$1 \times 8N$	$1 \times 8N$
total	$62N$	$34N$

Table 7.3: Accuracy of scheme 2 for different dimensions.

edge size	normalized error
$0.32\,\mu m$	0.0250
$0.64\,\mu m$	0.0124
$1.28\,\mu m$	0.0056
$2.56\,\mu m$	0.0031

simulation of their hysteresis loop. The normalized error, defined as

$$\text{error} = \sqrt{\frac{\sum_{i=1}^{N} |\mathbf{H}_{ms,i}^{FFT2} - \mathbf{H}_{ms,i}^{FFT1}|^2}{\sum_{i=1}^{N} |\mathbf{H}_{ms,i}^{FFT1}|^2}} \tag{7.23}$$

is shown in table 7.3 for different sample dimensions. The fields $\mathbf{H}_{ms}^{FFT1}$, computed in scheme 1 are considered as a reference. Table 7.3 shows that the error decreases for larger sample dimensions to less than one percent. This is because in larger monocrystals the magnetostatic potential is smoother than in the small monocrystals. This results in a more accurate numerical approximation of the gradient (7.22). To demonstrate this Fig. 7.2 shows magnetic configurations in different planes of the sample with edges of $1.28\,\mu m$ together with the magnetostatic field values and the local normalized error in the same planes. As expected, the largest errors occur near the domain walls where the variations of the magnetic potential are larger leading to larger errors on the magnetostatic field values. Furthermore, it should be noted that higher order approximations for the gradient operator only lead to small improvements in accuracy.

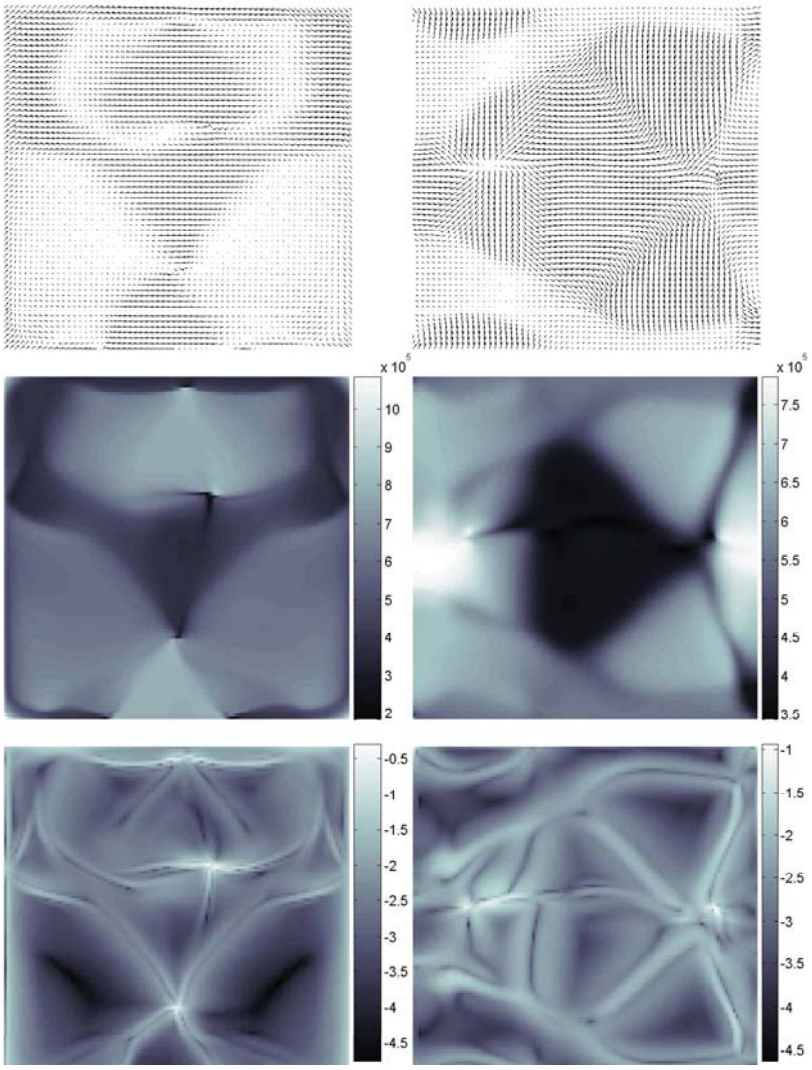

Figure 7.2: Locally averaged magnetization (top), amplitude of the magnetostatic field $[Am^{-1}]$ (middle) and local normalized error on a logarithmic scale (bottom) in planes $x = 0.0\,\mu m$ (left) and $z = 0.16\,\mu m$ (right) of an iron cubic sample with edges of $1.28\,\mu m$.

7.4. Description of infinite periodic structures in the FFT scheme

From Chapter 3 it is clear that the geometry of the ferromagnetic sample has a large influence on the magnetization dynamics and consequently on the

hysteresis properties. Macroscopically, this is expressed by the demagnetizing tensor of the sample. As seen in Section 3.6 the demagnetizing factors decrease for increasing elongating shapes. In the limit for infinitely elongated samples, the influence of the magnetostatic effects are reduced to zero in the longitudinal direction. In this way, only the demagnetizing effects in the cross section together with the other micromagnetic interactions determine the magnetization process.

In what follows, we will determine the magnetostatic field in one period $\mathcal{P}$ of an infinite ferromagnetic structure, periodic in one or two directions $d = 1$ or $d = 2$. Figure 7.3 shows e.g. a geometry, which is periodic in one dimension. The fields, computed in one FD cell, originate from the uniformly magnetized FD cells in the period and all their images. Note that this is different from the standard periodic boundary conditions when FFTs are used without zero padding, see Fig. 7.1. We recall that it makes no sense to compute magnetostatic interactions in a geometry which is infinite in the three dimensions (see Section 3.7).

The discretized magnetostatic field $\mathbf{H}_{ms}$ in a point $\mathbf{r}$ originating from the infinite periodic structure is given by

$$\mathbf{H}_{ms}(\mathbf{r}_i) = -\frac{M_s}{4\pi} \sum_{\substack{j=1 \\ j\neq i}}^{\infty} \int_{\mathcal{V}} \nabla_i \nabla_i \frac{1}{|\mathbf{r}_i - \mathbf{r}_j + \boldsymbol{\rho}|} \, \mathrm{d}\boldsymbol{\rho} \cdot \mathbf{m}_j. \tag{7.24}$$

Here, we let ∇ act on $\mathbf{r}_i$, which is identical to ∇ acting on $\boldsymbol{\rho}$ as in (6.30). Due to the periodicity, we can restrict ourself to compute the magnetic fields in points $\mathbf{r} \in \mathcal{P}$. When $\mathcal{P}$ is a cube with edge length L, it holds that all quantities $f(\mathbf{r})$ are invariant under a translation $\mathbf{n}L$

$$f(\mathbf{r}) = f(\mathbf{r} + \mathbf{n}L) \tag{7.25}$$

with $\mathbf{n}$ an integer vector with components in the infinite directions. When for instance periodicity is described in the x- and y-direction $\mathbf{n}$ is

$$\mathbf{n} = n_x \mathbf{e}_x + n_y \mathbf{e}_y \qquad n_x, n_y \in \mathbb{Z}. \tag{7.26}$$

The periodicity particularly holds for the magnetization $\mathbf{m}(\mathbf{r}_j)$, which enables us to write (7.24) as

$$\mathbf{H}_{ms}(\mathbf{r}_i) = -\frac{M_s}{4\pi} \sum_{j=1}^{N'} \sum_{\mathbf{n}\in\mathbb{Z}^d} \int_{\mathcal{V}} \nabla_i \nabla_i \frac{1}{|\mathbf{r}_i - (\mathbf{r}_j + \mathbf{n}L + \boldsymbol{\rho})|} \, \mathrm{d}\boldsymbol{\rho} \cdot \mathbf{m}_j. \tag{7.27}$$

The prime on the first summation indicates that the term $i = j$ does not contribute when $\mathbf{n} = [0,0,0]$, further $\mathbb{Z}^d$ is the domain of integers in the d periodic directions in which $\mathbf{n}$ is defined, see (7.26).

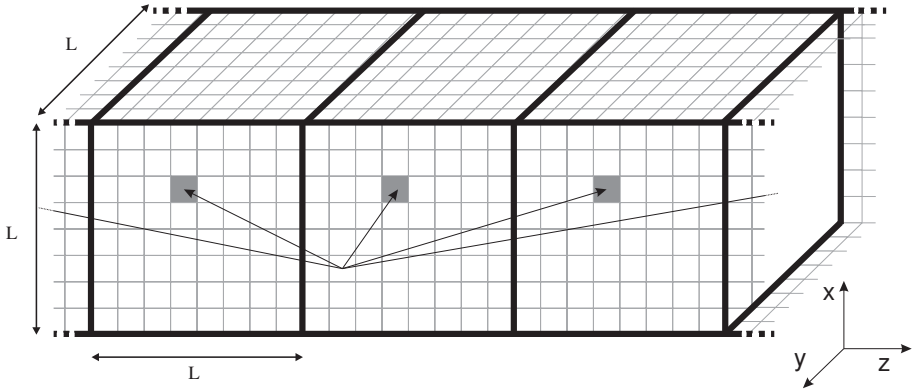

Figure 7.3: An infinite periodic ferromagnetic structure. The magnetostatic field in one FD cell originates from FD cells in the considered period and there periodic images.

7.4.1 Direct evaluation of the infinite sum

To compute the infinite sum (7.27), one can choose to only account for a finite number of periods and neglect the contributions from FD cells in far away periods. In that way, expression (7.27) is rewritten as

$$\mathbf{H}_{ms}(\mathbf{r}_i) = \sum_{j=1}^{N'} \sum_{\mathbf{n}\in\mathbb{Z}^d}^{\text{finite}} \mathbf{g}(\mathbf{r}_i - (\mathbf{r}_j + \mathbf{n}L)) \cdot \mathbf{m}_j \tag{7.28}$$

When the Green's function matrices are adjusted to

$$\mathbf{g}^*(\mathbf{r}) = \sum_{\mathbf{n}\in\mathbb{Z}^d}^{\text{finite}} \mathbf{g}(\mathbf{r} - \mathbf{n}L) \tag{7.29}$$

the same approach as in Section 7.3.1 can be followed to evaluate (7.28). Moreover, zero padding is not required in the periodic directions since the input data is periodic.

This direct summation approach is not very efficient since the series are only slowly convergent and thus a large number of periods has to be taken into account in order to well approximate the infinite periodic structure. However, because the evaluation of the periodic Green's function matrix is performed in the set up phase of the algorithm, one can follow this approach when periodicity is described in only one dimension. When periodicity is assumed in two dimensions, we will rely on the Ewald summation technique to sum the contributions to the magnetostatic field of the periodic images in a fast and accurate way.

7.4.2 Ewald summation technique

Ewald summation techniques are developed in the study of layered structures [84] and in the area of molecular dynamic simulations [85, 86]. Here, often very large molecules are described in the present of a solvent. The numerical simulations determine the slowly decaying electrostatic forces between the thousands of atoms in the molecules. In the simulations, periodic boundary conditions are employed to minimize the surface effects. In micromagnetism, the Ewald summation technique has been used by Berkov et al. [87, 88] and Lebecki et al. [89].

We have seen that the contributions from far away FD cells can be perfectly approximated by the fields generated by corresponding dipoles. Hence, in what follows we will compute the magnetostatic field $\mathbf{H}_{ms}^{dip}$ generated by dipoles which are periodically placed in the center of the FD cells

$$\begin{aligned}\mathbf{H}_{ms}^{dip}(\mathbf{r}_i) &= -\frac{M_s}{4\pi}\sum_{j=1}^{N'}\sum_{\mathbf{n}\in\mathbb{Z}^d}\mathbf{h}_{ms}^{dip}(\mathbf{r}_i-(\mathbf{r}_j+\mathbf{n}L))\\ &= -\frac{M_s}{4\pi}\sum_{j=1}^{N'}\sum_{\mathbf{n}\in\mathbb{Z}^d}\nabla\nabla\frac{1}{|\mathbf{r}_i-(\mathbf{r}_j+\mathbf{n}L)|}\cdot\mathbf{m}_j.\end{aligned} \tag{7.30}$$

To compute the exact magnetostatic field (7.27) the influence of the fields generated from neighboring FD cells will be corrected later on

$$\mathbf{H}_{ms}(\mathbf{r}_i) = \mathbf{H}_{ms}^{dip}(\mathbf{r}_i) + \sum_{\text{j=neighbors}}\left[\mathbf{h}_{ms}^{FD}(\mathbf{r}_i-\mathbf{r}_j)-\mathbf{h}_{ms}^{dip}(\mathbf{r}_i-\mathbf{r}_j)\right]. \tag{7.31}$$

Reformulation in fast converging series

When the Ewald summation technique is applied, expression (7.30) for $\mathbf{H}_{ms}^{dip}$ is evaluated efficiently. Since the kernel $1/|\mathbf{r}|$ decreases only slowly with growing r, a large number of terms in the sum (7.30) have to be taken into account to have an accurate result, classically resulting in a highly time inefficient evaluation scheme. To alleviate this problem, a diffuse magnetization is added and substracted in each FD cell oriented in the opposite direction of the local (discrete) magnetization dipole, see Fig. 7.4. In every FD cell j, this diffuse screening magnetization $M_s\mathbf{m}_j^{scr}(\mathbf{r})$ compensates for the actual magnetization $M_s\mathbf{m}_j$, which makes the resulting magnetostatic field decay rapidly to zero at a prescribed distance. In accordance with the electrostatic Ewald summation, we choose the screening magnetization to be Gaussian. To compensate a (normalized) magnetic dipole $\mathbf{m}_0$ in the origin, the (normalized) screening

magnetization $\mathbf{m}_0^{scr}$ is

$$\mathbf{m}_0^{scr}(\mathbf{r}) = -\mathbf{m}_0 \left(\frac{\beta}{\pi}\right)^{3/2} e^{-\beta r^2} \tag{7.32}$$

The screening magnetization is added to and subtracted from $\mathbf{m}(\mathbf{r})$, resulting in

$$\begin{aligned}\mathbf{H}_{ms}^{dip}(\mathbf{r}_i) = -\frac{M_s}{4\pi} \sum_{j=1}^{N'} \sum_{\mathbf{n}\in\mathbb{Z}^d} \nabla_i \nabla_i \frac{1}{|\mathbf{r}_i - (\mathbf{r}_j + \mathbf{n}L)|} \\ \cdot \left[\mathbf{m}_j + \mathbf{m}_j^{scr}(\mathbf{r}_i - (\mathbf{r}_j + \mathbf{n}L)) - \mathbf{m}_j^{scr}(\mathbf{r}_i - (\mathbf{r}_j + \mathbf{n}L))\right].\end{aligned} \tag{7.33}$$

We can split this expression in two sums, a direct sum $\mathbf{H}_{ms}^{dir}(\mathbf{r}_i)$ that is converging fast in real space and a reciprocal sum leading to $\mathbf{H}_{ms}^{scr}(\mathbf{r}_i)$, related with the screening potentials that is converging fast in Fourier space.

$$\mathbf{H}_{ms}^{dip}(\mathbf{r}_i) = \mathbf{H}_{ms}^{dir}(\mathbf{r}_i) + \mathbf{H}_{ms}^{scr}(\mathbf{r}_i). \tag{7.34}$$

Both sums are shown in Fig. 7.4.

Direct sum

Since the $\mathbf{m}_j^{scr}(\mathbf{r})$ compensates for $\mathbf{m}_j$, the direct sum

$$\begin{aligned}\mathbf{H}_{ms}^{dir}(\mathbf{r}_i) = -\frac{M_s}{4\pi} \sum_{j=1}^{N'} \sum_{\mathbf{n}\in\mathbb{Z}^d} \nabla_i \nabla_i \frac{1}{|\mathbf{r}_i - (\mathbf{r}_j + \mathbf{n}L)|} \\ \cdot \left[\mathbf{m}_j + \mathbf{m}_j^{scr}(\mathbf{r}_i - (\mathbf{r}_j + \mathbf{n}L))\right]\end{aligned} \tag{7.35}$$

converges very fast. Hence, only a small number of terms, i.e. a small number of periods have to be taken into account in the summation. The exact number of terms for a given precision depends on how well the magnetization is compensated for. This depends on the width of the Gaussian distribution. For β in 7.32 very large, the Gaussian distribution evolves towards a delta function which compensates the magnetization perfectly. For small values of β more terms have to taken into account. This is shown in Fig. 7.4. The standard FFT techniques are adopted to compute the direct sum in a fast way.

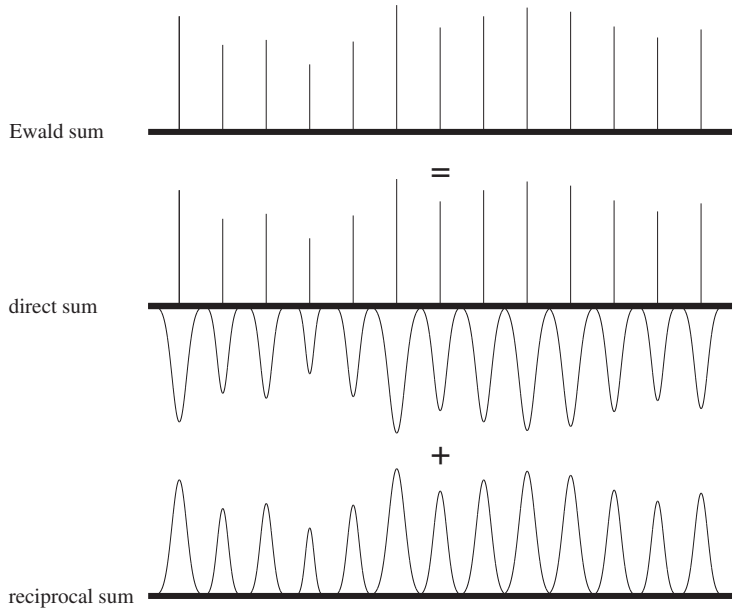

Figure 7.4: The slowly converging infinite Ewald sum is reformulated as the sum of two fast converging series. As a combination of the actual magnetizations and the compensating screening magnetizations, the direct sum converges fast in real space. The sum of compensating screening magnetizations converges fast in reciprocal, Fourier space.

Reciprocal sum

The reciprocal sum

$$\begin{aligned}\mathbf{H}_{ms}^{scr}(\mathbf{r}_i) &= \frac{M_s}{4\pi}\sum_{j=1}^{N'}\sum_{\mathbf{n}\in\mathbb{Z}^d}\nabla_i\nabla_i\frac{1}{|\mathbf{r}_i-(\mathbf{r}_j+\mathbf{n}L)|}\cdot\mathbf{m}_j^{scr}(\mathbf{r}_i-(\mathbf{r}_j+\mathbf{n}L)) \\ &= \frac{M_s}{4\pi}\sum_{j=1}^{N}\sum_{\mathbf{n}\in\mathbb{Z}^d}\nabla_i\nabla_i\frac{1}{|\mathbf{r}_i-(\mathbf{r}_j+\mathbf{n}L)|}\cdot\mathbf{m}_j^{scr}(\mathbf{r}_i-(\mathbf{r}_j+\mathbf{n}L)) \\ &\quad -\mathbf{H}_{self}^{scr}(\mathbf{m}_i)\end{aligned} \tag{7.36}$$

is only slowly convergent. In the first expression, the self contribution of the screening magnetization corresponding to $i=j$, $\mathbf{n}=[0,0,0]$ is omitted, while in the second expression, this term is included and subtracted afterwards. The sum is only slowly convergent in real space, but will converge fast in Fourier space (reciprocal space).

The magnetostatic field originating in the screening magnetizations (7.36) can also be written in terms of its corresponding potential, $\mathbf{H}_{ms}^{scr}=-\nabla\psi_{ms}^{scr}$.

Then $\mathbf{H}_{ms}^{scr}$ is determined by solving the Poisson problem $\nabla^2\psi_{ms}^{scr} = -M_s\nabla\cdot\mathbf{m}^{scr}$. Rewritten in Fourier space, these expressions result in

$$\widetilde{\mathbf{H}}_{ms}^{scr}(\mathbf{k}) = -\mathbf{k}\widetilde{\psi}_{ms}^{scr}(\mathbf{k}) \tag{7.37}$$

and

$$k^2\widetilde{\psi}_{ms}^{scr}(\mathbf{k}) = -M_s\mathbf{k}\cdot\widetilde{\mathbf{m}}^{scr}(\mathbf{k}). \tag{7.38}$$

Based on (7.32), the total screening magnetization $\mathbf{m}^{scr}(\mathbf{r})$ is defined as

$$\begin{aligned}\mathbf{m}^{scr}(\mathbf{r}) &= \sum_{j=1}^{N}\sum_{\mathbf{n}\in\mathbb{Z}^d}\mathbf{m}_j^{scr}\left(\mathbf{r}-(\mathbf{r}_j+\mathbf{n}L)\right)\\ &= -\sum_{j=1}^{N}\sum_{\mathbf{n}\in\mathbb{Z}^d}\mathbf{m}_j\left(\frac{\beta}{\pi}\right)^{3/2}e^{-\beta|\mathbf{r}-(\mathbf{r}_j+\mathbf{n}L)|^2}\end{aligned} \tag{7.39}$$

The Fourier transform of this screening magnetization (7.39) is given by

$$\begin{aligned}\widetilde{\mathbf{m}}^{scr}(\mathbf{k}) &= -\int\sum_{j=1}^{N}\sum_{\mathbf{n}\in\mathbb{Z}^d}\mathbf{m}_j\left(\frac{\beta}{\pi}\right)^{3/2}e^{-\beta|\mathbf{r}-(\mathbf{r}_j+\mathbf{n}L)|^2}e^{-\imath\mathbf{k}\cdot\mathbf{r}}\,\mathrm{d}\mathbf{r}\\ &= -\sum_{j=1}^{N}\sum_{\mathbf{n}\in\mathbb{Z}^d}\mathbf{m}_j e^{-\imath\mathbf{k}\cdot\mathbf{r}_j}e^{-\imath\mathbf{k}\cdot\mathbf{n}L}\\ &\quad\times\left(\frac{\beta}{\pi}\right)^{3/2}\int e^{-\beta|\mathbf{r}-(\mathbf{r}_j+\mathbf{n}L)|^2}e^{-\imath\mathbf{k}\cdot\left[\mathbf{r}-(\mathbf{r}_j+\mathbf{n}L)\right]}\,\mathrm{d}\left[\mathbf{r}-(\mathbf{r}_j+\mathbf{n}L)\right]\\ &= -\sum_{j=1}^{N}\sum_{\mathbf{n}\in\mathbb{Z}^d}\mathbf{m}_j e^{-\imath\mathbf{k}\cdot\mathbf{r}_j}e^{-\imath\mathbf{k}\cdot\mathbf{n}L}e^{-k^2/4\beta}.\end{aligned} \tag{7.40}$$

Due to the periodicity (7.25), it holds that ($\boldsymbol{\nu}$ is an integer vector)

$$\begin{aligned}\mathbf{m}^{scr}(\mathbf{r}+\boldsymbol{\nu}L) &= -\mathbf{m}\left(\frac{\beta}{\pi}\right)^{3/2}e^{-\beta|\mathbf{r}-[\mathbf{r}_j+(\mathbf{n}L-\boldsymbol{\nu}L)]|^2}\\ &= \mathbf{m}^{scr}(\mathbf{r}),\end{aligned} \tag{7.41}$$

and analogously in Fourier space. Fourier transforming $\mathbf{m}_j^{scr}(\mathbf{r}+\boldsymbol{\nu}L)$ as outlined above yields

$$\mathcal{F}ourier\left\{\mathbf{m}_j^{scr}(\mathbf{r}+\boldsymbol{\nu}L)\right\} = -\sum_{j=1}^{N}\sum_{\mathbf{n}\in\mathbb{Z}^d}\mathbf{m}_j e^{-\imath\mathbf{k}\cdot\mathbf{r}_j}e^{-\imath\mathbf{k}\cdot(\mathbf{n}+\boldsymbol{\nu})L}e^{-k^2/4\beta}, \tag{7.42}$$

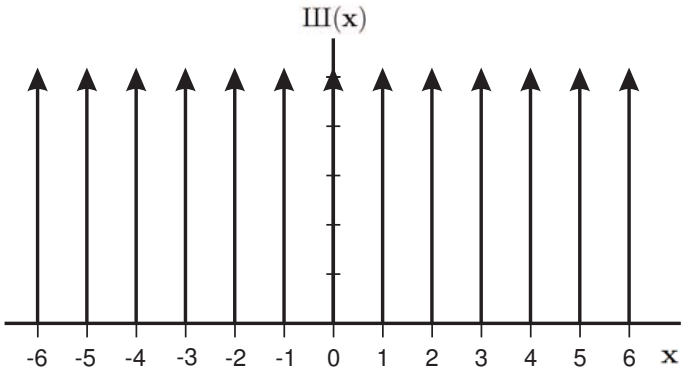

Figure 7.5: 1D comb or Shah function $\mathrm{III}(x) = \sum_{n=-\infty}^{\infty} \delta(x-n)$.

which should be identical to (7.40). Hence the non zero values of the $\mathbf{k}$ vectors are restricted to

$$\mathbf{k} = \frac{2\pi}{L}\mathbf{I} \qquad \mathbf{I} \in \mathbb{Z}^d. \tag{7.43}$$

Consequently, whenever $\mathbf{k} = \frac{2\pi}{L}\mathbf{I}$, $\mathbf{I} \in \mathbb{Z}^d$ the sum $\sum_{n\in\mathbb{Z}^d} e^{-\imath \mathbf{k}\cdot\mathbf{n}L}$ reduces to

$$\sum_{n\in\mathbb{Z}^d} 1 = \infty. \tag{7.44}$$

With the use of delta Dirac function $\delta(x)$ (infinite when $x = 0$ and zero when $x \neq 0$)

$$\sum_{\mathbf{n}\in\mathbb{Z}^d} e^{-\imath \mathbf{k}\cdot\mathbf{n}L} = \sum_{I\in\mathbb{Z}^d} \delta(\mathbf{k} - \frac{2\pi}{L}\mathbf{I}). \tag{7.45}$$

An infinite sum of uniformly placed delta functions is per definition the comb or Shah function

$$\mathrm{III}(\mathbf{x}) \stackrel{\text{def}}{=} \sum_{I\in\mathbb{Z}^d} \delta(\mathbf{x} - \mathbf{I}). \tag{7.46}$$

The 1D comb function is shown in Fig. 7.5. Hence, the Fourier transform of the screening magnetization $\mathbf{m}^{scr}(\mathbf{r})$ is

$$\widetilde{\mathbf{m}}^{scr}(\mathbf{k}) = -\sum_{j=1}^{N} \mathbf{m}_j e^{-\imath \mathbf{k}\cdot\mathbf{r}_j} e^{-k^2/4\beta} \mathrm{III}\left(\frac{L}{2\pi}\mathbf{k}\right). \tag{7.47}$$

Combining (7.38) and (7.47) yields the screening potential in Fourier space

$$\begin{aligned}\widetilde{\psi}_{ms}^{scr}(\mathbf{k}) &= -M_s \frac{\mathbf{k}}{k^2} \cdot \widetilde{\mathbf{m}}^{scr}(\mathbf{k}) \\ &= M_s \sum_{j=1}^{N} \frac{\mathbf{k}}{k^2} \cdot \mathbf{m}_j e^{-\imath \mathbf{k} \cdot \mathbf{r}_j} e^{-k^2/4\beta} \text{III}\left(\frac{L}{2\pi}\mathbf{k}\right).\end{aligned} \tag{7.48}$$

Note that we have to assume $\widetilde{\psi}_{ms}^{scr}(\mathbf{0}) = 0$. We can do this since the Fourier contribution at $\mathbf{k} = 0$ corresponds to the zero spatial frequency component of the screening potential in real space, i.e. the (constant) average of the potential. In general, a potential is only determined except for a constant: $\nabla\psi = \nabla(\psi' + C^{st})$, hence we can choose this constant to compensate for the average of the potential. Inverse Fourier transforming this result provides the screening potential in real space

$$\psi_{ms}^{scr}(\mathbf{r}_i) = M_s \frac{1}{L^3} \int \sum_{j=1}^{N} \frac{\mathbf{k}}{k^2} \cdot \mathbf{m}_j e^{\imath \mathbf{k} \cdot (\mathbf{r}_i - \mathbf{r}_j)} e^{-k^2/4\beta} \text{III}\left(\frac{L}{2\pi}\mathbf{k}\right) \mathrm{d}\mathbf{k}. \tag{7.49}$$

Due to the Dirac functions in the 3D comb function, the integral over total space reduces to a sum over distinct $\mathbf{k}$ values

$$\psi_{ms}^{scr}(\mathbf{r}_i) = M_s \frac{1}{L^3} \sum_{\mathbf{k} \neq 0} \sum_{j=1}^{N} \frac{\mathbf{k}}{k^2} \cdot \mathbf{m}_j e^{\imath \mathbf{k} \cdot (\mathbf{r}_i - \mathbf{r}_j)} e^{-k^2/4\beta}. \tag{7.50}$$

Combining (7.37), (7.38) and (7.47) yields the screening magnetostatic field in Fourier space

$$\begin{aligned}\widetilde{\mathbf{H}}_{ms}^{scr}(\mathbf{k}) &= -M_s \frac{\mathbf{k}\mathbf{k}}{k^2} \cdot \widetilde{\mathbf{m}}^{scr}(\mathbf{k}) \\ &= -M_s \sum_{j=1}^{N} \frac{\mathbf{k}\mathbf{k}}{k^2} \cdot \mathbf{m}_j e^{-\imath \mathbf{k} \cdot \mathbf{r}_j} e^{-k^2/4\beta} \text{III}\left(\frac{L}{2\pi}\mathbf{k}\right).\end{aligned} \tag{7.51}$$

Inverse Fourier transforming this result provides the screening magnetostatic field in real space

$$\mathbf{H}_{ms}^{scr}(\mathbf{r}_i) = -M_s \frac{1}{L^3} \sum_{\mathbf{k} \neq 0} \sum_{j=1}^{N} \frac{\mathbf{k}\mathbf{k}}{k^2} \cdot \mathbf{m}_j e^{\imath \mathbf{k} \cdot (\mathbf{r}_i - \mathbf{r}_j)} e^{-k^2/4\beta}. \tag{7.52}$$

Due to the $e^{-k^2/4\beta}$ term, both the series (7.50) and (7.52) converge rapidly. The parameter β determines how many terms one should include in the sum to reach a given precision. When β is large, more terms have to contribute to the sum and vice versa. Note that these are conclusions are opposite when

compared to those for the direct sum. When a small number of terms is sufficient for convergence of the direct sum, a large number of terms is needed to guarantee the convergence of the reciprocal sum. In [90] it is shown that for $\beta = \pi/L$ both series converge at the same rate.

Self contribution to the reciprocal sum

In the reciprocal sum, a contribution of the screening magnetization to itself is also included. This self contribution has to be subtracted from the result, see (7.35). The self contribution is determined by solving the problem

$$\begin{aligned} \nabla^2 \psi^{scr}_{self}(\mathbf{r}) &= -M_s \nabla \cdot \mathbf{m}^{scr}_0(\mathbf{r}) \\ &= M_s \nabla \cdot \mathbf{m}_0 \left(\frac{\beta}{\pi}\right)^{3/2} e^{-\beta r^2}. \end{aligned} \tag{7.53}$$

Therefore the auxiliary problem

$$\nabla^2 \psi'^{scr}_{self}(\mathbf{r}) = \frac{1}{r}\frac{\partial^2}{\partial r^2}\left(r\psi'^{scr}_{self}(\mathbf{r})\right) = \left(\frac{\beta}{\pi}\right)^{3/2} e^{-\beta r^2} \tag{7.54}$$

is first solved. This differential equation has the solution

$$\psi'^{scr}_{self}(\mathbf{r}) = -\frac{1}{4\pi}\frac{\mathrm{erf}(\sqrt{\beta}r)}{r} \tag{7.55}$$

with $\mathrm{erf}(x)$ the error function. Now expression (7.53) can be written as

$$\begin{aligned} \nabla^2 \psi^{scr}_{self}(\mathbf{r}) &= M_s \nabla \cdot \mathbf{m}_0 \nabla^2 \psi'^{scr}_{self}(\mathbf{r}) \\ &= \nabla^2 M_s \nabla \cdot \mathbf{m}_0 \psi'^{scr}_{self}(\mathbf{r}) \end{aligned} \tag{7.56}$$

which yields

$$\begin{aligned} \psi^{scr}_{self}(\mathbf{r}) &= M_s \mathbf{m}_0 \cdot \nabla \psi'^{scr}_{self}(\mathbf{r}) \\ &= M_s \left(m_{0,x}\frac{\partial}{\partial x} + m_{0,y}\frac{\partial}{\partial y} + m_{0,z}\frac{\partial}{\partial z}\right) \psi'^{scr}_{self}(\mathbf{r}) + C, \end{aligned} \tag{7.57}$$

with C some constant. This constant is chosen zero since it does not affect the resulting magnetostatic field. The contribution for the x-component is

$$\begin{aligned} & M_s m_{0,x}\frac{\partial}{\partial x}\left\{-\frac{1}{4\pi}\frac{\mathrm{erf}(\sqrt{\beta}r)}{r}\right\} \\ &\quad = \frac{M_s m_{0,x}}{4\pi}\frac{\mathrm{erf}(\sqrt{\beta}r)}{r^{3/2}}x - M_s m_{0,x}\frac{\sqrt{\beta}}{2\pi^{3/2}}\frac{e^{-\beta r^2}}{r^2}x. \end{aligned} \tag{7.58}$$

In the limit for **r** going to zero this contribution goes to zero. The contributions of the y and z component are determined in an analogous way, which results in a zero self contribution generated by the screening magnetization. Hence expression (7.52) completely determines the reciprocal sum (7.36), which can also be computed using the standard FFT techniques.

7.5. Conclusion

In this chapter, we have introduced numerical schemes to evaluate the magnetostatic interactions based on fast Fourier transforms. The use of FFTs drastically reduces the memory requirements from $\mathcal{O}(N^2)$ to $\mathcal{O}(N)$ and the CPU time from $\mathcal{O}(N^2)$ to $\mathcal{O}(N \log N)$ to compute the magnetostatic field in each FD cell. The FFT based $\mathbf{H}_{ms}$ evaluation schemes differ in the memory requirements, the CPU time needed to compute a field distribution and the obtained accuracy. The high accuracy $\mathbf{H}_{ms}$ evaluation scheme computes the fields up to machine precision, but has the largest memory requirements and CPU time. The low accuracy $\mathbf{H}_{ms}$ evaluation scheme is faster and requires less memory but results in less accurate results.

In most 'classical' micromagnetic applications the field computations have to have a high accuracy since one is interested in the exact magnetization processes present on the microscopic time and length scale. For these applications the high accuracy $\mathbf{H}_{ms}$ evaluation scheme should be used. In most of these 'classical' micromagnetic simulations rather small samples are investigated, so there is no strong need here to reduce the memory requirements and CPU time. This need however is strongly present in micromagnetic hysteresis simulations. Hence, from a computational point of view it would be advantageous to use the low accuracy $\mathbf{H}_{ms}$ evaluation scheme. In Chapter 9 we will discuss the impact of the low accuracy evaluation of $\mathbf{H}_{ms}$ in micromagnetic hysteresis simulations.

Further, numerical procedures are presented to compute the magnetostatic field in periodic structures. As outlined in Chapter 3, these procedures must be used if one aims at reducing the demagnetizing effects in a ferromagnetic sample along one or two dimensions.

CHAPTER 8

Fast Multipole Method based evaluation of the magnetostatic field

8.1. Introduction

FFT schemes as described in the previous chapter have been very popular to reduce the computational cost for the evaluation of the magnetostatic field to $\mathcal{O}(N \log N)$. However, all these FFT schemes have some drawbacks: (i) the domain under study has to be a rectangular prism. Hence, more complex geometries have to be embedded in a rectangular domain, adding FD cells containing no magnetic material, which introduces some overhead; (ii) all FD cells have to be equal in size and placed on a regular grid excluding the possibility of adaptive discretization; (iii) FFT based schemes use a large amount of memory resources largely due to the need of zero padding. On the other hand, as shown in the previous chapter, FFT based schemes are very fast and robust so they should be used as a reference to study the performance of other numerical schemes for the evaluation of the magnetostatic field.

In order to overcome (some of) the drawbacks FFT schemes encounter, numerical schemes can be adopted describing the generated magnetostatic fields in terms of multipole expansions. These multipole schemes all go back to the Fast Multipole Method (FMM) introduced by L. Greengard in [91]. The fast multipole method is adopted far numerous physical problems: electrostatic problems e.g. [92], fluid dynamics e.g. [93], molecular dynamics e.g. [94], electromagnetic scattering problems e.g. [95], acoustics e.g. [96], etc. When static electromagnetic problems are considered –as in the considered micromagnetic problem– the FMM scales $\mathcal{O}(N)$ and could thus be faster than FFT

based $\mathbf{H}_{ms}$ evaluation schemes. In the micromagnetic research area the use of multipole methods is not yet well spread. The Fast Fourier Transform on Multipole (FFTM) technique [97] has been developed by Ong et al. as a combination of the FMM and FFT method. They have used this scheme to describe recording techniques e.g. [98]. This method is more flexible then a pure FFT scheme and has a controllable error bound. However, the performance of the FFTM scheme has not yet been compared with e.g. a pure FFT scheme. The method still needs a considerable amount of memory resources, while the authors state in [98] '*However, as the two algorithms scale differently with p, FFTM is not necessarily more efficient than FMM*', with p referring to the number of multipole coefficients (see further). Visscher et al. use an FMM algorithm based on Cartesian expansions, see e.g. [99].

This Chapter presents an FMM scheme based on spherical harmonic expansions for the evaluation of the magnetostatic field in a ferromagnetic body developed during the presented PhD. In the next section we will describe how the FD geometry discretization is handled in the context of the FMM algorithm. Later it is described how the far and near field computations are elaborated. The performance of the presented FMM scheme is investigated by comparing it with the high accuracy FFT scheme presented in the previous section.

8.2. Geometry description

The three dimensional ferromagnetic body can have all possible shapes. It is divided into cubical FD cells using a tree structure defining the *FMM tree* as described in [91]. The ferromagnetic body is enclosed by a cubic box. This enclosing box is called the *root*: the box on *level zero* of the FMM tree. On a next level (*level one*) the root box is divided into 8 smaller cubical boxes with identical volumes. These are called the *children* of the root box. Vice versa, the root box is the *parent* box of the 8 smaller boxes. This division is performed recursively until the boxes on the lowest level (level LEV) in the tree have the desired dimension. In the case of a non-cubic ferromagnetic body, the boxes that do not contain any magnetic material are neglected. The resulting FD discretization is analogous with the discretization presented in Chapter 6. In what follows the body will be considered cubical. This does not affect the applicability of the scheme to non-cubic ferromagnetic bodies. Other definitions used to describe the FMM tree:

- Two boxes are said to be *neighbors* if they are at the same refinement level and share a boundary point (a box is a neighbor of itself).
- Two boxes are said to be *well separated* if they are at the same refinement level and are not neighbors.

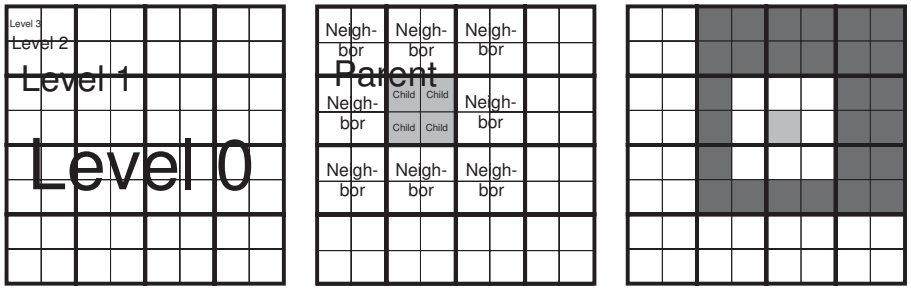

Figure 8.1: Definitions used in the FMM theory. The definitions in the middle figure are with respect to the gray colored box. The dark colored boxes in the right figure define the interaction list of the gray colored, central box.

- With each box i an *interaction list* is associated, consisting of the children of the neighbors of i's parent which are well separated from box i.

These definitions are illustrated in Fig. 8.1.

The bookkeeping of the boxes is based on the binary structure of the FMM tree [100]. At each level L the boxes get an identity number (*id*) from 0 to $8^L - 1$. The binary tree structure allows to determine various quantities using computations that can be implemented at bit-level (using bit shift procedures). This results into bookkeeping computations which are negligible compared with other computations: given the *id* and the level of a box, the parent of the box, the neighbors of the box and the center coordinates of the box are found almost instantaneously when the binary structure of the tree is exploited. Vice versa, the *id* of the box containing a point with given coordinates at a given level can be determined also almost instantaneously.

In this implementation of the FMM algorithm, the boxes on the lowest level LEV are called basis boxes. Each basis box itself is further subdivided in cubical FD cells. The number of FD cells in a basis box is 8^{lev}: in each dimension 2^{lev} FD cells. Hence, the total (cubical) geometry contains $8^{LEV+lev}$ FD cells. Figure 8.2 shows a geometry described with a tree containing 2 levels ($LEV = 2$) and basis boxes containing 2^{lev} ($lev = 3$) FD cells in each direction.

In the FMM theory a distinction is made between boxes that are *far* from each other and boxes that are *near* to each other. Boxes that are far from each other interact via their *far field* which is outlined in Section 8.3. Neighboring basis boxes interact with each other via near field computations, this is outlined in Section 8.4. The dimensions of the basis boxes will influence the time spent on near and far field computations. Depending on the difference in computation time of the far field computations and the near field computations an optimal tree can be constructed. Indeed, for a geometry with 8^{tot_lev} FD cells different parameters LEV and lev can be combined such that

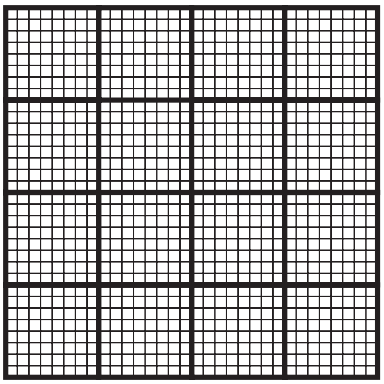

Figure 8.2: A tree with $LEV = 2$ and $lev = 3$.

$LEV + lev = tot\_lev$, i.e. different sizes of basis boxes can be used. The optimal size of the basis boxes depends on the computational time. This discussion is repeated in Section 8.5.

8.3. Far field computations

This section explains the computations of the magnetostatic fields due to FD cells that are part of well separated basis boxes. It is shown how the magnetic field is rewritten in terms of expansions in spherical harmonics. The far field computations are based on the classical FMM theory of L. Greengard [91]. This classical theory is summarized and extended to magnetic dipole sources. The used translation operators are accelerated, exploiting symmetries and convolution structures. It is the intention to develop an algorithm that allows to compute the magnetostatic fields multiple times for different magnetic configurations in a fast way. Hence, generic computations are performed as much as possible during the set up phase of the algorithm in order to avoid duplicating computations.

8.3.1 Classical FMM theory

As described in Chapter 3, the magnetostatic field in a point $\mathbf{r}$ generated by a FD cell with volume V' ($\mathbf{r} \notin V'$) can be written as

$$\begin{aligned}\mathbf{H}_{ms}(\mathbf{r}) &= -\frac{M_s}{4\pi}\int\limits_{V'} \nabla\nabla\frac{1}{|\mathbf{r}-\mathbf{r}'|}\cdot\mathbf{m}(\mathbf{r}')\,\mathrm{d}\mathbf{r}' \\ &= \frac{M_s}{4\pi}\nabla\int\limits_{V'}\left[\nabla'\frac{1}{|\mathbf{r}-\mathbf{r}'|}\right]\cdot\mathbf{m}(\mathbf{r}')\,\mathrm{d}\mathbf{r}'\end{aligned} \tag{8.1}$$

where the ∇' operator acts on $\mathbf{r}'$. We repeat that all FD cells are considered to be uniformly magnetized with a fixed magnetization amplitude M_s and a varying magnetization orientation given by the unit vector $\mathbf{m}(\mathbf{r}')$. The vectors $\mathbf{r}$ and $\mathbf{r}'$ are defined in spherical coordinates as

$$\begin{aligned}\mathbf{r}' &\rightarrow (\rho,\alpha,\beta) \\ \mathbf{r} &\rightarrow (r,\theta,\phi).\end{aligned}$$

Now the kernel $1/|\mathbf{r}-\mathbf{r}'|$ can be rewritten in an expansion of spherical harmonics, using the spherical harmonic addition theorem for Legendre polynomials $P_n(x)$ [53]. In the case of $\rho < r$ this gives

$$\begin{aligned}\frac{1}{|\mathbf{r}-\mathbf{r}'|} &= \sum_{n=0}^{\infty}\frac{\rho^n}{r^{n+1}}P_n\left(\frac{\mathbf{r}\cdot\mathbf{r}'}{rr'}\right) \\ &= \sum_{n=0}^{\infty}\sum_{m=-n}^{n}\rho^n Y_n^{-m}(\alpha,\beta)\frac{Y_n^m(\theta,\phi)}{r^{n+1}}.\end{aligned} \tag{8.2}$$

The spherical harmonic $Y_n^m(\theta,\phi)$ is defined as

$$Y_n^m(\theta,\phi) = \sqrt{\frac{(n-|m|)!}{(n+|m|)!}}P_n^{|m|}(\cos(\theta))e^{\imath m\phi} \tag{8.3}$$

with

$$P_n^m(x) = (-1)^m(1-x^2)^{m/2}\frac{\mathrm{d}^m}{\mathrm{d}x^m}P_n(x). \tag{8.4}$$

The magnetostatic field (8.1) can now be written in terms of the scalar magnetic potential $\psi(\mathbf{r})$ as

$$\mathbf{H}_{ms}(\mathbf{r}) = \frac{M_s}{4\pi}\nabla\psi(\mathbf{r}). \tag{8.5}$$

When the addition theorem (8.2) is introduced, $\psi(\mathbf{r})$ is given by

$$\begin{aligned}\psi(\mathbf{r}) &= \int_{V'} \nabla' \sum_{n=0}^{\infty} \sum_{m=-n}^{n} \rho^n Y_n^{-m}(\alpha,\beta) \frac{Y_n^m(\theta,\phi)}{r^{n+1}} \cdot \mathbf{m}\,\mathrm{d}V' \\ &= \sum_{n=0}^{\infty} \sum_{m=-n}^{n} \left\{ \int_{V'} \nabla' \rho^n Y_n^{-m}(\alpha,\beta) \cdot \mathbf{m}\,\mathrm{d}V' \right\} \frac{Y_n^m(\theta,\phi)}{r^{n+1}} \\ &= \sum_{n=0}^{\infty} \sum_{m=-n}^{n} O_n^m(\mathbf{m}) \frac{Y_n^m(\theta,\phi)}{r^{n+1}}.\end{aligned} \tag{8.6}$$

This defines the expansion coefficients $O_n^m(\mathbf{m})$ of a FD cell with uniform magnetization $\mathbf{M} = M_s\mathbf{m}$. Now analytical expressions will be derived for the expansion coefficients.

Computation of the expansion coefficients $O_n^m(\mathbf{m})$ of a cubical FD cell

Above, the expansion coefficients $O_n^m(\mathbf{m})$ of a cubical FD cell with uniform magnetization $\mathbf{m}$ are defined as

$$O_n^m(\mathbf{m}) = \int_V \nabla \rho^n Y_n^{-m}(\alpha,\beta)\,\mathrm{d}V \cdot \mathbf{m}. \tag{8.7}$$

Applying Gauss' theorem gives

$$O_n^m(\mathbf{m}) = \int_{\partial V} \rho^n Y_n^{-m}(\alpha,\beta)\mathbf{u}\,\mathrm{d}S \cdot \mathbf{m} \tag{8.8}$$

with $\mathbf{u}$ the normal unit vector pointing outward of the cell and ∂V the boundary surface of the cell. The explicit computation of the expansion coefficients is done by determining the contributions from each surface of the cubical FD cell with edge length of 2Δ and adding them:

$$\begin{aligned}&O_n^m(\mathbf{m}) = \\ &\left(-\int_{-\Delta}^{\Delta}\int_{-\Delta}^{\Delta} \rho^n Y_n^{-m}(\alpha,\beta)\,\mathrm{d}x\,\mathrm{d}y \Big|_{z=-\Delta} + \int_{-\Delta}^{\Delta}\int_{-\Delta}^{\Delta} \rho^n Y_n^{-m}(\alpha,\beta)\,\mathrm{d}x\,\mathrm{d}y \Big|_{z=\Delta} \right) m_z \\ &+ \left(-\int_{-\Delta}^{\Delta}\int_{-\Delta}^{\Delta} \rho^n Y_n^{-m}(\alpha,\beta)\,\mathrm{d}x\,\mathrm{d}z \Big|_{y=-\Delta} + \int_{-\Delta}^{\Delta}\int_{-\Delta}^{\Delta} \rho^n Y_n^{-m}(\alpha,\beta)\,\mathrm{d}x\,\mathrm{d}z \Big|_{y=\Delta} \right) m_y \\ &+ \left(-\int_{-\Delta}^{\Delta}\int_{-\Delta}^{\Delta} \rho^n Y_n^{-m}(\alpha,\beta)\,\mathrm{d}y\,\mathrm{d}z \Big|_{x=-\Delta} + \int_{-\Delta}^{\Delta}\int_{-\Delta}^{\Delta} \rho^n Y_n^{-m}(\alpha,\beta)\,\mathrm{d}y\,\mathrm{d}z \Big|_{x=\Delta} \right) m_x.\end{aligned} \tag{8.9}$$

When $\rho^n Y_n^{-m}(\alpha,\beta)$ is expressed in Cartesian coordinates

$$\rho^n Y_n^{-m}(\alpha,\beta) = (x^2+y^2+z^2)^{n/2}\sqrt{\frac{(n-|m|)!}{(n+|m|)!}}P_n^{|m|}\left(\frac{z}{\sqrt{x^2+y^2+z^2}}\right)\left(\frac{x-\imath y}{\sqrt{x^2+y^2}}\right)^m \tag{8.10}$$

and the resulting expressions are simplified exploiting some symmetry properties. This leads to

$$O_n^m(\mathbf{m}) = \sqrt{\frac{(n-|m|)!}{(n+|m|)!}}\times$$

$$\begin{cases} \text{n even} & 0 \\ \text{n odd, m odd} & \begin{aligned} &2m_x\int_{-\Delta}^{\Delta}\int_{-\Delta}^{\Delta}(\Delta^2+y^2+z^2)^{\frac{n}{2}}P_n^{|m|}\left(\frac{z}{\sqrt{\Delta^2+y^2+z^2}}\right) \\ &\qquad\times\mathcal{R}\mathrm{e}\left(\frac{\Delta-\imath y}{\sqrt{\Delta^2+y^2}}\right)^m \mathrm{d}y\,\mathrm{d}z \\ &+2m_y i\int_{-\Delta}^{\Delta}\int_{-\Delta}^{\Delta}(x^2+\Delta^2+z^2)^{\frac{n}{2}}P_n^{|m|}\left(\frac{z}{\sqrt{x^2+\Delta^2+z^2}}\right) \\ &\qquad\times\mathcal{I}\mathrm{m}\left(\frac{x-\imath\Delta}{\sqrt{x^2+\Delta^2}}\right)^m \mathrm{d}x\,\mathrm{d}z \end{aligned} \\ \text{n odd, m even} & \begin{aligned} &m_z\int_{-\Delta}^{\Delta}\int_{-\Delta}^{\Delta}(x^2+y^2+\Delta^2)^{\frac{n}{2}}\left[P_n^{|m|}\left(\frac{\Delta}{\sqrt{x^2+y^2+\Delta^2}}\right)\right. \\ &\qquad\left.-P_n^{|m|}\left(\frac{-\Delta}{\sqrt{x^2+y^2+\Delta^2}}\right)\right]\left(\frac{x-\imath y}{\sqrt{x^2+y^2}}\right)^m \mathrm{d}x\,\mathrm{d}y \end{aligned} \end{cases} . \tag{8.11}$$

Here and further on, the number of expansion coefficients is truncated to $n < p$. The expansion of the magnetic potential (8.6) is valid everywhere except inside the circumscribing sphere of the box [91].

The multipole (MP) expansions (8.11) are the basis of the FMM theory. The MP expansion (8.11) of a FD cell determines the magnetostatic field pattern radiated by a FD cell with a normalized magnetization $\mathbf{m}$. The origin of the coordinate system in which (8.11) is expressed coincides with the center of the considered FD cell. In the FMM algorithm, the MP expansions of the FD cells are now combined to define MP expansions of larger groups on lower levels. Therefore, the MP expansions of child boxes need to be expressed in coordinate systems of which the origin coincides with the center of the parent

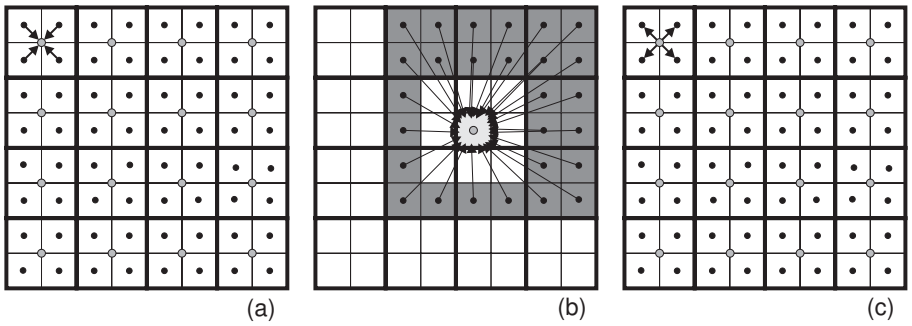

Figure 8.3: Sketch of (a) MP to MP translations, (b) MP to local translations and (c) local to local translations

box. These translation operations are performed by the MP to MP translations, shown in Fig. 8.3.a.

To compute the magnetostatic field in a group, the outgoing MP expansions from well separated groups are reformulated: the magnetostatic field generated by well separated groups, described by their MP expansions is translated into a local expansion valid in the considered group. This reformulation of a MP expansion of a source group into a local expansion valid in a receiver group is performed by the MP to local translations. The resulting expression for the local expansion is described in a coordinate system of which the origin coincides with the center of the receiving group. The translation operations are performed by the MP to local translations, shown in Fig. 8.3.b.

The local expansions valid in each parent box are recursively translated in to local expansions valid in the boxes of their children. Therefore, the local expansion of the parent needs to be reformulated in the coordinate system of which the center coincides with the center of the considered child. The translation operations are performed by the local to local translations, shown in Fig. 8.3.c.

Once the local expansion is known in the center of a basis box, the magnetostatic field in each FD cell of the basis box is computed by the local to field operator. In what follows, the analytical expressions for these translation operators are presented. An extended discussion on the translation of MP expansions and local expansions as well as error bounds can be found in [101].

MP to MP translation operator

To translate a MP expansion O_n^m from the center of a box to a MP expansion M_j^k at the center of its parent, the following translation operator is used

$$M_j^k = \sum_{n=0}^{j} \sum_{m=\max(k+n-j,-n)}^{\min(k+j-n,n)} (-1)^n \imath^{|k|-|m|-|k-m|} \frac{A_n^m A_{j-n}^{k-m}}{A_j^k} r^n Y_n^{-m}(\theta,\phi) O_{j-n}^{k-m}. \tag{8.12}$$

(r, θ, ϕ) are the spherical coordinates of the center of the parent, seen in the coordinate system of the considered box. A_n^m is defined as:

$$A_n^m = \frac{(-1)^n}{\sqrt{(n-m)!(n+m!)}}. \tag{8.13}$$

For each parent box, 8 MP to MP translations have to be performed as shown in Fig. 8.3.a.

MP to local translation operator

To translate a MP expansion O_n^m from the center of a box to a local expansion L_j^k at the center of a box at the same level, the following translation operator is used

$$L_j^k = \sum_{n=0}^{p-1} \sum_{m=-n}^{n} (-1)^j \imath^{|k-m|-|k|-|m|} \frac{A_n^m A_j^k}{A_{j+n}^{m-k}} \frac{Y_{j+n}^{m-k}(\theta,\phi)}{r^{j+n+1}} O_n^m. \tag{8.14}$$

(r, θ, ϕ) are the spherical coordinates of the center of the box to where the MP expansion is translated, seen in the coordinate system of the considered box. As mentioned before, p is the truncation value of the included expansion coefficients ($j < p$ and n<p). Figure 8.3.b sketches the MP to local translations. It is clear that for each box, $6^3 - 3^3 = 189$ MP to local translations have to be performed (except for the boxes near the edge of the computation domain).

Local to local translation operator

To translate a local expansion O_n^m from the center of a parent box to a local expansion at the center of a child, the following translation operator is used

$$L_j^k = \sum_{n=j}^{p-1} \sum_{m=k-n+j}^{k-j+n} \imath^{|m|-|m-k|-|k|} \frac{A_{n-j}^{m-k} A_j^k}{A_n^m} r^{n-j} Y_{n-j}^{m-k}(\theta,\phi) O_n^m. \tag{8.15}$$

(r, θ, ϕ) are the spherical coordinates of the center of the child box, seen in the coordinate system of the parent box. For each parent box, 8 local to local translations have to be performed as shown in Fig. 8.3.c.

Local to field translation operator

To compute the field in a point $(\mathrm{r}, \theta, \phi)$ in a basis box with local expansion L_n^m at the center of the basis box, the gradient has to be taken of the scalar potential $\psi(\mathbf{r})$

$$\begin{aligned}\mathbf{H}_{ms}(\mathbf{r}) &= \frac{M_s}{4\pi}\nabla\psi(\mathbf{r}) \\ &= \frac{M_s}{4\pi}\sum_{n=0}^{p}\sum_{m=-n}^{n} L_n^m \nabla r^n Y_n^m(\theta,\phi).\end{aligned} \tag{8.16}$$

After the action of the gradient operator on $r^n Y_n^m$ the expression is rotated back to Cartesian coordinates, which results in

$$\begin{aligned}\mathbf{H}_{ms} =& \frac{M_s}{4\pi}\begin{bmatrix}\cos\phi\sin\theta & \cos\phi\cos\theta & -\sin\phi \\ \sin\phi\sin\theta & \sin\phi\cos\theta & \cos\phi \\ \cos\theta & -\sin\theta & 0\end{bmatrix} \\ &\times \begin{bmatrix}\sum\sum L_n^m n r^{n-1} Y_n^m(\theta,\phi) \\ \sum\sum L_n^m r^{n-1}\sqrt{\frac{(n-|m|)!}{(n+|m|)!}}\left(-\frac{\cos\theta}{\sin\theta}(n+1)P_n^{|m|}(\cos\theta)\right. \\ \qquad\qquad \left. +\frac{1}{\sin\theta}(n-|m|+1)P_{n+1}^{|m|}(\cos(\theta))\right)e^{\imath m\phi} \\ \sum\sum \imath L_n^m m \frac{r^{n-1}}{\sin\theta} Y_n^m(\theta,\phi)\end{bmatrix},\end{aligned} \tag{8.17}$$

where the sums are performed over n $(0 \le n < p)$ and m $(-n \le m \le n)$.

Scaling of the classical FMM translation operators

The expansion coefficients of the spherical harmonics – MP expansions and local expansions – are stored in a vector storage scheme. Since the number of expansion coefficients is truncated to $n < p$, there are p^2 expansion coefficients. In this storage scheme, the computation of the MP coefficients of a FD cell (8.11) needs $3p^2$ multiplications. Indeed, the integrals in (8.11) are identical for every FD cell (all FD cells have equal dimensions), thus they can be computed in the set up phase of the algorithm and stored in three vectors ($O_{n,x}^m$, $O_{n,y}^m$ and $O_{n,z}^m$). The MP expansion $\mathbf{O}_n^m(\mathbf{m})$ of a FD cell with uniform normalized magnetization $\mathbf{m} = [m_x, m_y, m_z]$ is then determined by a linear combination of the three vectors $O_{n,x}^m$, $O_{n,y}^m$ and $O_{n,z}^m$

$$\mathrm{O}_\mathrm{n}^\mathrm{m}(\mathbf{m}) = m_x O_{n,x}^m + m_y O_{n,y}^m + m_z O_{n,z}^m. \tag{8.18}$$

Since the MP and local expansion coefficients are stored in a vector, the action of the MP to MP, the MP to local and the local to local translation operators as

given in (8.12), (8.14) and (8.15) can be seen as matrix-vector products which are performed by p^4 multiplications. All translation matrices are computed and stored in the set up phase of the algorithm.

In that way the MP expansion of a basis box containing 8^{lev} FD cells can be computed by first computing the 8^{lev} MP expansion in each FD cell and then translating the 8^{lev} MP expansions to the center of the basis box. This is performed using $8^{lev} \times 3p^2 + 8^{lev} \times p^4$ multiplications. When the MP to MP translation operators (8.12) are denoted by $T^q_{jk,nm}$ ($q = 1,...,8^{lev}$), this scheme looks like

$$M^k_j = \sum_{q=1}^{8^{lev}} \sum_n \sum_m T^q_{jk,nm} \left(m^q_x \mathrm{O}^m_{n,x} + m^q_y \mathrm{O}^m_{n,y} + m^q_z \mathrm{O}^m_{n,z} \right). \tag{8.19}$$

This is accelerated by computing the *translated* MP expansions $\sum_n \sum_m T^q_{jk,nm} \mathrm{O}^m_{n,i}$, ($q = 1,...,8^{lev}$ and $i = x,y,z$) of the FD cells in the set up phase and storing these 3×8^{lev} translated expansions. In that way, the resulting MP expansion is computed by making a linear combination of the *translated* quantities $\sum_n \sum_m T^q_{jk,nm} \mathrm{O}^m_{n,i}$

$$M^k_j = \sum_{q=1}^{8^{lev}} \left(m^q_x \sum_n \sum_m T^q_{jk,nm} \mathrm{O}^m_{n,x} + m^q_y \sum_n \sum_m T^q_{jk,nm} \mathrm{O}^m_{n,y} + m^q_z \sum_n \sum_m T^q_{jk,nm} \mathrm{O}^m_{n,z} \right). \tag{8.20}$$

This scheme needs only $3 \times 8^{lev} p^2$ multiplications to determine the MP expansion of a basis box.

Applying the local to field translation operator (8.17) on a local expansion leads to $3p^2$ multiplications relating the 3 components of the magnetostatic field with the p^2 local expansion coefficients, in matrix notation: $\mathbf{H}_{ms} = \mathbf{G}^m_n(r,\theta,\phi)\mathbf{L}^m_n$. The 8^{lev} different local to field translation matrices $\mathbf{G}^m_n(r,\theta,\phi)$ are computed and stored in the set up phase of the algorithm.

8.3.2 Acceleration of the MP to local translations

In the presented scheme, the computation of the MP expansion of a basis box and the local to field translations are $\mathcal{O}(p^2)$ operations, while the MP to MP, the MP to local and the local to local translations are $\mathcal{O}(p^4)$ operations. In this scheme the number of MP to local translations is very large. Indeed, since each box on each level has an interaction list containing 189 boxes (boundary effects not taken into account) 189 MP to local translations have to be performed per box. This is in contrast to the 8 MP to MP translations and 8 local to local translations performed for each box in the FMM tree. To illustrate this, Table 8.1 shows the exact number of MP to MP, MP to local an local to local translations in the case of a cubic body discretized using different numbers of levels.

Table 8.1: Number of translation operators in a cube discretized using different numbers of levels

# levels	N	MP to MP	MP to local	local to local
4	4096	512	56448	512
5	32768	4608	640584	4608
6	262144	37376	6039504	37376
7	2097152	299520	52337672	299520
8	16777216	2396672	435570912	2396672

N is the total number of basis boxes. From this table it is understood that almost all execution time in the far field computations goes to the translation of MP expansions to local expansions. In what follows, our attention will go to the acceleration of the MP to local translation.

Many accelerated translation schemes are proposed for the MP to local translation operator. In [101] a scheme is described where all translations are performed in the z-direction after a local rotation of the MP coefficients. In this coordinate system the translation operators scale p^3. The rotation of the MP coefficients towards this coordinate system and the back-rotation of the computed local coefficients scale also as $\mathcal{O}(p^3)$. These rotations have to be performed on each MP expansion and differs for each direction of the translation. Another faster MP to local translation scheme, also proposed by L. Greengard in [101] uses the plane wave expansion instead of the MP expansion to translate the radiation spectrum of a box. Once the plane wave (i.e. exponential) expansion is known, the translation operator is diagonal, hence the translation scales as $\mathcal{O}(p^2)$. The computation of the plane wave expansion from the MP expansion and the computation of the local expansion from the plane wave expansion are $\mathcal{O}(p^3)$ calculations. This conversion from MP expansion to plane expansion has to be performed on each MP expansion, but can be used for any translation in any direction. The conversion of the resulting local plane wave expansion into the local expansion is also an $\mathcal{O}(p^3)$ calculation. This scheme is fast, but has some overhead. Especially for small p the gains are minimal. Other implementations of the MP to local operator are based on the classical $\mathcal{O}(p^4)$ formulation but optimally exploit the use of basic linear algebra subprogram (BLAS) routines [102]. The different schemes are sketched in Fig. 8.4.

FFT-accelerated MP to local translation scheme: theory

Another scheme, proposed by Elliott and Board Jr. [103] uses the fact that the MP to local translation operator (8.14) can be written as a convolution, see

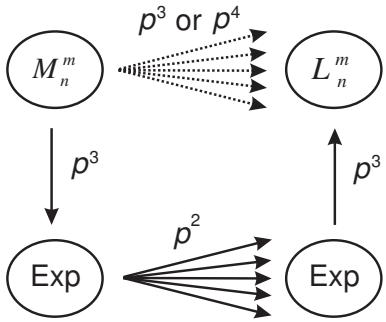

Figure 8.4: Sketch of the MP to local translation schemes using the classical matrix-vector multiplication scheme (top, $\mathcal{O}(p^4)$), using rotation based translation operators (top, $\mathcal{O}(p^3)$) and using plane wave based translation operators (bottom).

also [94, 104]. This can be seen as follows:

$$L_j^k = \sum_{n=0}^{p-1} \sum_{m=-n}^{n} (-1)^j \imath^{|k-m|-|k|-|m|} \frac{A_n^m A_j^k}{A_{j+n}^{m-k}} \frac{Y_{j+n}^{m-k}(\theta,\phi)}{r^{j+n+1}} O_n^m \tag{8.21}$$

$$\frac{(-1)^j \imath^{|k|}}{A_j^k} L_j^k = \sum_{n=0}^{p-1} \sum_{m=-n}^{n} \frac{\imath^{|k-m|}}{A_{j+n}^{m-k}} \frac{Y_{j+n}^{m-k}(\theta,\phi)}{r^{j+n+1}} \imath^{-|m|} A_n^m O_n^m \tag{8.22}$$

$$\frac{(-1)^j \imath^{|k|}}{A_{-j}^k} L_{-j}^k = \sum_{n=0}^{p-1} \sum_{m=-n}^{n} \frac{\imath^{|k-m|}}{A_{-j+n}^{m-k}} \frac{Y_{-j+n}^{m-k}(\theta,\phi)}{r^{-j+n+1}} \imath^{-|m|} A_n^m O_n^m \tag{8.23}$$

$$= \sum_{n=0}^{p-1} \sum_{m=-n}^{n} \frac{\imath^{|k-m|}}{A_{-(j-n)}^{-(k-m)}} \frac{Y_{-(j-n)}^{-(k-m)}(\theta,\phi)}{r^{-(j-n)+1}} \imath^{-|m|} A_n^m O_n^m. \tag{8.24}$$

Equation (8.24) has a convolution structure. Indeed, entities $(-1)^j \imath^{|k|} / A_{-j}^k L_{-j}^k$, defined by parameters j and k, are computed through a summation of entities $\imath^{-|m|} A_n^m O_n^m$, defined by parameters n and m, multiplied by a function that is only defined by the differences $k-m$ and $j-n$. Hence, equation (8.24) can be written as the convolution

$$y_{-n}^m = h_{-n}^m \star x_n^m \tag{8.25}$$

with

$$y_n^m = \frac{(-1)^n \imath^{|m|}}{A_n^m} L_n^m \tag{8.26}$$

$$h_n^m = \frac{\imath^{|m|}}{A_n^{-m}} \frac{Y_n^{-m}}{r^{n+1}} \tag{8.27}$$

$$x_n^m = \imath^{-|m|} A_n^m O_n^m. \tag{8.28}$$

Here, the negative values $-n$ in y_n^m and the function h_n^m give rise to local expansions and spherical harmonics with negative degrees. Therefore, the entities y_n^m and h_n^m are extended to negative values as follows

$$y_{-n}^m = y_n^m \tag{8.29}$$
$$h_{-n}^m = h_n^m. \tag{8.30}$$

The negative degrees $-n$ affect the alignment of the corresponding matrices $\mathbf{x}$ and $\mathbf{h}$ in coefficient space. For $p = 3$ the matrix $\mathbf{h}$ is

$$\mathbf{h} = \begin{bmatrix} h_0^0 & 0 & 0 & 0 & 0 & 0 & h_{-4}^0 & h_{-3}^0 & h_{-2}^0 & h_{-1}^0 \\ 0 & 0 & 0 & 0 & 0 & 0 & h_{-4}^1 & h_{-3}^1 & h_{-2}^1 & h_{-1}^1 \\ 0 & 0 & 0 & 0 & 0 & 0 & h_{-4}^2 & h_{-3}^2 & h_{-2}^2 & 0 \\ 0 & 0 & 0 & 0 & 0 & 0 & h_{-4}^3 & h_{-3}^3 & 0 & 0 \\ 0 & 0 & 0 & 0 & 0 & 0 & h_{-4}^4 & 0 & 0 & 0 \\ 0 & 0 & 0 & 0 & 0 & 0 & 0 & 0 & 0 & 0 \\ 0 & 0 & 0 & 0 & 0 & 0 & h_{-4}^{-4} & 0 & 0 & 0 \\ 0 & 0 & 0 & 0 & 0 & 0 & h_{-4}^{-3} & h_{-3}^{-3} & 0 & 0 \\ 0 & 0 & 0 & 0 & 0 & 0 & h_{-4}^{-2} & h_{-3}^{-2} & h_{-2}^{-2} & 0 \\ 0 & 0 & 0 & 0 & 0 & 0 & h_{-4}^{-1} & h_{-3}^{-1} & h_{-2}^{-1} & h_{-1}^{-1} \end{bmatrix}. \tag{8.31}$$

The matrix has values up to degree $2(p-1)$ since these also occur in the MP to local translation operator (8.14). This so called double height kernel [102] gives rise to matrices with dimensions $2(2p-1) \times 2(2p-1)$. For $p = 3$ the matrices $\mathbf{x}$ and $\mathbf{y}$ in (8.25) are

$$\mathbf{x} = \begin{bmatrix} x_0^0 & x_1^0 & x_2^0 & 0 & 0 & 0 & 0 & 0 & 0 & 0 \\ 0 & x_1^1 & x_2^1 & 0 & 0 & 0 & 0 & 0 & 0 & 0 \\ 0 & 0 & x_2^2 & 0 & 0 & 0 & 0 & 0 & 0 & 0 \\ 0 & 0 & 0 & 0 & 0 & 0 & 0 & 0 & 0 & 0 \\ 0 & 0 & 0 & 0 & 0 & 0 & 0 & 0 & 0 & 0 \\ 0 & 0 & 0 & 0 & 0 & 0 & 0 & 0 & 0 & 0 \\ 0 & 0 & 0 & 0 & 0 & 0 & 0 & 0 & 0 & 0 \\ 0 & 0 & 0 & 0 & 0 & 0 & 0 & 0 & 0 & 0 \\ 0 & 0 & x_2^{-2} & 0 & 0 & 0 & 0 & 0 & 0 & 0 \\ 0 & x_1^{-1} & x_2^{-1} & 0 & 0 & 0 & 0 & 0 & 0 & 0 \end{bmatrix} \text{ and } \mathbf{y} = \begin{bmatrix} y_0^0 & 0 & 0 & 0 & 0 & 0 & 0 & 0 & y_{-2}^0 & y_{-1}^0 \\ 0 & 0 & 0 & 0 & 0 & 0 & 0 & 0 & y_{-2}^1 & y_{-1}^1 \\ 0 & 0 & 0 & 0 & 0 & 0 & 0 & 0 & y_{-2}^2 & 0 \\ 0 & 0 & 0 & 0 & 0 & 0 & 0 & 0 & 0 & 0 \\ 0 & 0 & 0 & 0 & 0 & 0 & 0 & 0 & 0 & 0 \\ 0 & 0 & 0 & 0 & 0 & 0 & 0 & 0 & 0 & 0 \\ 0 & 0 & 0 & 0 & 0 & 0 & 0 & 0 & 0 & 0 \\ 0 & 0 & 0 & 0 & 0 & 0 & 0 & 0 & y_{-2}^{-2} & 0 \\ 0 & 0 & 0 & 0 & 0 & 0 & 0 & 0 & y_{-2}^{-1} & y_{-1}^{-1} \end{bmatrix}. \tag{8.32}$$

These matrices need no further zero padding to avoid disturbing side effects originating in the cyclic nature of the Fourier transformation. Moreover, the matrix dimensions can still be reduced by removing the p^{th} to $(2p-1)^{th}$ column containing only zeros. In (8.31) and (8.32) the fourth, fifth and sixth column can be removed: in general this leads to matrix dimensions of $(3p-2) \times 2(2p-1)$.

FFT accelerated MP to local scheme: stability issues

The discussion above seems to appear complete, but the implementation of it leads to numerical instabilities due to the A_n^m factors, the ρ^n term in the MP expansions (8.7) and the $r^{-(n+1)}$ term in the functions h_n^m (8.27), which may cause the coefficients to vary by many orders of magnitude. This results in inaccurate evaluations of the Fourier transforms. To alleviate this problem, the coefficients need to be scaled for a unit box before the FFT method can be applied. To translate the MP expansion of a box with edges 2Δ the elements y_n^m (8.26), h_n^m (8.27) and x_n^m (8.28) have to be redefined as

$$y_n^m = \frac{(-1)^n \imath^{|m|}}{A_n^m} (2\Delta)^{n+1} L_n^m \tag{8.33}$$

$$h_n^m = \frac{\imath^{|m|}}{A_n^{-m}} \left(\frac{2\Delta}{r}\right)^{n+1} Y_n^{-m} \tag{8.34}$$

$$x_n^m = \frac{\imath^{-|m|} A_n^m}{(2\Delta)^n} O_n^m. \tag{8.35}$$

For single precision computations, this solves the problem only for $p < 7$. For larger p values, the quantities A_n^m vary too much in magnitude. In the computation of the magnetostatic field considered here, values of $p < 7$ turn out to be sufficient, see further. When a higher accuracy is required, more expansion coefficients are needed. For these higher p-values the FFT scheme is still applicable, but a block decomposition of the matrices $\mathbf{y}$, $\mathbf{h}$ and $\mathbf{x}$ has to be made [103, 94, 104] leading to a slower algorithm.

Scaling of the FFT accelerated MP to local scheme

The paragraphs above explain how the MP to local translation is accelerated with fast Fourier transforms. In the set up phase of the algorithm the transfer matrices $\mathbf{h}$ are computed, Fourier transformed and stored. These matrices are identical on every level because of the rescaling to transfer matrices of unit boxes. They only differ depending on the (rescaled) vector $\mathbf{r}$ which defines the translation. In total 316 different transfer matrices exist.

Once the aggregation step of the FMM algorithm is performed (i.e. the MP expansions are translated from the lowest level up to the highest level) the MP expansion in every box on every level are known. Before starting the disaggregation step, for each MP expansion the corresponding Fourier transformed matrix $\tilde{\mathbf{x}}$ is computed (the tilde indicates Fourier transformed quantities) and stored. These computations consist of two phases. First the MP expansion values M_n^m are multiplied with $i^{-|m|} A_n^m (2\Delta)^{-n}$ and stored at the corresponding place in the matrix $\mathbf{x}$. These are $\mathcal{O}(p^2)$ computations. The values $i^{-|m|} A_n^m (2\Delta)^{-n}$ differ for every level and are computed in the set up phase of

the algorithm. Second, the matrix $\mathbf{x}$ is Fourier transformed. This is performed using FFTW [83] which results in an $\mathcal{O}(p^2 \log p)$ algorithm. Since the MP expansion coefficients are not needed any more when the $\tilde{\mathbf{x}}$ is known, both entities can be stored in the same memory space, reducing memory requirements.

Once the Fourier transformed matrices $\tilde{\mathbf{x}}$ are computed and stored for every box on every level, the disaggregation step starts. During the disaggregation step, the MP expansions of the boxes in the interaction list (189, considering no side effects) are translated towards the considered box. This is performed by adding the point wise multiplications of the matrices $\tilde{\mathbf{x}}$ of the source boxes with the corresponding Fourier transformed transfer functions $\tilde{\mathbf{h}}$. When no side effects are considered 189 translations consisting of $(3p-2)2(2p-1)$ multiplications have to be performed. Hence, the translations itself require $\mathcal{O}(p^2)$ operations. Once all point wise products are performed and added $\tilde{\mathbf{y}}$ is known.

In the next step $\tilde{\mathbf{y}}$ is Fourier transformed back to real space, which is an $\mathcal{O}(p^2 \log p)$ computation. The resulting local expansion values are extracted from the matrix $\mathbf{y}$, divided by the quantity $(-1)^n \imath^{|m|} (2\Delta)^{n+1} / A_n^m$ and stored. These computations scale as $\mathcal{O}(p^2)$. The values $(-1)^n \imath^{|m|} (2\Delta)^{n+1} / A_n^m$ differ for every level and are computed in the set up phase of the algorithm.

The total FFT accelerated scheme is shown in Fig. 8.5. This scheme is much faster since the fast execution of the 189 point wise products exceeds the overhead in the scheme (rescaling, copies, Fourier transformations). An analog scheme can be elaborated to perform the MP to MP and the local to local translations, however, the time gain for these translations is not guaranteed for small p since only 8 translations occur for each box instead of 189. It is not possible to perform the aggregation and disaggregation completely in Fourier space, for a further discussion see [103].

8.3.3 Exploiting symmetries

The translation operations can still be accelerated when symmetry properties of the spherical harmonics are exploited. The MP and local expansion coefficients satisfy the following symmetries:

$$M_n^{-m} = \overline{M_n^m} \tag{8.36}$$

$$L_n^{-m} = \overline{L_n^m}. \tag{8.37}$$

The redundant negative orders $-m$ can be omitted and only the positive orders $0 \leq m < p$ have to be stored. This reduces the memory needed to store a MP expansion and a local expansion from p^2 numbers to $p(p+1)/2$ numbers. In what follows we will comment on the time and memory gains that are obtained when these symmetries are incorporated.

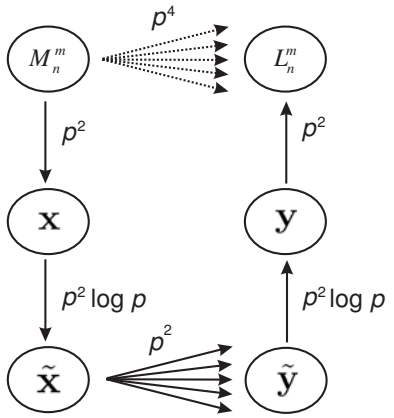

Figure 8.5: Sketch of the MP to local translation schemes using the classical matrix-vector multiplication scheme (top), using FFT accelerated translation operators (bottom).

Acceleration of the MP to MP and the local to local translation

Since only the positive orders of the expansion coefficients are stored, the expansions of the source (the child in the case of a MP to MP translation and the parent in case of a local to local translation) have to be extended with the negative orders before the actual translation. Second, the translated expansions (only these with positive order m) can be determined by performing a matrix vector product of roughly half the size (the matrix has dimensions $p(p+1)/2 \times p^2$). Compared with the classical translation scheme outlined in (8.3.1), this scheme is roughly twice as fast. However, since the number of MP to MP translations and local to local translations is small compared with the number of MP to local translations, the total time gain is negligible. The most important gain here is the memory reduction obtained for the storage of the MP and local expansions and the translation matrices.

Acceleration of the MP to local translation

In the MP to local translation operator, the symmetries (8.36) and (8.37) give also rise to possible memory reduction and faster execution times. Indeed, half of the data in the Fourier transformed matrices $\tilde{\mathbf{x}}$, $\tilde{\mathbf{h}}$ and $\tilde{\mathbf{y}}$ is conjugated to the other half. Consequently, in the MP to local translation scheme only half of the elements have to be taken into account: when the matrices $\mathbf{x}$ are Fourier transformed, only half of the matrix $\tilde{\mathbf{x}}$ is stored, i.e. $(3p-2)(2p-1)$ elements. During the actual translation, only these elements have to be taken into account for the point wise multiplication. When this is done for all 189 boxes in the interaction list, the second half of the matrix $\tilde{\mathbf{y}}$ is reconstructed

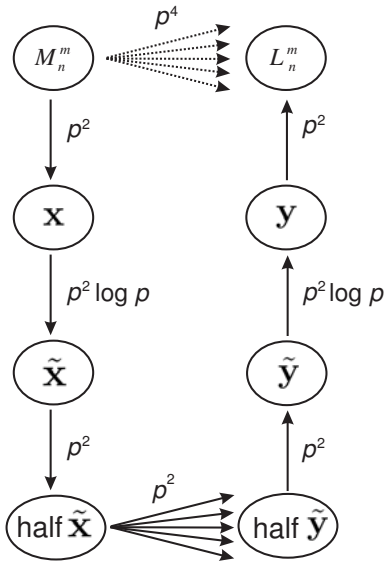

Figure 8.6: Sketch of the MP to local translation schemes using the classical matrix-vector multiplication scheme (top), using FFT accelerated translation operators and exploiting the symmetries in the Fourier transformed matrices (bottom). This scheme has half the number of point wise products compared with the scheme of Fig. 8.5.

based on the first half. After inverse Fourier transforming the matrix, the local expansion is extracted. The MP to local translation scheme is shown in Fig. 8.6.

In this scheme the number of point wise products is halved in comparison with the scheme outlined in section 8.3.2. Since the MP to local translation is responsible for almost the total execution time for the far field computations, this part of the CPU time is roughly halved when this scheme is used. Also the memory needs are reduced: instead of storing the total number of $(3p-2)2(2p-1)$ elements of the matrix $\tilde{\mathbf{x}}$ in each box, only half of the elements has to be stored.

Acceleration of the local to field translation

In section 8.3.1 it was outlined that magnetic field components $H_{ms,i}$ $(i = x,y,z)$ are computed by the matrix-vector product $\mathbf{H}_{ms} = \mathbf{G}_n^m \mathbf{L}_n^m$. Since also the elements of the local to field translation matrix $\mathbf{G}$ satisfy the symmetry property

$$G_{n,i}^{-m} = \overline{G_{n,i}^m} \tag{8.38}$$

the number of multiplications for the determination of the magnetic field from the local expansions is decreased to less then half of the original number of multiplications:

$$H_{ms,i} = \sum_{n=0}^{p-1} \left[\mathcal{R}e(G^0_{n,i})\mathcal{R}e(L^0_{n,i}) + 2 \sum_{m=1}^{n} \left\{ \mathcal{R}e(G^m_{n,i})\mathcal{R}e(L^m_{n,i}) - \mathcal{I}m(G^m_{n,i})\mathcal{I}m(L^m_{n,i}) \right\} \right]. \tag{8.39}$$

Hence, the elements with negative order in the transfer matrix do not have to be computed (set up phase) and stored.

8.4. Near field computations

Up to now all mathematical machinery is provided to calculate the magnetostatic field $\mathbf{H}_{ms}$ originating from FD cells in basis boxes that are well separated, i.e. from FD cells in basis boxes that are not adjacent to the considered basis box. To compute the total magnetic field in a FD cell also the FD cells in the adjacent basis boxes ($3^3 - 1 = 26$ in number) and the FD cells in the considered basis box itself have to be taken into account. This so called *near field* has to be computed and added to the far field contribution. The expression for the magnetostatic field $\mathbf{H}_{ms}(\mathbf{r}_i)$ in the center of a FD cell i originating from N FD cells with uniform normalized magnetization $\mathbf{m}_j$, box center in $\mathbf{r}_j$ $j = 1 \ldots N$ and volume V is given by

$$\mathbf{H}_{ms}(\mathbf{r}_i) = -\frac{M_S}{4\pi} \sum_{j=1}^{N} \int_V \nabla \frac{(\mathbf{r}_i - \mathbf{r}_j + \boldsymbol{\rho}) \cdot \mathbf{m}_j}{|\mathbf{r}_i - \mathbf{r}_j + \boldsymbol{\rho}|^3} \, \mathrm{d}\boldsymbol{\rho}. \tag{8.40}$$

This expression is identical to (8.1). Applying Gauss' theorem on it gives

$$\mathbf{H}_{ms}(\mathbf{r}_i) = -\frac{M_S}{4\pi} \sum_{j=1}^{N} \int_{\partial V} \frac{(\mathbf{r}_i - \mathbf{r}_j + \boldsymbol{\rho}) \cdot \mathbf{m}_j}{|\mathbf{r}_i - \mathbf{r}_j + \boldsymbol{\rho}|^3} \, \mathbf{u}_S \, \mathrm{d}\boldsymbol{\rho} \tag{8.41}$$

with $\mathbf{u}_S$ the normal unit vector pointing outward of the surface ∂V of the FD cell. The integration has to be performed over each cell with identical volume V. Since a classical computation scales $\mathcal{O}(N^2)$, the computations have to be accelerated exploiting the convolution structure of (8.41) as in the FFT scheme presented in the Chapter 7. The used formula are those of the direct magnetostatic evaluation scheme described in Section 7.3.1. An analogous description is possible based on the magnetostatic evaluation scheme using the magnetic potential described in Section 7.3.2. For the computation of the near interac-

tions, two numerical schemes exploiting the convolution structure of (8.41) are possible, both based on FFTs.

8.4.1 Near interactions with FFTs: scheme I

In this scheme the vector $\mathbf{r}_i - \mathbf{r}_j$ between two FD cells is rewritten with respect to the centers of their basis boxes

$$\mathbf{r}_i - \mathbf{r}_j = \mathbf{r}'_i - \mathbf{r}'_j - \Lambda^q. \tag{8.42}$$

The vector Λ^q points from the center of the considered basis box to the center of the q^{th} neighbor (q=1,...,27). This is shown in Fig. 8.7. The total magnetostatic field (8.41) is now written as

$$\mathbf{H}_{ms}(\mathbf{r}'_i) = -\frac{M_S}{4\pi} \sum_{q=1}^{27} \sum_{j=1}^{8^{lev}} \int_{\partial V} \frac{(\mathbf{r}'_i - \mathbf{r}'_j - \Lambda^q + \boldsymbol{\rho}) \cdot \mathbf{m}(\mathbf{r}_j)}{|\mathbf{r}'_i - \mathbf{r}'_j - \Lambda^q + \boldsymbol{\rho}|^3} \mathbf{u}_S \, \mathrm{d}S. \tag{8.43}$$

In this near interaction scheme, the FD cells of each basis box are taken into account one basis box after another. Written as a convolution product this becomes

$$\mathbf{H}_{ms}(\mathbf{r}) = \sum_{q=1}^{27} \mathbf{g}(\mathbf{r}, \Lambda^q) \star \mathbf{m}(\mathbf{r}), \tag{8.44}$$

with $\mathbf{g}(\mathbf{r}, \Lambda^q)$ the Green function which in this case is a symmetrical tensor

$$\mathbf{g}(\mathbf{r}, \Lambda^q) = -\frac{M_S}{4\pi} \int_{\partial V} \frac{\mathbf{r} - \Lambda^q + \boldsymbol{\rho}}{|\mathbf{r} - \Lambda^q + \boldsymbol{\rho}|^3} \mathbf{u}_S \, \mathrm{d}S. \tag{8.45}$$

With λ the size of the edges of the basis boxes, Λ^q is one of the 27 vectors

$$\Lambda^q = I\lambda\mathbf{e}_x + J\lambda\mathbf{e}_y + K\lambda\mathbf{e}_z \qquad \begin{cases} I & = -1, 0, 1 \\ J & = -1, 0, 1 \\ K & = -1, 0, 1 \end{cases}. \tag{8.46}$$

Expressions (8.41) to (8.45) make clear that the magnetostatic field $\mathbf{H}_{ms}$ in the FD cells of the considered basis box (the one in the middle of Fig. 8.7) is computed by:

1. Zero padding the magnetization vectors of the basis boxes separately.
2. Fourier transforming the magnetization data of step 1.
3. Performing the point by point products of the Fourier transformed magnetization vectors (from step 2) with the proper Green function tensor $\mathbf{g}(\mathbf{r}, \Lambda^q)$ and adding the 27 results.

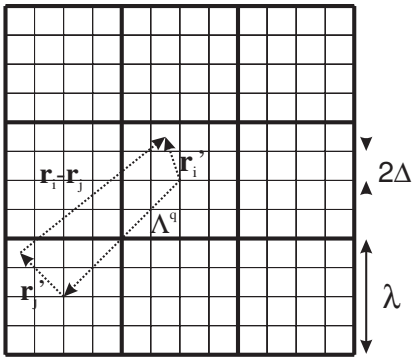

Figure 8.7: Vectors used in the near interaction scheme I.

4. Inverse Fourier transforming the result from step 3 to real space.
5. Selecting the magnetostatic fields from the data obtained in step 4.

The elements of the Green function tensors $\mathbf{g}(\mathbf{r},\Lambda^q)$ of (8.45) are given in Appendix A. The Green function tensors are computed and Fourier transformed during the set up phase of the algorithm. The zero padding in the three dimensions is needed to avoid side effects due to the cyclic nature of Fourier transforms. Hence, all Fourier transforms have dimensions $2 \cdot 2^{lev} \times 2 \cdot 2^{lev} \times 2 \cdot 2^{lev}$.

8.4.2 Near interactions with FFTs: scheme II

This scheme uses the expression (8.41) without redefinitions of vectors. Written as a convolution product, expression (8.41) looks like

$$\mathbf{H}_{ms}(\mathbf{r}) = \mathbf{g}(\mathbf{r}) \star \mathbf{m}(\mathbf{r}) \tag{8.47}$$

with

$$\mathbf{g}(\mathbf{r}) = -\frac{M_S}{4\pi} \int\limits_{\partial V} \frac{\mathbf{r}+\boldsymbol{\rho}}{|\mathbf{r}+\boldsymbol{\rho}|^3}\, \mathbf{u}_S \, \mathrm{d}S. \tag{8.48}$$

This is the same expression as the one used in the direct magnetostatic evaluation scheme presented in Chapter 7. The elements of the Green function tensors $\mathbf{g}(\mathbf{r})$ of (8.48) are given in Appendix A. In this scheme, the magnetic data of all the neighboring basis boxes and the considered basis box itself is translated to the considered basis box in one computation step. Therefore the magnetic data of all the basis boxes have to be rearranged and zero padded. Hence the magnetostatic field $\mathbf{H}_{ms}$ is computed by

1. Assembling and zero padding the magnetization data.

2. Fourier transforming the input from step 1.
3. Performing the point wise products of the Fourier transformed vectors from step 2 with the Green function tensor $\mathbf{g}(\mathbf{r})$
4. Inverse Fourier transforming the result from step 3.
5. Selecting the magnetostatic fields from the considered basis box from the result of step 4.

Since in each direction 3 basis boxes are considered in this scheme, the dimension of the block to be Fourier transformed is $3 \cdot 2^{lev} \times 3 \cdot 2^{lev} \times 3 \cdot 2^{lev}$. Then, after zero padding, all Fourier transforms should have dimensions $6 \cdot 2^{lev} \times 6 \cdot 2^{lev} \times 6 \cdot 2^{lev}$. However, the zero padding is needed for not 'spoiling' the Fourier transformed data with side effects due to the cyclic nature of the Fourier transforms. In this scheme, one is only interested in the data computed for the central basis box and not in the magnetostatic fields computed for the neighboring boxes. Hence, the data for these neighboring basis boxes can be spoiled with side effects. Taking this into account, the magnetic data needs only one third of zero padding (2^{lev} zeros) in each direction, reducing the dimensions of the Fourier transforms to $4 \cdot 2^{lev} \times 4 \cdot 2^{lev} \times 4 \cdot 2^{lev}$.

8.4.3 Computational complexity

In what follows, the data matrices used in the convolution products will be denoted by a capital. A tilde denotes the Fourier transformed values of the matrices. In that way the matrices containing the zero padded values of the magnetic components of the considered FD cells are denoted by M_x, M_y and M_z while the elements of the Green function tensors (8.45) and (8.48) are matrices G_{xx}, G_{xy}, G_{xz}, G_{yy}, G_{yz} and G_{zz}.

The first near interaction scheme is comparable with the MP to local translation in the far field computations. Indeed, in a preparatory step of the near field computations, the magnetization data of all basis boxes is Fourier transformed. This consists of two phases: for the three components x, y, z the magnetization data is copied into a zero padded matrix, this is an $\mathcal{O}(n^3)$ operation (with $n = 2^{lev}$ the number of FD cells in one direction in a basis box). The three matrices are then Fourier transformed ($\mathcal{O}((2n)^3 \log 2n)$ operations) and stored. Thus with N_{box} the number of basis boxes, there are $3N_{box}$ forward Fourier transforms of dimensions $2 \cdot 2^{lev} \times 2 \cdot 2^{lev} \times 2 \cdot 2^{lev}$. These Fourier transformed magnetization values are used (27 times pro basis box) during the actual computation of the magnetostatic field.
The first step in the actual computation of the near fields in a basis box consists

of performing the point wise products.

$$\tilde{H}_{x,i} = \sum_{q=1}^{27} \left[\tilde{G}^q_{xx,i} \tilde{M}^q_{x,i} + \tilde{G}^q_{xy,i} \tilde{M}^q_{y,i} + \tilde{G}^q_{xz,i} \tilde{M}^q_{z,i} \right] \tag{8.49}$$

$$\tilde{H}_{y,i} = \sum_{q=1}^{27} \left[\tilde{G}^q_{xy,i} \tilde{M}^q_{x,i} + \tilde{G}^q_{yy,i} \tilde{M}^q_{y,i} + \tilde{G}^q_{yz,i} \tilde{M}^q_{z,i} \right] \tag{8.50}$$

$$\tilde{H}_{z,i} = \sum_{q=1}^{27} \left[\tilde{G}^q_{xz,i} \tilde{M}^q_{x,i} + \tilde{G}^q_{yz,i} \tilde{M}^q_{y,i} + \tilde{G}^q_{zz,i} \tilde{M}^q_{z,i} \right] \tag{8.51}$$

Since the magnetization data and the Green function values have real values in real space, half of the data is adjoint to the other half in Fourier space. When this property is exploited, each translation of Fourier transformed magnetization values to the considered basis box takes roughly $9(2n)^3/2$ multiplications. For one basis box these computations have to be performed 27 times: once for each neighboring box and once for the considered box itself. So, in total their are $27 \times 9(2n)^3/2 = 972\,n^3$ multiplications pro basis box. The results are added to each other. The resulting Fourier transformed magnetostatic field values $\tilde{H}_x$, $\tilde{H}_y$ and $\tilde{H}_z$ are then inverse Fourier transformed ($\mathcal{O}((2n)^3 \log 2n)$ operations) and the magnetostatic field values are extracted out of the result ($\mathcal{O}(n^3)$ operations). Thus with N_{box} the number of basis boxes, there are also $3N_{box}$ inverse Fourier transforms of dimensions $2 \cdot 2^{lev} \times 2 \cdot 2^{lev} \times 2 \cdot 2^{lev}$.

In the second near interaction scheme the forward Fourier transformations of the magnetization data are not computed in a preparatory step since the Fourier transformed magnetizations $\tilde{M}_x$, $\tilde{M}_y$ and $\tilde{M}_z$ are only used once pro basis cell (in contrast with scheme I). This also means that this data is not stored in every basis cell, saving roughly $3 \times 8^{lev+1} N_{box}$ complex numbers of memory. The first step in the computation of the magnetostatic field in a basis box is the assembly of the 3 zero padded matrices M_x, M_y and M_z containing the magnetization data of the 27 basis boxes ($\mathcal{O}(27 \times n^3)$ operations). In a second step this data is forward Fourier transformed ($\mathcal{O}((4n)^3 \log 4n)$ operations). With N_{box} the number of basis boxes, there are $3N_{box}$ forward Fourier transforms of dimensions $4 \cdot 2^{lev} \times 4 \cdot 2^{lev} \times 4 \cdot 2^{lev}$. Then the Fourier transformed data is multiplied point wise with the Fourier transformed Green tensor elements

$$\tilde{H}_{x,i} = \tilde{G}_{xx,i} \tilde{M}_{x,i} + \tilde{G}_{xy,i} \tilde{M}^{y,i} + \tilde{G}_{xz,i} \tilde{M}_{z,i} \tag{8.52}$$

$$\tilde{H}_{y,i} = \tilde{G}_{xy,i} \tilde{M}_{x,i} + \tilde{G}_{yy,i} \tilde{M}^{y,i} + \tilde{G}_{yz,i} \tilde{M}_{z,i} \tag{8.53}$$

$$\tilde{H}_{z,i} = \tilde{G}_{xz,i} \tilde{M}_{x,i} + \tilde{G}_{yz,i} \tilde{M}^{y,i} + \tilde{G}_{zz,i} \tilde{M}_{z,i}. \tag{8.54}$$

Hence, there are $9(4n)^3/2 = 288\,n^3$ multiplications pro basis box, which is a much smaller number then in scheme I. Moreover, since the matrices G_{xx},

G_{xy}, G_{xz}, G_{yy}, G_{yz} and G_{zz} containing the Green tensor elements are even, their Fourier transformed matrices $\tilde{G}_{xx}$, $\tilde{G}_{xy}$, $\tilde{G}_{xz}$, $\tilde{G}_{yy}$, $\tilde{G}_{yz}$ and $\tilde{G}_{zz}$ have only strictly real values. This means that the point wise products are not $complex \times complex$ multiplications as in scheme I, but $real \times complex$ multiplications, which are performed roughly twice as fast.
The resulting Fourier transformed magnetostatic field values $\tilde{H}_x$, $\tilde{H}_y$ and $\tilde{H}_z$ are then inverse Fourier transformed ($\mathcal{O}((4n)^3 \log 4n)$ operations) and the field values are extracted out of the result ($\mathcal{O}(n^3)$ operations). Thus there are also $3N_{box}$ inverse Fourier transforms of dimensions $4 \cdot 2^{lev} \times 4 \cdot 2^{lev} \times 4 \cdot 2^{lev}$.

Hence, comparing the two schemes, one concludes that scheme II is the most memory efficient since the Fourier transformed values are not stored in each basis box. The time efficiency depends on two considerations. First, the number of FFTs is equal: $3N_{box}$ forward and $3N_{box}$ inverse FFTs in both schemes, but the dimensions of the Fourier transformed matrices are different. In scheme I the matrix dimensions are half of those in scheme II ($2n \times 2n \times 2n \leftrightarrow 4n \times 4n \times 4n$), resulting in a *much faster execution of the FFTs in the first scheme*. Second, in scheme I there are $972n^3$ $complex \times complex$ point wise products, while in the second scheme there are $288n^3$ $real \times complex$ point wise products, resulting in a *much faster execution of the point wise product in the second scheme*. Which of the two schemes is the fastest depends thus partly on how fast the FFTs are executed. In Appendix B it is shown how the evaluation of the 3D FFTs can be optimized by excluding the 1D FFTs on rows that contain only zeros. Since in both schemes a large part of the CPU time goes to the evaluation of FFTs, the application of the optimal implementations presented in Appendix B are indispensable.

8.4.4 Timing of the two near interaction schemes

After incorporating the optimal FFT schemes, a comparison between the two near interaction schemes is possible to determine the fastest scheme. Table 8.2 shows the timings of the subroutines and the total timing for the computation of the near interactions for one basis box. One concludes that the second near interaction scheme is by far faster than the first near interaction scheme for all sizes of the basis box. In scheme I almost all computation time goes to the computation of the point wise products while in the second near interaction scheme most of the computation time is divided between the assembling of the magnetization matrices, the forward and inverse Fourier transforms and the point wise products. Moreover, the second scheme needs much less memory. Indeed, in scheme I the three Fourier transformed magnetization matrices have to be stored in each basis box, while this is not the case in the second scheme. It is obvious that the second scheme is used in the algorithm to compute the near interactions. However, since the FFT scheme for the near

Table 8.2: Timing of the two near interaction schemes for one basis box in milliseconds, (Fw: forward, Inv: inverse). The simulations are performed using one processor of a dual core AMD Opteron 270 (2×2 cores) machine with 8 Gbyte memory.

	scheme I			scheme II		
lev	2	3	4	2	3	4
copy **m** [ms]	0.002	0.013	0.083	0.028	0.420	2.43
FFT Fw [ms]	0.007	0.083	0.844	0.114	1.100	11.8
products [ms]	0.540	3.680	52.5	0.078	0.745	6.71
FFT Inv [ms]	0.013	0.093	0.790	0.055	0.570	7.55
copy $\mathbf{H}_{ms}$ [ms]	0.004	0.001	0.05	0.004	0.011	0.12
Total [ms]	0.566	3.870	54.27	0.279	2.846	28.61

interactions introduces some overhead, the direct classical computation of the magnetostatic field is faster for basis boxes with $lev < 2$.

8.5. Performance study

This section discusses the performance of the presented FMM algorithm. To evaluate the time and memory consumption, comparison is made with the high accuracy (pure) FFT scheme presented in Chapter 7. Since all computations – FMM and FFT – are conducted with single precision, this corresponds to a precision of about 6 digits. In what follows, simulations are conducted on cubical magnetic bodies to evaluate the performance of the FMM algorithm. The discretization is done as explained in section 8.2, so all FD cells are equal in size and placed on a regular grid. As discussed in the introduction, these conditions are optimal for the use of an FFT scheme. Hence, it can be expected that the FFT scheme will outperform the FMM scheme with respect to CPU time. However, the difference in CPU time between both schemes under these FFT suited conditions should be acceptable. The slower execution time of the FMM scheme should be compensated with a smaller memory consumption and more flexible applicability of the FMM scheme. The simulations are performed using one processor of a dual core AMD Opteron 270 (2×2 cores) machine with 8 Gbyte memory.

8.5.1 CPU time and memory consumption

As mentioned above, cubic magnetic bodies will be considered. This geometry is discretized using 8^{tot_lev} FD cells. For a geometry with 8^{tot_lev} FD cells different parameters LEV and lev can be combined, i.e. different sizes of basis boxes can be used. The optimal size of the basis boxes depends on the total computation time of the algorithm. Table 8.3 shows the CPU times for the computations of the magnetostatic fields for samples of different sizes. The used

Table 8.3: Timing of the FMM algorithm for different sample dimensions. Between brackets is mentioned how the total number of levels is divided between far field and near field computations ($LEV - lev$). The last row shows the run time for the FFT scheme.

$64 \times 64 \times 64$		$128 \times 128 \times 128$		$256 \times 256 \times 256$		$512 \times 512 \times 512$	
$(5-1)$	9.17 s	$(6-1)$	78.83 s	$(7-1)$	663.1 s		
$(4-2)$	2.03 s	$(5-2)$	17.66 s	$(6-2)$	148.4 s	$(7-2)$	20 min 21 s
$(3-3)$	1.57 s	$(4-3)$	12.88 s	$(5-3)$	104.6 s	$(6-3)$	14 min 59 s
$(2-4)$	1.76 s	$(3-4)$	14.25 s	$(4-4)$	115.2 s	$(5-4)$	18 min 16 s
		$(2-5)$	17.06 s	$(3-5)$	138.3 s		
				$(2-6)$	152.8 s		
FFT	0.264 s	FFT	2.22 s	FFT	22.3 s		

Table 8.4: Memory consumption of the FMM scheme with optimal ($LEV - lev$) division and of the FFT scheme.

	$64 \times 64 \times 64$	$128 \times 128 \times 128$	$256 \times 256 \times 256$	$512 \times 512 \times 512$
FMM	16 MB	64 MB	0.48 GB	3.78 GB
FFT	82 MB	654 MB	5.23 GB	41.9 GB (estimation)

number of MP expansions p is equal to 6, which is the largest possible p-value avoiding stability problems for the MP to local translation (see section 8.3.2). Between brackets, the number of levels in the far field computations, LEV, and the number of levels in the near field computations, lev, is mentioned. In the last row the CPU times for the FFT algorithm are shown.

For all sample dimensions the FMM simulations with $lev = 3$ need the least execution time. This means that in all simulations the optimal size of the basis boxes is $8 \times 8 \times 8$ FD cells (512 FD cells in total). When compared with the FFT scheme, the FMM scheme is slower, for $64 \times 64 \times 64$ a factor 5.95, for $128 \times 128 \times 128$ a factor 5.80 and for $256 \times 256 \times 256$ a factor 4.70. In the FMM scheme with optimal lev parameter, about 85% of the time goes to near interaction computations.

The memory consumption of the FMM scheme with optimal ($LEV - lev$) ratio and of the FFT scheme is given in Table 8.4 for the different sizes of the sample from table 8.3. There is a remarkable difference in memory needs between the two algorithms (roughly a factor 11 for large dimensions). The sample with dimensions $512 \times 512 \times 512$ can only be computed with the FMM scheme since only 8 Gbyte memory is available. The difference in memory needs is due to the very large matrices in the FFT scheme used for the FFTs (zero padded magnetization data, zero padded field data and Green tensor data).

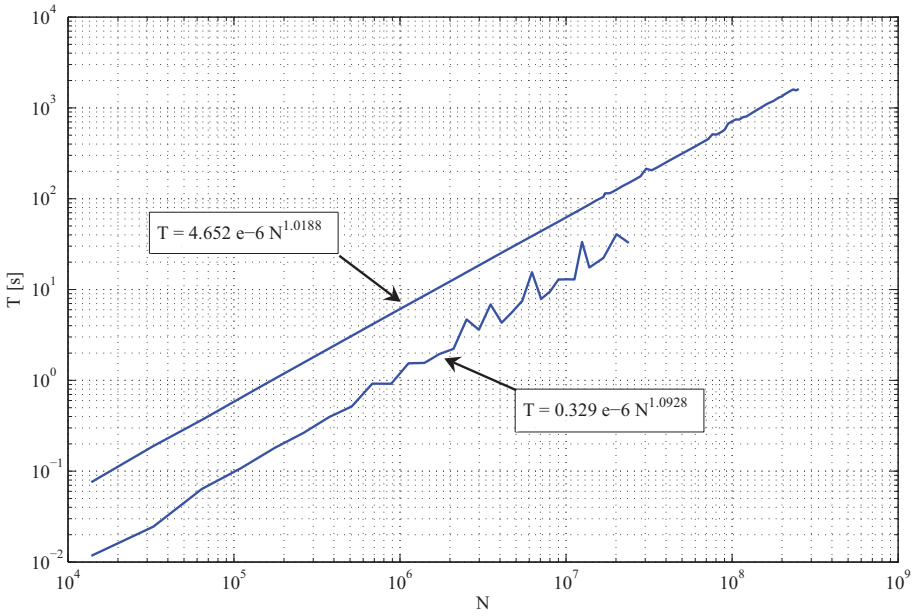

Figure 8.8: CPU time (T) for the evaluation of the magnetostatic field in a cubic magnetic body versus the number of FD cells (N) used to discretize the sample. The upper curve: FMM scheme, the lower curve: FFT scheme.

The scaling of both algorithms is shown in Fig. 8.11 over a large range of sample dimensions. The CPU time of the FMM scheme depends almost perfectly linear on the number of FD cells – $\mathcal{O}(N^{1.0188})$ dependence – while the CPU time of the FFT scheme has a small supralinear dependence on the number of FD cells – $\mathcal{O}(N^{1.0928})$ dependence. The CPU time spent on a fast Fourier transform of a matrix depends vastly on the dimensions of the matrix. FFTW performs best for matrices with dimensions that are products of small primes

$$N = 2^a 3^b 5^c 7^d 11^e 13^f \tag{8.55}$$

with e+f = 0 or 1. Other sizes are computed by means of a slow, general purpose algorithm [83]. This explains the jumps in the FFT curve in Fig. 8.8 for large N values. Indeed, while dimensions grow, the sizes for which the condition (8.55) is met are more scattered. Hence for larger dimensions, more jumps are expected, which makes the difference in CPU time between the FMM and FFT scheme even smaller for these large dimensions.

Table 8.5: Normalized root-mean-square error of the FMM algorithm for different sample dimensions. Between brackets is mentioned how the total number of levels is divided between far field and near field computations ($LEV - lev$).

$64 \times 64 \times 64$		$128 \times 128 \times 128$		$256 \times 256 \times 256$	
$(5-1)$	$2.17e-3$	$(6-1)$	$2.35e-3$	$(7-1)$	$2.48e-3$
$(4-2)$	$2.13e-3$	$(5-2)$	$2.30e-3$	$(6-2)$	$2.44e-3$
$(3-3)$	$1.98e-3$	$(4-3)$	$2.22e-3$	$(5-3)$	$2.37e-3$
$(2-4)$	$1.54e-3$	$(3-4)$	$2.01e-3$	$(4-4)$	$2.24e-3$
		$(2-5)$	$1.49e-3$	$(3-5)$	$1.96e-3$
				$(2-6)$	$1.36e-3$

8.5.2 Accuracy

The accuracy of the far field computations depends on the order of multipoles p used in the computations of the far field. The near field computations are computed with an accuracy corresponding to machine precision. Because of the stability problems encountered in the MP to local translations the maximum number of multipoles p is limited to six (in this implementation), see section 8.3.2. Theoretical considerations about the accuracy of the FMM scheme are given in [101] where error bounds are given. Here, the error on the magnetostatic field values computed with the FMM scheme, is given by comparing the results of the FMM simulations with the results of the FFT simulations.

To make this comparison, magnetic samples in a micromagnetic equilibrium state encountered in the simulation of their hysteresis loops are used. This is done for different sample dimensions. The normalized root-mean-square error for different LEV/lev parameters and different sample dimensions are shown in table 8.5. The normalized root-mean-square error is defined as

$$\text{error} = \sqrt{\frac{1}{N}\sum_{i=1}^{N}\frac{|\mathbf{H}_{ms,i}^{FMM} - \mathbf{H}_{ms,i}^{FFT}|^2}{|\mathbf{H}_{ms,i}^{FFT}|^2}} \tag{8.56}$$

From Table 8.5 it is clear that the error slightly increases when the dimensions of the sample increase. Further, the error decreases when the size of the basis boxes increases. This is when lev is large. This is because for large basis boxes a relatively large number of interactions is computed using near field computations which have an accuracy corresponding to the machine precision.

The magnetic configurations in different planes of the sample with dimensions of $128 \times 128 \times 128$ FD cells are shown in Fig. 8.9 together with the magnetostatic field values and the local normalized error in the same planes. The local normalized error depends on the position in the basis boxes: at the edges of the basis boxes, the largest errors occur.

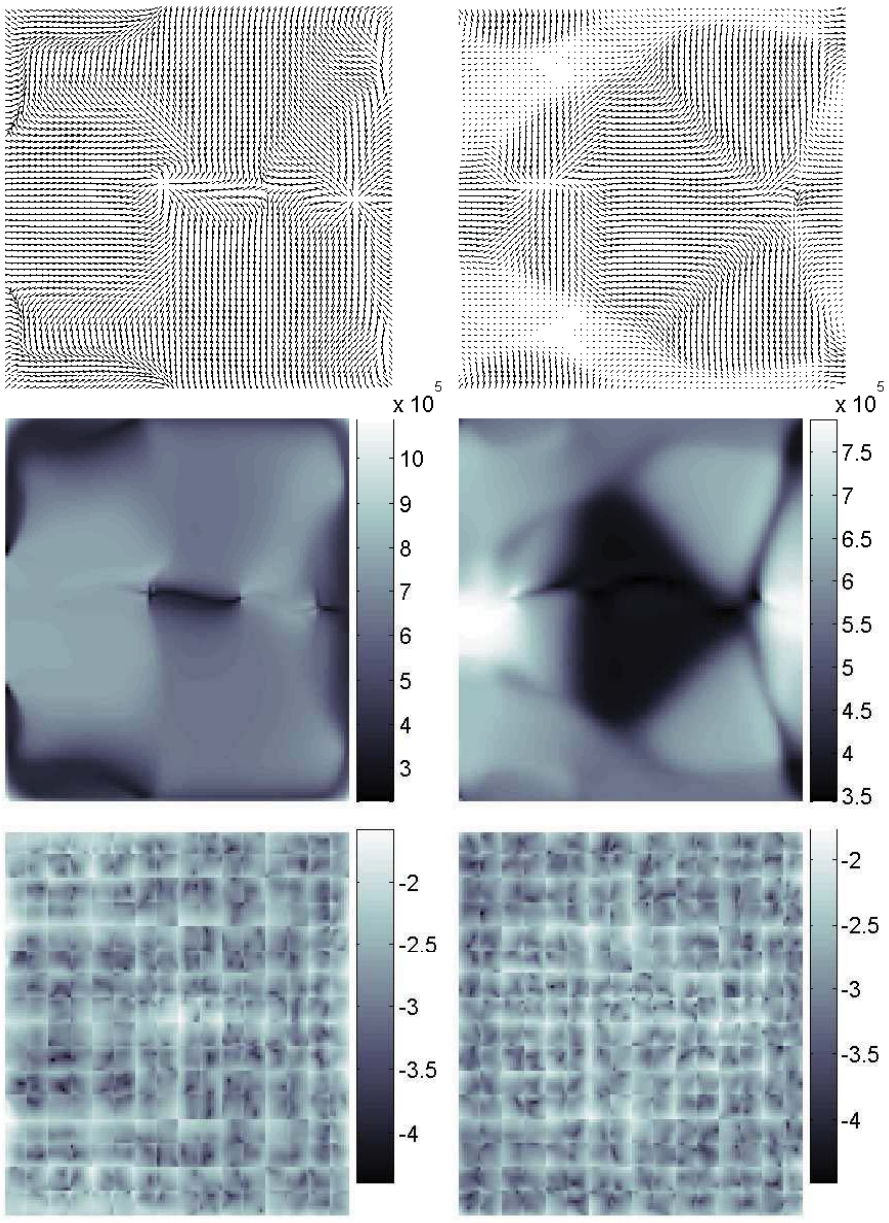

Figure 8.9: Magnetization (up), amplitude of the magnetostatic field (middle) and normalized rms error on a logarithmic scale (bottom) in planes $z = 0$ (left) and $z = 16$ (right) of a sample with dimensions $128 \times 128 \times 128$ FD cells.

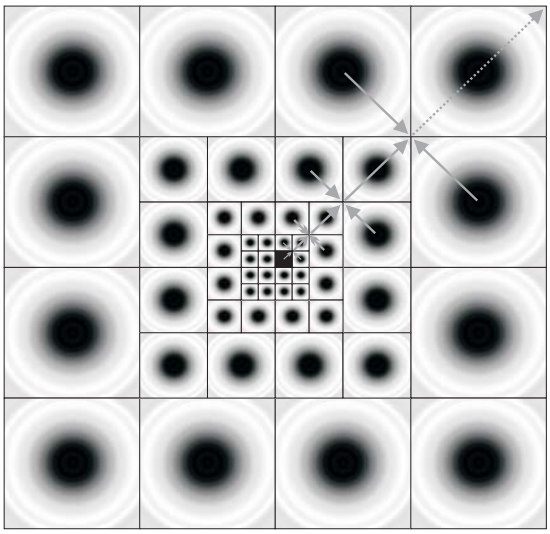

Figure 8.10: Top view of a structure periodic in 2 directions (periodicity in the plane of the sheet of the paper). Extra levels are introduced to describe an infinite periodic structure. The black cell is one period of the infinite structure.

8.6. Periodic boundary conditions in the FMM scheme

In the FMM scheme it is possible to describe a periodic structure that approximates an infinite periodic structure in one or more dimensions. Indeed, when the aggregation phase of the FMM algorithm is performed up to the root level, the MP expansion of one period is known. Since the MP expansions of all periodic images are identical, the influence of all periodic image volumes on the period under study can be described in series and summed. This can be done by employing Ewald summation methods [105]. However, a more straightforward method can be used.

In this FMM implementation distant periodic images are included by introducing extra tree levels. In Fig. 8.10 the black square represents the considered volume which is infinitely repeated in the two dimensions of the paper. The aggregation phase of the FMM algorithm reveals the MP expansion of the root (level zero). Now, when periodicity is described in one or more directions extra levels are introduced, for which the aggregation phase is continued: on the first extra level the children are the root and its periodic images which have identical MP expansions (the MP expansion of the root, see Fig. 8.10). If the structure is periodic in only one or two dimensions, empty boxes are considered in the non-periodic dimension as is shown in Fig. 8.11. This is repeated for LEV_{extra} levels. For an extra level i, the children in the MP to MP trans-

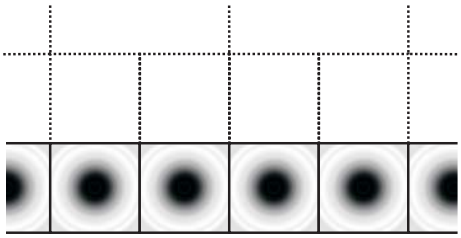

Figure 8.11: Front view of the periodic structure of Fig. 8.10. In the non-periodic direction, empty boxes are added.

lation have always identical MP expansions (computed in the $(i-1)^{th}$ extra aggregation step) or have no MP expansion in the non-periodic direction(s). In this way the MP expansions of clusters of periodic images are computed on different levels (see Fig. 8.11).

In the disaggregation phase, extra disaggregations are conducted on the extra introduced levels. On each level of this extra disaggregation phase one is only interested in the local expansion of the first child (the others are nothing but copies). Once the local expansion in the root box is known the usual disaggregation phase can continue. However, when the MP expansion of a neighbor outside the boundaries of the considered volume is needed, one has to take the identical MP expansion of the image box inside the considered volume. This results in extra translations MP to local translations compared with the non-periodic case.

This scheme introduces only a negligible overhead compared with the non-periodic case since only a small number of extra levels needs to be introduced to well approximate an infinite number of periodic images. The introduction of 5 extra levels describes a periodic structure containing 6144 periods in each dimension.

8.7. Conclusion

In this chapter, a highly efficient FMM scheme for the evaluation of the magnetostatic field is presented. The performance is evaluated by comparing it with the high accuracy FFT based $\mathbf{H}_{ms}$ evaluation scheme of Chapter 7. As in most numerical algorithms there is a trade off between memory usage and execution time. Here the memory savings are very large –about a factor 11– while the execution time is a factor 4 to 5 larger, compared with the FFT scheme. This trade off becomes better for non-cubical shapes. Indeed, in the FMM scheme only the magnetic sample is discretized while in the FFT scheme an enclosing rectangular prism has to be discretized (magnetic body and air). The use of

the presented FMM scheme can thus be advantageous for large complex geometries as writing heads etc particulary when storage capacities are limited.

However, for the simulations conducted in this PhD the CPU time is the bottle neck, far more than memory requirements. Furthermore, the considered geometries (or periods in a periodic structure) are rectangular prisms, which makes FFT based schemes advantageous in our application. From this Chapter, we can conclude that for a cuboid geometry the expected cross-over point between the FFT based $\mathcal{O}(N \log N)$ computations and the FMM based $\mathcal{O}(N)$ computations is only reached for very large geometries, i.e. very large N. In this respect, in the rest of this PhD FFT based schemes are used to compute the magnetostatic field.

The execution time of the FMM scheme could be decreased in a more complex variant of this FMM scheme. Here, the discretization can be made adaptive, using FD cells of different size. In this way domains could be discretized using large FD cells, while small FD cells can still be used to discretize the domain walls. When the domain configuration changes in time, the meshing of the ferromagnetic sample should also change. The discretization should thus be adaptive in space and time, which makes the implementation not straight forward. Extending the presented FMM scheme with adaptive discretization will dramatically improve its performance, but is not performed in this PhD work.

CHAPTER 9

Influence of low accuracy computations in the micromagnetic hysteresis scheme

9.1. Introduction

When considering hysteresis properties, one is predominantly interested in magnetization processes in micromagnetically large objects with dimensions in the order of micrometers and larger. On this length scale the study of magnetization processes is typically based on the domain theory [106]. Here, uniform magnetization regions are assumed through the complete sample. Since this assumption is not always valid, micromagnetic simulations should be able to validate and probably improve the results obtained by the domain theory. Ideally, the micromagnetic computations should be worked out with the same spatial and numerical accuracy as used in the 'classical' micromagnetic research domains as e.g. magnetic recording etc. However, in micromagnetic (hysteresis) simulations that describe magnetization processes in much larger non-ideal ferromagnetic samples as electrical steels, the accuracy which is aimed at is much lower, particulary because the materials' microstructure itself is only known to a certain extent. Indeed, the samples simulated in the 'classical' micromagnetic research domains differ vastly from these studied in the hysteresis schemes.
First, the classical samples have a well-known microscopic texture without any lattice defects. Contrary, the electrical steel samples consist of numerous

grains of which only a distribution of lattice orientations is known. They contain all kinds of lattice defects: edge and screw dislocations, interstitials, microcracks, etc. The exact locations of these defects is not known, only a defect density and statistical spreading can be assumed.
Second, the dimensions of the studied samples differ a lot. The 'classical' samples have dimensions in the order of 10 to 100 nm, while the electrical steel samples are much larger, bulk like. The size of the simulated electrical steel samples is limited by the memory resources available and the CPU time.

Classically, the discretization size is imposed by the exchange length, see Section 2.3.2. Together with a careful description of the exchange interaction this guarantees the *most accurate* simulation of the magnetization processes in the small magnetic samples under study [55, 107]. In this chapter we will investigate the influence of a larger discretization size in the micromagnetic hysteresis scheme. Here, the use of a discretization size larger than the exchange length corresponds to a low level homogenization, which results in a less accurate evaluation of the exchange field and of the magnetostatic field. On the other hand the CPU time and memory requirements will be vastly decreased.

Further we have seen in Chapter 7 that a low accuracy FFT based $\mathbf{H}_{ms}$ evaluation scheme can be used that reduces the CPU time and memory requirements. Here, only the accuracy of the magnetostatic field is affected. In this chapter, we will also investigate the influence of the low accuracy $\mathbf{H}_{ms}$ evaluation on the simulated hysteresis loop.

9.2. Influence of space discretization size

The use of a small discretization size Δ not only drastically increases the number of FD cells N for a given sample, it has also a large impact on the microscopic time step δt needed in the time stepping scheme. Indeed, in Section 6.3.3 it was demonstrated that, when smaller FD cells are used, smaller microscopic time steps δt have to be used in the predictor-corrector semi-analytical time stepping scheme to guarantee convergence between two successive equilibrium magnetization states. When Δ is decreased with a factor 10, the maximum δt for which the system converges decreases by roughly a factor 100. Hence, the use of small FD cells not only leads to more FD cells, but moreover the time stepping of the LL-equation in all these FD cells has to be performed with smaller time steps δt, leading to an increasing number of time steps.

9.2.1 Simulations

For a given sample, the CPU time needed to simulate the hysteresis loop is dramatically reduced when larger discretization sizes Δ are used. However, in the classical micromagnetic research areas, the exchange length is seen as the

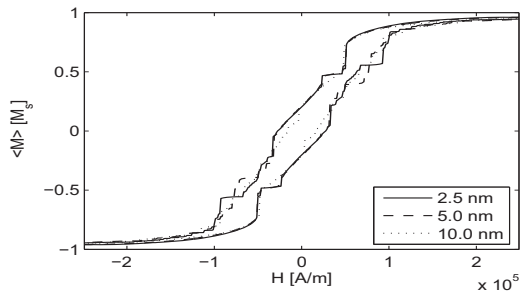

Figure 9.1: Hysteresis loops of an iron sample using different discretization sizes Δ.

Table 9.1: Simulation data for the simulated loops of Fig. 9.1

Δ [nm]	N	δt [ps]	$\#\delta t$	CPU time
2.5	8388608	0.5	27036	$103h15min$
5.0	1048576	1.0	14627	$8h33min$
10	131072	5.0	1163	$7min46sec$

maximum discretization size because on a smaller scale no inhomogeneities can be present. In the electrical steel samples (iron) the exchange length is about 2.8 nm. To examine if the exchange length is also an upper bound in the micromagnetic hysteresis model for electrical steels, hysteresis loops are simulated for an iron sample with dimensions of $0.32\,\mu m \times 1.28\,\mu m \times 0.32\,\mu m$ using different discretization sizes. The external field is applied along the longest edge of the sample. A discretization size of 2.5 nm (slightly smaller than the exchange length), 5.0 nm and 10 nm is considered. The hysteresis loops are shown in Fig. 9.1.

The loops are very similar: they have the same slope and enclose a similar surface, two important aspects of electrical steels for their performance in electromagnetic devices. Table 9.1 shows the simulation data for the loops of Fig. 9.1. The total number of FD cells used to discretize the sample increases enormously when smaller discretization sizes Δ are taken. As already mentioned, smaller time steps δt are used when Δ is decreased. When the microscopic time step δt decreases, the total number of microscopic time steps $\#\delta t$ to simulate the hysteresis loop increases. The massive differences in CPU time mentioned in the last column of Table 9.1 are due to a combination of two factors: (i) more microscopic time steps δt are required when a smaller discretization size Δ is used and (ii) a single time step δt needs more CPU time when a smaller discretization size Δ is used. Since the computation time scales as $\mathcal{O}(N \log N)$, the CPU time increases rapidly with increasing number of FD cells.

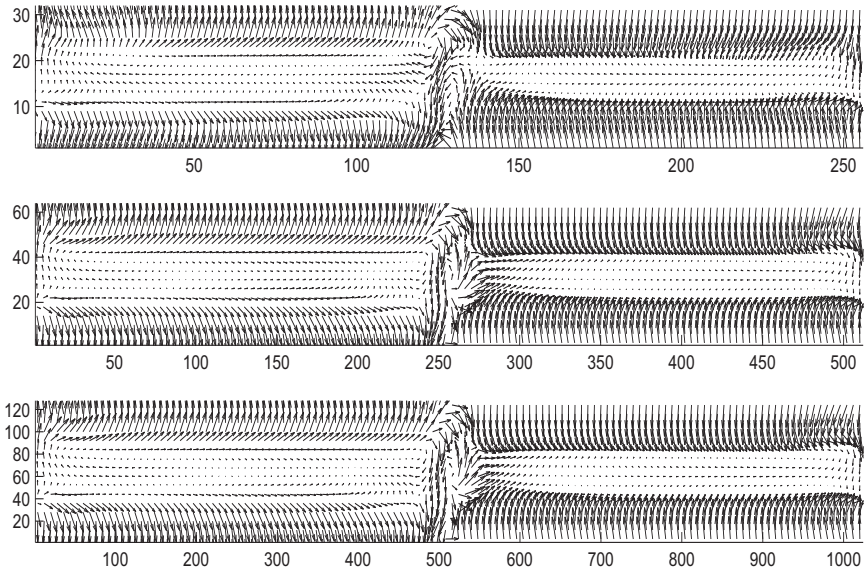

Figure 9.2: Remanent magnetization pattern for the loops of Fig. 9.1 simulated with different discretization sizes: $\Delta = 10\,\text{nm}$ (top), $\Delta = 5.0\,\text{nm}$ (middle) and $\Delta = 2.5\,\text{nm}$ (bottom).

The hysteresis loops shown in Fig. 9.1 only give information about the macroscopic magnetization of the ferromagnetic sample. The micromagnetic hysteresis model also allows us to see if identical magnetization configurations are passed through. Fig. 9.2 shows the microscopic magnetization pattern in a plane parallel to the applied field for the loops of Fig. 9.1 at zero applied field (remanent magnetization). It is clear that almost identical magnetization configurations lead to the loops of Fig. 9.1. The small differences in the magnetization loops can be neglected. Indeed, since the internal structure of the sample is not completely known, the uncertainty of the microscopic properties of the sample introduces an uncertainty on its hysteresis loop. Another example is shown in Fig. 9.3 where a sample with dimensions $0.32\,\mu m \times 2.56\,\mu m \times 0.32\,\mu m$ is simulated using different discretization sizes ($\Delta = 2.5\,\text{nm}$, $7.5\,\text{nm}$ and $10\,\text{nm}$). The loops again enclose similar surfaces and have the same slope, furthermore they differ significantly from those in Fig. 9.1. When the loops of Fig. 9.1 and Fig. 9.3 are compared identical conclusions can be drawn about the influence of the sample geometry on the hysteresis loops, regardless of the used discretization. The simulation times are respectively 404 h, 1 h 30 min and 19 min.

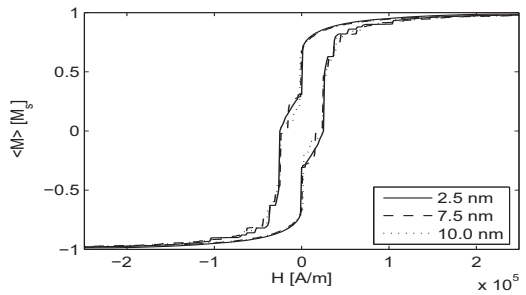

Figure 9.3: Hysteresis loops of an iron sample using different discretization sizes Δ.

9.2.2 Conclusion

From the presented simulations it is clear that discretization sizes larger than the exchange length can be used in the micromagnetic hysteresis scheme. However, the discretization size should be sufficiently small with respect to other characteristic length scales in the material such as the thickness of a domain wall (about 70 nm in Fe) and the dimensions of vortex states (about 35 nm in Fe). Considering this together with the massive differences in CPU time and memory needs justifies the use of a discretization length up to 10 nm. Indeed, when studying magnetic properties of electrical steels, the small precision improvement when a physically justified discretization size of $\Delta = 2.5\,nm$ is used, cannot justify the huge increase of CPU time compared with the computations where e.g. $\Delta = 10$ nm is used.

9.3. Influence of low accuracy $\mathbf{H}_{ms}$ evaluations

In this context, the question also arises to what extent the use of lower accuracy $\mathbf{H}_{ms}$ evaluation schemes influences the simulated macroscopic hysteresis behavior of micrometer sized ferromagnetic samples. This influence is investigated in this section for elongated iron samples ($\mu_0 M_s = 2.16$ T) with dimensions $0.5\,\mu m \times 0.5\,\mu m \times 16.0\,\mu m$, $1.0\,\mu m \times 1.0\,\mu m \times 32.0\,\mu m$ and $1.5\,\mu m \times 1.5\,\mu m \times 48.0\,\mu m$ are considered, discretized using 10 nm sized FD cells leading to $4\,10^6$, $32\,10^6$ and $108\,10^6$ FD cells respectively. All samples contain 32 grains with cubic anisotropy axes. Here, random stresses are added to simulate the grain boundaries. The elongated geometry is chosen since it is expected that the differences in the hysteresis loop shape will be most pronounced in this case. The external field is applied along the longest direction of the sample. In what follows, the samples will be referred to as *sample A*, *B* and *C* respectively. The semi-analytical predictor-corrector scheme is used

to time step the LLG equation. All simulations are performed using a multi-threaded implementation on an AMD Opteron 2350 machine (4x2 cores) with 32 GB of shared memory.

9.3.1 Simulations

The resulting hysteresis loops, with the magnetostatic field computed using the high and low accuracy $\mathbf{H}_{ms}$ evaluation scheme (referred to as scheme 1 and scheme 2 respectively, see Chapter 7) are shown in Fig. 9.4 to Fig. 9.6. Due to the elongated shape of the sample, the hysteresis loops take a large jump at the coercive field. In both Fig. 9.4 and 9.5 the coercive field values for the loops simulated with the high accuracy $\mathbf{H}_{ms}$ evaluation scheme are larger than the corresponding loop simulated with the lower accuracy $\mathbf{H}_{ms}$ evaluation scheme. This is understood as follows. When saturated at high (positive) external fields, the samples are in a stable micromagnetic equilibrium state. Diminishing the applied field makes the systems evolve from these stable states to metastable equilibrium states. When the applied field corresponds to the coercive field, domain structures are initiated which enable the magnetic system to reverse to the opposite magnetization state. The domain nucleation, needed to initiate such a domain structures, typically originates at points where small variations occur in the quantities describing the magnetic sample. If these variations are absent, large opposite external fields are required to initiate the reversal process. In the hysteresis loops based on the lower accuracy $\mathbf{H}_{ms}$ evaluation scheme, the numerical noise on the magnetostatic fields account for the small variations that nucleate the domain structure. In the loops simulated with the high accuracy $\mathbf{H}_{ms}$ evaluation scheme, such variations are absent and a higher opposite applied field is needed to initiate the magnetization reversal.

The coercive fields for the simulated hysteresis loops of the largest sample C have identical values and the resulting loops are very similar (see Fig. 9.6). However, the above reasoning still holds. Here, the micromagnetic equilibrium states before the reversal point are more stable and the numerical noise has only little influence. It is only at the coercive field that in both simulations domains are initiated leading to the magnetization reversal.

The stability of the successive micromagnetic equilibrium states is also expressed by the number of time steps needed to time step the LLG equation (and consequently the CPU time) between successive equilibrium states during the simulation of the hysteresis loops. The number of time steps $\#\delta t$ are given in Table 9.2, together with the CPU time and the memory requirements for the discussed simulations. For the loops of sample A and sample B, more time steps are needed when the low accuracy $\mathbf{H}_{ms}$ evaluation scheme is used. Indeed, due to the introduced numerical noise, the micromagnetic systems

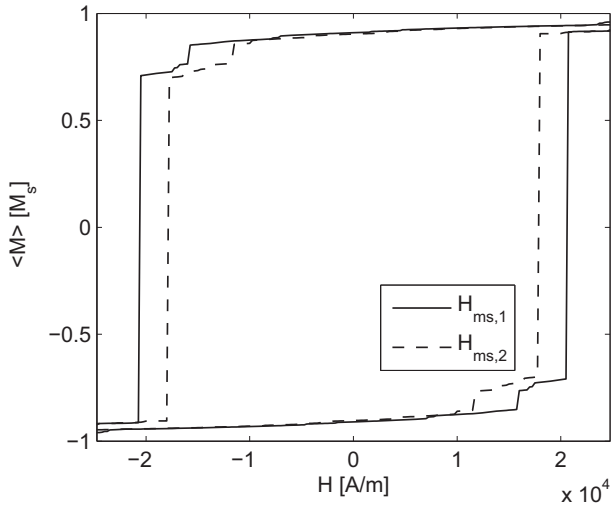

Figure 9.4: Hysteresis loops for a ferromagnetic sample A with dimensions $0.5\,\mu m \times 0.5\,\mu m \times 16.0\,\mu m$, computed using the high accuracy $\mathbf{H}_{ms}$ evaluation scheme (full line) and the low accuracy $\mathbf{H}_{ms}$ evaluation scheme (dashed line).

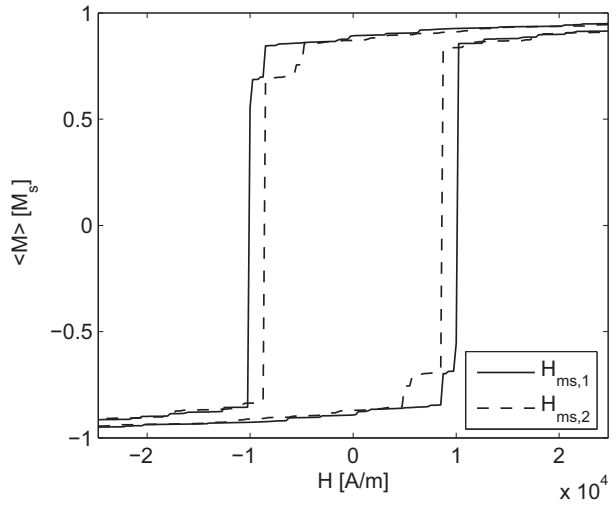

Figure 9.5: Hysteresis loops for a ferromagnetic sample B with dimensions $1.0\,\mu m \times 1.0\,\mu m \times 32.0\,\mu m$, computed using the high accuracy $\mathbf{H}_{ms}$ evaluation scheme (full line) and the low accuracy $\mathbf{H}_{ms}$ evaluation scheme (dashed line).

converge more slowly to the successive metastable equilibrium states when the lower accuracy $\mathbf{H}_{ms}$ evaluation scheme is used. This is not the case for the

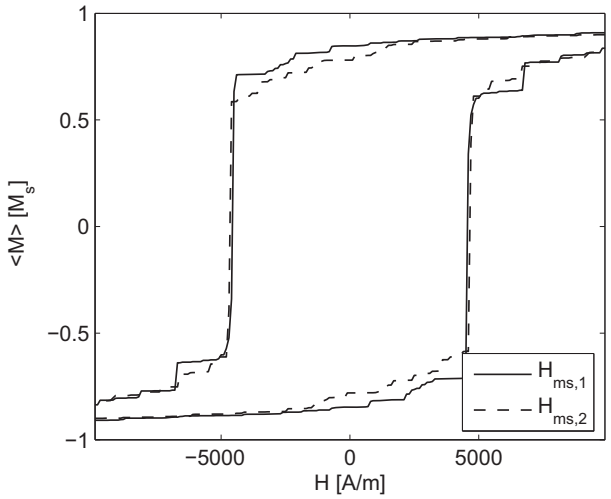

Figure 9.6: Hysteresis loops for a ferromagnetic sample C with dimensions $1.5\,\mu m \times 1.5\,\mu m \times 48.0\,\mu m$, computed using the high accuracy $\mathbf{H}_{ms}$ evaluation scheme (full line) and the low accuracy $\mathbf{H}_{ms}$ evaluation scheme (dashed line).

Table 9.2: Simulation data: hysteresis loops with different $\mathbf{H}_{ms}$ evaluation schemes.

simulation	$\#\delta t$	CPU time	Mem
sample A, scheme 1	1461	1 h 5 min	1.1 GB
sample A, scheme 2	1796	1 h 5 min	0.65 GB
sample B, scheme 1	4447	24 h 22 min	8.9 GB
sample B, scheme 2	6378	29 h 18 min	5.5 GB
sample C, scheme 1	11219	236 h 20 min	30.0 GB
sample C, scheme 2	11388	212 h 31 min	18.7 GB

hysteresis simulation of sample C. As outlined above, the successive equilibrium states are more stable, enabling the system to converge fast to the next equilibrium state despite the numerical noise.

From Table 9.2 it is also clear that when the $\mathbf{H}_{ms}$ evaluation scheme 2 is introduced in the micromagnetic hysteresis scheme instead of scheme 1 (i) the CPU time to compute a time step is reduced with about 15% and (ii) the memory requirements are reduced with 37%. A possible gain in the total CPU time depends on the stability of the system in every point of the hysteresis loop. Furthermore, one can conclude that for growing sample sizes (i) the number of time steps in the hysteresis simulation grows and (ii) the coercive fields diminish (see Fig. 9.4 to Fig. 9.6).

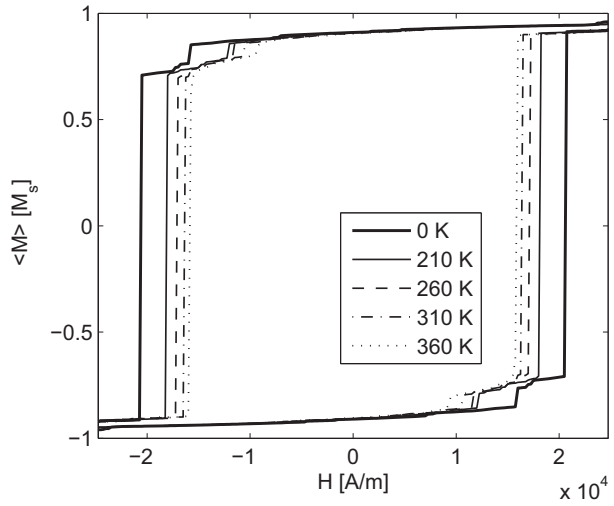

Figure 9.7: Hysteresis loops for the same ferromagnetic sample as in Fig. 9.4 (sample A), computed using the high accuracy $\mathbf{H}_{ms}$ evaluation scheme. Thermal effects are taken into account for different temperatures.

9.3.2 Influence of thermal fluctuations

Now, comparison is made with the influence of thermal fluctuations on the hysteresis behavior of the ferromagnetic samples. Therefore a random thermal fluctuation field is added to the effective field as explained in Section 2.6,

$$\mathbf{H}_{th} = \boldsymbol{\eta}(\mathbf{r},t)\sqrt{\frac{2\alpha k_B T}{|\gamma_G|\mu_0 M_s \Delta^3 \delta t}} \tag{9.1}$$

with δt the used time step and $\boldsymbol{\eta}(\mathbf{r},t)$ a stochastic vector whose components are Gaussian random numbers, uncorrelated in space and time, with zero mean value and dispersion 1. In the considered simulations, the damping constant α is 0.02, the FD cell size $\Delta = 10\,\text{nm}$ and the used time step δt is 2.5 ps. In Section 2.6 we explained that the thermal fluctuations make it possible to overcome energy barriers in the micromagnetic energy landscape of the considered ferromagnetic system. The larger the amplitude of the thermal fluctuations, the larger the energy barriers that can be overcome. Figures 9.7 to 9.9 show the simulated hysteresis loops for the ferromagnetic samples considered above. Here, the high accuracy magnetostatic field evaluation scheme 1 is used. The fluctuating thermal fields correspond to different temperatures (0 K, 210 K, 260 K, 310 K and 360 K). It is clear that for $T = 0\,\text{K}$ the thermal fields are zero and the resulting hysteresis loops correspond to the ones simulated in Section 9.3.1.

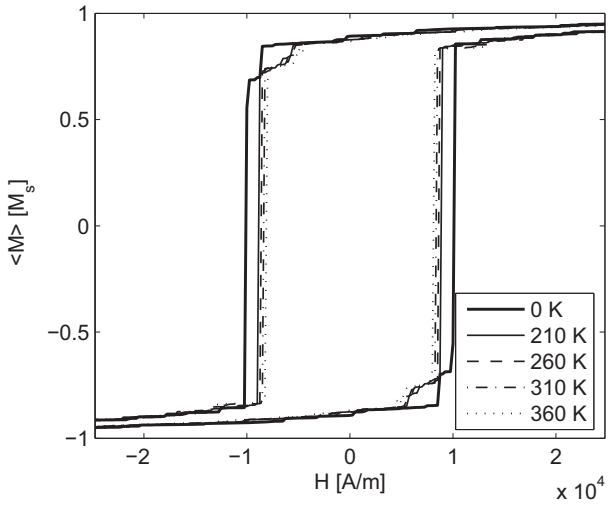

Figure 9.8: Hysteresis loops for the same ferromagnetic sample as in Fig. 9.5 (sample B), computed using the high accuracy $\mathbf{H}_{ms}$ evaluation scheme. Thermal effects are taken into account for different temperatures.

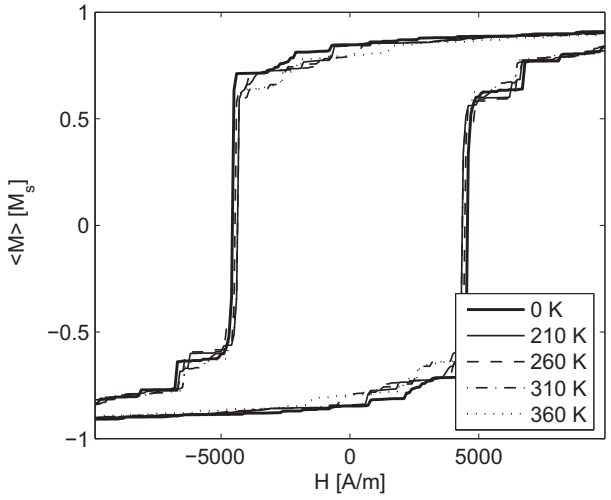

Figure 9.9: Hysteresis loops for the same ferromagnetic sample as in Fig. 9.6 (sample C), computed using the high accuracy $\mathbf{H}_{ms}$ evaluation scheme. Thermal effects are taken into account for different temperatures.

Figures 9.7 and 9.8 show the hysteresis loops corresponding to sample A and sample B. As expected, higher temperatures result in lower coercive field values. Indeed, at higher temperatures, the amplitude of the fluctuations rises,

Table 9.3: Simulation data: hysteresis loops for different temperatures.

simulation	$\#\delta t$	CPU time
sample A, 0 K	1461	1 h 5 min
sample A, 210 K	1639	1 h 12 min
sample A, 260 K	1825	1 h 19 min
sample A, 310 K	1827	1 h 20 min
sample A, 360 K	2159	1 h 34 min
sample B, 0 K	4447	24 h 22 min
sample B, 210 K	5790	37 h 49 min
sample B, 260 K	5643	36 h 52 min
sample B, 310 K	5753	37 h 35 min
sample B, 360 K	6328	42 h 11 min
sample C, 0 K	11 219	236 h 20 min
sample C, 210 K	13 220	262 h 11 min
sample C, 260 K	11 479	228 h 8 min
sample C, 310 K	12 466	246 h 44 min
sample C, 360 K	12 487	247 h 35 min

enabling the system to overcome larger energy barriers, resulting in a possible domain nucleation in more stable energy states. Hence, the magnetization reversal can take place at smaller applied fields. The hysteresis loops at different temperatures for sample C with dimensions $1.5\,\mu m \times 1.5\,\mu m \times 48.0\,\mu m$, shown in Fig. 9.9, are almost identical. Since the successive equilibrium states are more stable compared to the ones in sample A and B, the thermal fluctuations only have a negligible influence on the hysteresis loop. For applied fields somewhat smaller than the coercive field, the energy barriers are still too large to be overcome by the thermal fluctuations and to initiate the magnetization reversal.

In these simulations, the temperature can also have a large impact on the number of time steps and thus on the CPU time. This is shown in Table 9.3. For sample A and B, the number of time steps $\#\delta t$ increases for higher temperatures, while this is much less pronounced for sample C. In sample A and B, higher temperatures (i.e. rising amplitudes of the fluctuating thermal field) make the micromagnetic systems converge more slowly to successive equilibrium points. The larger fluctuations open up a higher number of possible energy paths between successive (metastable) equilibrium points, resulting in more time steps and larger CPU times. For the hysteresis simulation of sample C, the successive equilibrium states are more stable and the energy paths between the equilibrium states are more confined. Hence the thermal fluctuations do not have a large impact on the total number of time steps.

9.3.3 Comparison

Now we can compare the results described in sections 9.3.1 and 9.3.2. In both simulation series, noise terms of very different origin influence the hysteresis behavior. For a given magnetic configuration, the numerical noise in section 9.3.1 is constant, while the thermal noise still depends on the used time step δt and discretization size Δ, see expression (9.1). However, similar conclusions can be drawn concerning their influence. Indeed, the same mechanisms are at the origin of the possible variations of the coercive fields. The numerical noise on the $\mathbf{H}_{ms}$ evaluation on the one hand and the thermal fluctuations on the other hand, can initiate domain nucleation at smaller applied fields compared to the loops computed with the high accuracy $\mathbf{H}_{ms}$ evaluation scheme at $T = 0\,\mathrm{K}$. The possible reduction of the coercive field depends in both cases on the stability of the equilibrium states in every point of the hysteresis loop. From Table 9.2 and Table 9.3 it is also clear that, given a micromagnetic system, the low accuracy evaluation of $\mathbf{H}_{ms}$ or the addition of thermal fluctuations has the same impact on the number of time steps required for the simulation of the hysteresis loop. When the system runs through metastable equilibrium states, more time steps are required in both cases.

When thermal fluctuations are considered in a certain sample, the coercive field $H_c(T)$ increases monotonically to $H_c(T = 0)$ for decreasing temperatures and thus decreasing amplitudes of the thermal field $\mathbf{H}_{th}$. In the same way, smaller numerical noise levels should lead to increasing coercive fields, converging to $H_c(T = 0\,\mathrm{K})$ when numerical noise is zero. To examine this, the simulations of Fig. 9.4 on sample A are redone with the $\mathbf{H}_{ms}$ evaluation scheme 2. The discretization however is refined to FD cells with halved dimensions ($\Delta = 5\,\mathrm{nm}$) leading to a higher accuracy. The hysteresis loop is shown in Fig. 9.10 together with the loops of Fig. 9.4 ($\Delta = 10\,\mathrm{nm}$, $\mathbf{H}_{ms}$ evaluated with scheme 1 and 2). From Fig. 9.10 it is clear that, as expected, the hysteresis loop simulated with $\mathbf{H}_{ms}$ scheme 2 and $\Delta = 5\,nm$ has an intermediate coercive field, since the magnetostatic field evaluations in the considered simulation have also an intermediate precision.

9.3.4 Conclusion

When we interpret these results in the framework of the micromagnetic hysteresis modeling we can see that the hysteresis loops in Fig. 9.10 are very similar, but not identical. Indeed, on the microscopic level, the space and time behavior of the magnetization is slightly different. However, it is clear that the same magnetic processes dominate the hysteresis behavior of the ferromagnetic sample and identical conclusions concerning the macroscopic magnetic behavior can be drawn independent of the used $\mathbf{H}_{ms}$ evaluation scheme. This shows that the low accuracy $\mathbf{H}_{ms}$ evaluation scheme can be used in micromag-

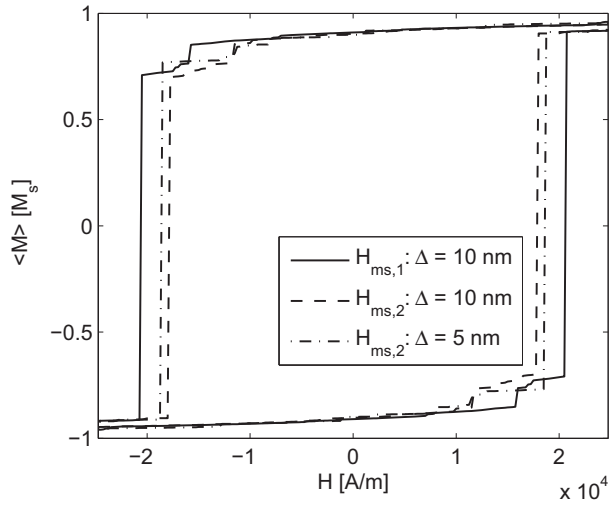

Figure 9.10: Hysteresis loops for sample A, computed using the high accuracy $\mathbf{H}_{ms}$ evaluation scheme, $\mathbf{H}_{ms}$ scheme 2 with discretization size $\Delta = 10\,\text{nm}$ and $\mathbf{H}_{ms}$ scheme 2 discretization size $\Delta = 5\,\text{nm}$.

netic hysteresis simulations. Furthermore, the origin of the small variations in the hysteresis loops is now clarified: the introduced numerical noise initiates the domain reversal at smaller coercive fields and larger numerical noise levels give rise to smaller coercive fields. Although the numerical noise is not Gaussian distributed and is not uncorrelated in space and time, these conclusions are identical to the conclusions drawn from simulations with additional thermal noise. Indeed, the influence of the thermal fluctuations depends in the same way on the stability of the successive micromagnetic equilibrium points. Moreover, the differences in the hysteresis loops simulated with the low accuracy $\mathbf{H}_{ms}$ evaluation scheme are of the same magnitude as encountered when thermal fluctuations for moderate temperatures are taken into account.

Part III

Applying the Micromagnetic Scheme

CHAPTER 10

Classical micromagnetic applications

As mentioned frequently in this PhD thesis, the micromagnetic scheme is designed and optimized to describe magnetization phenomena in multiple magnetic domain sized ferromagnetic materials. However, as already demonstrated by the comparison of simulation results for switching processes in Section 6.4, the numerical scheme is also perfectly suited to describe magnetization processes in the more classical research domain of submicrometer sized magnetic samples. In this chapter we will show some other examples where the developed micromagnetic scheme provides results to better understand the magnetization processes in small ferromagnetic samples.

10.1. Influence of geometry and temperature in nanostrips

10.1.1 Introduction

Recently, there has been a growing interest in magnetic nanostructures, studying how particular magnetic properties can be tailored by properly changing their structural geometry [108]. Potential applications range from data storage devices to high-resolution magnetic field sensors. Within this context, the investigation of the micromagnetic behavior of magnetic nanoparticles is fundamental to understand their overall properties. Thus, increasing attention has been devoted to the computation of magnetization reversal processes, starting from the space-time integration of the LLG equation [109, 110, 111].

This section numerically studies the micromagnetic behavior of permalloy nanostrips with variable size and end shape, considering triangular tips and nucleation pads. The analysis evidences how the scaling factor and the

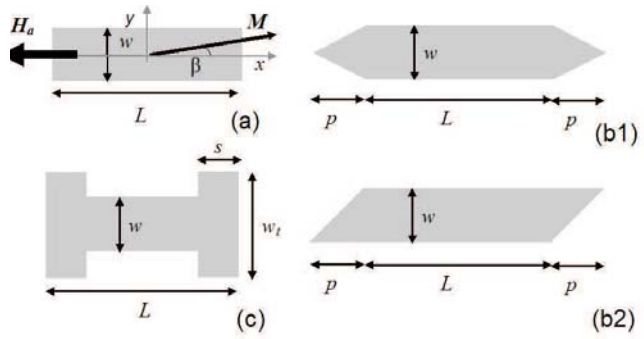

Figure 10.1: Studied samples with reference to the geometrical parameters considered in the analysis. The thickness varies between 5 nm and 209 nm.

local shape anisotropy due to end effects play a fundamental role in the interplay of magnetostatic and exchange energies, and consequently on the reversal mechanism. At sub-micrometer length scale, the switching processes are also affected by magnetization fluctuations induced by thermal agitation. The introduction of thermal noise enables the selection of the geometrical configurations characterized by a higher thermal stability. This research is elaborated in collaboration with the Istituto Nazionale di Ricerca Metrologica (INRIM, Turin, Italy).

10.1.2 Numerical analysis

The attention is focused on a magnetic nanostrip, with variable longitudinal size L (order of some hundreds of nanometers) and width w. The aim is to evidence the role of sample dimension, end shape and temperature on the magnetization reversal mechanism under the action of an external field. The geometric parameters of the different analyzed configurations are depicted in Fig. 10.1. The basic strip is rectangular and three scaling factors are considered, varying length L from 200 nm to 800 nm and width w from 25 to 100 nm. At the same time, the thickness t is increased from 5 nm to 20 nm, keeping the sample aspect ratio fixed. Configurations (b1) and (b2) show symmetric or asymmetric tips at the nanostrip ends, while in configuration (c) nucleation pads are added to the rectangular strip. In all configurations, the initial magnetization is uniform in the sample, making an angle β with the x-axis. A constant negative field H_a is applied along the x-axis. The nanostrip material is permalloy with $M_s = 860\,\mathrm{kA/m}$, $K_u = 0$ and $A = 13\,\mathrm{pJ/m^3}$. The damping constant α is assumed to be equal to 0.02. For each basic rectangular nanostrip considered

here, modifications of the shape have been analyzed, introducing symmetric or asymmetric triangular tips or nucleation pads at the ends.

Role of size and end shape

To evidence the effects of nanostrip size and end shape, we have initially excluded the thermal noise influence by setting the temperature to zero. The switching dynamics is studied by applying a sufficiently large magnetic field ($H_a = 100\,\mathrm{kA/m}$) in the negative x-direction. To facilitate the reversal process, the initial magnetization, which is assumed uniformly distributed, makes an angle β of 5 degrees with the x-axis (see Fig. 10.1.a).

First, we focus on rectangular strips, evidencing how the switching mode is strongly determined by the sample size [111]. When $L = 200\,\mathrm{nm}$, the reversal starts with the nucleation of two symmetric domain walls at the ends of the nanostrip, where the magnetostatic field exhibits its highest value. Then the domain walls propagate along the longitudinal direction with a rotational motion, which leads to oscillations of the perpendicular components of the magnetization. When the walls approach the sample center, two vortices nucleate and the peak of exchange energy is reached. This is shown in the top halve of Fig. 10.2

When $L = 800\,\mathrm{nm}$ the dynamic behavior starts with the formation of two vortices at the ends which, successively, move towards the nanostrip center, see bottom halve of Fig. 10.2. The 400 nm long strip shows an intermediate behavior, with the nucleation of two asymmetric domain walls at the ends that propagate towards the center, evolving in more complex magnetization patterns with respect to the 200 nm long sample. Since the magnetization reversal is driven by the phenomena occurring at the nanostrip ends, where strong magnetostatic fields arise, we explore the possibility of accelerating the reversal processes by considering nanostrips with different end geometries. As an example, Fig. 10.3 evidences the influence of triangular tips (shapes b), reporting the relaxation time τ (i.e. the time elapsing until the longitudinal magnetization component M_x becomes zero) versus parameter p, which represents the height of the triangular ends. For low values of p, a slight reduction of τ can be observed. For a symmetric structure end (shape b1), when the reversal is driven by vortex nucleation ($L = 800\,\mathrm{nm}$), the presence of the triangular tips has a weaker influence. For smaller sample sizes, a further increase of p interferes with the domain wall formation up to a critical value, beyond which the reversal does not take place. In this case, the local shape anisotropy forces the magnetization to align antiparallel to the external field, reaching an equilibrium configuration. On the contrary, when considering a rectangular strip with the same transversal dimension w and longitudinal dimension equal to $(L + 2p)$, the reversal occurs also when p reaches the critical value. Finally, Fig. 10.3 evidences how for an asymmetric structure (shape b2), when $L = 400\,\mathrm{nm}$,

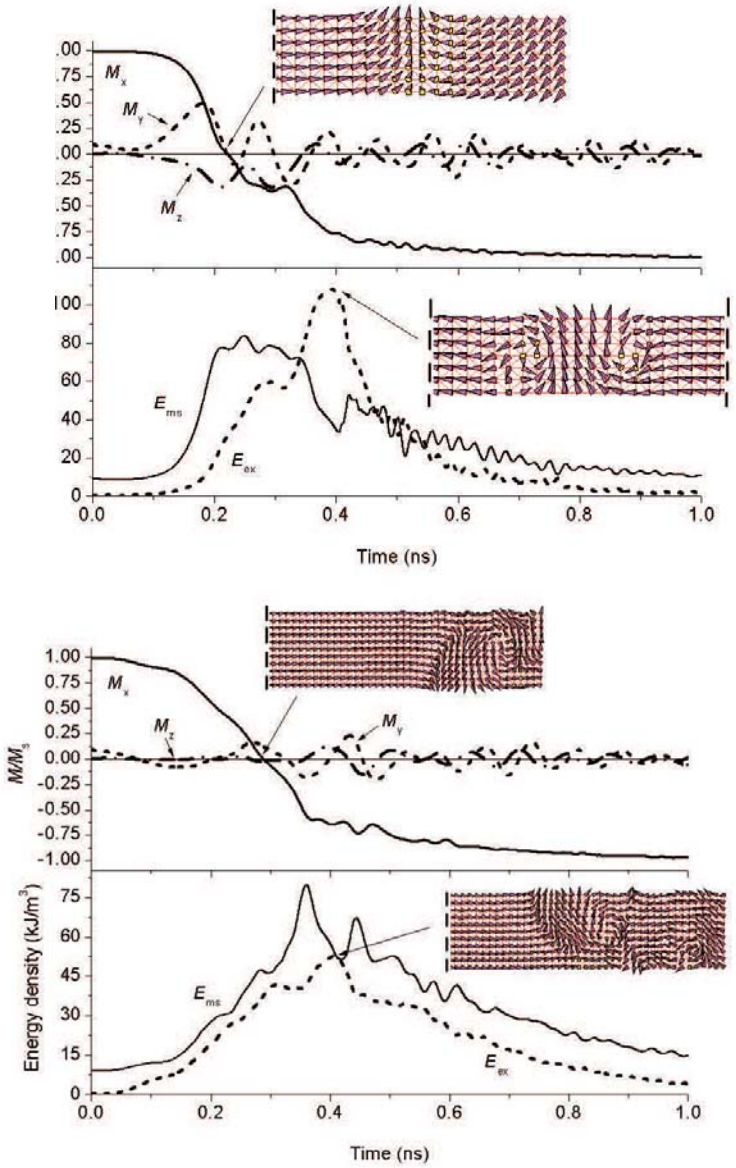

Figure 10.2: Time evolution of the average magnetization components and specific magnetostatic (E_{ms}) and exchange (E_{exch}) energy terms of the rectangular nanostrips of length equal to 200 nm (top) and 800 nm (bottom). The magnetization snapshots at the instant when $M_x = 0$ and at the instant of maximum exchange energy are shown. Due to symmetry, only one end of the strip or its central portion are reported.

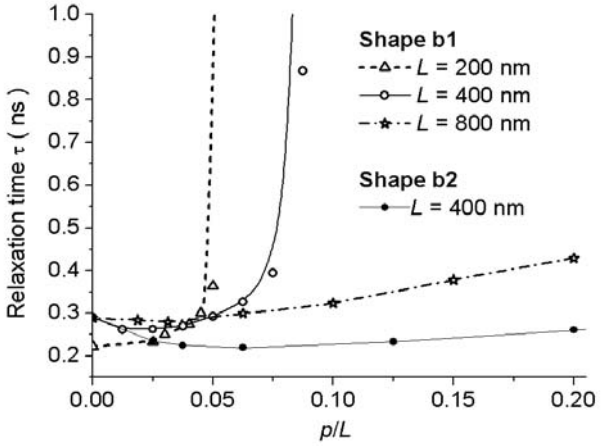

Figure 10.3: Relaxation time versus geometric parameter p (normalized to L), for shapes (b1) and (b2). For the first end structure, three different values of L are considered. The external field H_a has an amplitude of 100 kA/m.

the presence of triangular tips facilitates the domain wall creation, leading to a reduction of τ.

The effect of nucleation pads at the nanostrip ends (shape c) is analyzed by varying parameter s and fixing w_t to $1.8w$. Generally, this end shape advantages the reversal mechanism with a consequent decrease of τ, which can reach a minimum when properly choosing parameter s, see Fig. 10.4. A strong dependence on geometrical configuration is found also with large sample sizes. When $L = 800$ nm, τ reduces to approximately one third when parameter s is equal to $\sim 0.3L$. A further increment of s up to $0.5L$ (rectangular strip with width equal to w_t) limits the effect of the geometry.

When $L = 400$ nm, the nucleation pads advantage the creation and propagation of asymmetric domain walls inside the pads. For low values of s (up to $0.1L$), it has been observed that when the wall is going to be expelled from the pad, there is the nucleation of a vortex and an antivortex at the pad corners, see Fig. 10.5. For high values of s, this structure does not appear, but the larger extension of the pad enables the increase of the propagation velocity of the transverse wall.

The presence of nucleation pads reduces the coercive field. In contrast to the rectangular strip case, the switching occurs also when the external field is 50 kA/m (bottom Fig. 10.4). In this case, there is a shift of the minimum of the relaxation time towards lower values of s, while for higher values the influence of the geometric configuration becomes weak.

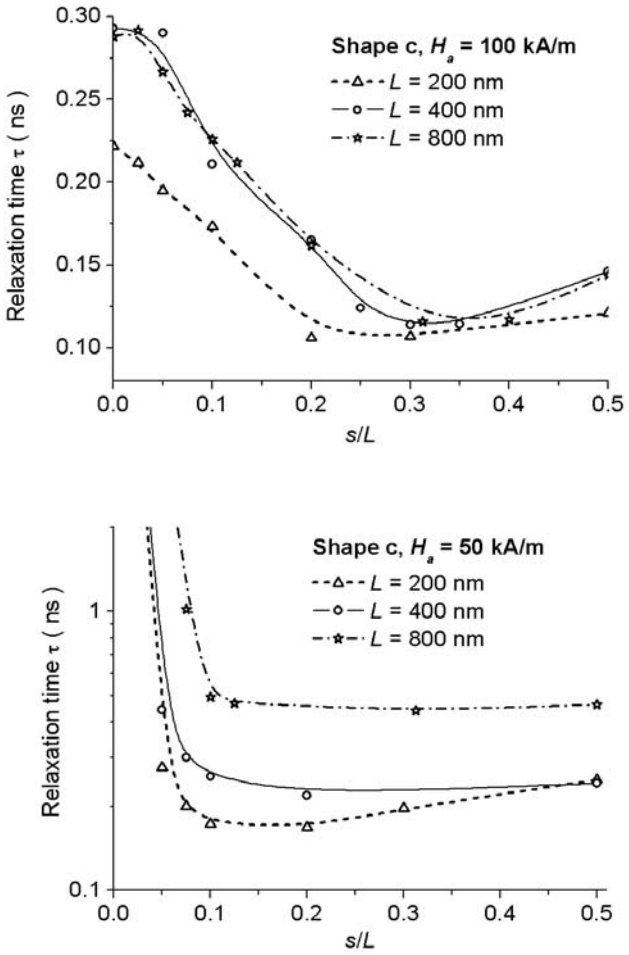

Figure 10.4: Relaxation time versus geometric parameter s, for nanostrip shape (c) with nucleation pads. The external field H_a has an amplitude of 100 kA/m (top) and 50 kA/m (bottom).

Role of temperature

In this subsection, the nanostrip is initially saturated along the x-direction ($\beta = 0$) and a constant external field is applied antiparallel to the magnetization. If this field is lower than the coercive one, the system lies in a metastable equilibrium state, that would not decay by itself if thermal effects are not taken into account. As outlined in Section 2.6, thermal fluctuations add a stochastic energy of kinetic nature to the Gibbs free energy. This extra amount of energy

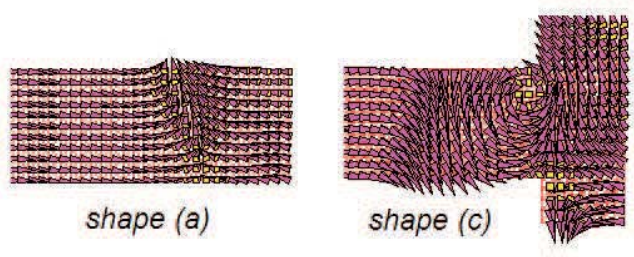

Figure 10.5: Comparison of magnetization snapshots at time instant $t = 0.16\,\text{ns}$ for shapes (a) and (c), whit parameter $s = 0.1\,L$ and $L = 400\,\text{nm}$. In the nanostrip with nucleation pads, the domain wall has already disappeared. Due to symmetry, only on end of the strip is reported.

can induce the system to jump across energy barriers and initiate the transition towards another equilibrium state. In this case, the system can evolve even in the absence of an external field, losing a fraction of its initial magnetization.

The analysis is here performed considering a temperature ranging from 0.04 K up to 340 K and a time interval of 1.5 ns. Depending on the size and the stability of the geometric configuration, the magnetic sample responds in a different way to thermal noise addition. When $H_a = 0\,\text{A/m}$, for the rectangular strip of length equal to 400 nm, the equilibrium state reached after 1.5 ns is characterized by a strong reduction of the average value of M_x at the temperature increase (see top part of Fig. 10.6). For temperatures up to $\sim 10\,\text{K}$, the sample stays saturated, while at 340 K, M_x reduces to $\sim 0.7 M_s$. When $H_a = 50\,\text{kA/m}$, which corresponds to a field lower than the coercive one, the magnetization reverses starting from a temperature of $\sim 50\,\text{K}$. Increasing the external field up to 100 kA/m, thermal effects accelerate the switching process also at very low temperatures. In the considered time window, a further increment of temperature leads to a detriment of the final average value of M_x of the same order of the decrease reached in the absence of the external field. As shown in the bottom part of Fig. 10.6, up to $\sim 50\,\text{K}$ the relaxation time τ is characterized by a strong reduction with temperature rise, due to the more efficient dissipation of the system energy. Successively, the value of τ stabilizes and then slightly increases, with a corresponding rise of the global time needed for switching. This is due to the fact that at high temperatures the presence of thermal fluctuations opposes to the reaching of the opposite saturation state.

Figure 10.6 evidences also the stability of the geometric configuration obtained with shape b1, when parameter p is equal to $0.1\,L$ and $L = 400\,\text{nm}$. For the considered temperature range, when $H_a = 0\,\text{A/m}$, a magnetization

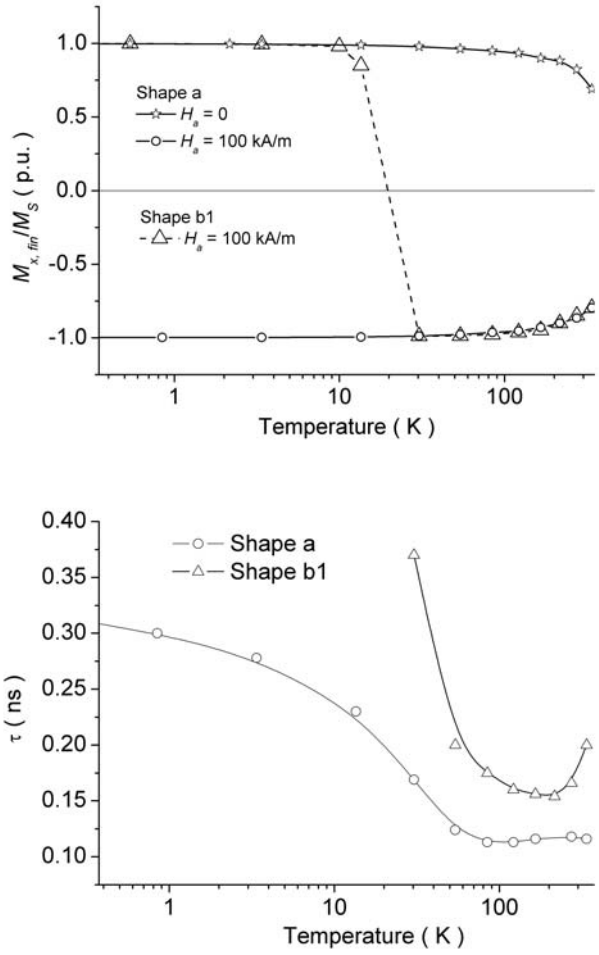

Figure 10.6: Top: Role of temperature on the final average value of M_x after 1.5 ns (top) and the reversal time (bottom) for shape (a), when $H_a = 0$ A/m and 100 kA/m. For the two considered shapes L equals 400 nm. The dashed line in the top figure is just a guide for the eye.

decay does not appear. When applying a 100 kA/m external field, a temperature higher than ~ 20 K is required to obtain the magnetization reversal. Once reached the switching point, the reduction of the average final value of M_x corresponds to the one obtained with the rectangular strip.

Finally, we have studied how, when including thermal noise, the nanostrip behavior is strongly dependent on the scaling factor, the decrease of which

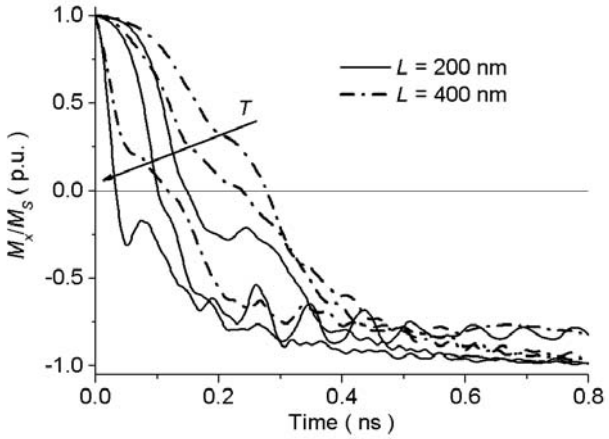

Figure 10.7: Effect of temperature on the time evolution of the average magnetization component M_x for two rectangular nanostrips ($L = 200\,\text{nm}$ and $L = 400\,\text{nm}$) under an external field of $100\,\text{kA/m}$. The curves reported in the figure correspond to temperature values of 3.4 K, 13.5 K and 340 K.

can determine a more reactive response to thermal agitation. As an example, Fig. 10.7 compares the switching dynamics obtained when $L = 200\,\text{nm}$ and $L = 400\,\text{nm}$, for different values of temperature when $H_a = 100\,\text{kA/m}$. For the same temperature amplitude of 340 K, the relaxation time is ~ 2.5 times lower when $L = 200\,\text{nm}$.

10.1.3 Conclusion

The influence of scaling factor, end shape and thermal fluctuations has been investigated in nanostrips with a longitudinal dimension of few a hundreds of nanometers. Different reversal mechanisms are observed, depending on the sample size. The analysis has evidenced the fundamental role of end shape on initial magnetization processes and, consequently, on the relaxation time. It has been found that the presence of sharp triangular tips at the strip ends can prevent the magnetization reversal, when considering small samples. On the contrary, the addition of nucleation pads at the strip ends can accelerate the switching processes and reduce the coercive field.

Thermal fluctuations have a destabilizing effect on the micromagnetic system resulting in equilibrium states that could not be obtained at zero temperature. The inclusion of thermal noise can induce switching at fields lower than the coercive one and also in very stable geometric configurations.

10.2. Thermally initiated reversal modes in infinite periodic wires

10.2.1 Introduction

In Section 3.7 we have seen that the magnetostatic fields are closely related to the sample geometry and have a substantial effect on the magnetic behavior, which makes it difficult to draw general conclusions about the magnetic properties of the material independent from the sample geometry. By considering an infinitely long geometry, the demagnetizing effects are reduced to zero in the longitudinal direction. In this way, only demagnetizing effects in the cross section together with the other micromagnetic interactions determine the magnetization process. In this section we investigate the 3D reversal mechanisms in infinitely long ferromagnetic wires.

In *finite* wires, the magnetization reversal initiates at the ends of the geometry due to the interaction with the large demagnetizing fields, see e.g. [112]. In the considered infinite magnetic wires, the magnetization reversal is initiated by thermal fluctuations in the body of the material. The thermal fluctuations are considered as small perturbations on the other energy terms. This assures that the thermal fluctuations only initiate the magnetization reversal, but do not influence the reversal itself. The reversal mechanisms depending on the cross sectional dimensions and the iron lattice orientation are studied.

10.2.2 Micromagnetic framework

In the micromagnetic simulations, monocrystal ferromagnetic wires with square cross section are considered. The Zeeman (i.e. the applied field $\mathbf{H}_a$), exchange, (cubic) anisotropy and magnetostatic interactions are taken into account by their corresponding magnetic field, contributing to the effective field

$$\mathbf{H}_{eff} = \mathbf{H}_a + \mathbf{H}_{exch} + \mathbf{H}_{ani} + \mathbf{H}_{ms}. \tag{10.1}$$

The computations are restricted to a computational domain of $N \times N \times N$ finite difference (FD) cells. This computational domain is repeated periodically along the z-direction, as presented in Section 7.4.

In the considered simulations, the wire is initially uniformly magnetized in the positive z-direction: $\mathbf{M} = M_s \mathbf{e}_z$. Due to the infinite structure of the wire, this magnetization state does not introduce magnetostatic fields: $\mathbf{H}_{ms}^{uniform} = 0$. Indeed, no magnetic poles are generated on the surface of the wire or in the wire itself. Furthermore, in this uniform magnetization state the exchange field is also zero, $\mathbf{H}_{exch}^{uniform} = 0$, since

$$\mathbf{H}_{exch}(\mathbf{r}) \propto \nabla^2 \mathbf{M}(\mathbf{r}). \tag{10.2}$$

The external field is applied along the z-direction and diminished to possibly large negative values to ensure the magnetization reversal: $\mathbf{H}_a = H_a \mathbf{e}_z$. Furthermore, the anisotropy field can have an initial non negative value when the magnetization does not align with a crystallographic axis of the iron lattice. Hence, when uniformly magnetized, the effective field (10.1) in the wire is constant throughout the wire

$$\mathbf{H}_{eff}^{uniform} = H_a \mathbf{e}_z + \mathbf{H}_{ani}^{uniform}. \tag{10.3}$$

From the LLG equation,

$$\frac{\partial \mathbf{M}}{\partial t} = \frac{\gamma_G}{1+\alpha^2} \mathbf{M} \times \mathbf{H}_{eff} + \frac{\alpha \gamma_G}{(1+\alpha^2) M_s} \mathbf{M} \times (\mathbf{M} \times \mathbf{H}_{eff}) \tag{10.4}$$

it is clear that changes in magnetization are depending on the torque $T(\mathbf{r}) = \mu_0 \mathbf{M}(\mathbf{r}) \times \mathbf{H}_{eff}(\mathbf{r})$. This implies that when $\mathbf{H}_{ani}^{uniform} = 0$, no torque is exerted on the local magnetization and the magnetization state will stay unchanged, whatever the amplitude of the opposite applied external field is.

The switching process can be activated by thermal agitation, leading to fluctuations of the magnetization around the described equilibrium state, see Section 2.6. A small thermal field $\delta \mathbf{H}_{th}$ is added to the effective field (10.1) as a spatially and temporally uncorrelated white noise term. The standard deviation of the Gaussian distributed thermal fluctuations is taken such that the thermal field is a small perturbation on the other terms in the effective field. In this way the torque in a uniformly magnetized wire with $\mathbf{H}_{ani}^{uniform} = 0$ becomes non zero.

$$T(\mathbf{r}) = \mu_0 \mathbf{M} \times \delta \mathbf{H}_{th}(\mathbf{r}) \tag{10.5}$$

Following the LLG equation (10.4), this torque can initiate a change in the magnetization. By keeping $\delta \mathbf{H}_{th}$ small, we guarantee that reversal is only initiated at metastable energy states which only need a small amount of energy to destabilize the micromagnetic system. Once the reversal is started, other effective field terms become much larger then the thermal field, which ensures that the reversal process itself is not influenced by the thermal fluctuations. Here, the focus is on the reversal modes. To study the influence of $\delta \mathbf{H}_{th}$ on the time instant when the initialization of the reversal takes place, Monte Carlo simulations would be needed [113] implying a huge number of simulations. This is out of the scope of this work.

10.2.3 Reversal modes

In the considered simulations, the external applied field is decreased in a stepwise way. For each new value of the applied field the micromagnetic dynamics

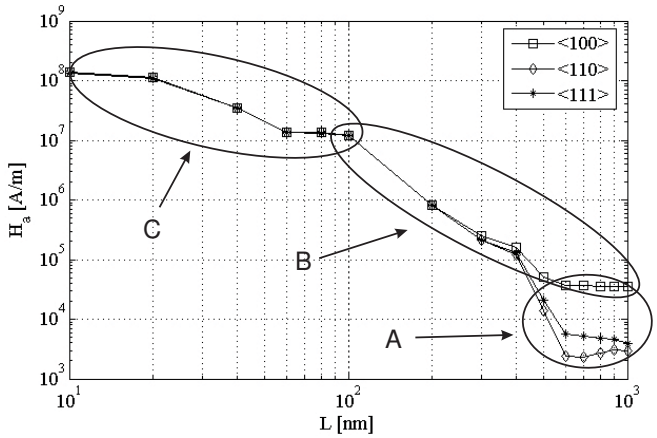

Figure 10.8: Reversal fields for ferromagnetic wires with cross sections L and different lattice orientations. The different reversal modes are depicted: reversal with (A) domain formation, (B) vortex formation and (C) precessional switching combined with buckling.

are computed during $1\,ps$ using the predictor-corrector semi analytical time stepping, see Section 6.3. If no reversal is initiated, the applied field is decreased to the next value, if the reversal takes place, the $\mathbf{H}_a$ is kept constant until equilibrium is reached. The damping constant α is taken 0.1 and the standard deviation of the amplitude of the thermal fields is taken $100\,Am^{-1}$, which guarantees $\delta\mathbf{H}_{th}$ is only a perturbation. The material properties of iron are used: the exchange length is about $2.8\,nm$ while the anisotropy constants K_1 and K_2 are $0.48\,10^5\,Jm^{-3}$ and $-0.50\,10^5\,Jm^{-3}$ respectively. The cross sectional dimensions $L \times L$ are varied from $L = 10\,nm$ to $L = 1\,\mu m$ for iron wires with the easy, medium and hard magnetization axis ($< 100 >$, $< 110 >$ and $< 111 >$) along the infinite $z-$direction. Figure 10.8 shows the applied fields for which the z-component of the magnetization passes through zero. These values should be interpreted qualitatively: the actual reversal points depend on the time for which the applied field is kept constant and on the standard deviation of the amplitude of $\mathbf{H}_{th}$, i.e. on the temperature.

Depending on the cross sectional dimensions and the lattice axes orientation, there is a smooth transition between three different reversal modes depicted as A, B and C in Fig. 10.8. Representative magnetization configurations in planes perpendicular to the z-direction (left) and planes along the z-direction (right) are shown in Fig. 10.9 for the three reversal modes.

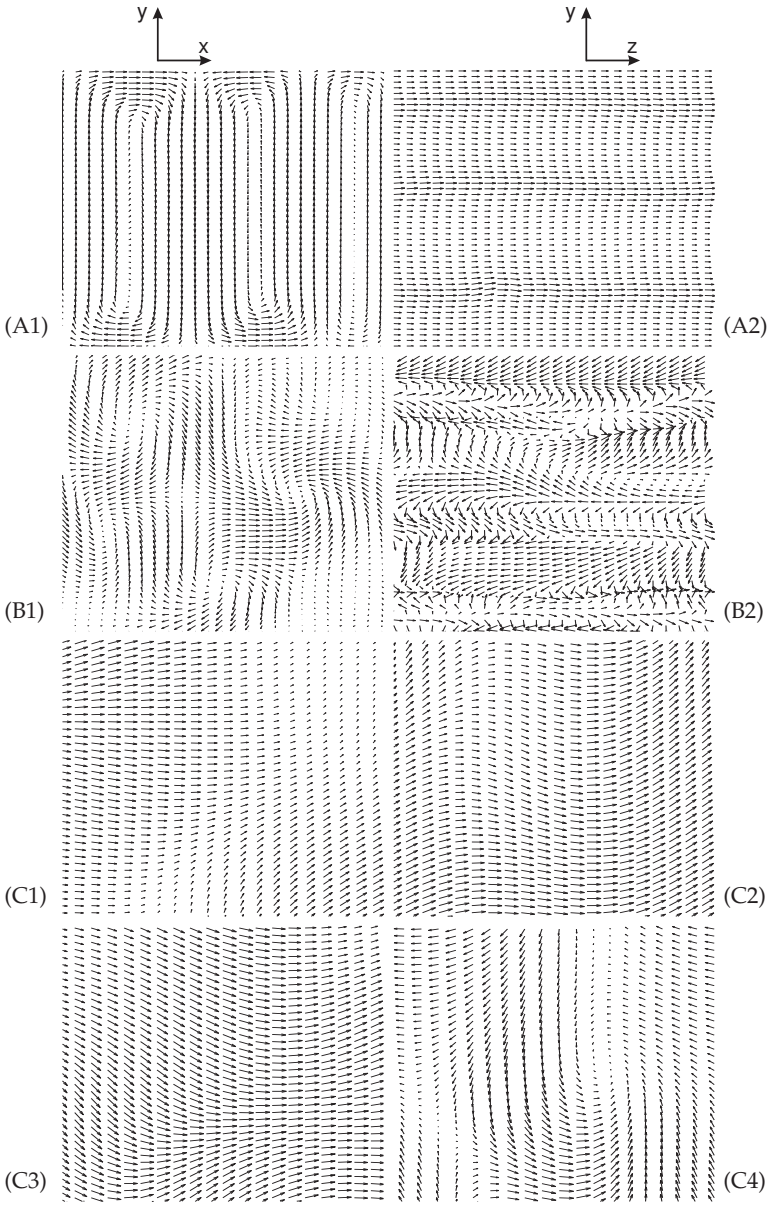

Figure 10.9: Representative magnetization patterns perpendicular to (left) and parallel to (right) the z-direction, during the reversal of iron wires with cross sections (A) $800\,nm \times 800\,nm$, (B) $200\,nm \times 200\,nm$ and (C) $10\,nm \times 10\,nm$. For the wire with $L = 10\,nm$ two successive time instants are considered. The $< 110 >$ direction of the crystallographic axis is oriented along the z-direction.

Domain formation

For wires with large cross section ($L \geq 500\,nm$) and with the $< 111 >$ or $< 100 >$ direction along the z-direction, domains are formed during the reversal process as can be seen in Fig. 10.10.A1 for a wire with cross section $L = 800\,nm$. The evolution of the average demagnetizing, anisotropy and exchange energy density (ϕ_{demag}, ϕ_{ani} and ϕ_{exch} respectively) are shown in Fig. 10.10 during reversal for the wire with the $< 110 >$ along the z-direction. As expected, the exchange and demagnetizing energy are zero and the anisotropy energy is constant until the reversal is initiated. Since domains are formed, ϕ_{demag} and ϕ_{exch} stay relatively small during the reversal. Indeed, near the edges of the wire, the magnetization stays aligned with the surface. Hence small magnetic charges are only introduced in the domain walls, but not on the wire edges, reducing the demagnetizing energy. Since in the domains the magnetization is divergence free the exchange energy is only non-zero in the domain walls. Furthermore, ϕ_{ani} is reduced during the reversal process since domains are oriented along easy magnetization directions $< 100 >$. All energy terms vary in the same order of magnitude and thus all have influence on the reversal process. Since the energy terms in the wire stay small during the reversal process, the reversal can be initiated at moderate fields, see Fig. 10.8. From Fig. 10.9.A2 it is clear that this domain reversal process is invariant in the z-direction.

For wires with identical cross sectional dimensions and easy magnetization direction $< 100 >$ along the z- direction, also the anisotropy energy is initially zero and extra energy has to be put into the system to sustain an increase of ϕ_{ani} at the start of the reversal process, i.e. larger applied fields are required as shown in Fig. 10.8. During the reversal process itself the extra amount of energy is distributed among all energy terms leading to a reversal with domains as well as vortices.

Vortex formation

Domains cannot be formed in wires with cross sections $L < 500\,nm$ because the characteristic width of a domain wall (about $70\,nm$ [5]) is too large compared to the sample dimensions. For wires with cross sections $100\,nm < L < 500\,nm$ the reversal process is dominated by vortices. Figure 10.9.B1 and 10.9.B2 show magnetization configurations for a wire with $L = 200\,nm$ and $< 110 >$ axes along the infinite direction while Fig. 10.11 shows the evolution of the energy density terms during reversal. At a certain applied field, the thermal perturbations initiate different vortices, with axis along the z-direction, in the sample. Figure 10.11 shows that at the start of the reversal process, the demagnetizing energy density is very large, while the exchange density is relatively small. Later in time however, the demagnetizing energy is reduced and the exchange

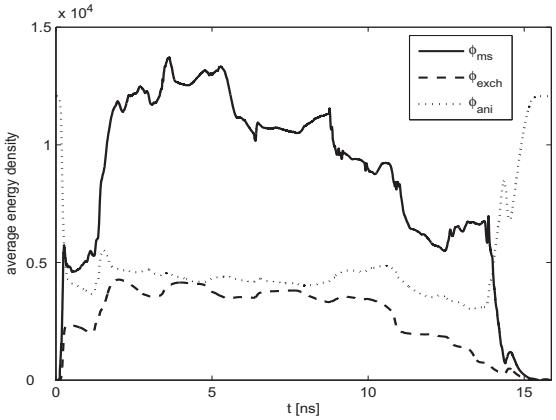

Figure 10.10: Average demagnetizing, anisotropy and exchange energy density during the reversal process of a Fe wire with $L = 800\,nm$ and $< 110 >$ axis along the z-direction.

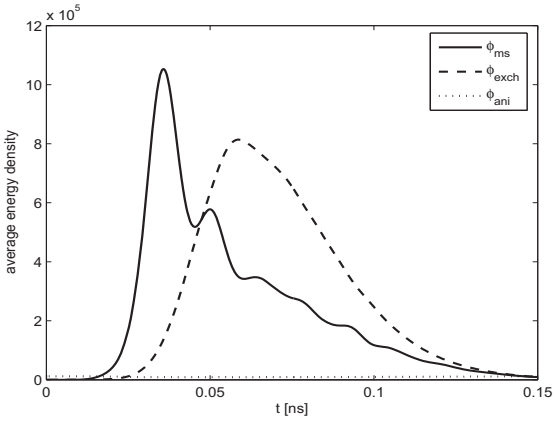

Figure 10.11: Average demagnetizing, anisotropy and exchange energy density during the reversal process of a Fe wire with $L = 200\,nm$ and $< 110 >$ axis along the z-direction.

energy is increased. It is clear that the influence of the anisotropy interaction is negligible. The exchange energy during the reversal is increasing with smaller cross sectional dimensions. This results in larger applied fields required to sustain the reversal as depicted in Fig. 10.8. As can be seen from Fig. 10.9.B2 this reversal mode is 3D in nature which shows the necessity of using a 3D model as presented here.

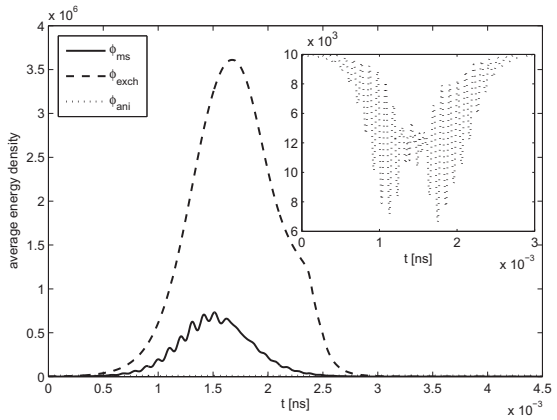

Figure 10.12: Average demagnetizing, anisotropy and exchange energy density during the reversal process of a Fe wire with $L = 10\,nm$ and $< 110 >$ axis along the z-direction. An enlarged view of ϕ_{ani} is shown in the top right corner.

Precessional switching combined with buckling

In wires with yet smaller cross sections, also the formation of various vortices is impossible because the characteristic width of a single vortex (up to $35\,nm$) is too large compared to the sample dimensions. Figures 10.9.C1 to 10.9.C4 show magnetization configurations for a wire with $L = 10\,nm$ and $< 110 >$ axes along the z-direction. The reversal process is dominated by a precessional switching of the magnetization with rotation axis along the z-direction, see Fig. 10.9.C1, combined with buckling along the z-direction characterized by the zigzag magnetization pattern in Fig. 10.9.C2. The amplitude of the buckling effect increases during the reversal process until one single vortex with axis perpendicular to the longitudinal direction is initiated, see 10.9.C4. In Fig. 10.12 the evolution of the average demagnetizing, exchange and anisotropy energy density is shown. The exchange energy density is very large during the reversal. Indeed, since the variations in magnetization in Figs. 10.9.C1 to 10.9.C4 take place at a very small length scale, ϕ_{exch} becomes very large, such that also the demagnetizing interactions (and moreover the anisotropy interactions) influence this reversal mode only very little. The precessional movement of the magnetization is the origin of the oscillatory behavior of the anisotropy energy and –to a lesser degree– of the demagnetizing energy. Indeed, during the precessional movement, the magnetization aligns alternately with easy and less easy magnetization directions, while the demagnetizing fields change according to magnetizations pointing towards a corner or towards an edge of the wire.

In [89], Lebecki et al. described curling modes outside the buckling mode limit. These are not encountered in the considered simulations. Due to the highly inhomogeneous nature (in space, orientation and amplitude) of the thermal fluctuations, reversal is initiated at certain nucleation points in the material. These nucleation points evolve in vortices. Hence, vortex formation is favored over the curling reversal mode.

The same set of simulations is also performed for a wire with circular cross sectional geometry. For this geometry, similar reversal modes are encountered when the cross sectional dimensions are varied and similar applied fields are required to ensure the reversal. This shows that the cross section geometry has no influence on the reversal mechanism. During the reversal, other magnetization patterns are encountered, but they are also dominated by domain formation, vortex formation and precessional switching combined with buckling.

10.2.4 Conclusion

The presented periodic, 3D description of infinitely long magnetic wires allows the description of magnetic reversal modes for a wide range of cross sectional dimensions. For this geometry, thermal fluctuations are required to initiate the magnetization reversal. In wires with large cross sections, the anisotropy, the demagnetizing and the exchange interaction all have their influence on the magnetization reversal leading to domain formation. For smaller cross sections ($L < 500\,nm$), vortex formation determines the reversal and the influence of anisotropy interactions are negligible. In wires with cross sections $L < 100\,nm$, the reversal is performed by a precessional switching process combined with buckling. Here, the exchange interaction is dominant. In general, the amount of energy and thus the amplitude of the opposite applied fields required to ensure magnetic reversal increases for smaller cross sections.

CHAPTER 11

Micromagnetic study of magnetic domains

11.1. Introduction

Due to the large sample dimensions, it has long been unrealistic to apply full micromagnetic simulations to study the domain configurations in larger ferromagnetic materials. Therefore, on a length scale larger than 1 μm, magnetic domain studies typically rely on the *domain theory*. As the micromagnetic theory is a simplified model based on the homogenization of the interactions present on the atomic level, the domain theory is a simplified model based on the interactions described in the micromagnetic theory. In that way, the micromagnetic theory and the domain theory can be seen as a second and third level model respectively. In [106], Hubert and Schäfer define the length scale of the atomic theory smaller than 1 nm, the micromagnetic length scale from 1 nm to 1 μm and the domain theory length scale from 1 μm to 1 mm.

In the domain theory, micromagnetic equilibrium domain configurations are studied. In the theory it is assumed that the complete sample is comprised of *uniform magnetic regions*, minimizing the micromagnetic Gibbs free energy in the studied sample. Fine scale magnetization entities as the structure of domain walls are not resolved in the model, but are taken into account by estimating their characteristic energy contribution to the total Gibbs free energy. The theory is capable of predicting various magnetization configurations, depending on the microscopic material properties. Since the micromagnetic scheme, developed in this PhD, is capable of simulating magnetic processes at a length scale larger than 1 μm, it can also be used to study some cases that were only possible before within the domain theory. This can be beneficial since also non-uniformly magnetized regions can exist in the micromag-

netic approach. Moreover, fine scale magnetization entities as domain walls and vortex states (when domains are nucleated) are described much more accurately. In what follows we will concentrate on the micromagnetic study of magnetic domains in platelets with perpendicular uniaxial anisotropy.

11.2. Geometry description

In the following simulations a platelet with thickness $D = 0.8\,\mu$m is considered. Figure 11.1 shows the platelet in the used coordinate system. To obtain equilibrium domain configuration states in the xy-plane, the platelet is taken infinite in the z-direction, while maintaining a finite dimension L in the x-direction. In all simulations the thickness D is considerably smaller than the width L of the platelet. In the infinite direction, a periodic structure is considered with a period of length 320 nm as described in Section 7.4. Material parameters corresponding to those of cobalt are considered: saturation magnetization $\mu_0 M_s = 1.82\,$T and exchange stiffness $A = 1.510^{-11}\,$J/m, while the uniaxial anisotropy constant K_u is varied. In such samples, under zero applied field, domains can be expected as presented in Fig. 11.1. Indeed, the domain configurations are invariant in the infinite direction, while the domains are oriented along the uniaxial anisotropy axis. No magnetic charges are present at the outer edges, nor at the surface of the platelet due to the presence of closure domains. In the sketched closure domains, the magnetization is perpendicular to the uniaxial anisotropy axis. This will affect the closure domain structure as will be discussed later on. All domain configurations which are presented in the figures of this chapter correspond to cross sections parallel to the xy-plane.

11.3. Micromagnetic equilibrium states

To simulate magnetic domains using the micromagnetic scheme, one has to start from a known micromagnetic equilibrium state. In practice, this always corresponds to a uniform magnetization obtained by saturating the sample in one direction using a high external field. When the external field is reduced, the uniform magnetization state becomes unstable and magnetic domains are formed. In this case, the platelet is initially saturated in the infinite z-direction. First, the field is reduced to $0.0\,\mathrm{Am}^{-1}$. Depending on the material characteristics, this large applied field jump triggers the domain formation. If this is not the case, small negative fields are applied to start the domain formation. Second, the external field is varied to come to the equilibrium domain configuration at the coercive field. In the simulations, a spatial discretization of 10 nm is used which is three times larger than the exchange length ($l_{exch} = 3.37\,$nm).

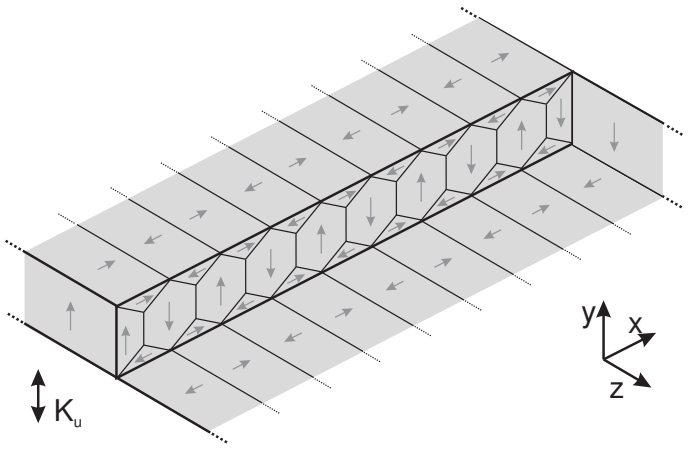

Figure 11.1: Geometry of the considered platelet. The uniaxial anisotropy axis in perpendicular to the platelet. Domains are formed in the sample as sketched in a plane perpendicular to the z-direction.

As discussed in Section 9.2, this is an appropriate discretization scale since we are only interested in the domain structure and not in the magnetization processes on the nanometer length scale.

First a platelet is considered with $L = 5.12\,\mu$m and anisotropy constant $K_u = 200\,\mathrm{kJ/m^3}$. Figure 11.2 shows the domain configuration in the xy-plane at the coercive field ($< M >= 0$). Domains of different sizes, magnetized along the uniaxial anisotropy axis, are visible together with closure domains on the top and bottom face of the platelet. In the central part, a concertina pattern as predicted in [114] is formed, while larger domains are formed near the outer edges. Similar domain configurations are experimentally observed using Kerr microscopy [115, 106]. This combination of small domains in the center and large domains near the outer edges could not be predicted starting from the domain theory, which already shows the added value of micromagnetic simulations in the magnetic domain research.

In what follows, we will investigate the magnetization processes starting from the equilibrium state of Fig. 11.2 when applying increasing fields along the x, y and z-axis respectively and then decreasing the field back corresponding to a magnetization for which $< \mathbf{M} >= 0$. Here it is ensured that the sample only goes to a near-saturation state ($| < \mathbf{M} > | = 0.99 M_s$) to avoid that the domain structure is completely destroyed.

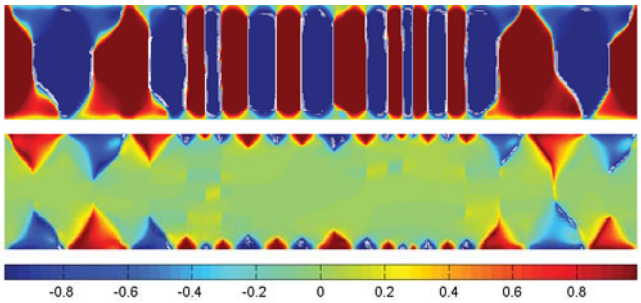

Figure 11.2: Equilibrium domain configuration obtained after reducing the applied field from saturation in the z-direction. Top: x-component of the local magnetization, bottom: y-component of the local magnetization, both in normalized values with respect to M_s.

11.3.1 Magnetization sweep in the x-direction

First an increasing field is applied in the x-direction. Some equilibrium domain configurations are shown in Figs. 11.3 and 11.4 for the $x-$ and the $y-$component respectively. Two different stages can be distinguished. For moderate fields, the closure domains oriented in the direction of the external field grow while the closure domains oriented in the opposite direction shrink without changing the magnetization in the vertically oriented domains. Once the domains, oriented in the opposite direction, have completely disappeared, the closure domains oriented along the external field further increase at the expense of the vertically oriented domains. This mechanism is combined with a coherent rotation that changes the magnetization in the body of the vertically oriented domains towards the direction of the increasing applied field. This phenomenon starts in the central region of the platelet.

Figure 11.5 shows some equilibrium domain configuration during decrease of the external field to $< M >= 0$ starting from the almost saturated state in the $x-$direction obtained above. A concertina pattern is again created. The domain pattern nucleates at the outer edges of the platelet and grows towards the middle of the sample. In the central region of the platelet the left-to-right and right-to-left growing domain structures meet, giving rise to a mismatch in the domain pattern. Furthermore, the same magnetization processes as encountered when going to saturation (described above) take place in reverse order: first, the closure domains oriented in the direction of the decreasing field shrink combined with a coherent rotation in the vertical domains towards the y-direction and, second, closure domains oriented in the opposite direction of the decreasing field emerge and grow at expense of the closure domains oriented along the applied field. It should be noted that, (i) except for the central mismatch, all domains have about the same width and no bound-

ary effects take place as originally encountered before the sweep and (ii) the displacement of 90 degree domain walls together with the coherent rotation dominate the magnetization processes.

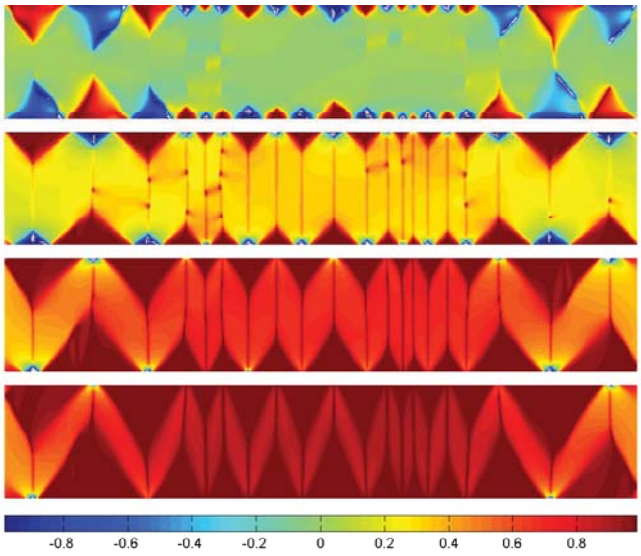

Figure 11.3: Evolution of the domain structure when going from the equilibrium state corresponding to Fig. 11.2 to saturation in the x-direction. The colors represent the x-component of the local magnetization, normalized with respect to M_s. The applied fields are (from top to bottom): $0.0\,\mathrm{kAm^{-1}}$, $100.0\,\mathrm{kAm^{-1}}$, $200.0\,\mathrm{kAm^{-1}}$ and $250.0\,\mathrm{kAm^{-1}}$.

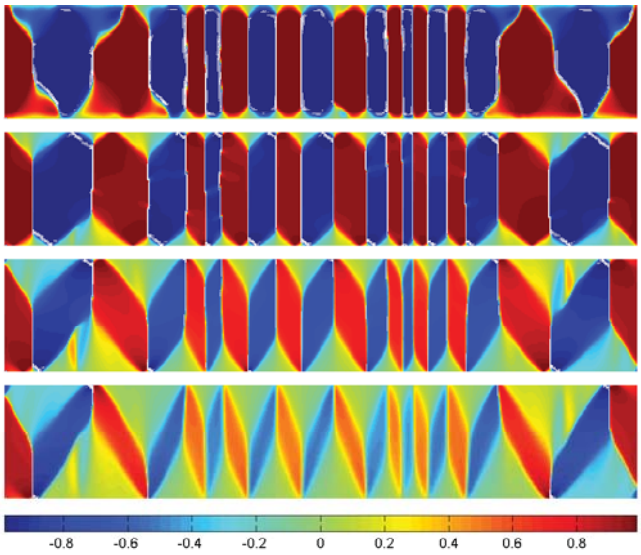

Figure 11.4: Evolution of the domain structure when going from the equilibrium state corresponding to Fig. 11.2 to saturation in the x-direction. The colors represent the y-component of the local magnetization, normalized with respect to M_s. The applied fields are (from top to bottom): $0.0\,\mathrm{kAm^{-1}}$, $100.0\,\mathrm{kAm^{-1}}$, $200.0\,\mathrm{kAm^{-1}}$ and $250.0\,\mathrm{kAm^{-1}}$.

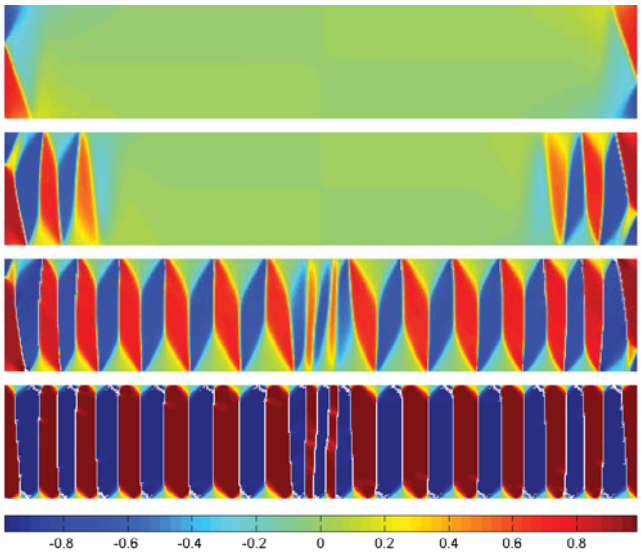

Figure 11.5: Evolution of the domain structure when coming from an almost saturated state in the x-direction to the magnetization state corresponding to $< \mathbf{M} >= 0.0$. The colors represent the local y-component of the magnetization, normalized with respect to M_s. The applied fields are (from top to bottom): $390.0\,\mathrm{kAm}^{-1}$, $260.0\,\mathrm{kAm}^{-1}$, $215.0\,\mathrm{kAm}^{-1}$ and $0.0\,\mathrm{kAm}^{-1}$.

11.3.2 Magnetization sweep in the y-direction

Some equilibrium domain configurations when going to near-saturation in the (positive) y-direction are shown in Figs. 11.6 and 11.7. As expected, the domains oriented in the direction of the applied field grow at the expense of the domains oriented in the opposite direction, due to the movement of 180 degree domain walls, see Fig. 11.7. It is only at high applied fields that the magnetization in the closure domains starts rotate towards saturation.

Now the field is again reduced, bringing the domain configuration back to $< \mathbf{M} >= 0$. This gives rise to the formation of perfectly symmetrical domain configurations, as shown in Fig. 11.8. For decreasing fields, a growing number of domains oriented in the opposite direction of the external field are introduced. These domains all have the same width when created and do not grow continuously. Hence, this is clearly an irreversible magnetization process. At $< \mathbf{M} >= 0$, the domains oriented in the positive y-direction have different thicknesses.

Note that (i) the fields required to saturate the sample in the y-direction are much larger than those required for saturation in the x-direction due to the larger demagnetizing effects, (ii) the displacement of 180 degree domain

walls dominate the magnetization processes when going to saturation and (iii) irreversible magnetization processes dominate the transition to $< \mathbf{M} >= 0$.

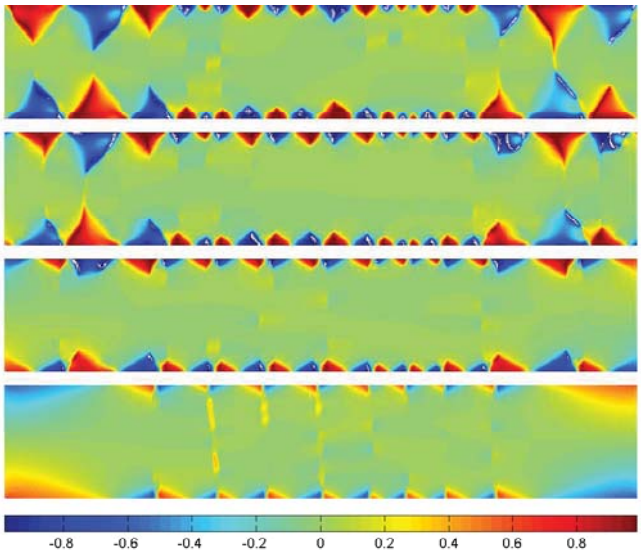

Figure 11.6: Evolution of the domain structure when going from the equilibrium state corresponding to Fig. 11.2 to saturation in the y-direction. The colors represent the x-component of the local magnetization, normalized with respect to M_s. The applied fields are (from top to bottom): $0.0\,\mathrm{kAm^{-1}}$, $300.0\,\mathrm{kAm^{-1}}$, $600.0\,\mathrm{kAm^{-1}}$ and $1000.0\,\mathrm{kAm^{-1}}$.

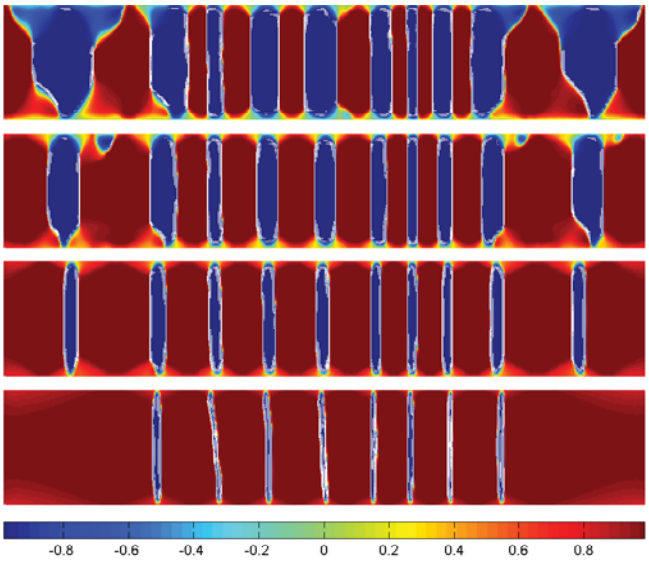

Figure 11.7: Evolution of the domain structure when going from the equilibrium state corresponding to Fig. 11.2 to saturation in the y-direction. The colors represent the y-component of the local magnetization, normalized with respect to M_s. The applied fields are (from top to bottom): $0.0\,\mathrm{kAm^{-1}}$, $300.0\,\mathrm{kAm^{-1}}$, $600.0\,\mathrm{kAm^{-1}}$ and $1000.0\,\mathrm{kAm^{-1}}$.

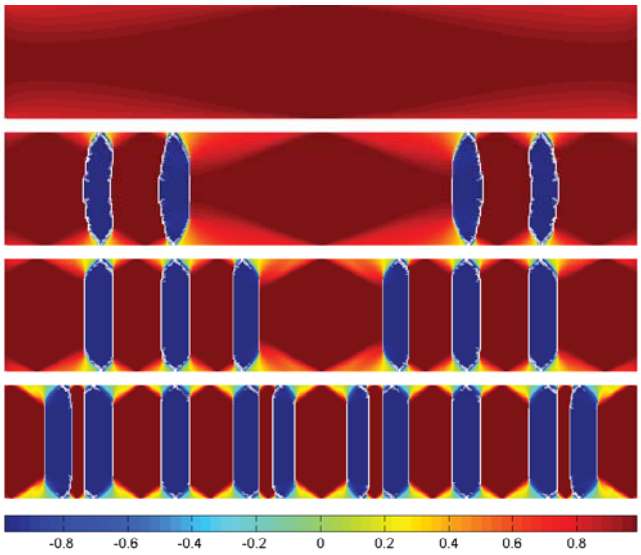

Figure 11.8: Evolution of the domain structure when coming from an almost saturated state in the y-direction to the magnetization state corresponding to $< \mathbf{M} >= 0$. The colors represent the local y-component of the magnetization, normalized with respect to M_s. The applied fields are (from top to bottom): $360.0\,\mathrm{kAm}^{-1}$, $300.0\,\mathrm{kAm}^{-1}$, $180.0\,\mathrm{kAm}^{-1}$ and $0.0\,\mathrm{kAm}^{-1}$.

11.3.3 Magnetization sweep in the z-direction

Equilibrium configurations when going to near-saturation in the z-direction are shown in Figs. 11.9 and 11.10. The magnetization process is completely determined by coherent rotation towards the increasing external applied field. The inner domains in the concertina pattern maintain their shape, but have an ever growing magnetization component in the direction of the increasing field. At high applied fields, the larger domains near the outer edges start to brake up in smaller domains. Near saturation, all magnetic domains disappear.

Now the external field is again decreased to obtain the magnetization state $< \mathbf{M} >= 0$, see Fig. 11.11. It is clear that the concertina pattern is now introduced in the complete sample, thus also at the outer edges of the platelet. First domains start to form in the center of the platelet. Also for decreasing fields, the magnetization process is completely dominated by the reversible coherent rotation of the magnetization. Throughout the whole sample, the domain width variation is limited.

To summarize: (i) no domain wall movement takes place, (ii) coherent rotation dominates the magnetization processes and (iii) the concertina pattern is stabilized when coming back from near saturation.

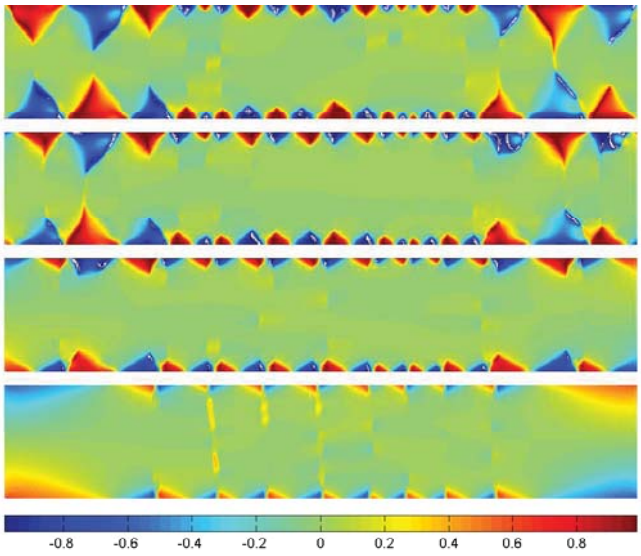

Figure 11.9: Evolution of the domain structure when going from the equilibrium state corresponding to Fig. 11.2 to saturation in the z-direction. The colors represent the z-component of the local magnetization, normalized with respect to M_s. The applied fields are (from top to bottom): $0.0\,\mathrm{kAm^{-1}}$, $100.0\,\mathrm{kAm^{-1}}$, $200.0\,\mathrm{kAm^{-1}}$ and $275.0\,\mathrm{kAm^{-1}}$.

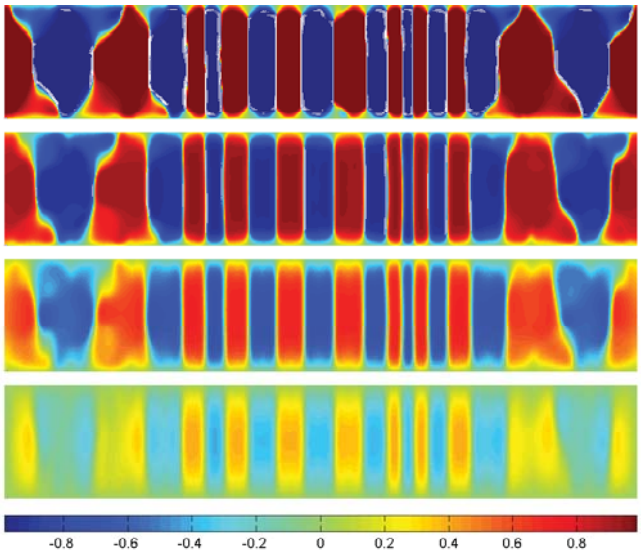

Figure 11.10: Evolution of the domain structure when going from the equilibrium state corresponding to Fig. 11.2 to saturation in the z-direction. The colors represent the y-component of the local magnetization, normalized with respect to M_s. The applied fields are (from top to bottom): $0.0\,\mathrm{kAm^{-1}}$, $100.0\,\mathrm{kAm^{-1}}$, $200.0\,\mathrm{kAm^{-1}}$ and $275.0\,\mathrm{kAm^{-1}}$.

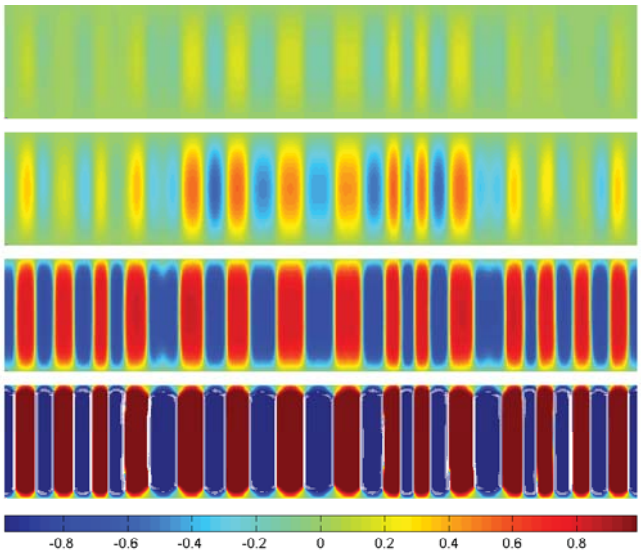

Figure 11.11: Evolution of the domain structure when coming from an almost saturated state in the z-direction to the magnetization state corresponding to $< \mathbf{M} >= 0$. The colors represent the local y-component of the magnetization, normalized with respect to M_s. The applied fields are (from top to bottom): $240.0\,\mathrm{kAm}^{-1}$, $180.0\,\mathrm{kAm}^{-1}$, $150.0\,\mathrm{kAm}^{-1}$ and $0.0\,\mathrm{kAm}^{-1}$.

11.4. Domain structure vs. anisotropy strength

The domain structures obtained after the sweep in the z-direction are now investigated more into detail for a varying uniaxial anisotropy strength K_u. Since for these domain configurations, the effects of the outer edges are diminished (see Fig. 11.11), it is possible to compare the simulated domain geometries with the one predicted by the domain theory in the case of a platelet which is infinite in both the x- and the z-directions (i.e. with only a finite thickness D). Within the framework of the domain theory the thickness d of the domains and the shape of the closure domains can be predicted, both depending on the anisotropy strength K_u. A summary of the domain theory analysis is given below. Further, the predictions are verified by micromagnetic simulations.

11.4.1 Domain theory

Following the domain theory, magnetic domains are formed with the magnetization aligned along the easy magnetization direction [4]. Indeed, the domain structure avoids the formation of magnetic charges and thus minimizes the magnetostatic energy (see Chapter 3). However, since domains are formed,

additional energy contributions have to be taken into account. First, in the considered platelet with out of plane uniaxial anisotropy, the closure domains are not magnetized along an easy magnetization direction and thus a certain amount of anisotropy energy is introduced. This energy contribution is proportional with the surface of the closure domains. Second, a certain amount of domain wall energy is also added to the system. This energy contribution grows for decreasing domain width (more walls are formed) and thus prevents the formation of arbitrarily small domains. The trade of between the different energy contributions determines the domain width and the structure of the closure domains.

Domain theory description of the Landau structure.

The most simple model for the magnetic domains in the considered platelet is the Landau structure. This domain structure was already sketched in Fig. 11.1 and is also shown in Fig. 11.12 (left). Here the magnetization in the closure domains is perfectly parallel to the surface of the platelet. Since no magnetic charges are present in the system, the magnetostatic energy is minimal. The anisotropy energy in the structure is proportional to the surface of the closure domains and thus grows for an increasing domain width. In contrary, the total domain wall energy becomes smaller for larger domains. The equilibrium domain width is thus a trade off between the energy in the domain walls and the energy in the closure domains. The total energy per unit area in the xz-plane (see Fig. 11.1) is given by

$$\phi_{tot} = \phi_{dw}\frac{D}{d} + \phi_{cl}d. \tag{11.1}$$

Here, D is the sample thickness, d is the domain thickness, ϕ_{dw} is the domain wall energy per unit area of the domain wall (i.e. yz-plane) and ϕ_{cl} is the energy per unit area of the closure domains. The equilibrium domain width is obtained by minimization of (11.1)

$$d = \sqrt{\frac{\phi_{dw}D}{\phi_{cl}}} \tag{11.2}$$

Here, it is assumed that the thickness of the platelet is large with respect to the extension of the closure domains. The 180 degree domain wall energy ϕ_{dw} can be determined analytically [4], while the energy in the closure domains ϕ_{cl} depends on the structure of the closure domains.

Generalized domain theory description of closure domains

As mentioned before, the magnetization in the closure domains of the considered platelet is not aligned with an easy magnetization axis. Hence, depending on the anisotropy strength, it can be expected that the magnetization in the closure domain is not completely parallel to the sample surface. In an improved domain model, the possibility of a region between the closure domains with out-of-plane magnetization is considered, see Fig. 11.12 (middle). This introduces a second parameter (the width of this region) to be optimized for. This region with out-of-plane magnetization leads to smaller closure domains and thus a smaller anisotropy energy, but also introduces magnetic charges and thus some magnetostatic energy. In this perspective, a good parameter to describe the shape of the closure domains is

$$Q = \frac{2K_u}{\mu_0 M_s^2}. \tag{11.3}$$

The enumerator $\mu_0 M_s^2/2$ corresponds to the magnetostatic energy of a platelet, uniformly magnetized in the out-of-plane direction. Hence, Q is a measure for the ratio of the anisotropy strength and the strength of the magnetostatic interaction. Depending on its value, different domain structures can be distinguished as shown in Fig. 11.12. For small K_u, the magnetostatic energy contribution is much larger than the anisotropy energy. In this case, closure domains are expected with a magnetization parallel to the sample surface, avoiding magnetic charges. This corresponds to the *Landau structure* described above. For larger Q, the magnetization along the easy axis is more favored. It is expected that the surface of the closure domains decreases, not only due to a reduction of the domain width as in the Landau structure, but also due to the formation of out-of-plane magnetization regions between the closure domains, which results in an increase of the magnetostatic energy. This domain configuration is known as the *partial Landau-Kittel structure*. For increasing Q, the anisotropy interaction becomes more dominant and the out-of-plane magnetized region in between the closure domains grows. In the limit $Q \gg 1$ the closure domains disappear completely and the so called *open Kittel structure* is formed.

Refined domain theory description of closure domains

In the above model, the magnetization in the actual closure domains stays always parallel to the platelet surface. Hubert [106] refined the structure of the closure domains by introducing magnetic domains with tilted magnetization. In this viewpoint, each closure domain is split in two uniformly magnetized regions with a magnetization direction between the easy axis and the surface orientation, see Fig. 11.13. For a small anisotropy strength, the closure domain

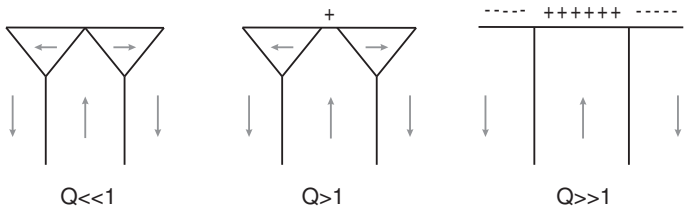

Figure 11.12: Domain structures for varying values of Q. Left: Landau structure, middle partial Landau-Kittel structure, right: open Kittel structure.

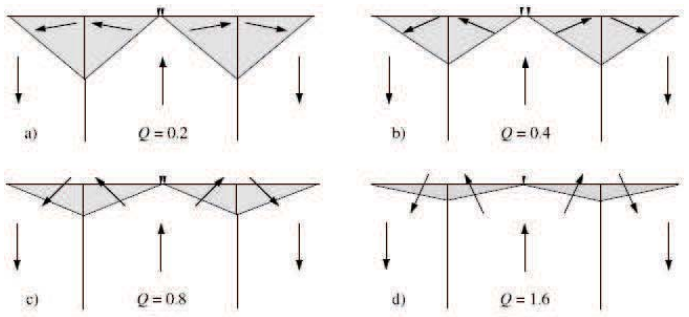

Figure 11.13: Closure domains with tilted magnetization angle in the domain model of Hubert, taken from [106].

is magnetized almost parallel to the surface and no magnetic charges are introduced. For a larger anisotropy strength, the magnetization is tilted more out of the plane and larger magnetic charges are introduced. Here a third parameter, the tilting angle is introduced.

Summary on the domain theory approach

It should be noted that the considerations made within the domain theory are all based on analytical formulae. Starting from the assumption that only uniformly magnetized regions are present in the sample, the different energy contributions are determined. The minimization of the total energy with respect to the model parameters yields the equilibrium domain structure. The complexity of the domain model determines its accuracy. Here, the most simple model is the Landau structure where only one parameter determines the domain configuration (the domain width). Considering a second parameter –the intermediate space between two closure domains– in the domain model enables to describe the Landau, partial Landau-Kittel and the Kittel structure,

shown in Fig. 11.12. In the refined model of Hubert, a third parameter (the tilting angle) is introduced to further improve the domain model, see Fig. 11.13.

11.4.2 Micromagnetic simulations

The domain structure in a platelet is now studied using micromagnetic simulations. Here, the uniaxial anisotropy strength is varied from $K_u = 10\,\mathrm{kJ/m^3}$ to $K_u = 400\,\mathrm{kJ/m^3}$. As mentioned before, the studied domain structures are obtained by first going to the $< M >= 0$ magnetization state starting from saturation in the z-direction and then simulating a magnetization sweep going to near saturation and back to $< M >= 0$. In this way, the boundary effects of the outer edges are minimized as shown in Section 11.3.3. In order to have a large number of domains in the platelet, the dimension L in the x-direction is enlarged from $L = 10.24\,\mu$m for large K_u to $L = 40.96\mu$m for small K_u.

Domain width versus anisotropy strength

The equilibrium domain configuration in a segment of the platelet is shown in Figs. 11.14 and 11.15 for $K_u = 40\,\mathrm{kJ/m^3}$, $K_u = 200\,\mathrm{kJ/m^3}$ and $K_u = 400\,\mathrm{kJ/m^3}$. From Fig. 11.14 it is clear that –as predicted by the domain theory– the surface of the closure domains decreases for increasing K_u. Consequently, the domain width decreases as shown in Fig. 11.15. It is clear that, within each platelet there is some small variation on the domain width.

A plot of the average domain width, together with its variance versus the anisotropy strength K_u is shown in Fig. 11.16. Generally, the domain width decreases for increasing K_u. The distinct character of the number of domains that fits in the cross section of the platelet is still visible although already a very large dimension L is considered. This proofs the need for considering more extended platelets when K_u decreases. For illustrative purposes, a curve $d = C_1 + C_2/\sqrt{K_u}$ is fit.

Closure domain geometry versus anisotropy strength

Closure domains in the platelets with anisotropy constant $K_u = 40\,\mathrm{kJ/m^3}$, $K_u = 200\,\mathrm{kJ/m^3}$ and $K_u = 400\,\mathrm{kJ/m^3}$ are shown in Figs. 11.17 to 11.19. In general, it is clear that none of the closure domains has a completely uniform magnetization and the closure domains have no localized domain walls as assumed by the domain theory. The domain configuration obtained in the platelet with $K_u = 40\,\mathrm{kJ/m^3}$ corresponds to the Landau structure. The closure domains touch each other and have only a very small out-of-plane component near the surface, hence about no magnetic charges are introduced. For larger K_u it becomes more difficult to distinguish separated closure domains. The

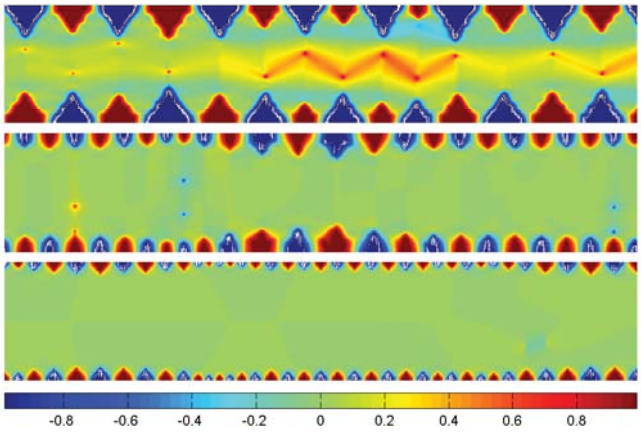

Figure 11.14: Part of the magnetic domain configuration for different uniaxial anisotropy values. The colors represent the local x-component of the magnetization, normalized with respect to M_s. Top: $K_u = 40\,\mathrm{kJ/m^3}$, middle: $K_u = 200\,\mathrm{kJ/m^3}$, bottom: $K_u = 400\,\mathrm{kJ/m^3}$.

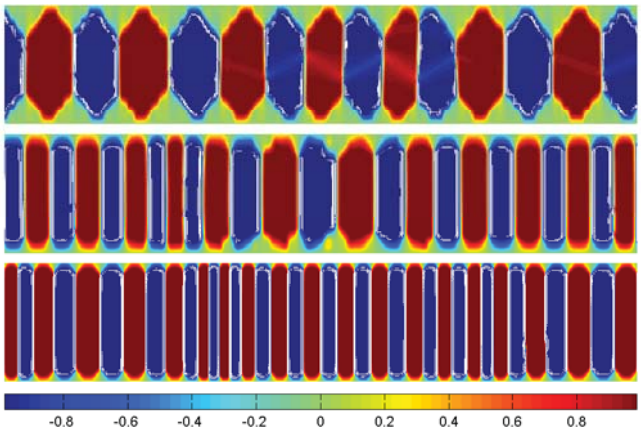

Figure 11.15: Part of the magnetic domain configuration for different uniaxial anisotropy values. The colors represent the local y-component of the magnetization, normalized with respect to M_s. Top: $K_u = 40\,\mathrm{kJ/m^3}$, middle: $K_u = 200\,\mathrm{kJ/m^3}$, bottom: $K_u = 400\,\mathrm{kJ/m^3}$.

magnetization configuration near the surface is characterized by a more continuous magnetization rotation between two oppositely magnetized domains. For increasing K_u, the region where the flux lines close becomes smaller. The magnetization has a growing out-of-plane component, which minimizes the anisotropy energy, but leads to a larger magnetostatic energy.

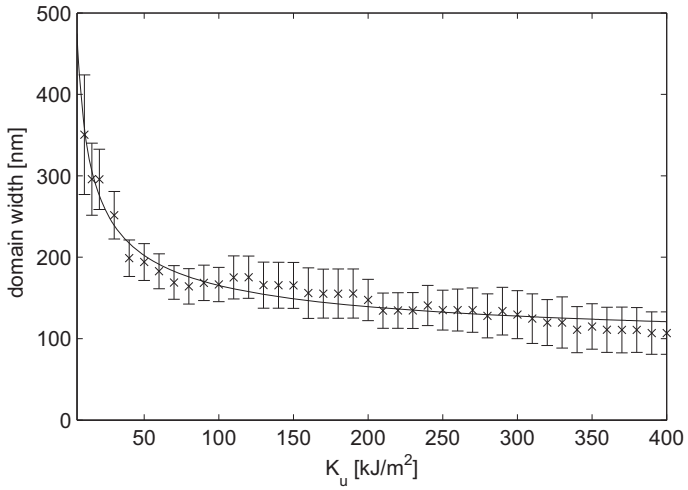

Figure 11.16: Domain width d versus anisotropy strength K_u. For illustrative purposes, a curve $d = C_1 + C_2/\sqrt{K_u}$ is fit to the data.

It is clear that the partial Landau-Kittel structure is not able to describe the closure domains of Figs. 11.18 and 11.19: there are no distinct regions with a magnetization parallel to the sample surface, nor distinct regions with only an out-of-plane magnetization component in between the closure domains. The closure domain description with tilted magnetic domains proposed by Hubert approximates the simulated domain structure in the best way. Although no uniformly magnetized domains are formed in the closure region, the theory is able to describe the growing out-of-plane magnetization component.

Problems encountered in the micromagnetic simulations

It is hard to simulate domain structures in the considered platelet with $K_u < 10\,\mathrm{kJ/m^3}$. Not only the sample dimension need to be increased further, but it also becomes much harder to make the micromagnetic system evolve towards an equilibrium state comprised of magnetic domains. In practice, for these low values of K_u it becomes impossible to start from saturation in the infinite z-direction since this is then a stable micromagnetic equilibrium state. Indeed, since the anisotropy strength is only small, it does not introduce the torque needed to pull the magnetization away from the saturated state. Furthermore it is difficult to simulate domain structures with $K_u > 500\,\mathrm{kJ/m}$. In this case, the magnetostatic interaction has a much smaller strength than the anisotropy interaction and the sample completely saturates along the perpendicular anisotropy axis without forming magnetic domains. A starting configuration different from saturation in the infinite direction is required to sim-

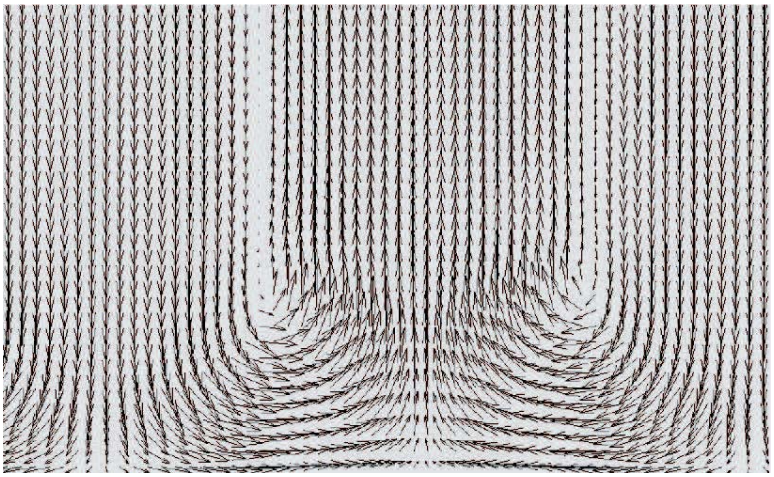

Figure 11.17: Simulated closure domains in a platelet with perpendicular uniaxial anisotropy strength $K_u = 40\,\mathrm{kJ/m^3}$.

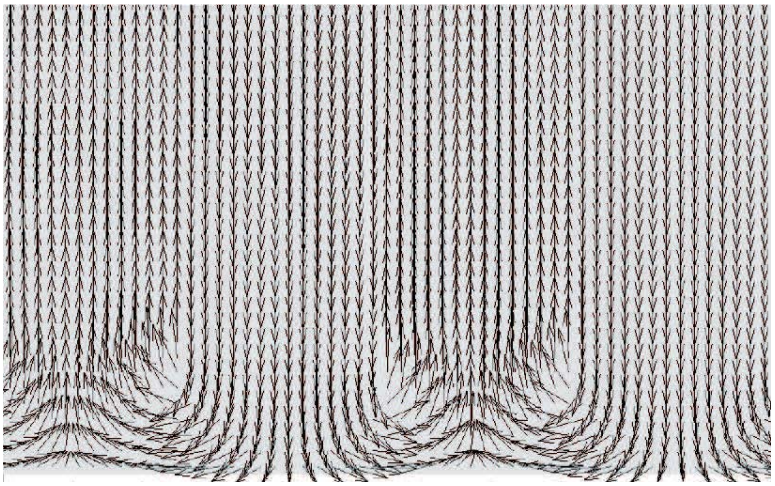

Figure 11.18: Simulated closure domains in a platelet with perpendicular uniaxial anisotropy strength $K_u = 200\,\mathrm{kJ/m^3}$.

ulate the open Kittel structure in the proposed finite platelet. However, one should be careful that the initial magnetization configuration does not favor one particular domain structure.

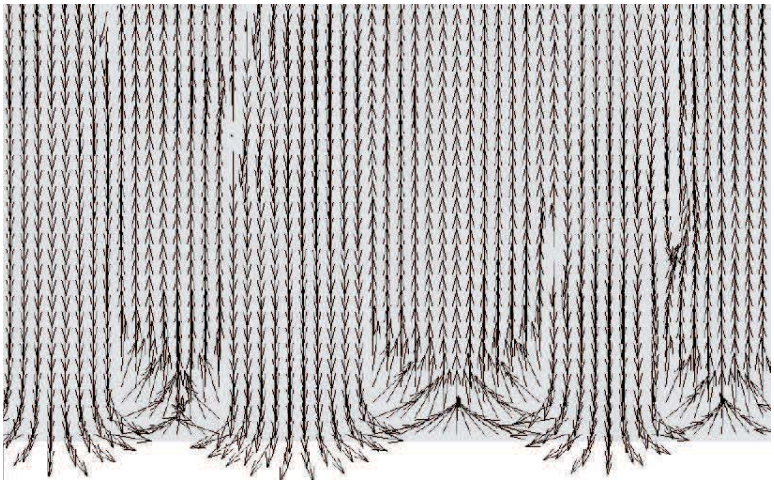

Figure 11.19: Simulated closure domains in a platelet with perpendicular uniaxial anisotropy strength $K_u = 400\,\mathrm{kJ/m^3}$.

11.5. Conclusions

This chapter has shown that, using the numerical scheme developed during this PhD, micromagnetic simulations are perfectly capable of describing magnetization processes on a length scale larger than 1 μm. The simulation results obtained in this chapter are a clear validation of the followed micromagnetic approach at the domain length scale. Indeed, similar domain configurations as e.g. shown in Figs. 11.3 and 11.4 are observed experimentally and simulated domain configurations for varying anisotropy strength are in agreement with the predictions made in the domain theory. In particular, the validity of using a discretization size which is larger than the exchange length is again demonstrated.

It is shown that, depending on the complexity of the used domain theory model, the domain structure in the platelet with perpendicular uniaxial anisotropy is more or less accurately described. The Landau model is only accurate for low anisotropy values while the open Landau-Kittel structure only poorly describes the structure of the closure domains for higher anisotropy constants. Indeed, the open Landau-Kittel structure assumes a magnetization parallel to the sample surface in the closure domains, but this is not found in the micromagnetic simulations. The refined domain model of Hubert allows closure domains with a uniform magnetization which is tilted with respect to anisotropy axis and is the best domain theory model to describe the domain structures over a wide range of anisotropy strengths.

From the micromagnetic simulations however, it is clear that for larger K_u no separated closure domains with uniform magnetization can be distinguished. In this case, the basic assumption of the domain theory, i.e. the existence of uniformly magnetized regions is not valid. Here, it is more obvious to define a closing region where the flux lines close in a continuous way, in stead of distinct closure domains. The simulations show how micromagnetic modeling can contribute to a better understanding of magnetization processes at the domain length scale.

CHAPTER 12

Micromagnetic study of hysteresis properties

12.1. Introduction

Macroscopic magnetic phenomena of ferromagnetic samples are predominantly studied based on their hysteresis properties. In Chapter 4, we have explained that due to the highly complex micromagnetic energy landscape, only few general hysteresis properties, valid in any magnetic material exist. These general properties are expressed by Madelung's rules, which describe the memory aspects in ferromagnetic materials (see Section 4.3.2). As the developed micromagnetic scheme is able to describe the hysteresis phenomena in ferromagnetic materials (see Section 6.5), the memory properties should intrinsically be present. The description of Madelung's rules is checked in a first section.

Further we have explained in Chapter 4 that the magnetic losses during one cycle of the applied field correspond to the surface of the hysteresis loop. From the hysteresis loop itself it is difficult to draw other energy related conclusions. The micromagnetic model however, is based on the Gibbs free energy present in the ferromagnetic system at every time instant. This allows us to study in detail the instantaneously added, dissipated and stored energy. To a certain extent, the same study can be performed in the Preisach model [39, 5, 116], which is the generally used classical model to describe rate-independent hysteresis processes. In a second section, we build up the Preisach distribution function starting from micromagnetic simulations and compare the instantaneous energy flows in both models.

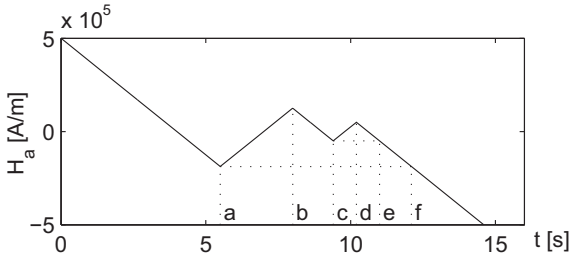

Figure 12.1: Evolution of the applied field. In the time stepping procedure the linearly varying parts are approximated with staircase like functions.

12.2. Memory properties in the micromagnetic hysteresis model

In Section 4.3.2 we introduced Madelung's rules as (i) the presence of *branching*, (ii) the *return-point-memory* and (iii) the *wiping-out-property*. Here it is demonstrated that the micromagnetic hysteresis scheme developed during the PhD work incorporates these properties. This is not obvious, since in contrast to macroscopic hysteresis models as the Preisach model [116], the memory properties are not build into the micromagnetic model by construction.

12.2.1 Simulation set up

For the evaluation of the magnetic memory behavior simulations are performed on samples containing two iron grains with dimensions $0.64\,\mu\text{m} \times 1.28\,\mu\text{m} \times 0.64\,\mu\text{m}$, with the crystal axes of the iron bcc lattice parallel to the sample edges. Since we are mainly interested in the macroscopic magnetic properties and not in the fine scale magnetization processes, the samples are discretized in FD cells with edges of $10\,nm$, see Section 9.2. In four simulations the samples contain respectively 0, 10, 20 and 40 dislocations (edge and screw dislocations).

The external field applied along the longest edges of the samples with 0, 10 and 20 dislocations is shown in Fig. 12.1. According to Madelung's rules, this profile should introduce minor loops. Indeed, at the time point *a* a second order loop will emanate with maximum magnetization at time point *b* and closing point at time point *f*, while a third order loop will emanate at time point *c* with maximum magnetization at time point *d* and closing point at time point *e*. The material parameters of iron as presented in Table 6.1 are taken as input.

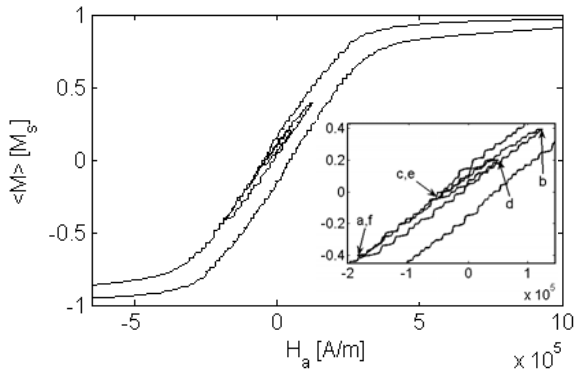

Figure 12.2: Magnetization curve for the sample containing 20 dislocations.

12.2.2 Macroscopic memory properties

In the case of 0, 10 and 20 dislocations the applied field gives rise to narrow hysteresis curves as e.g. shown in Fig. 12.2 for 20 dislocations. Consequently, the minor loops are very narrow. An analogous external field profile as in Fig. 12.1 with larger variations is applied on the sample with 40 dislocations. The magnetization curve is shown in Fig. 12.3. The large stresses introduced in the material by the large number of dislocations broaden the hysteresis loop. In all simulations, minor loops are formed as expected: (i) the magnetization paths for decreasing and increasing applied fields differ thus *branching* takes place, (ii) the macroscopic average magnetization in the time points a and f on the one hand, and c and e on the other hand coincide while their corresponding maximum magnetization points b and d differ significantly as described by the *return-point-memory* property and (iii) once the minor loops are closed the magnetization further evolves as if the closed loops did not exist at all, as described by the *wiping-out-property*. Hence, for the considered field variation of Fig. 12.1, the micromagnetic hysteresis model describes Madelung's rules.

12.2.3 Microscopic memory properties

The micromagnetic hysteresis model makes it possible to compare the microscopic magnetization states at the time points depicted in Fig. 12.1. To examine if also the *microscopic* magnetization configuration is recovered when minor loops close, the difference $\Delta(A \leftrightarrow B)$ between two magnetization states A and B is defined as the mean angle between the magnetic dipoles in corresponding FD cells of state A and B. Table 12.1 shows the difference in magnetization states for the four simulated samples at the time points depicted in Figs. 12.1, 12.2 and 12.3. The extreme magnetization points b and d differ substantially in

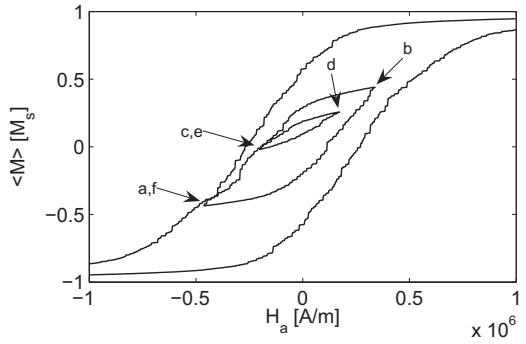

Figure 12.3: Magnetization curve for the sample containing 40 dislocations.

Table 12.1: difference in magnetization state [degrees]

	0 disl.	10 disl.	20 disl.	40 disl.
$\Delta(c \leftrightarrow d)$	20.22	24.18	19.59	21.21
$\Delta(c \leftrightarrow e)$	2.94	2.84	2.07	4.78
$\Delta(a \leftrightarrow b)$	77.73	76.49	62.83	61.83
$\Delta(a \leftrightarrow f)$	4.33	13.15	12.34	5.93

all cases. At the closing points, only small differences in magnetization pattern are present.

These small differences are due to small regions of the sample where the magnetization differs because a domain wall has just moved through the region or not. This is shown in Figs. 12.4 and 12.5 where the microscopic magnetization pattern in the sample is shown in a plane parallel to the applied field. These figures show the extremum points a, b and f of the second order loops for the samples with 20 and 40 dislocations. The chaotic magnetization patterns at the edges and in the middle of the sample are due to the random stress distribution induced by the grain boundaries. The top (time point a) and bottom (time point f) magnetization patterns differ only in small regions: in Fig. 12.4 the bottom left region in the right grain differs the most, while in Fig. 12.5 only the bottom left region in the left grain differs. Hence, one can conclude that in the considered numerical computations not only macroscopically the same magnetization state is reached, *return-point-memory*, but from these simulations one can assume that also microscopically a return-point-memory is described since similar magnetization states are reached when minor loops close.

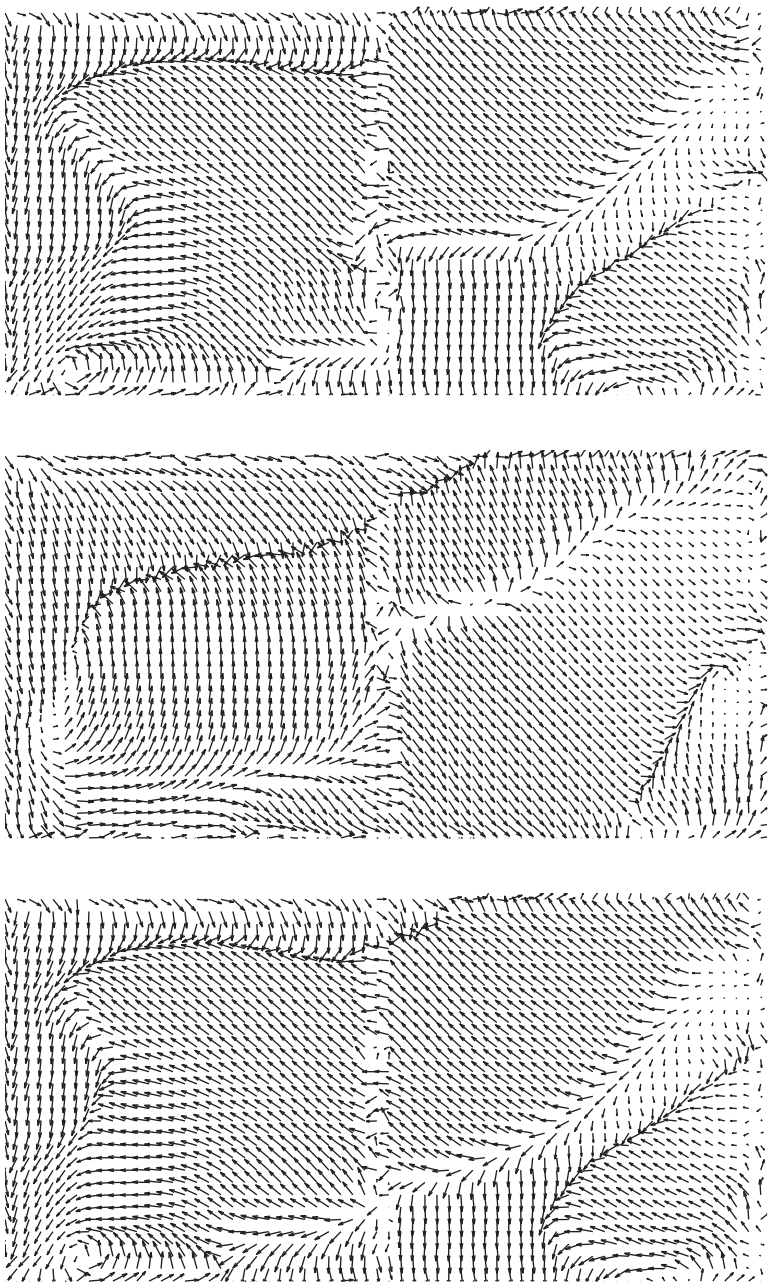

Figure 12.4: Magnetization pattern in the sample containing 20 dislocations at time point *a* (top), *b* (middle) and *f* (bottom).

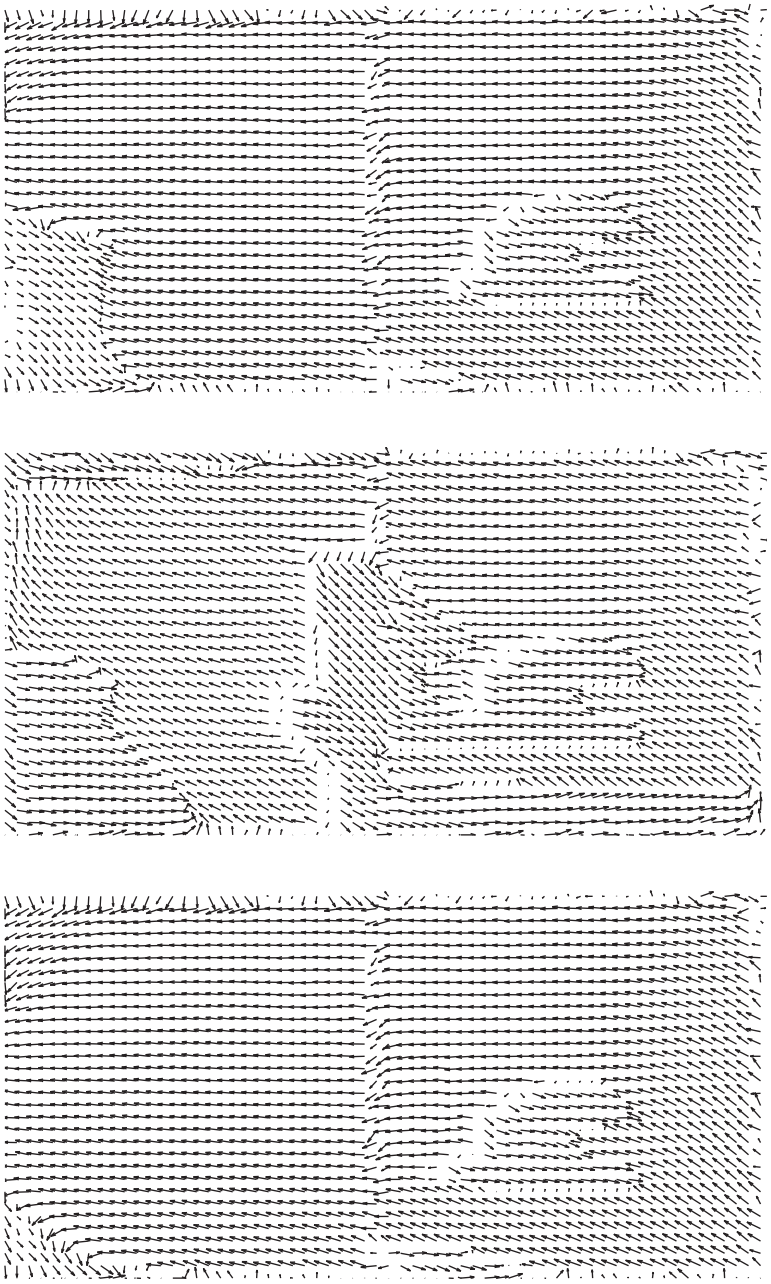

Figure 12.5: Magnetization pattern in the sample containing 40 dislocations at time point *a* (top), *b* (middle) and *f* (bottom).

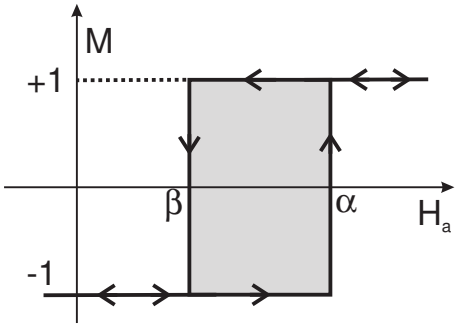

Figure 12.6: Elementary Preisach dipole with switching fields α and β.

12.3. Energy considerations in the micromagnetic hysteresis model and the Preisach model

Since the micromagnetic theory is based on the description of the total Gibbs free energy, the developed micromagnetic hysteresis model is able to give an insight in the energetic processes present in the ferromagnetic material during a cycle of the applied field, i.e. when running through the hysteresis loop. In this section, the micromagnetic energy description is compared to the description based on the classical Preisach model. This comparison not only provides a validation of the micromagnetic hysteresis model, but also shows how the developed micromagnetic simulations can be used to obtain a better understanding of hysteresis processes. First, a short overview is given on the classical Preisach model.

12.3.1 Classical Preisach hysteresis model: an overview [1]

In the classical Preisach model, the description of uniaxial rate independent hysteresis properties is based on an infinite collection of elementary magnetic dipoles [5,39,116]. The dipoles have an asymmetric rectangular hysteresis loop with switching fields commonly denoted by α and β ($\alpha \geq \beta$). In this section, all parameters α refer to the switching field of an elementary Preisach dipole and not to the micromagnetic damping constant. As shown in Fig. 12.6, the polarity of a given dipole (α, β) depends on the value of the applied field H_a and/or its history $H_{a,hist}$. For $H_a > \alpha$ the polarity η is $+1$. When H_a is now decreased, the polarity changes to -1 at $H_a = \beta$. The increasing branch of the dipole defines the polarity for increasing H_a values. Here, the polarity switches from -1 to $+1$ at $H_a = \alpha$.

To describe the hysteretic magnetic behavior of a ferromagnetic sample, first the reversible and the irreversible part of the magnetization loop is separated. The irreversible part is then represented by the Preisach distribution function (PDF) $P(\alpha,\beta)$, which corresponds to the statistical density of elementary dipoles (α,β). The magnetization in the Preisach model is now expressed as an integral over the entire elementary dipole collection

$$M(H_a) = M_{rev}(H_a) + M_{irr}(H_a, H_{a,hist}) \tag{12.1}$$

$$M_{irr}(H_a) = \frac{1}{2\mu_0}\int_{-\infty}^{+\infty} \mathrm{d}\alpha \int_{-\infty}^{\alpha} \eta(\alpha,\beta,H_a,H_{a,hist})P(\alpha,\beta)\,\mathrm{d}\beta. \tag{12.2}$$

The PDF $P(\alpha,\beta)$ is shown to be dependent on the microstructure of the ferromagnetic sample [117, 118]. The PDF characterizes the hysteretic behavior of a given sample. It can be interpreted as a blueprint of the magnetic hysteretic properties of a given sample. More details can be found in [44] and [119].

Obtaining the Preisach distribution function $P(\alpha,\beta)$

The PDF can be extracted from a number of experimentally or numerically obtained magnetization curves $M(H_a)$ covering the complete range of the major hysteresis loop. In practice these are first order magnetization loops or first order reversal curves (FORCs). The determination of the PDF encompasses four steps.

1. The experimental or numerical magnetization curves are smoothed using splines which approximate the original curves as close as possible. The splines meet the criterion $\mathrm{d}M/\mathrm{d}H_a > 0$, required in the next steps.
2. From equations (12.1) and (12.2) it is clear that the PDF covers only the irreversible magnetization behavior. Therefore, the reversible magnetization processes $M_{rev}(H_a)$ are extracted by considering the differential permeability at the reversal points. Indeed, at these points, only reversible magnetization processes occur and thus the reversible differential permeability $\mu_{rev}(H_a)$ can be defined. From this, the single valued magnetization curve $M_{rev}(H_a)$ is deduced

$$M_{rev}(H_a) = \int_0^{H_a} \left(\frac{\mu_{rev}(H)}{\mu_0} - 1\right) \mathrm{d}H. \tag{12.3}$$

   Consequently the irreversible magnetization curves are

$$M_{irr}(H_a) = M(H_a) - M_{rev}(H_a). \tag{12.4}$$

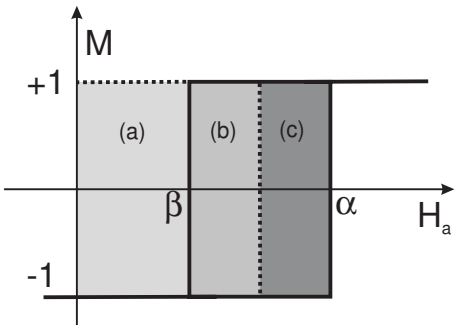

Figure 12.7: Elementary Preisach dipole with associated energy densities.

3. The set of irreversible magnetization curves $M_{irr}(H_a)$ is now rearranged into an Everett map [120]. The Everett function $E_{ev}(\alpha, \beta)$ is defined as

$$E_{ev}(\alpha, \beta) = \mu_0 |M_{irr}(\beta) - M_{irr}(\alpha)| \tag{12.5}$$

   with α an extremal value for the applied field H_a, and no extrema are evaded from the memory when passing from α to β.
4. Ultimately, the PDF is obtained by differentiating the Everett function

$$P(\alpha, \beta) = -\frac{\partial^2 E_{ev}(\alpha, \beta)}{\partial \alpha \partial \beta}. \tag{12.6}$$

Energy descriptions in the classical Preisach model

In the classical Preisach model, one can distinguish the instantaneous energy density that is added, stored and dissipated when running through the hysteresis loop by inspecting the elementary Preisach dipole [121]. The following energy densities can be associated with the areas shown in Fig. 12.7. During the switching process of the ascending branch, the area (a)+(b)+(c) corresponds to the energy density added by the source. From that, the area (c) and the area (a)+(b) correspond to the dissipated and the stored energy density in the system respectively. During the switching process of the descending branch, the area (a)+(b) corresponds to the stored energy density, while the areas (a) and (b) correspond to the energy density which is returned to the source and dissipated by the system respectively.

By extending the considerations made for an elementary dipole to all dipoles in the PDF that are switching when the applied field is altered, the irreversibly added energy density $\phi_{add,irr}$, the irreversibly stored energy density $\phi_{st,irr}$ and the dissipated energy density ϕ_{diss} can be distinguished at each time point of the hysteresis loop. For the ascending branch, an increase ΔH_a

of the applied field leads to

$$\Delta\phi_{add,irr} = \int_{H_a}^{H_a+\Delta H_a} \mathrm{d}\alpha \int_{H_{min}}^{\alpha} \alpha P(\alpha,\beta)\,\mathrm{d}\beta \tag{12.7}$$

$$\Delta\phi_{st,irr} = \int_{H_a}^{H_a+\Delta H_a} \mathrm{d}\alpha \int_{H_{min}}^{\alpha} \frac{\alpha+\beta}{2} P(\alpha,\beta)\,\mathrm{d}\beta \tag{12.8}$$

$$\Delta\phi_{diss} = \int_{H_a}^{H_a+\Delta H_a} \mathrm{d}\alpha \int_{H_{min}}^{\alpha} \frac{\alpha-\beta}{2} P(\alpha,\beta)\,\mathrm{d}\beta, \tag{12.9}$$

with H_{min} the last minimum of H_a kept in memory. For the descending branch, a decrease ΔH_a of the applied field leads to

$$\Delta\phi_{add,irr} = \int_{H_a}^{H_a-\Delta H_a} \mathrm{d}\beta \int_{\beta}^{H_{max}} \beta P(\alpha,\beta)\,\mathrm{d}\alpha \tag{12.10}$$

$$\Delta\phi_{st,irr} = \int_{H_a}^{H_a-\Delta H_a} \mathrm{d}\beta \int_{\beta}^{H_{max}} \frac{\alpha+\beta}{2} P(\alpha,\beta)\,\mathrm{d}\alpha \tag{12.11}$$

$$\Delta\phi_{diss} = \int_{H_a}^{H_a-\Delta H_a} \mathrm{d}\beta \int_{\beta}^{H_{max}} \frac{\beta-\alpha}{2} P(\alpha,\beta)\,\mathrm{d}\alpha, \tag{12.12}$$

with H_{max} the last maximum of H_a kept in memory. Note that negative values for the added energy density correspond to an energy flow from the system towards the source. Negative values for the stored energy density indicate that more energy is leaving the system (towards the source or by dissipation) than that energy is added to the system. By definition, the dissipated energy is always positive. Further, note that the reversible magnetization processes only have a contribution to the total added and stored energy density

$$\begin{aligned} \Delta E_{add,rev} = \Delta E_{st,rev} &= \int_{H_a}^{H_a\pm\Delta H_a} H\,\mathrm{d}B_{rev} \\ &= \int_{H_a}^{H_a\pm\Delta H_a} \mu_{rev}(H) H\,\mathrm{d}H. \end{aligned} \tag{12.13}$$

Here, the sign in the integral boundaries is determined by which branch is considered: negative for the descending branch and positive for the ascending branch.

12.3.2 Micromagnetic simulations and construction of the PDF

In the micromagnetic simulations, a relatively small system is considered with dimensions $0.32\,\mu\mathrm{m}\times 0.32\,\mu\mathrm{m}\times 5.12\,\mu\mathrm{m}$. As pointed out in the previous section, a large number of magnetization curves that cover the complete range of the hysteresis loop is required to well reconstruct the PDF. In experiments, one usually measures first order magnetization loops starting on the virgin curve

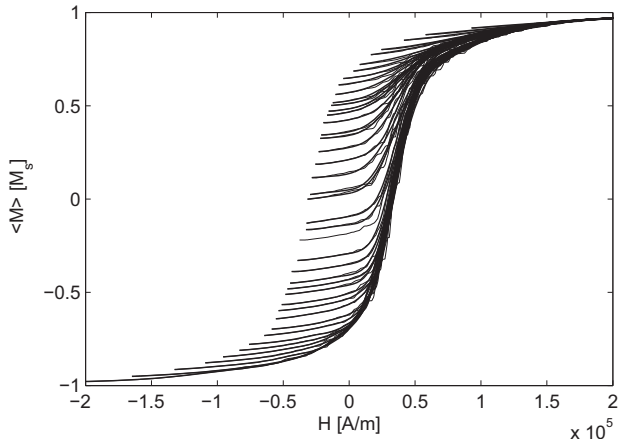

Figure 12.8: Simulated FORCs using the micromagnetic hysteresis scheme.

to reconstruct the PDF. However, in the micromagnetic simulations, it is very hard to determine the demagnetized state corresponding to $H_a = 0.0\,\mathrm{A/m}$ at which the virgin curve emanates, therefore FORCs are considered here.

The material parameters are taken such that the hysteresis loop is smooth and does not show too large magnetization jumps for varying H_a. In this way, FORCs can start at relatively equidistant steps in the magnetization. The sample comprises 16 grains in the elongated direction with random cubical easy axes orientations. The saturation magnetization is 2.16 T, the exchange stiffness is small: $0.2510^{-12}\,\mathrm{J/m}$ and the anisotropy constants are $K_1 = 0.4810^6\,\mathrm{J/m^3}$ and $K_2 = -0.5010^56\,\mathrm{J/m^3}$. The external field is applied in the elongated direction of the sample and ranges from $3.010^6\,\mathrm{A/m}$ to $-3.010^6\,\mathrm{A/m}$ with steps of $\Delta H_a = 400\,\mathrm{A/m}$. The simulated FORCs are shown in Fig. 12.8.

First, the FORCs are smoothed using splines and the reversible part is subtracted. The 'irreversible' curves are shown in Fig. 12.9. Note that the slope at the start of each FORC is zero. Based on the irreversible FORCs, the Everett function $E_{ev}(\alpha,\beta)$ is constructed and the PDF $P(\alpha,\beta)$ is determined by differentiation. The PDF is shown in Fig. 12.10. Note that the PDF has only non-zero values in the half plane $\alpha > \beta$. Furthermore, the constructed PDF has small areas with non-physical negative values. These originate in the crossing of the simulated FORCs in the region close to the coercive field of the limit cycle (see Fig. 12.8).

To test the accuracy of the extracted PDF, the major hysteresis loop is reconstructed from the PDF and compared with the original, hysteresis loop obtained from the micromagnetic simulations. Figure 12.11 shows the excellent

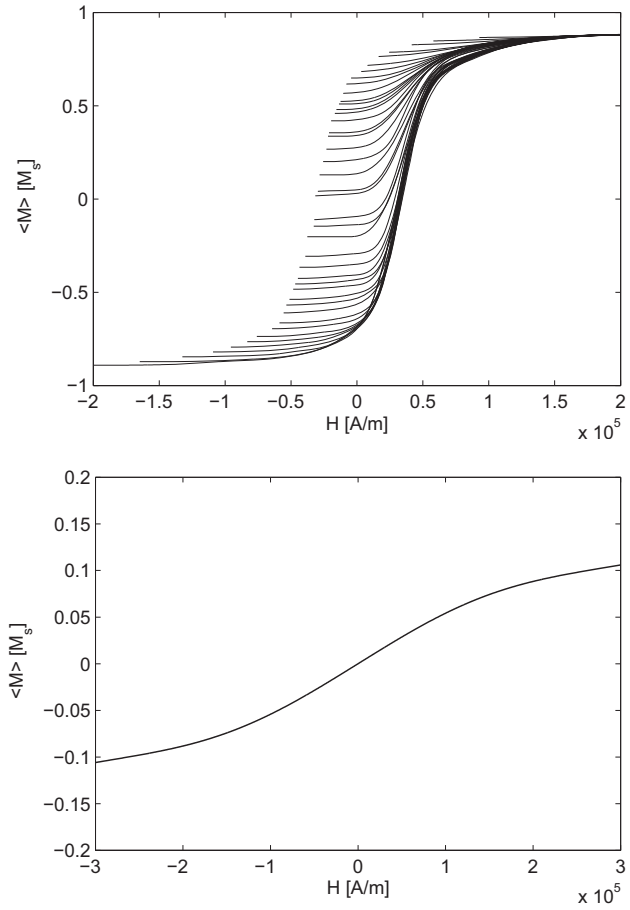

Figure 12.9: Irreversible part of the FORCs, smoothed using splines (top) and reversible part of the magnetization curves (bottom) corresponding to Fig. 12.8.

agreement between the reconstructed and the original hysteresis loop: the reconstructed loop is a smoothed version of the simulated hysteresis loop which shows Barkhausen jumps.

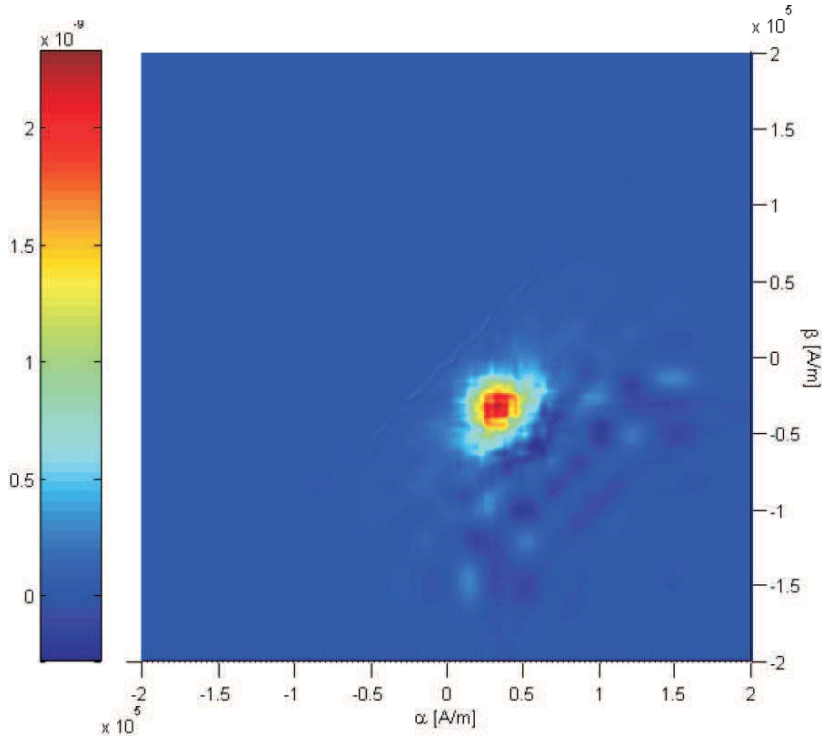

Figure 12.10: Reconstructed Preisach distribution function, based on the smoothed irreversible first order reversal curves of Fig. 12.9.

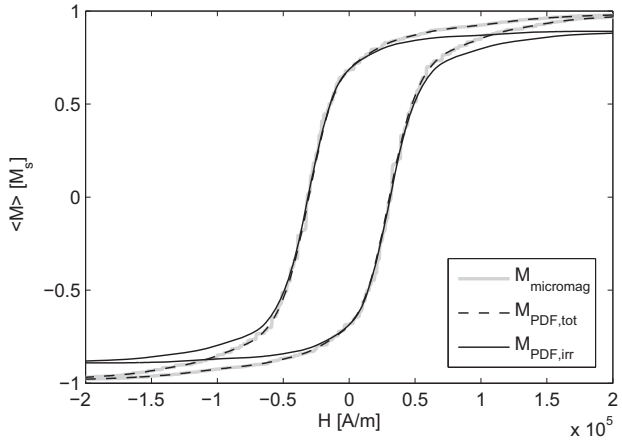

Figure 12.11: Simulated hysteresis loop compared with the hysteresis loop reconstructed from the PDF. For completeness, the irreversible hysteresis loop is also shown.

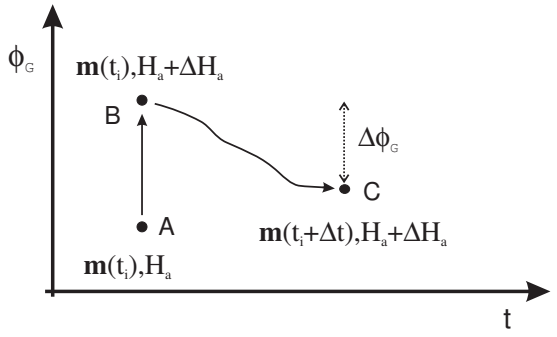

Figure 12.12: Dissipated energy density in the micromagnetic hysteresis model: the difference in Gibbs free energy $\Delta\phi_G$ corresponds to the dissipated energy density.

12.3.3 Energy flows in the micromagnetic hysteresis model

In the micromagnetic hysteresis model, the equilibrium magnetization fields $\mathbf{m}(\mathbf{r},t)$ are determined for successive constant values of the applied field H_a, as explained in Section 6.5. The energy variations during the transition between two successive equilibrium states is sketched in Fig. 12.12. At a given time point t_i, an external field H_a is applied and a corresponding equilibrium magnetization configuration $\mathbf{m}(t_i)$ is reached, state A. Now, the applied field takes a jump ΔH_a. This increases the energy in the system to a state B, which is unstable. Consequently, the original magnetization configuration $\mathbf{m}(t_i)$ evolves towards a new equilibrium magnetization configuration $\mathbf{m}(t_i+\Delta t)$ corresponding to state C. Referring to the quantities in Fig. 12.12, the energy density ϕ_{add} which is added to the system corresponds to

$$\begin{aligned}\Delta\phi_{add} =& \mu_0 M_s(\mathbf{H}_a+\Delta\mathbf{H}_a)\cdot[<\mathbf{m}(t_i+\Delta t)> - <\mathbf{m}(t_i)>] \\ &+ \mu_0(H_a+\Delta H_a)\Delta H_a\end{aligned} \tag{12.14}$$

The dissipated energy density ϕ_{diss} is the difference between the Gibbs free energy values at state B and state C, see Fig. 12.12. The conservation of energy principle then yields the stored energy density as

$$\Delta\phi_{st} = \Delta\phi_{add} - \Delta\phi_{diss}. \tag{12.15}$$

Note that in the micromagnetic hysteresis model, the different contributions to the instantaneously dissipated energy density can be distinguished. Indeed, the differences in the Zeeman, exchange, anisotropy and magnetostatic energy between state B and state C yield the corresponding dissipated energy densities.

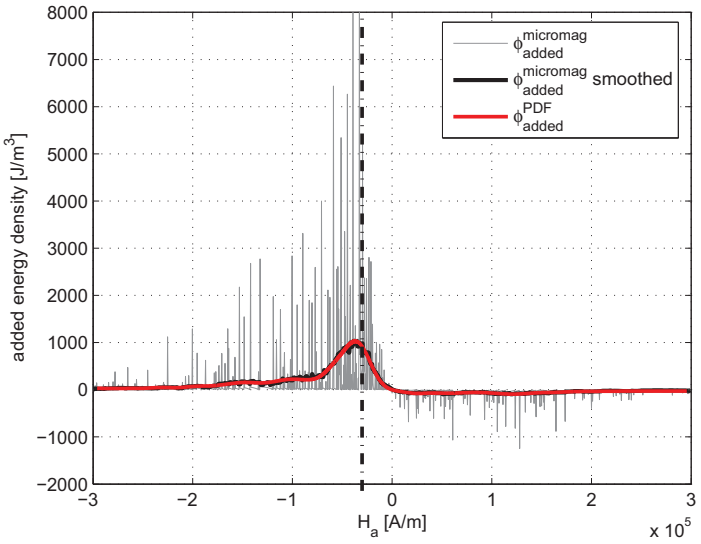

Figure 12.13: Instantaneously added energy density when running through the descending branch of the hysteresis loop shown in Fig. 12.11.

12.3.4 Discussion

In what follows we compare and comment on the energy flows in the ferromagnetic system when running through the descending branch. Similar conclusions can be drawn when running through the ascending branch. The instantaneously added, dissipated and stored energy densities as determined in the micromagnetic and the Preisach model are shown in Figs. 12.13, 12.14 and 12.15 respectively. The energy density curves derived from the micromagnetic model show a highly irregular behavior. Each spike corresponds to a Barkhausen jump at which large energy flows occur in the ferromagnetic system. Since the Preisach model incorporates a high level of smoothing, the resulting energy density curves are continuous. To facilitate the comparison between the micromagnetic and the Preisach data, a locally averaged version of the micromagnetic energy density curves is added to the figures. In all figures, the coercive field value is indicated with a dash-dotted line. Note that since the descending branch is considered, all curves in the following figures should be interpreted from right to left for increasing time (i.e. from positive to negative applied fields).

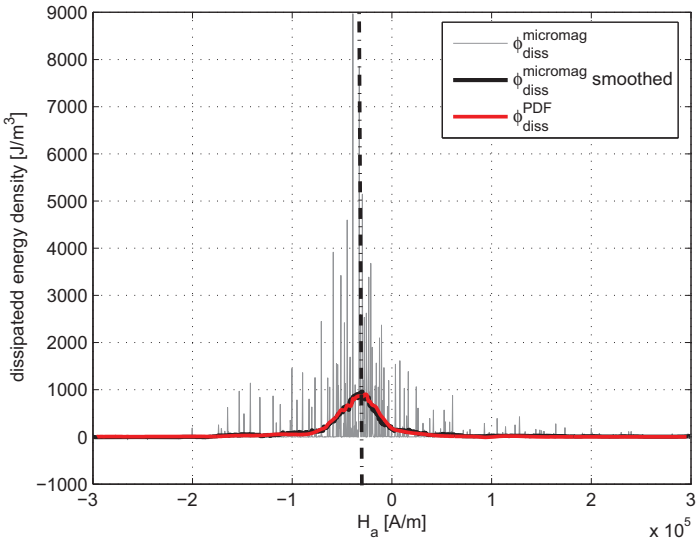

Figure 12.14: Instantaneously dissipated energy density when running through the descending branch of the hysteresis loop shown in Fig. 12.11.

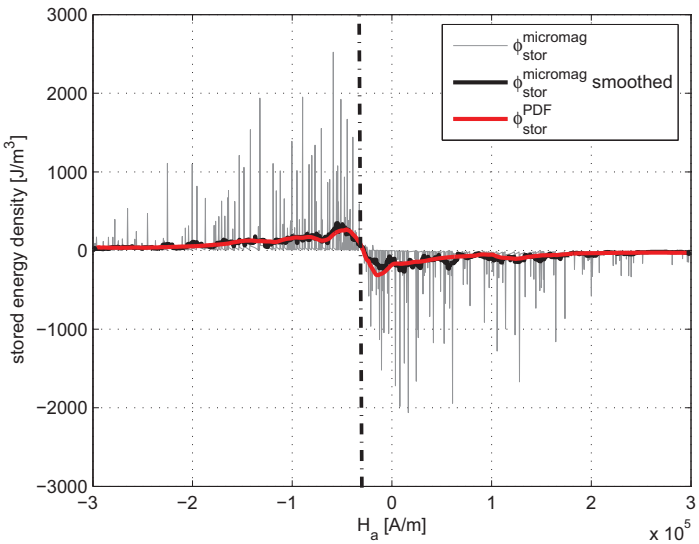

Figure 12.15: Instantaneously stored energy density when running through the descending branch of the hysteresis loop shown in Fig. 12.11.

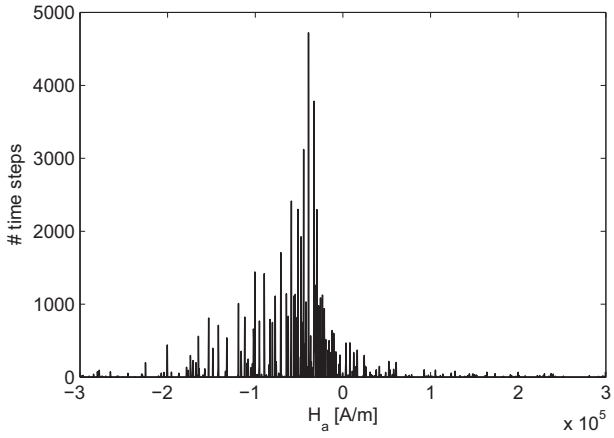

Figure 12.16: Number of time steps required to reach equilibrium at successive constant applied field values H_a when running through the descending branch from $H_a = 3 10^5$ A/m to $H_a = -3 10^5$ A/m.

Instantaneously added energy

The instantaneously added energy density in the two models is shown in Fig. 12.13. While returning from positive saturation to $H_a = 0.0$A/m the added energy is negative, which indicates that energy is flowing from the material towards the source. For negative applied fields, the added energy density is positive, indicating that energy is flowing from the source to the material. The largest amounts of energy are added at applied field values in the proximity of the coercive field. The expressions (12.10) and (12.14) used in the Preisach and micromagnetic description respectively result in coinciding curves.

Instantaneously dissipated energy

The instantaneously dissipated energy density in the two models is shown in Fig. 12.14. This energy flow corresponds to energy that is dissipated as heat during the irreversible magnetic processes which occur in the material, i.e. during the Barkhausen jumps. It represents the energy flow from the material towards the thermal bath and is thus per definition always positive. The curves in Fig. 12.14 have indeed only positive values. In the micromagnetic context, this is a consequence of the LLG equation which guarantees the continuous decrease in energy for constant applied fields, see Section 2.4.3. In the Preisach model, the positive values result from the prerequisite $\alpha \geq \beta$ and $P(\alpha, \beta) \geq 0$.

Most of the energy is dissipated for applied field values between 0.0 A/m and -1.0 10^5 A/m which roughly corresponds to an average magnetization between $\pm 0.8\, M_s$, see Fig. 12.11. This shows that most of the magnetic processes in this part of the hysteresis loop are irreversible in nature, while closer to saturation reversible processes are dominant. This is in correspondence with the theory presented in Section 4.3.1, Fig. 4.5. In the micromagnetic model, the number of time steps required to reach equilibrium at successive constant applied field values –shown in Fig. 12.16– is related with the 'irreversibility' of the magnetic process. Indeed, since large variations in the magnetization structure can occur during Barkhausen jumps, the simulation of these irreversible magnetization processes require a large number of time steps to come to the new equilibrium points. Only small changes in the magnetization structure occur during reversible magnetization processes, which leads to a small number of time steps required to reach new equilibrium points. In the Preisach description, all energy is dissipated when running through the *irreversible* hysteresis loop shown in Fig. 12.11. It is clear that the descending branch of the irreversible hysteresis loop has the largest slope in the range $-1.0\,10^5$ A/m$< H_a <$0.0 A/m.

Instantaneously stored energy

The instantaneously stored energy density in the two models is shown in Fig. 12.15. The agreement between both descriptions is perfect. When saturated in the positive direction, a large amount of energy is stored in the system. When reducing the external field, this energy is released towards the source or dissipated as heat giving rise to negative values for the instantaneously stored energy density. When the ferromagnetic system reaches the state corresponding to $\mathbf{M} = 0$ and $H_a = H_c$ –further called the *demagnetized state*– the system starts to absorb energy when the field is further reduced towards negative saturation. This leads to positive values for the instantaneously stored energy density. From these curves, it is clear that at the demagnetized state no energy is stored in the ferromagnetic system. Starting from this point, any field variation will result in an increase of the stored energy.

Instantaneous micromagnetic energy rearrangement

In the micromagnetic description of the instantaneously dissipated energy discussed above the difference in the total Gibbs free energy is considered as sketched in Fig. 12.12. In the same way one can consider the difference in the Zeeman energy ϕ_a, the magnetostatic energy ϕ_{ms}, the anisotropy energy ϕ_{ani} and the exchange energy ϕ_{exch} separately to come to instantaneous flow of the Zeeman energy , magnetostatic energy, anisotropy energy and exchange en-

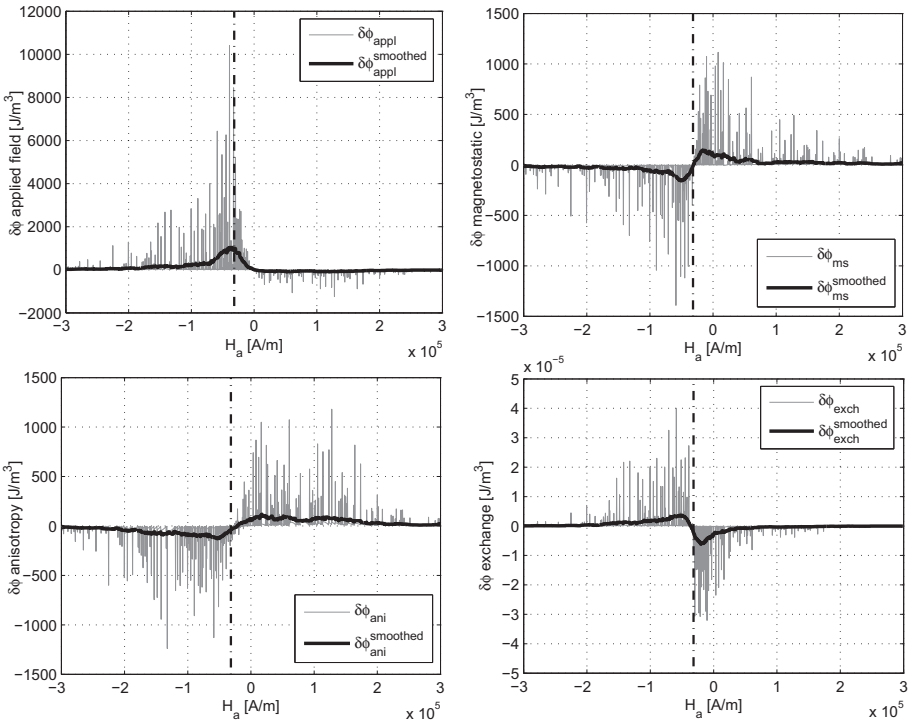

Figure 12.17: Instantaneous changes in energy density for the different micromagnetic energy terms. From left-top to right-bottom: Zeeman energy density, magnetostatic energy density, anisotropy energy density and exchange energy density.

ergy respectively. The corresponding instantaneous changes in micromagnetic energy densities $\delta\phi_a$, $\delta\phi_{ms}$, $\delta\phi_{ani}$ and $\delta\phi_{exch}$ are shown in Fig. 12.17.

It is clear that, although the total instantaneously dissipated energy is strictly positive, the instantaneous changes in the separate energy densities can have negative values. This indicates that energy is rearranged in the system while running through the hysteresis loop. In the saturated state, the Zeeman and the exchange energy are minimal because the sample is uniformly magnetized along the applied field, while the magnetostatic and the anisotropy energy are large. Indeed, large magnetic charges are formed at the sample edges and the local magnetization in the material is not aligned along an easy axis. When the applied field is reduced, the system evolves towards a magnetization state with closed flux lines and with the local magnetization mainly aligned along a local anisotropy axis. Hence, the magnetostatic and anisotropy energy gradually decrease, while the Zeeman and the exchange energy gradually increase. Consequently, the instantaneous magnetostatic and anisotropy energy flows are positive while the instantaneous Zeeman and in

the exchange energy flows are negative when the applied field is reduced to $H_a = 0.0\,\mathrm{A/m}$. The opposite internal energy rearrangements take place when going to saturation.

The Zeeman energy has the largest contribution to the total dissipated energy. The largest flows of Zeeman energy occur around the coercive field where the slope of the hysteresis loop is maximal. In this part of the hysteresis loop large portions of the ferromagnetic material are aligning with the applied field and the Zeeman energy is vastly reduced. Here, large portions of Zeeman energy are dissipated as heat or stored as magnetostatic, anisotropy and/or exchange energy.

The magnetostatic energy flow is positive until the demagnetized magnetization state is reached. Hence, magnetostatic energy is converted to heat and/or other micromagnetic energy contributions. The demagnetized state contains the minimal magnetostatic energy since all flux lines close in the material and only small magnetic charges are present in the domain walls. When going further to saturation, the net magnetization along the applied field direction grows together with the magnetic charges, leading to an increase of the magnetostatic energy and thus negative values for the instantaneous change in magnetostatic energy density $\delta\phi_{ms}$.

The instantaneous change of the anisotropy energy density has large contributions over a relatively broad range of the hysteresis loop. Whenever a region in the magnetic sample is aligning with a local easy axis, the anisotropy energy decreases leading to positive values for the anisotropy energy flow (when going to the demagnetized state). Whenever the magnetization in a region is rotating away from a local easy axis, anisotropy energy is built up (when going to saturation).

In the considered system, the exchange energy is negligible since the exchange stiffness A is very small. This was chosen so in order to have a smooth hysteresis loop with only small magnetization jumps, which was a prerequisite to have FORCs emanating at relatively equidistant magnetization values $< M >$, see Fig. 12.8. Although the exchange energy flows are negligible, the curve $\delta\phi_{exch}$ is still instructive. It is clear that the amplitude of the dissipated exchange energy is proportional to the slope of the hysteresis loop. The exchange energy is built up until the demagnetized magnetization state is reached. This demagnetized magnetization state is the most non-uniform equilibrium domain configuration when running through the hysteresis loop. Indeed, at this point the exchange energy density is maximal. When going further to saturation the sample gradually becomes more uniformly magnetized, leading to energy flows towards the thermal bath and the other energy terms.

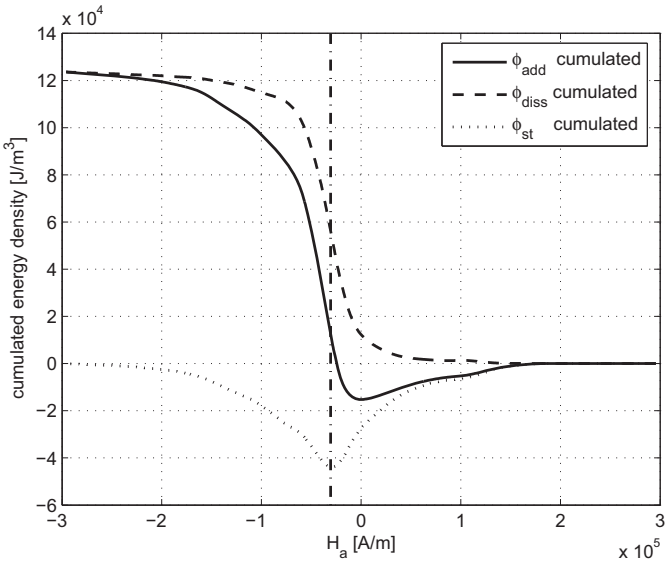

Figure 12.18: Simulated hysteresis loop compared with the hysteresis loop reconstructed from the PDF. For completeness, the irreversible hysteresis loop is also shown.

Cumulated energy flows

The cumulated added, dissipated and stored energy densities based on the Preisach description are shown in Fig. 12.18. The curves based on the micromagnetic description are very similar, but are not shown for clarity. At positive saturation, a maximal amount of energy is stored. This energy is released when going to the demagnetized state corresponding to the coercive field leading. Part of the energy is dissipated and part of the energy is sent back to the source. When going to negative saturation, exactly the same amount of energy is stored again in the system. This is clear from the cumulated stored energy density curve: it has a minimum at the coercive field value and is zero for positive as well as negative saturation. Since a part of the stored energy is sent to the source, the cumulated added energy density curve has negative values when going to the demagnetized state. However, from the moment $H_a = 0.0\,\mathrm{A/m}$, energy is running from the source towards the system, which results in a minimum at $H_a = 0.0\,\mathrm{A/m}$. The curve representing the cumulated dissipated energy density is strictly positive since the instantaneously dissipated energy is always positive. Both the cumulated added and stored energy density intersect at negative saturation, meaning that the net amount of energy which is added by the source when running through the hysteresis branch is all dissipated as heat by the ferromagnetic system.

The total dissipated energy density when running through the descending hysteresis branch equals in the Preisach description 125.6 kJ/m^3 and in the micromagnetic description 128.8 kJ/m^3. As outlined in Chapter 4, the total dissipated energy density when running through the complete hysteresis loop corresponds to the surface of the loop. Exploiting the symmetry in the hysteresis loop, it is clear that half the energy is dissipated when running through the descending branch and half of the energy is dissipated when running through the ascending branch, both corresponding to half the loop surface. For the simulated hysteresis loop shown in Fig. 12.11 half of the surface equals 126.7 kJ/m^3. The values obtained in the micromagnetic and Preisach description differ only by about one percent from this number, showing the perfect agreement of the Preisach and the micromagnetic description on the one hand and the macroscopic losses description based on the surface of the hysteresis loop on the other hand. In the Preisach model, this correspondence is incorporated theoretically in the model by construction. In the micromagnetic model, this result is something one expects based on the considerations made on the simple bistable system, see Section 4.2. However, the perfect agreement for the complex multi-stable micromagnetic system is striking.

12.4. Conclusions

In this chapter, a micromagnetic study of hysteresis related processes is performed. First, the memory properties in the developed micromagnetic hysteresis model were investigated. Since these macroscopic hysteresis properties are experimentally observed in all ferromagnetic materials, the micromagnetic hysteresis model should be able to describe them. In the performed simulations, all memory properties were recovered: the branching property, the return-point-memory and the wiping-out property. Moreover, the model shows that also microscopically similar magnetization configurations are reached when minor loops close, evidencing that at the microscopic level a return-point-memory also exists. This was not clear from the macroscopic models.

Second, energy flows towards and in the ferromagnetic sample when running through the hysteresis loop were studied. The Preisach distribution function was extracted from a set of micromagnetic simulated magnetization curves (FORCs). This enabled the discussion of the (instantaneously) added, dissipated and stored energy density in the ferromagnetic system both in the micromagnetic and in the Preisach model. A perfect agreement of the energy description in both models was found. Moreover, the micromagnetic hysteresis model was able to provide a better insight in the instantaneous energy rearrangements when running through the hysteresis loop. These energy rearrangements can only be described in the micromagnetic model.

This chapter shows that a large amount of characteristic properties in magnetic hysteresis processes as they were described in Chapter 4 are recovered in the micromagnetic simulations: the memory properties, the distinction between reversible and irreversible magnetization processes, the determination of losses, etc. Most of these properties are not built into the micromagnetic hysteresis model by construction as is the case for the Preisach model. However, the fact that they are recovered by the model demonstrates that the micromagnetic hysteresis model, developed during this PhD is physically sound, accurate and valuable. Furthermore, it is shown that it brings an added value to the better understanding of hysteresis processes.

CHAPTER 13

General conclusions and further research

Ferromagnetic materials are used in a wide range of applications. Depending on the application, the ferromagnetic objects have very different dimensions. Micromagnetic simulations are since long indispensable in the research on magnetic storage devices, magnetic data transmission, small magnetic sensors, etc. A large variety of micromagnetic numerical schemes have been developed to simulate the magnetic processes in these sub-micrometer sized ferromagnetic samples.

In this PhD, the aim was to extend the length scale on which micromagnetic simulations can be applied to much larger dimensions. In this way micromagnetic simulations become useful to study the relations between the microscopic properties of the material and the macroscopic magnetic behavior. A better understanding of these relations is required for the design of improved ferromagnetic materials, which e.g. minimize iron losses. Furthermore, the knowledge of these relations is important for the development of magnetic non-destructive evaluation techniques. A systematic study of the influence of each microstructural parameter is only possible in numerical simulations since in experiments it is hardly possible to alter just one material parameter without varying others.

Due to the large sample sizes, the existing micromagnetic schemes were not applicable in the new micromagnetic research domain of ferromagnetic materials with sample dimensions larger then $1\,\mu$m. During this PhD we developed a micromagnetic scheme which is able to simulate magnetic processes in 3D samples with dimensions ranging from 10 nm to about $10\,\mu$m. This enables the study of magnetic processes using micromagnetic simulations on length scales where one used to be restricted to the domain theory.

13.1. General conclusions

13.1.1 Numerical micromagnetic scheme

Most of the numerical micromagnetic schemes are based on the time stepping of the Landau-Lifshitz-Gilbert (LLG) equation. Every time step, the different interaction fields have to be computed throughout the material. Hence, the efficiency of the used numerical scheme strongly depends (i) on the number of evaluations of the interaction field, which is determined by time step length ensuring convergence and (ii) on the time and memory efficient evaluation of one single set of interaction fields.

In this PhD we have proposed two new time stepping schemes which enable the use of large time steps –the forward semi-analytical time stepping scheme and the predictor/corrector semi-analytical time stepping scheme– both based on an analytical solution of the LLG equation under constant effective field. The use of these time stepping schemes retains the three basic properties of the LLG equation: (i) a preservation of the amplitude of the magnetization field, (ii) a continuous decrease of the Gibbs free energy under constant applied field and (iii) the conservation of the Gibbs free energy in case of zero damping. Furthermore, due to the use of the analytical expression for the time evolution of the magnetization field, very large time steps can be taken with a minimum of field evaluations. This minimizes the required CPU time and the memory requirements. The accuracy of the time stepping scheme is extensively validated by comparing simulation results of switching processes supplied by our code on the one hand and by code developed at INRIM (Turin, Italy) and at NIST (Washington, US) on the other hand.

Furthermore, the time and memory efficient evaluation of one single set of interaction fields is optimized. The evaluation of the magnetostatic interaction field $\mathbf{H}_{ms}$ is by far the most time consuming. The classical evaluation of $\mathbf{H}_{ms}$ scales $\mathcal{O}(N^2)$. In this PhD we have accelerated the $\mathbf{H}_{ms}$ evaluation to $\mathcal{O}(N \log N)$ by using fast Fourier transforms (FFTs). Two FFT based $\mathbf{H}_{ms}$ evaluation schemes are proposed. One scheme is based on the direct relation between the magnetization field and the magnetostatic field. This scheme computes the magnetostatic field up to machine precision (given the used space discretization), but needs a considerable amount of memory resources. The second $\mathbf{H}_{ms}$ evaluation scheme uses the magnetic scalar potential. This scheme results in a low accuracy evaluation of the magnetostatic field (~ 1 percent error bound) but is faster and requires less memory. We have also shown how the magnetostatic field can be evaluated efficiently in periodic structures using FFTs.

Next to the use of FFTs, also the use of the fast multipole method (FMM) is studied to accelerate the magnetostatic field evaluation. This FMM scheme scales $\mathcal{O}(N)$ and can in theory outperform any FFT scheme. The classical

FMM scheme was accelerated by optimizing the implementation of the different translation operators and the near interaction computations. The resulting FMM implementation has a controllable error bound. Compared to the high accuracy FFT scheme, the memory savings are very large –about a factor 11– while the execution time is a factor 4 to 5 higher. This study has shown that the expected cross-over point where FMM based $\mathcal{O}(N)$ computations become faster than FFT based $\mathcal{O}(N \log N)$ computations is only reached for very large sample sizes. The FMM scheme allows an easy description of periodic boundary conditions.

Classically, micromagnetic simulations are used to simulate the space-time variation of the local magnetization in small ferromagnetic entities: $\mathcal{O}(10\,nm)$ to $\mathcal{O}(100\,nm)$. Here, an optimal accuracy is aimed at, implying the use of a spatial discretization smaller than the exchange length and a high accuracy evaluation of all effective field terms. When the micromagnetic scheme, presented in this PhD work, is used in this classical micromagnetic research domain, the small discretization and the high accuracy of the (magnetostatic) interaction fields are still required. In contrast, it is shown that a coarser space discretization (up to 4 times the exchange length) and a low accuracy magnetostatic field evaluation can be used when the micromagnetic scheme is applied in the study of magnetization processes in larger material samples, where the space-time resolution of the magnetization process is less important. This is e.g. the case when investigating the hysteresis properties of a ferromagnetic sample or when studying magnetic domain structures. We demonstrated that the use of a larger space discretization has a massive impact on the CPU time and the memory requirements while the changes in the macroscopic hysteresis properties are very limited. Furthermore, we have shown that the use of the faster, less memory requiring low accuracy $\mathbf{H}_{ms}$ evaluation scheme influences the macroscopic hysteresis behavior in the same way as when thermal fluctuations corresponding to moderate temperatures are considered.

13.1.2 Micromagnetic study of magnetic processes

To demonstrate the applicability of the developed micromagnetic scheme in the intended wide spatial range, we have used the scheme in three different research domains: (i) the classical micromagnetic research domain, considering the switching processes in different small ferromagnetic samples, (ii) the research domain classically covered by the domain theory, describing the domain configurations in magnetic materials and (iii) the magnetic hysteresis research domain, classically covered by macroscopic hysteresis models as the Preisach model.

In a first classical micromagnetic application, we investigated the influence of the size, shape and temperature on the reversal and/or relaxation pro-

cess in nanostrips with longitudinal dimensions of about 100 nm. It was found that especially the end shape of the strip has a large influence on the reversal nucleation process and consequently on the relaxation time (defined by the moment when the average magnetization is zero). Here, sharp triangular end shapes can prevent the magnetization reversal, while –on the contrary– the addition of nucleation pads accelerates the reversal process. Thermal fluctuations destabilize the micromagnetic system, resulting in smaller applied fields which initiate the reversal process and faster relaxation times.
A second classical micromagnetic application investigated in this PhD is the existence of different reversal mechanisms in infinitely long ferromagnetic wires with varying cross sectional dimensions, ranging from 10 nm to 1 μm. We concluded that, depending on the cross sectional dimensions, different micromagnetic energy terms were dominant, resulting in different reversal mechanisms. In wires with cross section $L < 100$ nm, the reversal is performed by a precessional switching process combined with buckling. In wires with cross sections 100 nm$< L < 500$ nm, multiple vertices are formed which enable the reversal. In wires with a yet larger cross section, the magnetostatic and anisotropy interaction becomes more important leading to the formation of magnetic domains during the switching process. In general, smaller external fields have to be applied to initiate the reversal process for increasing cross sectional dimensions.

The developed micromagnetic scheme is also used to study the magnetic domain configurations in platelets with perpendicular uniaxial anisotropy. The evolution of the equilibrium domain configurations when reaching to near saturation in different directions and then back to $< \mathbf{M} >= 0$ were investigated. For the obtained equilibrium states at $< \mathbf{M} >= 0$, a comparison with the domain theory was made. Here, different domain theory models describe the expected magnetic domains on a theoretical basis, depending on the strength of the anisotropy constant. It was found that only the refined domain theory model designed by Hubert to a large extent describes the complexity of the simulated (closure) domain configurations over the complete studied range of anisotropy strengths. The micromagnetic simulations revealed that, for large anisotropy constants, it is more appropriate to define continuous closure regions instead of distinct closure domains. This study demonstrates the validity of the developed micromagnetic scheme for sample dimensions larger than 1 μm. It again validates the use of a discretization size larger than the exchange length in the appropriate research domains, see conclusions above. Furthermore, the added value of performing micromagnetic simulations on the length scale larger than 1 μm is proven.

Ultimately, the micromagnetic hysteresis scheme is used to investigate some hysteresis properties of ferromagnetic materials. Experimentally, the memory properties described by Madelung's rules were proven to be general

hysteresis properties which consequently should be described by any hysteresis model. While Madelung's rules are incorporated by construction in macroscopic hysteresis models, this is not the case for the micromagnetic hysteresis model. Hence, the fact that the developed micromagnetic hysteresis model describes the memory properties validates the model as a proper hysteresis model. Moreover, our simulations assume that not only a macroscopic return-point-memory property exists, but that to a large extent also microscopically the same magnetization state is obtained (microscopic return-point-memory). This shows the added value of the micromagnetic hysteresis scheme.
In a second hysteresis research topic, the energy flows in the ferromagnetic system when running through the hysteresis loop are investigated and compared to the Preisach model description. The instantaneous added, dissipated and stored energy density was determined at each time point, based on the micromagnetic hysteresis computations and based on the Preisach distribution function obtained from the micromagnetic simulations. A striking correspondence was obtained, which again validates the micromagnetic hysteresis model. Moreover, the micromagnetic simulations were able to reveal the energy rearrangements in the ferromagnetic material at each time point. Hence, the micromagnetic hysteresis model contributes to a better understanding of the hysteretic energy processes. This is important when one aims to minimize hysteresis losses. The total losses during one cycle of the applied field were in perfect agreement with the macroscopic theory.

13.2. Suggestions for further research

13.2.1 Suggestions regarding the numerical scheme

Concerning the implementation of the numerical micromagnetic scheme, we have mainly focused on the efficient evaluation of the magnetostatic field. The FFT schemes for the evaluation of the magnetostatic field are highly optimized so modifications of the algorithms itself will only lead to incremental accelerations. However, in the last years, more dedicated, high performing computer hardware has become affordable. This opens opportunities to further speed up the simulations or to describe yet larger sample dimensions.

We implemented our algorithms to be executed on multiple cores present in one single machine, using a multi-threaded code. This corresponds to the use of multiple processors and one common memory within one computer. Another option is to run the micromagnetic code on a network of computers, which all have their own processors and their own memory. In such a computer configuration, one is not limited by the memory resources available in one machine. In theory, one can have massive time gains or one can compute ever larger systems when using an increasing number of computing

units. However, since the memory is distributed over different machines, the communication between the machines has to be scheduled in the implementation using MPI-algorithms. Hence, the efficiency of the algorithm strongly depends on the implementation.

In the end, one will come to a maximum problem size which can be treated using purely micromagnetic simulations, given the computer resources and the time available. In the next few years, this maximum problem size will probably still be substantially smaller than the samples on which magnetic measurements are performed. These have a cross sectional surface in the order of $0.5\,\text{mm} \times 10\,\text{mm}$. Hence, one will have to revert to a multilevel magnetic scheme. On the microscopic level of such a scheme, the basic micromagnetic interactions have to be properly described as discussed in this PhD. Parameters which are characteristic for the magnetization processes on the microscopic level should then be extracted and passed through to the macroscopic level, where the remaining coarse level interactions are taken care of. Furthermore, there should be some coupling from the macroscopic level back to the microscopic level. One can only succeed in the development of such a multilevel scheme if one has a thorough understanding of the magnetic processes present on the microscopic scale.

13.2.2 Suggestions regarding hysteresis simulation

In Section 5.4.1 we stated that the development of a numerical micromagnetic (hysteresis) scheme is a truly multiphysics problem which cannot be tackled at once. This forced us to make some assumptions in the research performed during this PhD. It is clear that each of the assumptions restricts the applicability of the hysteresis scheme. Hence, to broaden the applicability of the developed micromagnetic scheme and, consequently, to obtain a more complete insight in the physics of the magnetic processes, all of the assumptions could be alleviated in further research. In what follows, we give a short overview of the corresponding opportunities and challenges:

1. In this PhD thesis, we have considered the stress and strain distribution in the ferromagnetic material as a known input for the magnetoelastic interactions. Analytical expressions are provided for the stress distribution around a single edge and a single screw dislocation and around an inclusion. Further, some assumptions were made about the stress field introduced by a grain boundary. The evaluation of the actual stress field introduced in the material by the lattice imperfections is however much more complicated and requires *micromechanic computations*. A lot of work still has to be performed in this research domain.

2. In this PhD work, we restricted ourselves to the relaxed approach to describe the magnetoelastic interaction. This approach was only valid for low magnetostrictive materials. In this approach, the influence of the local stress field on the magnetization is taken into account, but the influence of the (changing) magnetization on the stress field and thus on the microstructure of the material is disregarded. The complete description of this interplay between the local stress field and the local magnetization requires the solution of the complete magneto-mechanical problem at each time step. This results in computations comparable to the evaluation of the magnetostatic field and enables the *description of magnetostrictive effects*.

3. Further, we only studied quasi-static hysteresis loops. Hence no eddy currents were considered. Referring to the loss theory of Bertotti, this means that classical losses and excess losses are not embedded in the model. *Incorporating the eddy currents in the numerical computations*, will improve the micromagnetic description. The evaluation of the eddy currents has a computational burden comparable to the evaluation of the magnetostatic field and has to be performed at each time step. Hence, also here, sophisticated numerical techniques will have to be adopted. When the eddy currents are introduced in the model one can start making the comparison between the losses in the loss theory of Bertotti and the losses in the micromagnetic scheme. This different, micromagnetic approach to obtain the frequency depending losses in the material will give a better insight in the loss mechanisms and the loss theory itself.

Including these suggestions in the micromagnetic (hysteresis) scheme will also be valuable in the development of magnetic non destructive evaluation techniques. Indeed, a hysteresis scheme which correctly describes the interaction between the imperfect microstructure of the ferromagnetic material and the macroscopic magnetization is indispensable in this context. A systematic study of the influences of each microstructural parameter will be time consuming, but will bring many advantages. Furthermore, eddy current simulations independent from the micromagnetic computations are proven to be valuable for magnetic non destructive evaluation [122].

Appendices

APPENDIX A

Green's function elements in FFT accelerated schemes

The Green's tensor elements in the high accuracy FFT based $\mathbf{H}_{ms}$ evaluation scheme used in Section 7.3.1 and in the near interaction scheme II of Section 8.4.2 are obtained by elaborating the surface integrals in (7.10) using Gauss quadrature formula.

$$g_{xx}(x,y,z) = \frac{-M_s}{4\pi} \int_{-1}^{1}\int_{-1}^{1} \left\{ \frac{x+1}{[(x+1)^2+(y+\eta)^2+(z+\zeta)^2]^{3/2}} - \frac{x-1}{[(x-1)^2+(y+\eta)^2+(z+\zeta)^2]^{3/2}} \right\} \mathrm{d}\eta\, \mathrm{d}\zeta, \tag{A.1}$$

$$g_{yy}(x,y,z) = \frac{-M_s}{4\pi} \int_{-1}^{1}\int_{-1}^{1} \left\{ \frac{y+1}{[(x+\xi)^2+(y+1)^2+(z+\zeta)^2]^{3/2}} - \frac{y-1}{[(x+\xi)^2+(y-1)^2+(z+\zeta)^2]^{3/2}} \right\} \mathrm{d}\xi\, \mathrm{d}\zeta, \tag{A.2}$$

$$g_{zz}(x,y,z) = \frac{-M_s}{4\pi} \int_{-1}^{1}\int_{-1}^{1} \left\{ \frac{z+1}{[(x+\xi)^2+(y+\eta)^2+(z+1)^2]^{3/2}} - \frac{z-1}{[(x+\xi)^2+(y+\eta)^2+(z-1)^2]^{3/2}} \right\} \mathrm{d}\xi\, \mathrm{d}\eta, \tag{A.3}$$

$$g_{xy}(x,y,z) = \frac{-M_s}{4\pi} \int_{-1}^{1}\int_{-1}^{1} \left\{ \frac{y+\eta}{[(x+1)^2+(y+\eta)^2+(z+\zeta)^2]^{3/2}} - \frac{y+\eta}{[(x-1)^2+(y+\eta)^2+(z+\zeta)^2]^{3/2}} \right\} d\eta\, d\zeta, \tag{A.4}$$

$$g_{xz}(x,y,z) = \frac{-M_s}{4\pi} \int_{-1}^{1}\int_{-1}^{1} \left\{ \frac{z+\zeta}{[(x+1)^2+(y+\eta)^2+(z+\zeta)^2]^{3/2}} - \frac{z+\zeta}{[(x-1)^2+(y+\eta)^2+(z+\zeta)^2]^{3/2}} \right\} d\eta\, d\zeta, \tag{A.5}$$

$$g_{yz}(x,y,z) = \frac{-M_s}{4\pi} \int_{-1}^{1}\int_{-1}^{1} \left\{ \frac{z+\zeta}{[(x+\xi)^2+(y+1)^2+(z+\zeta)^2]^{3/2}} - \frac{z+\zeta}{[(x+\xi)^2+(y-1)^2+(z+\zeta)^2]^{3/2}} \right\} d\xi\, d\zeta. \tag{A.6}$$

The Green's vector elements in the low accuracy FFT based $\mathbf{H}_{ms}$ evaluation scheme used in Section 7.3.2 are obtained by elaborating the surface integrals in (7.18) using Gauss quadrature formula or can be evaluated using analytical functions [61].

$$f_x(x,y,z) = \frac{M_s}{4\pi} \int_{-1}^{1}\int_{-1}^{1} \left\{ \frac{1}{[(x+1)^2+(y+\eta)^2+(z+\zeta)^2]^{1/2}} - \frac{1}{[(x-1)^2+(y+\eta)^2+(z+\zeta)^2]^{1/2}} \right\} d\eta\, d\zeta, \tag{A.7}$$

$$f_y(x,y,z) = \frac{M_s}{4\pi} \int_{-1}^{1}\int_{-1}^{1} \left\{ \frac{1}{[(x+\xi)^2+(y+1)^2+(z+\zeta)^2]^{1/2}} - \frac{1}{[(x+\xi)^2+(y-1)^2+(z+\zeta)^2]^{1/2}} \right\} d\xi\, d\zeta, \tag{A.8}$$

$$f_z(x,y,z) = \frac{M_s}{4\pi}\int_{-1}^{1}\int_{-1}^{1}\left\{\frac{1}{[(x+\xi)^2+(y+\eta)^2+(z+1)^2]^{1/2}} - \frac{1}{[(x+\xi)^2+(y+\eta)^2+(z-1)^2]^{3/2}}\right\}\mathrm{d}\xi\,\mathrm{d}\eta. \tag{A.9}$$

The Green's tensor elements in the FFT accelerated computation of the near interactions using scheme I described in Section 8.4.1 are obtained by elaborating the surface integrals in (8.43) using Gauss quadrature formula.

$$g_{xx}{}^{I,J,K}(x,y,z) = \frac{-M_s}{4\pi}\int_{-1}^{1}\int_{-1}^{1}\left\{\frac{x-I\lambda+1}{[(x-I\lambda+1)^2+(y-J\lambda+\eta)^2+(z-K\lambda+\zeta)^2]^{3/2}} - \frac{x-I\lambda-1}{[(x-I\lambda-1)^2+(y-J\lambda+\eta)^2+(z-K\lambda+\zeta)^2]^{3/2}}\right\}\mathrm{d}\eta\,\mathrm{d}\zeta \tag{A.10}$$

$$g_{yy}{}^{I,J,K}(x,y,z) = \frac{-M_s}{4\pi}\int_{-1}^{1}\int_{-1}^{1}\left\{\frac{y-J\lambda+1}{[(x-I\lambda+\xi)^2+(y-J\lambda+1)^2+(z-K\lambda+\zeta)^2]^{3/2}} - \frac{y-J\lambda-1}{[(x-I\lambda+\xi)^2+(y-J\lambda-1)^2+(z-K\lambda+\zeta)^2]^{3/2}}\right\}\mathrm{d}\xi\,\mathrm{d}\zeta \tag{A.11}$$

$$g_{zz}{}^{I,J,K}(x,y,z) = \frac{-M_s}{4\pi}\int_{-1}^{1}\int_{-1}^{1}\left\{\frac{z-K\lambda+1}{[(x-I\lambda+\xi)^2+(y-J\lambda+\eta)^2+(z-K\lambda+1)^2]^{3/2}} - \frac{z-K\lambda-1}{[(x-I\lambda+\xi)^2+(y-J\lambda+\eta)^2+(z-K\lambda-1)^2]^{3/2}}\right\}\mathrm{d}\xi\,\mathrm{d}\eta \tag{A.12}$$

$$g_{xy}{}^{I,J,K}(x,y,z) = \frac{-M_s}{4\pi}\int_{-1}^{1}\int_{-1}^{1}\left\{\frac{y-J\lambda+\eta}{[(x-I\lambda+1)^2+(y-J\lambda+\eta)^2+(z-K\lambda+\zeta)^2]^{3/2}} - \frac{y-J\lambda+\eta}{[(x-I\lambda-1)^2+(y-J\lambda+\eta)^2+(z-K\lambda+\zeta)^2]^{3/2}}\right\}\mathrm{d}\eta\,\mathrm{d}\zeta \tag{A.13}$$

$$g_{xz}{}^{I,J,K}(x,y,z) =$$
$$\frac{-M_s}{4\pi}\int_{-1}^{1}\int_{-1}^{1}\left\{\frac{z-K\lambda+\zeta}{[(x-I\lambda+1)^2+(y-J\lambda+\eta)^2+(z-K\lambda+\zeta)^2]^{3/2}}\right. \tag{A.14}$$
$$\left.-\frac{z-K\lambda+\zeta}{[(x-I\lambda-1)^2+(y-J\lambda+\eta)^2+(z-K\lambda+\zeta)^2]^{3/2}}\right\}\mathrm{d}\eta\,\mathrm{d}\zeta$$

$$g_{yz}{}^{I,J,K}(x,y,z) =$$
$$\frac{-M_s}{4\pi}\int_{-1}^{1}\int_{-1}^{1}\left\{\frac{z-K\lambda+\zeta}{[(x-I\lambda+\xi)^2+(y-J\lambda+1)^2+(z-K\lambda+\zeta)^2]^{3/2}}\right. \tag{A.15}$$
$$\left.-\frac{z-K\lambda+\zeta}{[(x-I\lambda+\xi)^2+(y-J\lambda-1)^2+(z-K\lambda+\zeta)^2]^{3/2}}\right\}\mathrm{d}\xi\,\mathrm{d}\zeta$$

APPENDIX B

Accelerated computation of FFTs of zero padded matrices

The standard routine in FFTW [83] can be used for the execution of a 3D real to complex FFT. This is a very fast routine to Fourier transform matrices with real elements in 3D. A 3D FFT contains three phases, when transforming a matrix with dimensions $N \times N \times N$ these phases are: (i) Fourier transforming the N^2 arrays in z-direction, (ii) Fourier transforming the N^2 arrays in the y-direction and (iii) Fourier transforming the N^2 arrays in the x-direction. So in total their are $3N^2$ 1D FFTs of arrays of dimension N. As a consequence, when this routine is used to Fourier transform zero padded matrices, 1D FFTs are performed on arrays containing only zeros, which is useless. Omitting the 1D FFTs on arrays containing only zeros accelerates the 3D FFT.

In the case of a zero padded matrix as in the FFT schemes of Chapter 7 and in the near interaction scheme I described in Chapter 8 this is shown in Fig. B.1. The three different phases of the 3D FFT are shown, assuming a cubic 3D zero padded input matrix. From Fig. B.1.a it is clear that only a quarter of the z-arrays contains non-zero values, thus only $N^2/4$ 1D FFTs are performed. From Fig. B.2.b it is clear that after the Fourier transforms on the z-arrays only half of the y-arrays contains non-zero values, thus only $N^2/2$ 1D FFTs are performed. Fig. B.1.c shows that after the Fourier transforms on the z- and y-arrays all x-arrays contain non-zero values, thus all N^2 1D FFTs have to be performed. This means that only $7/4N^2$ 1D FFTs instead of $3N^2$ are performed during the forward Fourier transforms of the matrices in scheme I. For the inverse Fourier transforms, this scheme is performed in the opposite direction, starting with Fig. B.1.c and ending with Fig. B.1.a. Applying this scheme in the case of a cubical 3D input matrix reduces the time spent on the evaluation of FFTs to about 58% of the original time.

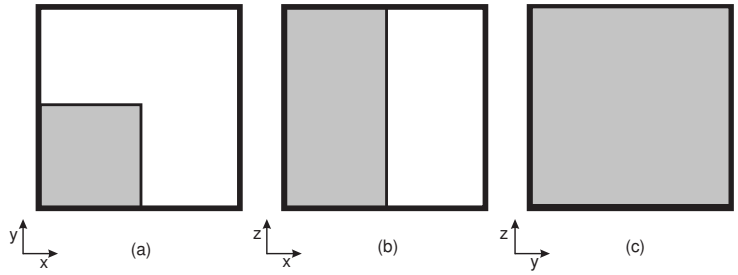

Figure B.1: Overview of the data during the different phases of the 3D forward FFT for a zero padded matrix. The gray areas correspond with arrays in the in-plane direction (a: z-direction, b: y-direction, c: x-direction) containing non-zero values.

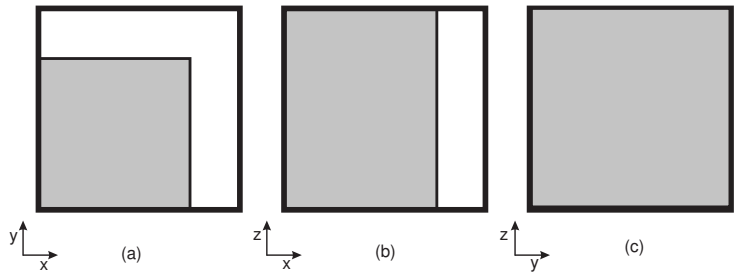

Figure B.2: Overview of the data during the different phases of the 3D forward FFT for a zero padded matrix as in near interaction scheme II. The gray areas correspond with arrays in the in-plane direction (a: z-direction, b: y-direction, c: x-direction) containing non-zero values.

In the case of a zero padded matrix as in near interaction scheme II described in Chapter 8, the three different phases of the forward 3D FFT are shown in Fig. B.2. From Fig. B.2.a it is clear that only $9/16$ of the z-arrays contain non-zero values, thus only $9/16\,N^2$ 1D FFTs are performed. From Fig. B.2.b it is clear that after the Fourier transforms on the z-arrays three quarters of the y-arrays contain non-zero values, thus only $3/4\,N^2$ 1D FFTs are performed. Fig. B.2.c shows that after the Fourier transforms on the z- and y-arrays all x-arrays contain non-zero values, thus all N^2 1D FFTs have to be performed. This means that only $37/16\,N^2$ instead of $3N^2$ 1D FFTs are performed during the forward Fourier transforms of the magnetization matrices in the near interaction scheme II. Applying this scheme on the computations of the 3D forward FFTs reduces the time spent on the forward FFTs to about 77% of the original time.

For the inverse 3D FFTs in near interaction scheme II described in Chapter 8, one is only interested in the results corresponding with magnetostatic fields

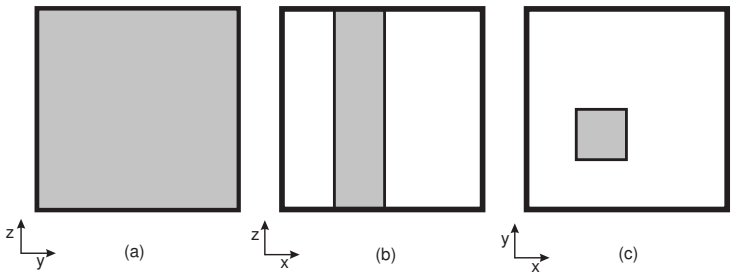

Figure B.3: Overview of the data during the different phases of the 3D inverse FFT as used in near interaction scheme II. The gray areas correspond with arrays in the in-plane direction (a: x-direction, b: y-direction, c: z-direction) containing meaningful values.

in the considered basis box, which is the one in the center of Fig. 8.6 of Chapter 8, moreover, all other data is spoiled by side effects of the Fourier transforms since the matrices containing the magnetization data where only zero padded with n zeros in every direction. Hence one can reduce the number of 1D FFTs to only FFTs on meaningful data, which is data that has influence on the resulting magnetostatic field values of the considered basis box. Fig. B.3 shows the arrays that contain meaningful data during the different phases of the inverse 3D FFT. From Fig. B.3.a it is clear that all the x-arrays contain meaningful data, thus all N^2 1D (inverse) FFTs have to be performed. From Fig. B.3.b it is clear that after the Fourier transforms on the x-arrays, only one quarter of the y-arrays contains meaningful data, thus only $N^2/4$ 1D (inverse) FFTs are performed. Fig. B.3.c shows that after the Fourier transforms on the x- and y-arrays only $1/16$ of the z-arrays contains meaningful data, thus only $N^2/16$ 1D (inverse) FFTs are performed. This means that only $21/16\,N^2$ in stead of $3N^2$ 1D (inverse) FFTs are performed during the inverse Fourier transforms of the magnetization matrices in scheme II. Applying this scheme on the computations of the 3D inverse FFTs in near interaction scheme II reduces the time spent on the inverse FFTs to about 43% of the original time.

Bibliography

[1] L. Vandenbossche, *Magnetic hysteretic characterization of ferromagnetic materials with objectives towards non-destructive evaluation of material degradation*. PhD thesis, Ghent University, 2009.

[2] G. Crevecoeur, S. P., D. L., V. L., and R. Van de Walle, "Analysis of the local material degradation near cutting edges of electrical steel sheets," *IEEE Transactions on Magnetics*, vol. 44, no. 11, pp. 3173–3176, 2008.

[3] L. Vandenbossche, L. Dupré, and J. Melkebeek, "Preisach based magnetic evaluation of fatigue damage progression," *Journal of Magnetism and Magnetic Materials*, vol. 290-291, pp. 486–489, 2005.

[4] H. Krönmuller and M. Fähnle, *Micromagnetism and the microstructure of ferromagnetic solids*. Max-Planck-Institut für Metallfoschung, Stuttgart, Germany: Cambridge University Press, 1994.

[5] G. Bertotti, *Hysteresis in magnetism*. San Diego, California, USA: Academic Press, 1998.

[6] F. Bitter, "On inhomogeneities in magnetization of ferromagnetic materials," *Physical Review*, vol. 38, pp. 1903–1905, 1903.

[7] P. Weiss, "L'hypothèse du champ moléculaire et la proprieté ferromagnétique," *Journal de Physique*, vol. 6, pp. 661–690, 1907.

[8] K. Sixtus and L. Tonks, "Propagation of large barkhausen discontinuities," *Physical Review*, vol. 37, pp. 930–958, 1931.

[9] J. Maxwell, *A treatise on Electricity and Magnetism*, vol. 1& 2. Oxford: Clarendon Press, 1873.

[10] F. Bitter, "Some properties of homogeneously cubic ferromagnetic lattices," *Physical Review*, vol. 42, pp. 697–707, 1932.

[11] L. Landau and E. Lifshitz, "On the theory of the dispersion of magnetic permeability in ferromagnetic bodies," *Physik Z. Sowjetunion*, vol. 8, pp. 153–169, 1935.

[12] W. Heisenberg, "Mehrkörperproblem und resonanz in de quantenmechanik," *Zeitschrift für Physik*, vol. 38, pp. 411–426, 1926.

[13] R. Coehoorn and G. Daalderop, "Magnetocrystalline anisotropy in new magnetic materials," *Journal of Magnetism and Magnetic Materials*, vol. 104, pp. 1081–1085, 1992.

[14] R. Bozorth, *Ferromagnetism*. Toronto - New York - London: D. Van Nostrand, 1951.

[15] H. Honda and S. Kaya, "Magnetization of single crystals of iron," *Schientific reports of Tohoku University*, vol. 15, pp. 721–753, 1992.

[16] F. Verheest, "Continuum mechanics," *Course Syllabus*, vol. Faculty of Science, Department of Mathematical Physics and Astronomy, Ghent University, 2004.

[17] T. Mura, *Micromechanics of Defects in Solids*. Dordrecht, The Netherlands: Marinus Nijhoff Publishers (Kluwer Academic Publishers), 1987.

[18] T. Gilbert, "A lagrangian formulation of the gyromagnetic equation of the magnetic field," *Physical Review*, vol. 100, p. 1243, 1955.

[19] R. Pry and C. Bean, "Calculation of the energy loss in magnetic sheet materials using a domain model," *Journal of Applied Physics*, vol. 29, pp. 532–533, 1958.

[20] W. Brown Jr., "Thermal fluctuations of a single-domain particle," *Physical Review*, vol. 130, no. 5, pp. 1677–1686, 1963.

[21] A. Aharoni, "Demagnetizing factors for rectangular ferromagnetic prisms," *Journal of Applied Physics*, vol. 83, no. 6, pp. 3432–3434, 1998.

[22] R. Cross, H. Mc Namara, and A. Pokrovskii, "Modelling macroeconomic flows related to large ensembles of elementary exchange operations," *Physica B*, vol. 403, pp. 451–455, 2008.

[23] D. Flynn, H. Mc Namara, P. O'Kane, and A. Pokrovskii, *Application of the Preisach model to soil-moisture hysteresis, in: The Science of Hysteresis*. Amsterdam, The Netherlands: Elsevier Science, 3 ed., 1995.

[24] J. O'Kane and D. Flynn, "Threshold, switches and hysteresis in hydrology form the pedon to the catchment scale: a non-linear systems theory," *Hydrology and Earth Systems Science*, vol. 11, no. 1, pp. 443–459, 2007.

[25] J. Alamia and G. Friedman, "Rate-independent transport processes in stirred granular medium," in *Proceedings of 7th International Symposium on Hysteresis Modeling and Micromagnetics*, (Gaithersburg, Maryland, USA), May 11-14, 2009.

[26] K. Minogue, H. Mc Namara, and D. Flynn, "Hysteresis in cognitive processes," in *Proceedings of 7th International Symposium on Hysteresis Modeling and Micromagnetics*, (Gaithersburg, Maryland, USA), May 11-14, 2009.

[27] H. Barkhausen, "Zwei mit hilfe der neuen verstarker entdeckte erscheinungen," *Zeitschrift für Physik*, vol. 20, pp. 401–403, 1919.

[28] E. Madelung, "The magnetisation by means of a quickly running current and the actual effect of the rutherford-marconi magnet detectors," *Annalen der Physik*, vol. 17, no. 10, pp. 861–890, 1998.

[29] J. Fidler and T. Schrefl, "Micromagnetic modelling – the current state of art," *Journal of Physics D: Applied Physics*, vol. 33, pp. R135–R156, 2000.

[30] K. Zhu and H. Bertram, "Recording and transition noise simulations in thin film media," *IEEE Transactions on Magnetics*, vol. 24, no. 6, pp. 2706–2708, 1988.

[31] K. Gao, J. Fernandez-de Castro, and H. Bertram, "A micromagnetic model of dual layer magnetic-recording thin films," *IEEE Transactions on Magnetics*, vol. 41, no. 11, pp. 4236–4241, 2005.

[32] G. Hughes, "Patterned media write designs," *IEEE Transactions on Magnetics*, vol. 36, no. 2, pp. 521–527, 2000.

[33] J. Miles, "Effect of grain size distribution on the performance of perpendicular recording media," *IEEE Transactions on Magnetics*, vol. 43, no. 3, pp. 955–967, 2007.

[34] T. Schrefl, G. Hrkac, D. Suess, W. Scholz, and J. Fidler, "Coercitivity and remanence in self-assemble fept nanoparticle arrays," *Journal of Applied Physics*, vol. 93, no. 10, pp. 7041–7043, 2003.

[35] R. Hertel, "Computational micromagnetism of mangnetization processes in nickel nanowires," *Journal of Magnetism and Magnetic Materials*, vol. 249, no. 1-2, pp. 251–256, 2002.

[36] V. Tiberkevich, I. Krivotorov, G. Gerhart, and A. Slavin, "Compensation of nonlinear phase noise in an in-plane-magnetized anisotropic spin-torque oscillator," *Journal of Magnetism and Magnetic Materials*, vol. 321, no. 16, pp. 153–155, 2009.

[37] J. Oti and S. Russek, "Micromagnetic simulations of magnetoresistive behavior of sub-micrometer spin-valve mram devices," *IEEE Transactions on Magnetics*, vol. 33, no. 5, pp. 3298–3300, 1997.

[38] A. Aharoni, "Micromagnetics: past, present and future," *Physica B*, vol. 306, pp. 1–9, 2001.

[39] F. Preisach, "Uber die magnetische nachwirkung," *Zeitschrift für Physik*, vol. 94, pp. 277–302, 1935.

[40] D. Jiles and D. L. Atherton, "Theory of ferromagnetic hysteresis," *Journal of Magnetism and Magnetic Materials*, vol. 61, pp. 48–60, 1986.

[41] H. Hauser, "Energetic model of ferromagnetic hysteresis," *Journal of Applied Physics*, vol. 75, no. 5, pp. 2584–2597, 1994.

[42] A. Van den Berg, L. Dupré, B. Van de Wiele, and G. Crevecoeur, "Meso hysteresis model for ferromagnetic materials by minimization of the micromagnetic free energy," *Journal of Applied Physics*, vol. 105, no. 7, p. Art. No. 07D513, 2009.

[43] L. Daniel, O. Hubert, N. Buiron, and R. Billardon, "Reversible magnetoelastic behavior: A multiscale approach," *Journal of Mechanics and physics of Solids*, vol. 56, pp. 1018–1042, 2008.

[44] L. Dupré, *Elektromagnetische karakterisatie van niet-georiënteerd elektroblik*. PhD thesis, Ghent University, 1995.

[45] P. Sergeant, *Laagfrequente magnetische afscherming van elektrische installaties*. PhD thesis, Ghent University, 2005.

[46] G. Crevecoeur, *Numerical methods for low frequency electromagnetic optimization and inverse problems using multi-level techniques*. PhD thesis, Ghent University, 2009.

[47] T. Hilgert, *Magnetische krachten en magnetostrictie in elektrisch staal en toepassingen op trillingen van elektrische machines en transformatoren*. PhD thesis, Ghent University, 2008.

[48] K. Cools, *Spectral properties of boundary integral equations: analysis and regularisation*. PhD thesis, Ghent University, 2008.

[49] I. Bogaert, *Broadband multilevel fast multipole methods*. PhD thesis, Ghent University, 2008.

[50] J. De Zaeytijd, *On the 3D electromagnetic quantitative inverse scattering problem: algorithms and regularization*. PhD thesis, Ghent University, 2009.

[51] S. Van den Bulcke and A. Franchois, "A full-wave 2.5d volume integral equation solver for 3d millimeter-wave scattering by large inhomogeneous 2d objects," *IEEE transactions on antennas and propagation*, vol. 57, no. 2, pp. 535–545, 2009.

[52] Y. Shu, M. Lin, and K. Wu, "Micromagnetic modeling of magnetostrictive materials under intrinsic stress," *Mechanics of Materials*, vol. 36, pp. 975–997, 2004.

[53] M. Abramowitz and I. Stegun, *Handbook of mathematical functions*. Dover, New York: National Bureau of Standards, 1970.

[54] A. Vansteenkiste, *Dynamics of magnetic vortices in nanodots: experiment and simulation*. PhD thesis, Ghent University, 2009.

[55] M. Donahue and D. Porter, "Exchange energy formulations for 3d micromagnetics," *Physica B*, vol. 343, pp. 177–183, 2004.

[56] O. Bottauscio, M. Chiampi, and A. Manzin, "Multiscale finite element solution of the exchange term in micromagnetic analysis of large bodies," *IEEE Transactions on Magnetics*, vol. 45, no. 11, pp. 5200–5203, 2009.

[57] F. Nabarro, "The mathematical theory of stationary dislocations," *Advances in Physics*, vol. 1, no. 3, pp. 269–395, 1952.

[58] G. Dieter, *Mechanical Metallurgy*. London: McGraw-Hill Book Company, 1988.

[59] D. Britton and M. Härting, "The influence of strain on point defect dynamics," *Advanced Engineering Materials*, vol. 4, no. 8, pp. 629–635, 2002.

[60] "Advanced structural geology," *Course Syllabus*, vol. Faculty of Science, University of Alabama.

[61] M. Schabes and A. Aharoni, "Magnetostatic interaction fields for a three-dimensional array of ferromagnetic cubes," *IEEE Transactions on Magnetics*, vol. 23, no. 6, pp. 3882–3888, 1987.

[62] M. d'Aquino, C. Serpico, and G. Miano, "Geometrical integration of landau-lifshitz-gilbert equation based on the mid-point rule," *Journal of Computational Physics*, vol. 209, pp. 730–753, 2005.

[63] X. Wang, C. Garcia-Cervera, and W. E, "A gauss-seidel projection method for micromagnetic simmuations," *Journal of Computational Physics*, vol. 171, pp. 357–372, 2001.

[64] P. Krishnaprasad and X. Tan, "Cayley transforms in micromagnetics," *Physica B*, vol. 306, pp. 195–199, 2001.

[65] P. Monk and O. Vacus, "Accurate discretization of a nonlinear micromagnetic problem," *Computational Methods in Applied Mechanics and Engineering*, vol. 190, no. 40-41, pp. 5243–5269, 2001.

[66] C. Serpico, I. Mayergoyz, and G. Bertotti, "Numerical technique for integration of the landau-lifshitz equation," *Journal of Applied Physics*, vol. 89, pp. 6991–6993, 2001.

[67] A. Spargo, P. Ridley, and G. Roberts, "Geometric integration of the gilbert equation," *Journal of Applied Physics*, vol. 93, pp. 6805–6807, 2003.

[68] J. Mathews, *Numerical Methods: for Mathematics, Science and Engineering*. Englewood Cliffs: Prentice-Hall Inc, 1992.

[69] D. Porter and M. Donahue, "Precession axis modification to a semianalytical landau-lifshitz solution technique," *Journal of Applied Physics*, vol. 103, p. Art. No. 07D920, 2008.

[70] B. Van de Wiele, A. Manzin, O. Bottauscio, M. Chiampi, L. Dupré, and F. Olyslager, "Finite difference and edge finite-element approaches for dynamic micromagnetic modelling," *IEEE Transactions on Magnetics*, vol. 44, no. 11, pp. 3137–3140, 2008.

[71] B. Van de Wiele, A. Manzin, L. Dupré, F. Olyslager, O. Bottauscio, and M. Chiampi, "Comparison of finite-difference and finite-element schemes for magnetization processes in 3-d particles," *IEEE Transactions on Magnetics*, vol. 45, no. 3, pp. 1614–1617, 2009.

[72] O. Bottauscio, M. Chiampi, and A. Manzin, "An edge element approach for dynamic micromagnetic modeling," *Journal of Applied Physics*, vol. 103, p. Art. No. 07D911, 2008.

[73] M. Donahue and D. Porter, *OOMF User's Guide*. NIST, Gaithersburg, MD, US, 1999.

[74] M. Donahue and D. Porter, "Micromagnetics on curved geometries using rectangular cells: error correction and analysis," *IEEE Transactions on Magnetics*, vol. 43, pp. 2878–2880, 2007.

[75] R. Boardman, H. Fangohr, and C. Simon, "Micromagnetic simulation of ferromagnetic part-spherical particles," *Journal of Applied Physics*, vol. 95, no. 11, pp. 7037–7039, 2004.

[76] W. Rave, K. Fabian, and A. Hubert, "Magnetic states of small cubic particles with uniaxial anisotropy," *Journal of Magnetism and Magnetic Material*, vol. 190, pp. 332–348, 1998.

[77] S. Yuan and H. Bertram, "Fast adaptive algorithms for micromagnetics," *IEEE Transactions on Magnetics*, vol. 28, no. 5, pp. 2031–2036, 1992.

[78] D. Berkov, "Numerical simulations of quasistatic remagnetization processes in fine magnetic particle systems," *Journal of Magnetism and Magnetic Material*, vol. 161, pp. 337–356, 1996.

[79] R. McMichael, M. Donahue, and G. Porter, "Comparison of magnetostatic field calculation methods on two-dimensional square grids as applied to a micromagnetic standard problem," *Journal of Applied Physics*, vol. 85, no. 8, pp. 5816–5818, 1999.

[80] K. Ramstöck, T. Leibl, and A. Hubert, "Optimizing stray field computations in finite-element micromagnetics," *Journal of Magnetism and Magnetic Materials*, vol. 135, no. 1, pp. 97–110, 1994.

[81] D. Berkov, K. Ramstöck, and A. Hubert, "Solving micromagnetic problems - towards an optimal numerical-method," *Physica Status Solidi A*, vol. 137, no. 1, pp. 207–225, 1993.

[82] W. Press, S. Teukolsky, W. Vetterling, and B. Flannerly, *Numerical recipes in C: the art of scientific computing*. Cambridge University Press, 1995.

[83] M. Frigo and S. Johnson, "The design and implementation of fftw3," *Proceedings of the IEEE*, vol. 93, no. 2, pp. 216–231, 2005.

[84] B. Baekelandt, *Study of advanced layered and periodic electromagnetic absorbers*. PhD thesis, Ghent University, 1997.

[85] A. Toukmaji and J. Board Jr., "Ewald summation techniques in perspective: a servey," *Computer Physics Communications*, vol. 95, pp. 73–92, 1996.

[86] Y. Shan, J. Klepeis, M. Eastwood, R. Dror, and D. Shaw, "Gaussian split ewald: A fast ewald mesh method for molecular simulation," *The Journal of Chemical Physics*, vol. 122, p. Art. No. 054101, 2005.

[87] D. Berkov and N. Gorn, "Quasistatic remagnetization processes in two-dimensional systems with random on-site anisotropy and dipolar interaction: Numerical simulations," *Physical Review B*, vol. 57, no. 22, pp. 14332–14343, 1998.

[88] N. Gorn, D. Berkov, P. Görnert, and D. Stock, "Comparison of the fast multipole and ewald methods for the evaluation of the magnetodipolar field in disordered systems," *Journal of Magnetism and Magnetic Materials*, vol. 310, pp. 2829–2831, 2007.

[89] K. Lebecki, M. Donahue, and M. Gutowski, "Periodic boundary conditions for demagnetization interactions in micromagnetic simulations," *Journal of Physics D: Applied Physics*, vol. 41, p. Art. No. 175005, 2008.

[90] B. Nijboer and F. De Wette, "On the calculation of lattice sums," *Physica*, vol. 23, pp. 309–321, 1957.

[91] L. Greengard, *The rapid evaluation of potential fields in particle systems*. Cambridge, MA, US: MIT Press, 1988.

[92] Y. Pan, "A fast multipole-method-based calculation of the capacitance matrix for multiple conductors above stratified dielectrical media," *IEEE Transactions on Microwave Theory and Techniques*, vol. 49, no. 3, pp. 480–490, 2001.

[93] N. Gumerov and R. Duraiswami, "Fast multipole method for the biharmonic equation in three dimensions," *Journal of Computational Physics*, vol. 215, no. 1, pp. 363–383, 2006.

[94] J. Kurzak and B. Pettitt, "Fast multipole methods for particle dynamics," *Molecular Simulation*, vol. 32, no. 10-11, pp. 775–790, 2006.

[95] D. Pissoort, M. E., D. Vande Ginste, and F. Olyslager, "Fast-multipole analysis of electromagnetic scattering by photonic crystal slabs," *Journal of Lightwave Technology*, vol. 25, no. 9, pp. 2847–2863, 2007.

[96] M. Fischer and L. Gaul, "A multipole galerkin boundary element method for acoustics," *Engineering Analysis with Boundary Elements*, vol. 28, no. 2, pp. 155–162, 2004.

[97] E. Ong, K. Lim, and H. Lee, "A fast algorithm for three-dimensional potential fields calculation: fast fourier transform on multipoles," *Journal of Computational Physics*, vol. 192, pp. 244–261, 2003.

[98] Z. Liu, H. Long, E. Ong, and E. Li, "A fast fourier transform on multipole algorithm for micromagnetic modeling of perpendicular recording media," *Journal of Applied Physics*, vol. 99, no. 8, p. Art. No. 08B903, 2006.

[99] G. Brown, T. Schulthess, D. Apalkov, and V. P.B., "Flexible fast multipole method for magnetic simulations," *IEEE Transactions on Magnetics*, vol. 40, no. 4, pp. 2146–2149, 2004.

[100] N. Gumerov, R. Duraiswami, and E. Borovikov, "Data structures, optimal choice of parameters and complexity results for generalized multilevel fast multipole methods in d dimensions," tech. rep., College Park, MD, US, 2003.

[101] L. Greengard and V. Rokhlin, "A new version of the fast multipole method for the laplace equation in three dimensions," *Acta Numerica*, vol. 6, pp. 229–269, 1997.

[102] O. Coulaud, P. Fortin, and J. Roman, "High performance blas formulation of the multipole-to-local operator in the fast multipole method," *Journal of Computational Physics*, vol. 227, pp. 1836–1862, 2008.

[103] W. Elliott and J. Board Jr., "Fast fourier transform accelerated fast multipole algorithm," *SIAM Journal on Scientific Computing*, vol. 17, pp. 198–415, 1996.

[104] P. Fortin, "Multipole-to-local operator in the fast multipole method: Comparison of fft, rotations and blas improvements," tech. rep., Cedex, France, 2005.

[105] M. Challacombe, C. White, and M. Head-Gordon, "Periodic boundary conditions and the fast multipole method," *Journal of Chemical Physics*, vol. 107, no. 23, pp. 10131–10140, 1997.

[106] A. Hubert and R. Schäfer, *Magnetic Domains*. Berlin - Heidelberg - New York: Springer Verlag, 1998.

[107] M. Donahue, "A variational approach to exchange energy calculations in micromagnetics," *Journal of Applied Physics*, vol. 83, no. 11, pp. 6491–6493, 1998.

[108] R. Skomski, "Nanomagnetics – topical review," *Journal of Physics: Condensed Matter*, vol. 15, pp. R841–R896, 2003.

[109] F. Ott, T. Maurer, G. Chaboussant, Y. Soumare, J.-Y. Piquemal, and G. Viau, "Effects of the shape of elongated magnetic paricles on the coercive field," *Journal of Applied Physics*, vol. 105, p. Art. No. 013915, 2009.

[110] M. Jaafar, R. Yanes, A. Asenjo, O. Cyuhbykalo-Fesenko, M. Vásquez, E. González, and J. Vicent, "Field induced vortex dynamics in magnetic ni nonotriangulars," *Nanotechnology*, vol. 19, p. 285717, 2008.

[111] Y. Nakatani, A. Thiaville, and J. Miltat, "Head-to-head domain walls in soft nano-strips: a rifined phase diagram," *Journal of Magnetism and Magnetic Materials*, vol. 290-291, pp. 750–753, 2005.

[112] R. Hertel and J. Kirschner, "Magnetization reversal dynamics in nickel nanowires," *Physica B*, vol. 343, pp. 206–210, 2004.

[113] U. Nowak and D. Hinzke, "Magnetic nanoparticles: the simulation of thermodynamic properties," *Advances in Solid State Physics*, vol. 41, pp. 613–622, 2001.

[114] H. van den berg, "Domain structures in soft-ferromagnetic thin-film objects," *Journal of Applied Physics*, vol. 61, pp. 4194–4199, 1987.

[115] J. McCord, A. Hubert, and A. Chizhik, "Domains in hysteresis patterned soft magnetic elements," *IEEE Transactions on Magnetics*, vol. 33, no. 5, pp. 3981–3983, 1997.

[116] I. Mayergoyz, *Mathematical models of hysteresis and their applications*. New York: Springer, 2003.

[117] V. Basso, G. Bertotti, A. Infortuna, and M. Pasquale, "Preisach model study of the connection between magnetic and microstructural properties of soft magnetic materials," *IEEE Transactions on Magnetics*, vol. 31, no. 6, pp. 4000–4005, 1995.

[118] L. Dupré, G. Ban, M. Von Rauch, and J. Melkebeek, "Modelling of microstructural effects on magnetic hysteresis properties," *Journal of Physics D: Applied Physics*, vol. 195, no. 1, pp. 233–249, 1999.

[119] D. Makaveev, *Karakteriseren en neuraal-netwerkgebaseerd modelleren van rotationele magnetisatie in niet-georiënteerd elektrisch staal*. PhD thesis, Ghent University, 2003.

[120] D. Everett, "A general approach to hysteresis – part 4, an alternative formulation of the domain model," *Transactions Faraday Society*, vol. 51, pp. 1551–1557, 1955.

[121] M. De Wulf, *Karakterisering en energieverliezen onder unidirectionele magnetisatie in relatie tot de microstructuur van zacht magnetische materialen*. PhD thesis, Ghent University, 2002.

[122] R. Albanese, G. Rubinacci, and F. Villone, "An integral computational model for crack simulation and detection via eddy currents," *Journal of Computational Physics*, vol. 152, pp. 736–755, 1999.

Research funded by a PhD grant of the Institute for the Promotion of Innovation through Science and Technology in Flanders (IWT-Vlaanderen).